Band Termination Spectroscopy of ^{157}Er

Thesis submitted in accordance with the requirements of
the University of Liverpool for the degree of Doctor of Philosophy

by Sarah Jane Gale

October 1994

Abstract

The region of rare earth nuclei with N$\simeq$90 are known as transitional nuclei, they are particularly rich in nuclear structure at high spin. The phenomenon studied in this work is the transition from collective rotation of the nucleus (prolate shape) to single particle behaviour (oblate shape) with the observation of band termination (all the available valence particles are fully aligned). A band termination state indicates the decline of static pairing correlations of the valence nucleons.

The balance and interplay between the collective and single paritcle methods of generating angular momentum have been studied in neighbouring nuclei. This work was proposed to determine if similar mechanisms are present in ^{157}Er.

The nuclear shape transition is expected to occur at high spin (low intensity), the sensitivity of the Eurogam Phase I spectrometer was utilised for the detection of these high spin states.

New and extended bands observed in ^{157}Er have been studied and related to those in ^{157}Ho [DR92] and ^{158}Er [JS94]. ^{158}Er has a prolate ground state deformation, the yrast structure is collective until spin, I, $\simeq 40\hbar$, where a single particle structure is yrast, indicating an oblate nuclear shape. Energetically favoured states in both ^{157}Er and ^{158}Er have been interpreted as a crossing of the prolate collective and the oblate single particle structures [IR86]. These favoured states can be obatined by organising the valence nucleons in an optimal way. Specific single particle configurations have been assigned to the favoured states by comparisson to ^{158}Er and cranked Nilsson-Strutinsky calculations [IR94].

The observation of single particle states is important in fixing the energy differences between single particle orbitals in the Nilsson model, resulting in the revision of the standard parameters used [RB90].

The level scheme was established at high spin using up to four-fold $\gamma-$ray concidences. The ^{114}Cd(^{48}Ca,5n)^{157}Er reaction was used at a bombarding energy of 210 MeV. Particularly favoured states have been established at $I^{\pi} = \frac{69}{2}^{+}, \frac{81}{2}^{+}, \frac{71}{2}^{+}, \frac{77}{2}^{-}, \frac{87}{2}^{-}$ and $\frac{89}{2}^{-}$.

The first high-K band in ^{157}Er has been observed in the data. Interpretation and quasi-particle assignment are made. This structure is compared with similar structures in the light erbium region.

Acknowledgements

I would Like to thank Professor P.J. Twin as head of department for allowing me to persue this research at the University of Liverpool. This analysis was carried out between October 1991 and 1994.

I would like to express gratitude to Professor J.F. Sharpey-Schafer, my supervisor, for his guidance and, more importantly, moral support. This analysis was made under the direction of my surrogate supervisor, Dr. John Simpson, who must be congratulated for his constant help and patience. I would also like to thank Dr. Mark Riley for his help and advice throughout this analysis, mainly via. electronic mail, and Dr. Ingemar Ragnarsson for his work on the theoretical aspects of this work. I would like to thank Dr. Eddie Paul for his help throughout my three years as a research student, his ability to recall any equation, reference or complete section of a Nilsson diagram at any moment, is not only helpful, it's damned impressive.

Many thanks the Crew of the Nuclear Structure Facility who provided the means necessary to run the ^{157}Er experiment, and, who must be congratulated for operating the NSF to exceptional standards for the 10 years it was operational.

Many thanks must go to Dr. Dave Radford who created the analysis packages used that made my life considerably easier. Thanks to Pete Jones for all the help with the computer problems.

I would like to thank the students of the Nuclear Structure Group for their support and the regular philosophical musings at The Oxford and my friends Andy and Gary for allowing me to kip on their floor while writing this thesis.

Finally, I would like to express gratitude towards my parents who have supported me throughout my years as a student.

Contents

Chapter 1

Nuclear Models

1.1 Introduction

With the discovery of the neutron by Chadwick in 1932 it became clear that the nucleus was composed of two types of particles, neutrons and protons. Unlike the proton, outside the nucleus the neutron is not stable, it has a half-life of ~10 minutes. The proton and neutron have approximately equal mass (mass difference ~0.2%) and are both fermions.

Contemporary physics has no complete theory of nuclear forces and therefore an adequate theory must be built using models created from a basis of experimental results.

1.2 Liquid Drop Model

This model describes the nucleus as a liquid, ie. a liquid drop. The properties of a nucleus described by the liquid drop model are listed below,

- low compressibility
- defined surface
- saturation of nuclear forces (at distances greater than the nuclear radius the effect of the force is zero)

The liquid drop model is efficient at reproducing bulk properties of the nucleus, one such property is the binding energy of the nucleus.

The Weissäcker semi-empirical mass formula [KK87], equation 1.1, reproduces binding energies for nuclei in terms of A, the atomic mass number, N the number of neutrons and Z the number of protons in the nucleus.

$$B(N,Z) = a_v A - a_s A^{2/3} - a_c \frac{Z^2}{A^{1/3}} - a_{sym} \frac{(N-Z)^2}{A} + \Delta(A) \qquad (1.1)$$

The term including a_v is the volume term, so named as it is proportional to A($\propto$ R^3, R = radius of the nucleus).

The second term is proportional to R^2 and is referred to as the surface term. This term describes the fact that nucleons near the surface contribute less to the binding energy than those in the 'interior'.

The third term is the Coulomb term, it contains the a_c constant. This term has been added to include the Coulomb repulsion between protons into the calculation.

The term including a_{sym} is the asymmetry term. As a result of the Coulomb repulsion between protons it is energetically favourable to fill the nucleus with neutrons rather than protons, this term has been added to reflect this.

The $\Delta(A)$ term is an additional correction to the asymmetry term, resulting from the observed effects of pairing in the nucleus (section1.6).

The values of the parameters a_v, a_s, a_c, a_{sym} and Δ are obtained from fits to experimental data.

The liquid drop model was the first attempt to apply a nuclear model in order to understand the basic mechanisms of the nucleus. This model gives a good fit to the experimentally measured binding energies of nuclei, although when individual results are examined discrepancies appear, manifestations of an apparent fine structure can be seen.

1.2.1 Deformation of the Nucleus

If the nucleus rotates or vibrates surface oscillations occur, resulting in a deformed liquid drop. Such a shape change can be described by parameterising the radius using spherical polar co-ordinates as shown in equation 1.2.

$$R(\theta,\phi) = R_\circ \left\{1 + \sum a_{\lambda\mu} Y_{\lambda\mu}(\theta,\phi)\right\} \qquad (1.2)$$

$\mathrm{Y}_{\lambda\mu}(\theta,\phi)$ are the spherical harmonics, $\alpha_{\lambda\mu}$ are spherical harmonic coefficients. λ indicates the multipolarity of the deformation surface oscillation and μ is an integer ranging from $-\lambda$ to $+\lambda$.

The liquid drop model is based on an incompressible nucleus implying a constant volume. The constant volume restriction is incorporated into the equation by the use of $R_\circ$ (equation 1.3), the radius of a sphere with a volume equal to that of the deformed nucleus.

$$R_\circ = r_\circ A^{1/3} \tag{1.3}$$

A = nuclear mass number. $r_\circ$ = 1.2 fm, determined empirically.

The coefficient α_{00} describes the change in nuclear volume. Due to the incompressibility of the nucleus the calculation of this coefficient is quite straightforward. For axially symmetric nuclei the lowest form of surface deformations are

$\lambda = 1$ (dipole deformation)

$\lambda = 2$ (quadrupole deformation)

The dipole mode of deformation is equivalent to a translation of the whole system. Equation 1.2 makes the centre of mass a function of deformation, which in an axially symmetric system is unrealistic. The corresponding $\alpha_{1\mu}$ coefficients are zero when the condition that the origin must always coincide with the centre of mass is satisfied. By considering the quadrupole mode of deformation five $\alpha_{2\mu}$ coefficients can be defined. These can be reduced to two real independent variables, α_{20} and α_{22}, giving a complete description of the system. The coefficients α_{20} and α_{22} describe the nucleus by the introduction of two new deformation parameters, γ and β_2.

$$\alpha_{20} = \beta_2 cos\gamma \tag{1.4}$$

$$\alpha_{22} = \frac{1}{\sqrt{2}}\beta_2 sin\gamma \tag{1.5}$$

β_2 reflects the differences between major and minor axes, the elongation of the axially symmetric shape.

$$\beta_2 = \frac{4}{3}\sqrt{\frac{\pi}{5}}\frac{\Delta R}{R_o} \tag{1.6}$$

β_2 positive $\longrightarrow$ prolate shape

β_2 negative $\longrightarrow$ oblate shape

The parameter γ, triaxiality, describes the shape of the nucleus. If γ is not a multiple of 60° the three spatial axes have different lengths. Figure 1.1 illustrates the shape of the nucleus at given values of γ.

1.2.2 Problems with the Liquid Drop Model

The effect of 'magic numbers' similar to those observed in atomic physics were observed experimentally. Examples of these shell effects can be found in general nuclear

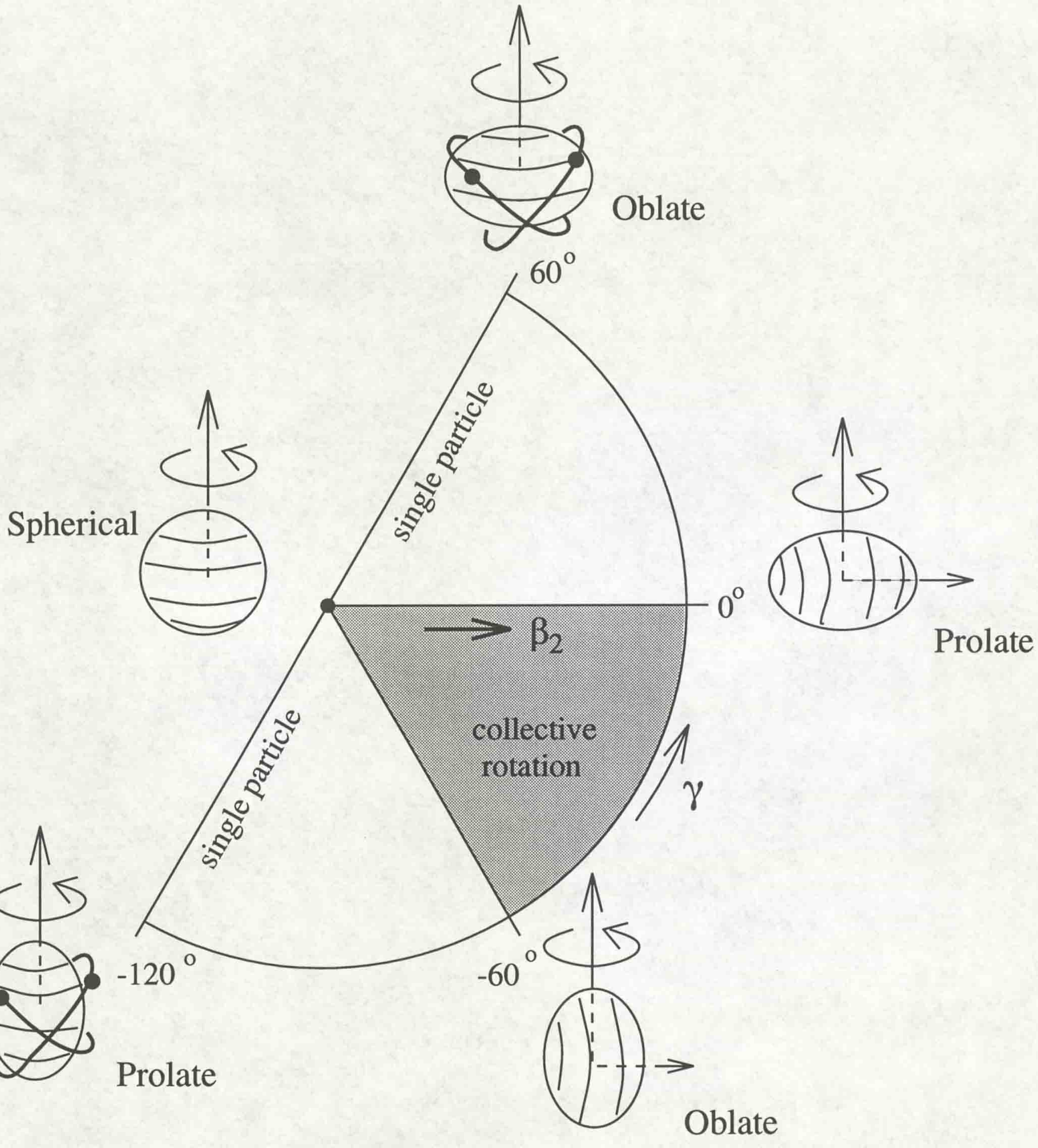

Figure 1.1: *Nuclear shapes described by the triaxiality parameter,* γ

physics references such as [KK87]. Such evidence implies a quantum structure of the nucleus which cannot be explained using the liquid drop model. Nucleons are fermions, the behaviour of such particles is restricted by the Pauli exclusion principle, two nucleons cannot occupy the same state (ie. have identical quantum numbers). This quantum nature of nucleons is not considered in the liquid drop model.

1.3 The Nuclear Force

From experimental data it has been shown that the forces between two protons are very similar to those between two neutrons, 'charge symmetry of nuclear forces'.

The deuteron (a proton bound to a neutron) gives information on the identity of the nuclear force. The very existence of the deuteron implies that there must be some degree of attraction between neutrons and protons, if only repulsive forces were acting the deuteron would not be a stable nucleus.

From experimental data it can be deduced that the nuclear force must fulfill the following criteria:

- a nucleon at the centre of the nucleus must feel no net force
- a nucleon at the surface will experience a net force towards the centre

In order to describe the nuclear force a potential must be developed that will reproduce experimental observations (the force is simply the derivative of the potential with respect to r, the nuclear radius). The nuclear Hamiltonian, $\hat{H}$, must have a potential and a kinetic energy term, in the form given in equation 1.7.

$$\hat{H} = \hat{T} + \hat{V} \tag{1.7}$$

where $\hat{T} = -\frac{\hbar^2}{2m}\nabla^2 =$ Kinetic energy and $\hat{V} =$ Potential energy

1.4 The Shell Model

Observations of magic numbers imply the nucleus has a shell structure similar to that used to describe electrons in the atom. The shell model is a method of organising nucleons into groups or shells. The position (the energy) of a particular nucleon in this hierarchy is totally dependent on its quantum identity, ie. its quantum numbers. The

shell model is a quantum mechanical model of the nucleus, a spherically symmetric system where neutrons and protons are treated separately.

It will be seen in chapters one and two that the search for an accurate nuclear potential involves the introduction and subsequent invalidation of nuclear symmetries. Nuclear symmetries are also referred to as quantum numbers. These symmetries describe the degeneracy of levels/states in the nucleus. As our understanding of nuclear mechanisms improves the number of true symmetries (those that are not violated by properties of nuclei, for example rotation of the nucleus) decreases and the level degeneracy is reduced.

The nucleus is regarded as a whole when applying the liquid drop model, whereas each nucleon is considered individually within the shell model. The shell model is also known as the independent particle model. When using a single particle model the total energy of the nucleus is equal to the sum of individual nucleon energy.

1.4.1 Nuclear Potentials

In order to describe complex nuclear systems the basic mechanism of a nuclear potential must be understood. In atomic physics the concept of a shell structure was developed from the idea of an electron 'orbiting' a central potential created by the nucleus. In the nucleus there is no equivalent central potential, therefore the theoreticians have to improvise.

1.4.2 The Mean Field

The mechanism used to describe an approximate central potential generated by the nucleons is the mean field. Each nucleon in the nucleus moves in a one body field created by the others, this determines the motion of the nucleon which in turn determines the field, the mean field is therefore self consistent.

The idea of the mean field is only possible because nucleons are fermions and can therefore move freely in the core without interacting with other nucleons. This is a property of the Pauli exclusion principle (PEP) which states that identical nucleons (neutrons or protons) cannot occupy the same state, ie have the same quantum numbers. If nucleons interacted in the core, scattering would take place. Due to PEP the nucleon would have to scatter into an empty energy level (set of quantum numbers). The nature of the core is such that no free energy levels are available, for scattering

to occur the nucleon would have to obtain enough energy to scatter from the core to the nearest available energy level. A gain in such a large amount of energy is unlikely. The smaller the momentum/energy of a nucleon the more important this restriction becomes. For a more detailed account of the mean-field see [SJ87].

The mean field is an approximation, a mathematical tool, it can be improved by the addition of residual interactions, such an interaction is discussed later.

The following nuclear potentials impose a structure on the mean field, an identity that is constantly improved to obtain better agreement with experimental results.

In the shell model the neutrons and protons occupy discrete energy levels in the nucleus. The nucleons are treated separately and a description of the nucleus, the total Hamiltonian, can be obtained by simply summing all the single particle Hamiltonians together, as shown below.

For each single particle (neutron or proton) a Hamiltonian can be written

$$\hat{h_i} = -\frac{\hbar^2}{2m}\nabla_i^2 + V(r_i) \tag{1.8}$$

The total Hamiltonian can be written

$$\hat{H} = \sum_{i=1}^{A}\left[-\frac{\hbar^2}{2m}\nabla_i^2 + V(r_i)\right] \tag{1.9}$$

1.4.3 Harmonic Oscillator

A commonly used mean field potential is the three dimensional harmonic oscillator, written in equation 1.10.

$$V(r) = \frac{m\omega_o^2}{2}(r^2 - R^2) \tag{1.10}$$

ω_o is the oscillator frequency. The shape of the harmonic oscillator, in two dimensions, is shown in figure 1.2. Using equation 1.7 and 1.10 the nuclear Hamiltonian including the harmonic oscillator is given in equation 1.11. The subscript 'ho' indicates the choice of harmonic oscillator as the nuclear potential.

$$\hat{H}_{ho} = -\frac{\hbar^2}{2m}\nabla^2 + \frac{m\omega_o^2}{2}(r^2 - R^2) \tag{1.11}$$

From this Hamiltonian energy eigen-values, E_{nl}, can be calculated, equation 1.12.

$$E_{nl} = \hbar\omega_o(N + \frac{3}{2}) = \hbar\omega_o(2n + l + \frac{3}{2}) \tag{1.12}$$

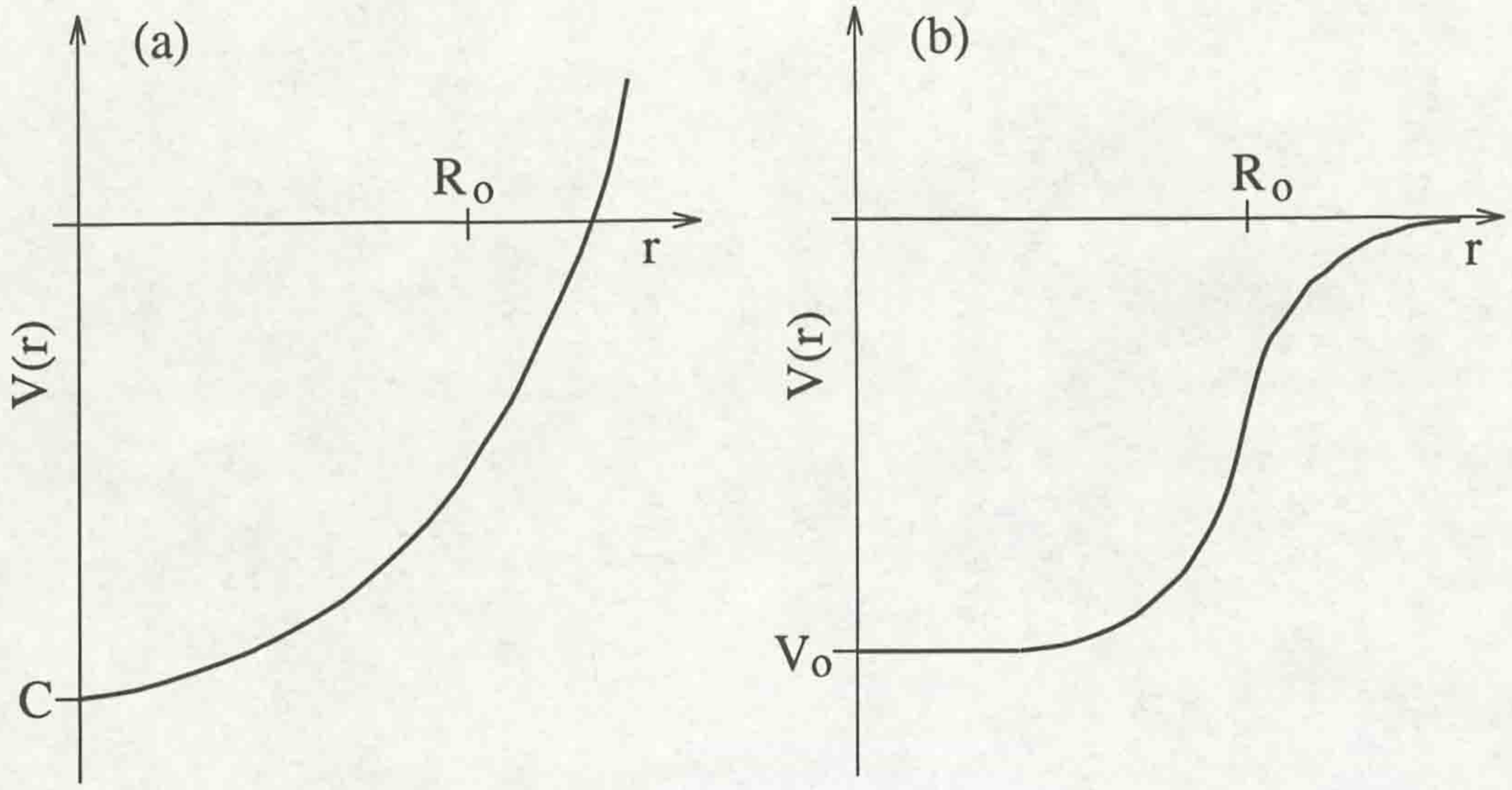

Figure 1.2: *Two dimensional illustrations of common nuclear potentials, (a) the harmonic oscillator potential, (b) the Woods-Saxon potential.*

where n is the principal quantum number, l is the orbital angular momentum quantum number and the factor of $\frac{3}{2}$ is present because a three dimensional harmonic oscillator is used.

The energy eigen-values form oscillator shells, each energy level has a degeneracy of :

$$2(2l+1)$$

For a potential to be successful the magic numbers observed experimentally must be duplicated, ie. the closure of shells should correspond to the magic numbers observed experimentally. Figure 1.3 shows the energy levels produced by the harmonic oscillator and the corresponding shell gaps (magic numbers).

1.4.4 Spin-Orbit Coupling

The harmonic oscillator is independent of the intrinsic angular momentum or 'spin' of the nucleons. In order to obtain a better agreement with experimental results, as with atomic physics, a term representing spin is added to the nuclear Hamiltonian, in the form of a spin-orbit interaction (coupling) term.

A classical illustration of spin-orbit coupling is shown in figure 1.4. It can be seen in the figure that the projection of $\underline{l}$ or $\underline{s}$ onto the axis of symmetry (z axis) is not a constant value, therefore the two quantum numbers l and s are not conserved (the

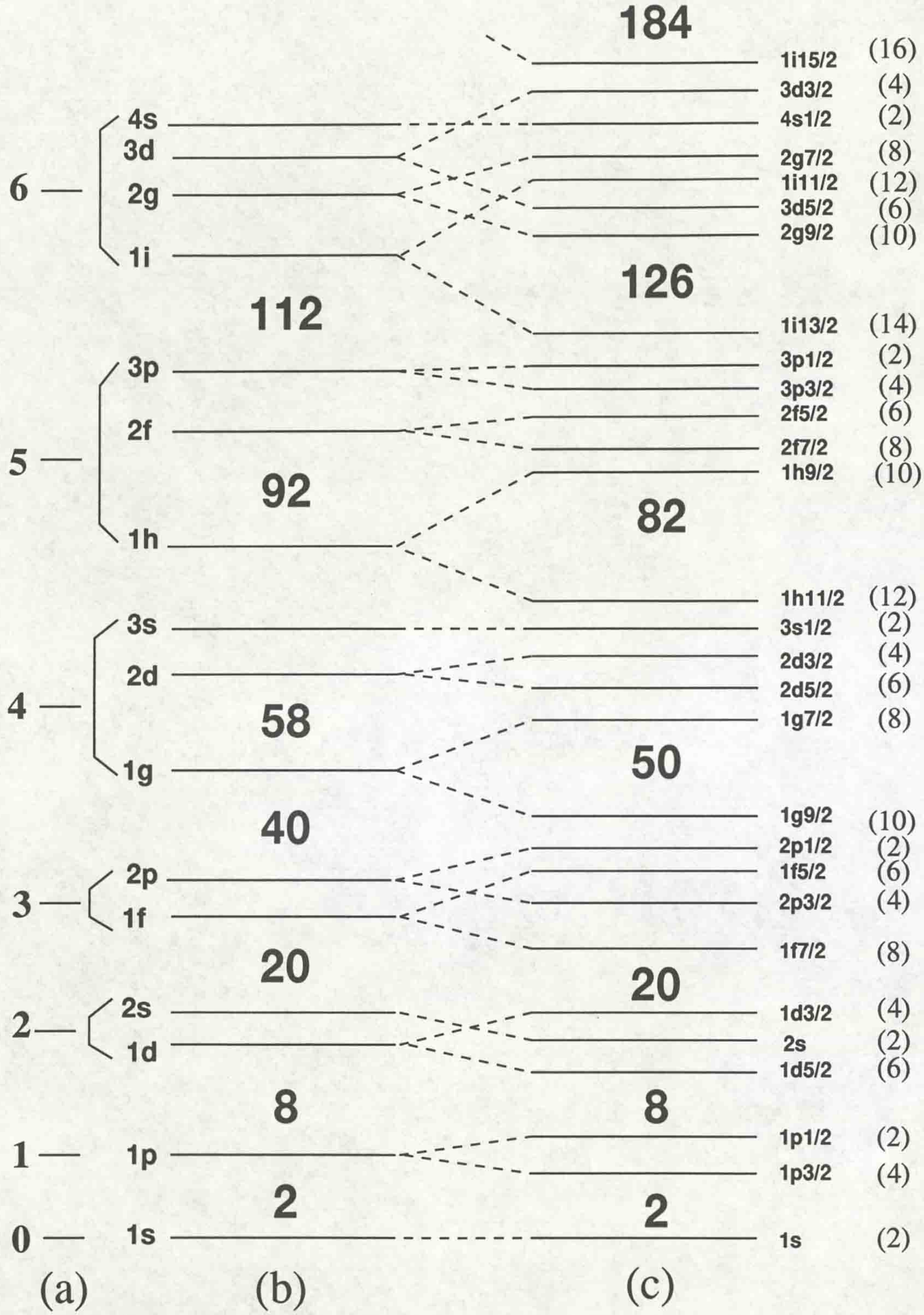

Figure 1.3: *Theoretical energy levels using, (a) the harmonic oscillator potential, the oscillator shells are labelled 1 to 6 in units of $\hbar\omega$, (b) The Woods-Saxon potential and (c) The Woods-Saxon potential with spin-orbit coupling [KK87]*

symmetries are broken). The sum of $\underline{l}$ and $\underline{s}$, $(= \underline{j})$ is conserved and introduces a new quantum number. This phenomenon is described by the spin-orbit interaction and is written in equation 1.13.

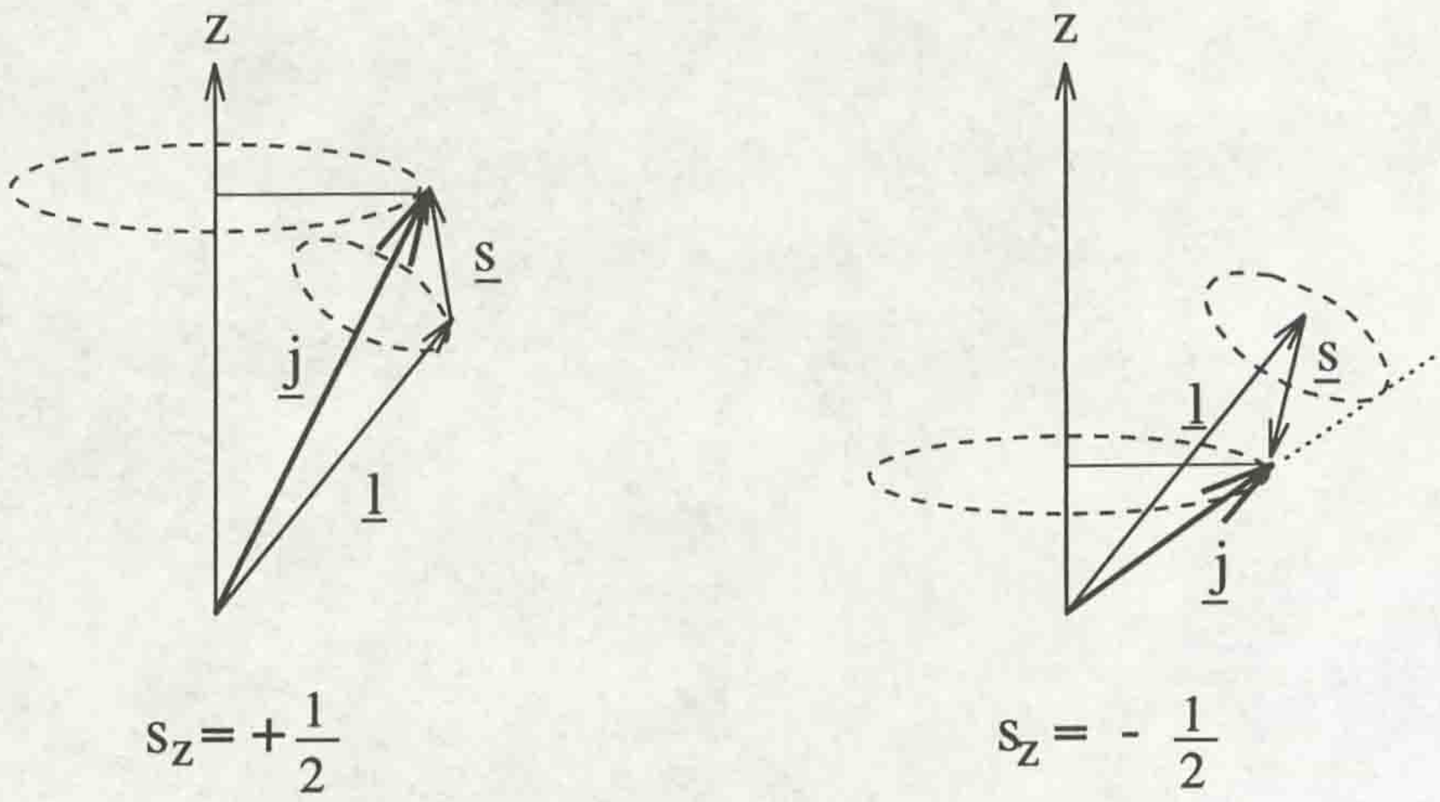

Figure 1.4: *Diagram illustrating the spin orbit coupling of a nucleon with (a) spin* $= +\frac{1}{2}\hbar$ *and (b) spin* $= -\frac{1}{2}\hbar$

$$\underline{j} = \underline{l} + \underline{s} \tag{1.13}$$

The calculation of the projection of $\underline{j}$ onto the symmetry axis, the quantum number j, is shown below.

$$< l_z >= \hbar m_l \quad \Longrightarrow \quad -l \leq m_l \geq l \tag{1.14}$$

$$< s_z >= \hbar m_s \quad \Longrightarrow \quad -s \leq m_s \geq s \tag{1.15}$$

$$< j_z >= \hbar m_j \quad \Longrightarrow \quad -j \leq m_j \geq j \tag{1.16}$$

where l,s and j are orbital, spin and total angular momentum respectively. The total measured spin for a nucleon is written:

$$m_j = m_l + m_s = m_l \pm \frac{1}{2} \tag{1.17}$$

To incorporate the spin-orbit coupling term into the Hamiltonian a potential energy form of the term, the spin-orbit potential, has to be used, as written in equation 1.18.

$$V_{so} = -f(r)\underline{l}.\underline{s} \tag{1.18}$$

where $\underline{l}.\underline{s}$ is the spin orbit term and $f(r)$ is a function of the potential. The new Hamiltonian now has the form

$$\hat{H} = \hat{T} + \hat{V_{ho}} + \hat{V_{so}} \tag{1.19}$$

$$= -\frac{\hbar^2}{2m}\nabla^2 + \frac{m\omega_o^2}{2}(r^2 - R_o^2) - f(r)\underline{l}.\underline{s} \tag{1.20}$$

The degeneracy of the levels is written

$$degeneracy = 2j + 1$$

The spin orbit term is very sensitive to orbitals with high angular momentum, j. The effect of spin-orbit coupling on high j levels is a reduction in the total energy of the level, due to their large angular momenta the energy of these levels decrease further and rapidly with deformation and rotation of the nucleus. These high j, low energy levels are referred to as intruder levels.

The addition of the spin-orbit interaction to the Hamiltonian reproduces experimental results more successfully. To improve the calculations further the nuclear potential is changed.

1.4.5 Woods-Saxon Potential

The Woods-Saxon potential (V_{ws}) is a more realistic, version of the harmonic oscillator. The harmonic oscillator potential remains finite at radii greater than that of the nucleus, which is clearly unrealistic as the nuclear force is zero outside the nucleus. The Woods-Saxon potential modifies the harmonic oscillator so that the potential is equal to zero beyond the nuclear radius. The shape of the potential well is given a more realistic flat bottom and the walls are made steeper. Figure 1.2 illustrates the differences between the harmonic oscillator and the Woods-Saxon potentials. The mathematical form of the Woods-Saxon potential is given below.

$$V_{ws} = \frac{-V_o}{1 + \exp[\frac{r - R_o}{a}]} \tag{1.21}$$

V_o is the potential depth ($\sim$50MeV), R_o is the nuclear radius (equation 1.3) and a is the surface thickness ($\simeq$0.5fm). The nuclear Hamiltonian can be rewritten

$$\hat{H} = \hat{T} + \hat{V_{ws}} + \hat{V_{so}} \tag{1.22}$$

$$\hat{H} = -\frac{\hbar^2}{2m}\nabla^2 + \frac{-V_o}{1 + \exp[\frac{r - R_o}{a}]} - f(r)\underline{l}.\underline{s} \tag{1.23}$$

1.4.6 Deformation

It has been assumed in the shell model so far that the nucleus is spherical, although experimental evidence indicates the presence of stably deformed nuclei. For example, measurements of quadrupole moments in nuclei imply a deformed nucleus (if mass

and charge distribution are spherically symmetric, the quadrupole moment will be zero). A more detailed description of the electromagnetic properties of the nucleus is given in chapter 3.

More evidence of a stably deformed nucleus is the observation of rotational bands. If the symmetry axis is the same as the axis of rotation of the nucleus, rotation of the system cannot be observed. With a spherically symmetric system the symmetry axis can be defined as any diameter of the sphere, therefore the axis of rotation is equivalent to the axis of symmetry. Rotation cannot be observed as the rotated system cannot be distinguished from the original state. If the nucleus is deformed and the axis of symmetry is not aligned with the axis of rotation, rotational structures can be observed.

In order to describe such stably deformed behaviour, a deformed potential must be used.

1.4.7 The Nilsson Model

The Nilsson model is a modification of the harmonic oscillator (see equation 1.10). Energy levels are calculated for a single particle moving in an axially symmetric deformed potential.

$$V_{nils} = V_{osc} - 2k\hbar\omega_o[\underline{l}.\underline{s} - \mu(l^2 - < l^2 >_N)] \tag{1.24}$$

where

$$V_{osc} = \frac{m}{2}[\omega_x^2 x^2 + \omega_y^2 y^2 + \omega_z^2 z^2]$$

The second part of the potential is a spin orbit coupling term. The $(l^2 - < l^2 >_N)$ term has been introduced to flatten the potential. The parameters k and μ are adjusted to fit experimental data. V_{osc} has been modified for axially symmetric shapes and the oscillator frequencies obtain the following form (the z axis is defined as the symmetry axis).

$$\omega_z = \omega_o(\varepsilon_2)(1 - \frac{2}{3}\varepsilon_2) \qquad \omega_x = \omega_y = \omega_o(\varepsilon_2)(1 + \frac{1}{3}\varepsilon_2)$$

the constant volume condition is conserved by

$$\omega_x\omega_y\omega_z = \overset{o}{\omega}_o{}^3 = \text{Constant}$$

$\overset{o}{\omega}_o$ is the value of $\omega_o(\varepsilon_2)$ at $\varepsilon_2 = 0$, this oscillator frequency is commonly calculated using the equation given below.

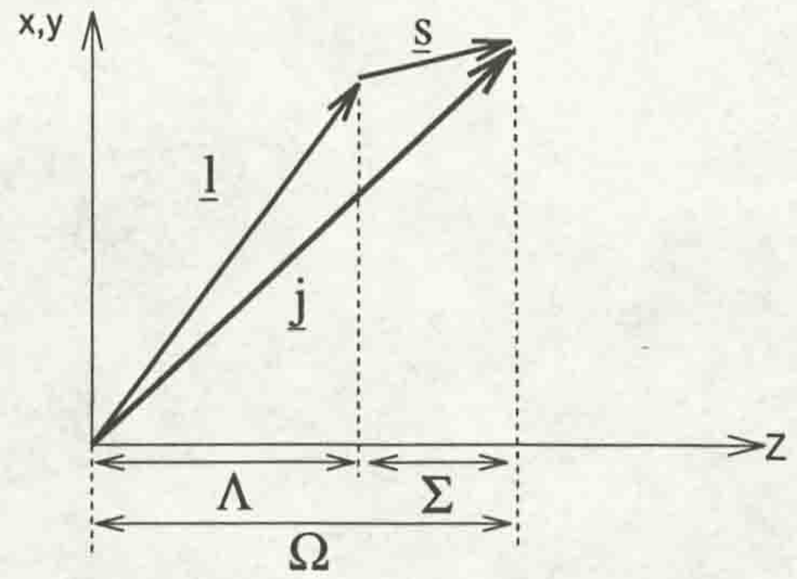

Figure 1.5: *Diagram illustrating the labelling of levels used in Nilsson diagrams.*

$$\hbar\,\overset{o}{\omega}_o \simeq 41A^{-1/3}\ \text{MeV}$$

$\hbar\omega_o$ used in equation 1.24 is calculated separately for neutrons and protons, the formula is given in equation 1.25 [BF86].

$$\hbar\omega_o = \hbar\,\overset{o}{\omega}_o\left[1 \pm \frac{(N-Z)}{3A}\right] = 41A^{-1/3}\left[1 \pm \frac{(N-Z)}{3A}\right] \tag{1.25}$$

$+$ for neutrons and $-$ for protons. N, Z and A are the number of neutrons, protons and the mass number respectively.

With this model a new deformation parameter describing the elongation of the axially symmetric shape is introduced, ε_2, see below. The deformation parameter, β_2 was introduced in section 1.2.1

$$\varepsilon_2 \simeq 0.95\beta_2 \tag{1.26}$$

The energy levels produced from this model, Nilsson levels, are described using a labelling scheme consisting of quantum numbers (illustrated in figure 1.5).
Λ and Ω are projections of orbital and total angular momentum onto the symmetry axis.

$[N, n_z, \Lambda]\Omega^\pi$ where $N =$ oscillator shell number
$n_z =$ number of quanta along the symmetry axis
$\pi =$ parity $= (-1^N)$, not always included in labels

The Nilsson levels are two-fold degenerate, each level can have an eigen-value of $\pm\Omega$. Figure 1.6 shows an example of a Nilsson diagram (single particle energy levels), it can be seen that levels with the same π and Ω do not cross, therefore these are the only quantum numbers conserved in this model.

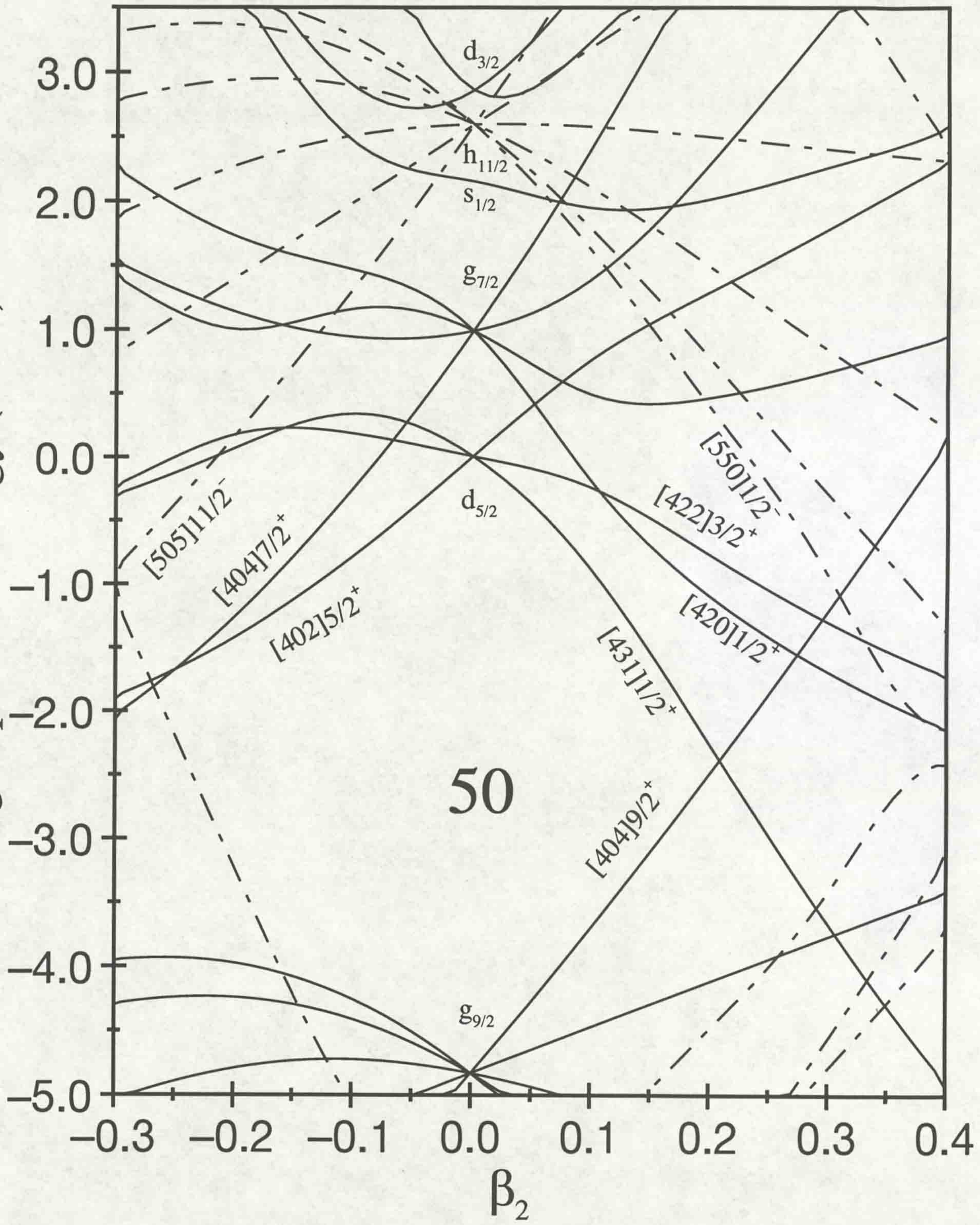

Figure 1.6: *Nilsson diagram for protons, calculated using the Woods-Saxon potential.*

1.4.8 Deformed Woods-Saxon Potential

When using the Nilsson model it was found that the $(l^2 - < l^2 >_N)$ term 'pushes' the levels down in energy too much. Therefore, to improve the nuclear potential, the Woods-Saxon potential (equation 1.22) was modified to incorporate deformation(equation 1.27), see reference [BF86].

$$V_{dws}(r,\beta) = \frac{-V_o}{1+\exp(\frac{dist_\Sigma(r,\beta)}{a})} \tag{1.27}$$

$dist_\Sigma(r,\beta)$ represents the distance from the nuclear surface, β is the deformation of the nucleus. Parameters are adjusted to reproduce experimental results.

The independent particle model using a deformed potential is very successful at calculating properties of nuclei in the ground state, mainly because such nuclei are near spherical. This method is not so effective when considering nuclei at greater deformations.

1.5 The Strutinsky Shell Correction

The liquid drop model is successful in reproducing the bulk properties (properties of the nucleus in which all nucleons contribute), whereas the shell model is successful at reproducing the fine structure of the nucleus. The Strutinsky shell correction is a method created to incorporate both models into a complete description of the nucleus addressing the problem of nuclear masses and their dependence on deformation. Initially the Nilsson level scheme was used to calculate the difference between the shell and liquid drop models in terms of occupation number and deformation. A strong correlation between the shell correction and the nuclear level density was observed, ie. the effect of shell gaps (magic numbers) [VS67].

Within the Strutinsky shell correction, these quantum effects are considered as small deviations from a uniform distribution, or oscillations. The liquid drop model is a macroscopic description of the nucleus assuming a uniform distribution of nucleons in phase space. The shell model assumes a quantal distribution of nucleons. With a smooth distribution of levels the binding energy per nucleon varies smoothly with the position of the Fermi level. With a shell structure the binding energy per nucleon oscillates with position of the Fermi level, depending on its position in the shell.

These deviations, the energy difference (δU), can be expressed as the difference between the shell model calculations (single particle energies summed over all the

occupied states), U, and the energy, $\overline{U}$, calculated over a uniform distribution of states. The correction is written:

$$\delta U_{shell} = U_{shell} - \overline{U}_{shell} \tag{1.28}$$

The shell model energy, U_{shell}, is calculated in equation 1.29 below.

$$U_{shell} = \sum E_\nu 2n_\nu \tag{1.29}$$

E_ν is the energy obtained from the Nilsson level scheme and n_ν is the occupation number. The occupation number is equal to either 1 or 0, $n_\nu = 0$ indicates the level is empty, $n_\nu = 1$ indicates occupation of the level. The factor of 2 is included as each Nilsson level can contain two nucleons, the nucleons must have spin of equal magnitude but opposite sign to satisfy the Pauli exclusion principle.
$\overline{U}$ describes the shell model energy calculated assuming a uniform distribution of nucleon states and is written

$$\overline{U} = 2\int_{-\infty}^{\overline{\lambda}} E\overline{g}(E)dE \tag{1.30}$$

$\overline{\lambda}$ is the Fermi level (chemical potential) and $\overline{g}(E)$ is a density of states function describing the uniform distribution of nucleon states in the nucleus. The density of states function is calculated by 'smearing' the level densities into a smooth distribution. The Fermi level is determined by applying the condition that the number of nucleons remain constant at any deformation. In the shell model, the Fermi level is defined as the average energy of the last filled and first unfilled level. As with equation 1.29 the factor of 2 in equation 1.30 represents two nucleons per energy level.

The total energy of the nucleus can be written

$$W = \overline{W}_{LDM} + \delta_{shell} \tag{1.31}$$

Where $\overline{W}$ is the the liquid drop model energy (see section 1.2).

The accuracy of the correction depends on the difference between the assumption of a uniform distribution of nucleons used in the uniform density of states function and the realistic distribution.

The Strutinsky correction can be used to reproduce experimental ground state energies of nuclei and their dependence on deformation. The accurate reproduction of experimental results has led to stable highly deformed nuclei, such as fission isomers to be predicted [VS67].

A complete Strutinsky correction including various other terms is discussed in section 2.3.

1.6 Pairing

Pairing is a residual interaction and is added to the shell model. The existence of this force was proposed to explain why the ground state spin of even-even nuclei is 0 and the reason such nuclei are strongly bound in comparison to their even-odd neighbours.

To obtain a ground state spin of 0 pairs of single particle states with the same quantum numbers appear to be treated specially. The nucleus apparently 'remembers' to keep the total angular momentum coupled to 0 (anti-parallel). This situation can only happen if there is an additional force with the following properties:

- attractive (even-even nuclei more strongly bound)
- short range, compared to nuclear dimensions (has to be attractive to pairs with the same quantum numbers and zero everywhere else)

To reflect the above the potential will have the form given in equation 1.32 below.

$$V_{pair} = \delta(r_1 - r_2) = 0 \tag{1.32}$$

The nature of this interaction is to scatter a pair of nucleons coupled to $\underline{J}_{pair}(=0)$ into another $\underline{J}'_{pair}(=0)$ state; $\underline{J}_{pair}$ and $\underline{J}'_{pair}$ describe the total angular momentum of the pair. This interaction is only realised for nucleons near the Fermi surface, deep inside the core no free energy levels are available, therefore scattering is unlikely to occur.

The pair of nucleons can be described as occupying the same orbital with the same quantum numbers, to satisfy the Pauli exclusion principle the nucleons must travel in opposite directions (time reversed orbits). The two nucleons in the pair will have total angular momentum of equal magnitude and opposite sign, giving a resultant value of zero for the pair. The pair of nucleons scatter many times into different orbits but always remain with $\underline{J}_{pair} = 0$, see figure 1.7.

The pairing interaction is strong, pairs of nuclei will spend noticeable amounts of time above the Fermi surface, leading to the smearing of the Fermi surface. If many pairs are involved the residual force will cause the nucleus to adopt a paired configuration.

The Hamiltonian describing this scattering process can be written:

$$\hat{H}_{pair} = -G \sum_{kk'} a_k^+ a_{\overline{k}}^+ \quad a_{k'} a_{\overline{k'}} \tag{1.33}$$

G is the average matrix element representing the residual interaction. This equation describes the following steps in the scattering of a pair. The pair of nucleons are

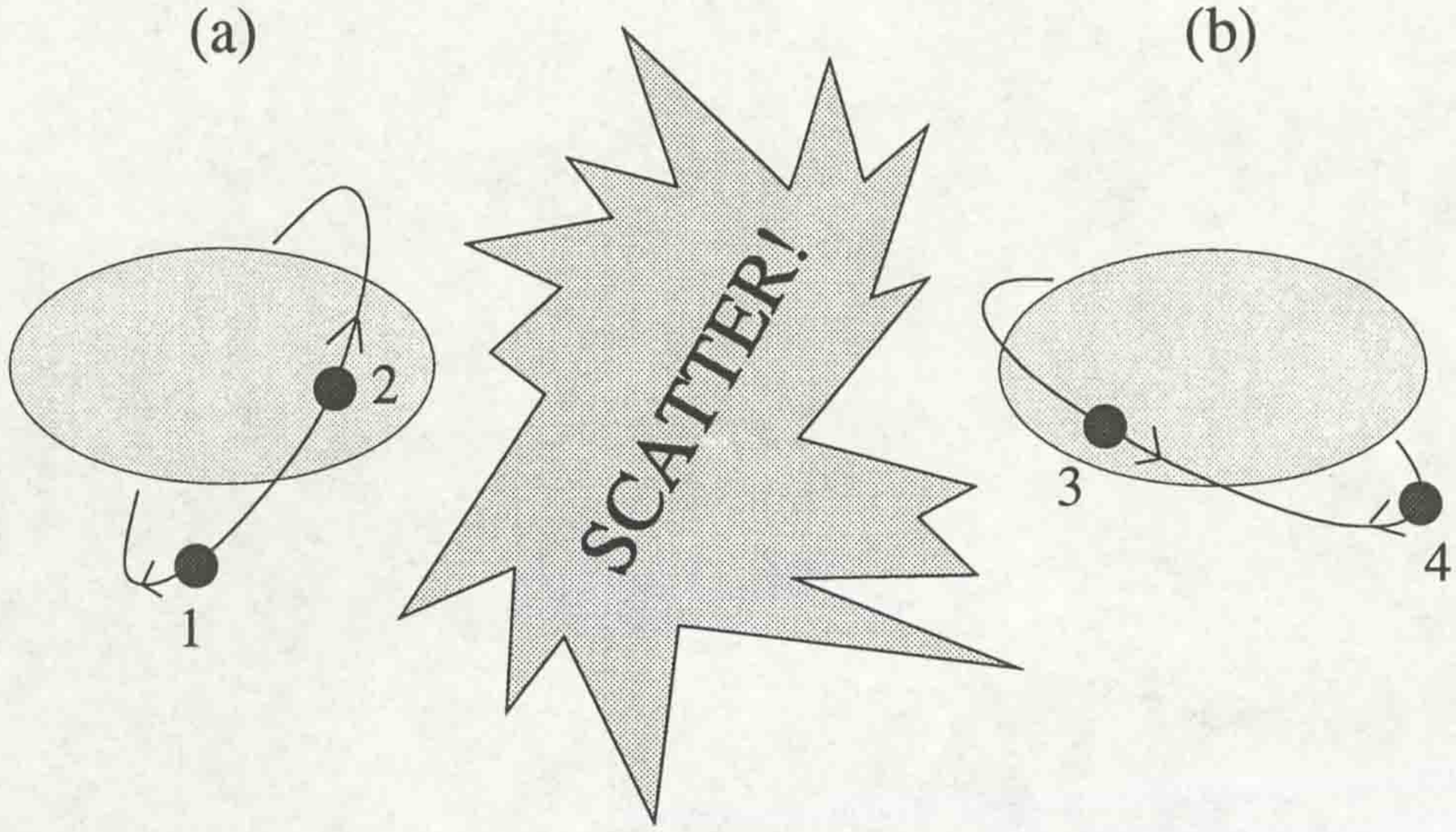

Figure 1.7: *A illustration of the scattering of a pair of nucleons initially in state (a) and finally in state (b). The condition* $J_{pair} = 0$ *is satisfied in both states (a) and (b).*

initially in state X each with total angular momentum $+\underline{J}_{k'}$ and $-\underline{J}_{k'}$, they scatter leaving state X unoccupied (represented by the annihilation operators $a_{k'}a_{\overline{k'}}$). The nucleons reappear in state Y with total angular momentum $+\underline{J}_k$ and $-\underline{J}_k$ (represented by the creation operators $a_k^+ a_{\overline{k}}^+$).

1.6.1 Quasiparticles

The introduction of pairing into nuclear models adds extra complications to an already complex system. As a result of pairing the nucleons constantly scatter above and below the Fermi surface. It is not practical to develop a full mathematical description of a system where the occupation of levels is constantly changing between hole and particle. It is therefore necessary to describe the probability of the occupation of a given level.

A common method used to simplify problems in quantum mechanics is to change the basis of the wave functions. Bogolyubov used this method by introducing the idea of quasiparticles instead of conventional nucleons. Quasiparticles are fictitious mathematical objects, they are neither particle or hole, but linear combinations of the old particle and hole wave functions. The destruction of a pair creates two quasiparticles, both have a combined particle-hole character. Quasiparticles are analogous to Cooper pairs (electron pairs) used to describe super conductivity in the BCS, Bardeen Cooper

Schreiffer, theory (for a general explanation see [PM84]). Theoretical solutions to the equations combining quasiparticles into the nuclear Hamiltonian are obtained using the Hartree-Fock method [JC82], these are called Hartree-Fock-Bogolyubov (HFB) calculations. In order to obtain realistic results from HFB calculations boundary conditions have to be imposed. One such condition is given in equation 1.34, defining the particle hole character of a quasiparticle.

$$\nu_k^2 + u_k^2 = 1 \tag{1.34}$$

ν_k^2 is the particle and u_k^2 the hole probability (=amplitude^2) of state k. The total probability of the state being hole, particle or a mixture of both must always equal unity. By applying BCS equations to the quasiparticles in the nucleus an expression for the probability of the occupation of an energy level can be obtained [RS80], see equation below.

$$P_\nu(e_\nu) = \frac{1}{2}\left[\frac{1 + e_\nu - \lambda}{\sqrt{(e_\nu - \lambda)^2 + \Delta^2}}\right] \tag{1.35}$$

λ is the average Fermi level (energy), Δ is the pairing gap parameter and e_ν is the energy of a given Woods-Saxon level. The quantity λ is a Lagrange multiplier, it is referred to as the Fermi energy as it represents the increase in energy with particle number, N (the number of neutrons or protons). The quantities λ and Δ can be calculated from the BCS equations and are written below. The value of the Fermi surface, is adjusted until N yields the correct expectation value.

$$N = \sum_\nu \frac{1}{2}\left(\frac{1 + e_\nu - \lambda}{(e_\nu - \lambda)^2 + \Delta^2}\right) \qquad G_n = \sum_\nu \frac{1}{\sqrt{(e_\nu - \lambda)^2 + \Delta^2}} \tag{1.36}$$

The particle number, N, enables the nucleus to keep its identity. G_n is the average matrix element of the residual interaction. Both N and G_n yield different solutions for protons and neutrons.

From BCS treatment, excitation energies of the quasiparticles can be calculated with respect to the Fermi level. The single particle energies calculated using the Woods-Saxon potential, e_ν^{ws}, have been used (although any potential can be used). The excitation energy of a quasiparticle, e_ν is written in equation 1.37.

$$e_\nu = \sqrt{(e_\nu^{ws} - \lambda)^2 + \Delta^2} \tag{1.37}$$

In the case of odd nuclei the odd nucleon is not in a quasiparticle pair and is equivalent to a single quasiparticle excitation, therefore the ground state spin and

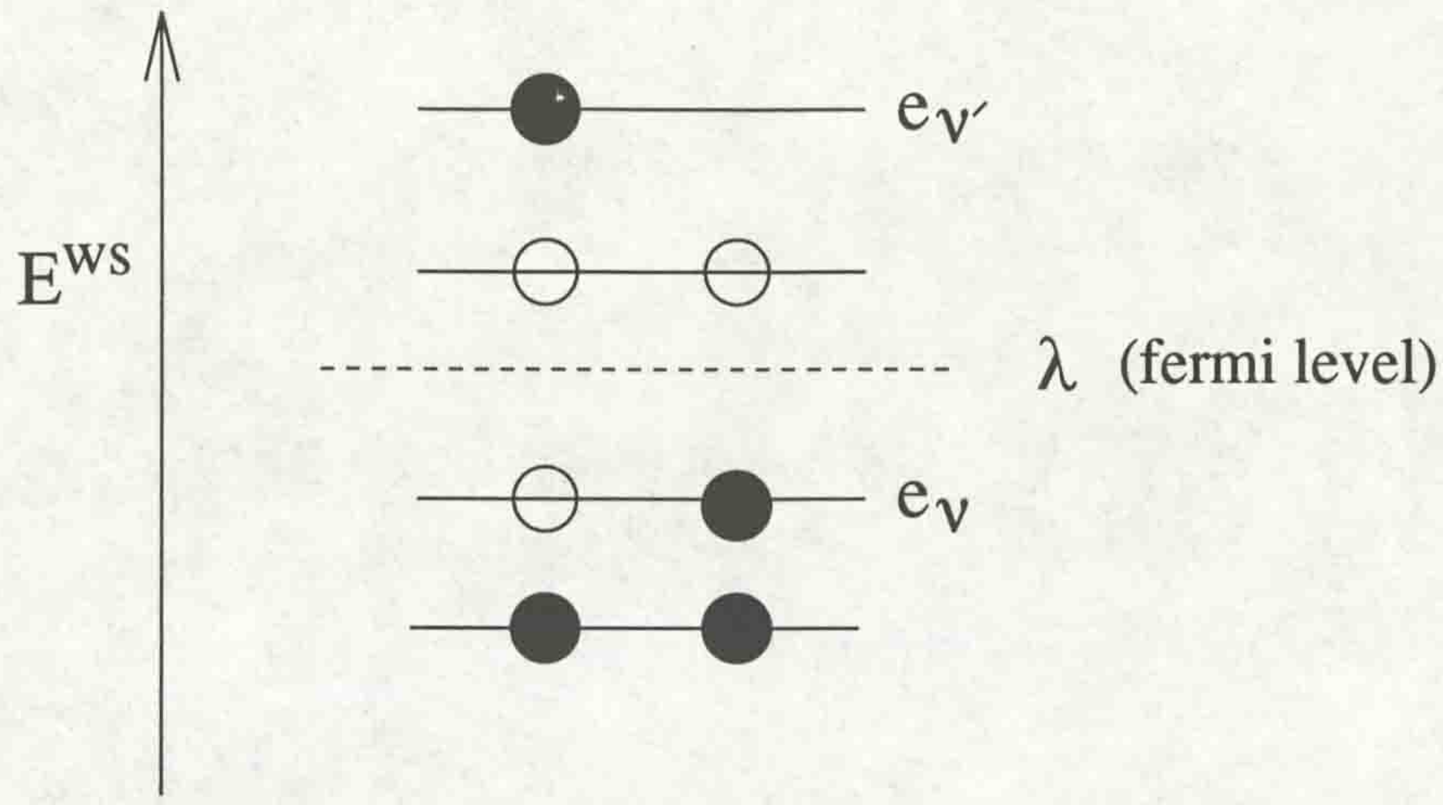

Figure 1.8: *Example of the excitation of a single particle/quasi particle near the Fermi surface.*

parity is completely dependent on the last unpaired quasiparticle. In the case of even-even nuclei all the quasiparticles are paired, a quasiparticle vacuum, the ground state spin and parity is therefore 0^+.

Figure 1.8 and the equations below illustrate the difference between a single particle excitation in an unpaired even-even nucleus and the same nucleus with pairing, where e_ν is the initial energy level and e'_ν is the final (excited) energy level.

Nucleus without pairing:

$$E_{exc} = \sqrt{(e'_\nu - \lambda)^2} + \sqrt{(e_\nu - \lambda)^2} \tag{1.38}$$

Nucleus with pairing:

$$E_{exc} = \sqrt{(e'_\nu - \lambda)^2 + \Delta^2} + \sqrt{(e_\nu - \lambda)^2 + \Delta^2} \tag{1.39}$$

It can be seen from the diagram and the equations above that an extra energy of at least 2Δ ($\simeq 1MeV$) is required to excite a particle in the nucleus with pairing. This extra energy is due to pairing in the nucleus, it is the energy required to break a pair of quasiparticles and explains why even-even nuclei are more strongly bound than their even-odd neighbours.

The total pairing Hamiltonian is written:

$$\hat{H}_{pair} = \Delta(P^+ + P^-) - \lambda\hat{N} \tag{1.40}$$

$\Delta(P^+ + P^-)$ represents the pairing correlations where P^+ and P^- are total creation and annihilation operators for the nucleus and Δ is the pairing gap. The creation

and annihilation operators for a single pair are written:

$$P_k^+ = a_k^+ a_{\overline{k}}^+ \quad P_{k'}^- = a_{k'} a_{\overline{k'}}$$

$\hat{H}_{pair}$ can now be added to the nuclear Hamiltonian. The nuclear Hamiltonian from equation 1.22 can now be written:

$$\hat{H} = \hat{T} + \hat{V}_{dws} + \hat{V}_{so} - \Delta(P^+ + P^-) - \lambda\hat{N} \tag{1.41}$$

Figure 2.3 illustrates the effect the pairing term has on the energy of the levels. Chapter 2 considers further the use of pairing in nuclear theory.

Chapter 2

Nuclear Rotation

2.1 Introduction

The shell model has been successful in predicting magic numbers and calculating energy levels within the nucleus, but it cannot explain fully experimental results. As the methods used for detecting gamma rays are improved increasingly subtle fine structure is observed.

The following section gives an example of nuclear structure observed experimentally that cannot be explained without the presence of nuclear rotation.

2.2 Collective Rotation

The nucleus can use collective rotation as a method of generating spin. To simplify calculations and understanding of nuclear mechanisms the nucleons are split further into two groups (protons and neutrons are still treated separately), core and valence nucleons.

Core nucleons - nucleons contained in closed shells

Valence nucleons - nucleons outside the last closed shell

The choice of core depends on the nucleus and deformation, usually depending on where shell gaps occur. The total angular momentum $\underline{I}$, can be written

$$\underline{I} = \underline{R} + \underline{J} \tag{2.1}$$

where $\underline{R}$ is the collective contribution from the core and $\underline{J}$ is the contribution from

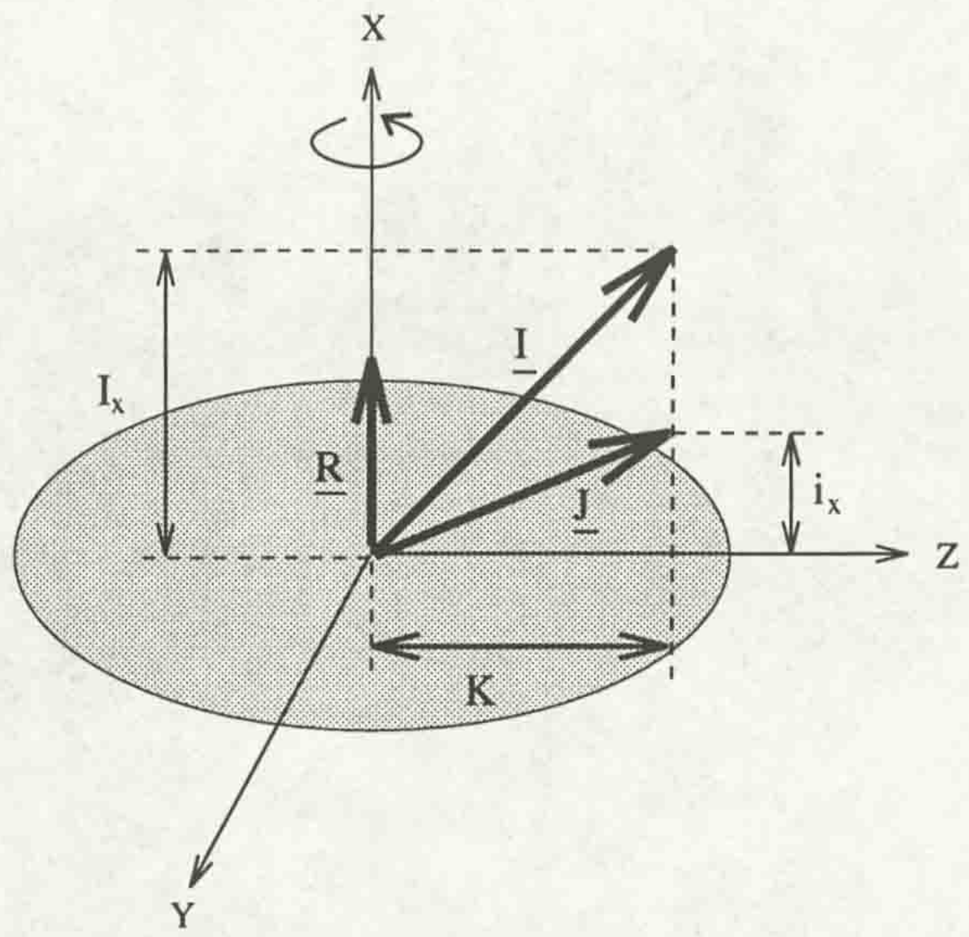

Figure 2.1: *The coupling of angular momenta from the core($\underline{R}$) with that of the valence nucleons($\underline{J}$) is illustrated in the body fixed system.*

the valence nucleons (single particle).

$$\underline{R} = \sum_{core,i} \underline{j}_i \qquad \underline{J} = \sum_{valence,i} \underline{j}_i$$

The coupling of valence and core nucleons is shown in figure 2.1, the convention of defining the x axis as the axis of rotation is used. The projection of $\underline{I}$ on to the symmetry (z) axis in the body fixed system is K, the projection onto the rotational axis is I_x. In this model both K and I_x are good quantum numbers. The K value (band-head) of a rotational band is equivalent to the Ω of the lowest level in the band. Ω is the projection of the angular momentum onto the symmetry axis (see section 1.4.7). Angular momenta from single particles are added together using the Gallagher Moskowski rule [GM58], equation 2.2 (Ω_1 and Ω_2 are single particle angular momenta).

$$\Omega = |\Omega_1 \pm \Omega_2| \tag{2.2}$$

The contribution of total angular momentum from the core is zero due to pairing and $K = 0$ for the ground state of an even-even nucleus. The K value therefore depends on the valence nucleons and the orbitals (configuration) they occupy.

The importance of the method of splitting nucleons into core and valence particles becomes apparent when dealing with nuclear excitation where the valence nucleons define the fine structure of the nucleus.

Collective rotation of the nucleus results in a rotational band, the energy levels of the bands are separated by $2\hbar$ (2 units of spin), connected by stretched electric quadrupole transitions.

For rotational bands (collective systems) the energies can be expressed as follows.

$$E_{rot}(I,K) = \frac{\hbar^2}{2\mathcal{J}}[I(I+1) - K^2] \tag{2.3}$$

The quantity $\mathcal{J}$ is the moment of inertia of the system. The moment of inertia of a nucleus depends on the mass distribution and the location of the axis of rotation.

Equation 2.3 follows the $I(I+1)$ rule. The gamma-ray energy of a transition, E_γ, is the difference between the initial and the final level. The initial level spin is defined as having spin $I+1$ and the final level $I-1$, the unit of spin, I is $\hbar$. The transition energy can then be written:

$$E_\gamma = E_{rot}^{initial}(I+1,K) - E_{rot}^{final}(I-1,K) \tag{2.4}$$

From equations 2.3 and 2.4 the following relation between theoretical and experimentally measured quantities can can be derived.

$$E_\gamma = \frac{\hbar^2}{2\mathcal{J}}(4I-2) \tag{2.5}$$

$$\hbar\omega = \frac{dE_{rot}}{dI} \simeq \frac{E_\gamma}{2} \tag{2.6}$$

The level lowest in spin of the rotational band is called the band-head. Each band-head has a different configuration, the band is therefore said to be 'based' on a particular configuration.

2.2.1 Backbending

Experimental results have shown evidence of deviations of the $I(I+1)$ rule in rotational bands (see equation 2.3). Examples of these effects are given in references [JS87] and [MR84b].

There are two methods of coupling the total intrinsic, single particle, angular momentum of the nucleus (total angular momentum generated by the the valence nucleons) to the core. The single particles can be aligned to the symmetry (z) axis, deformation aligned coupling (DAL), or the rotational (x) axis, rotationally aligned coupling (RAL). Figure 2.2 illustrates the DAL and RAL mechanisms for coupling valence nucleons to the core. The coupling is written in equation 2.7 below.

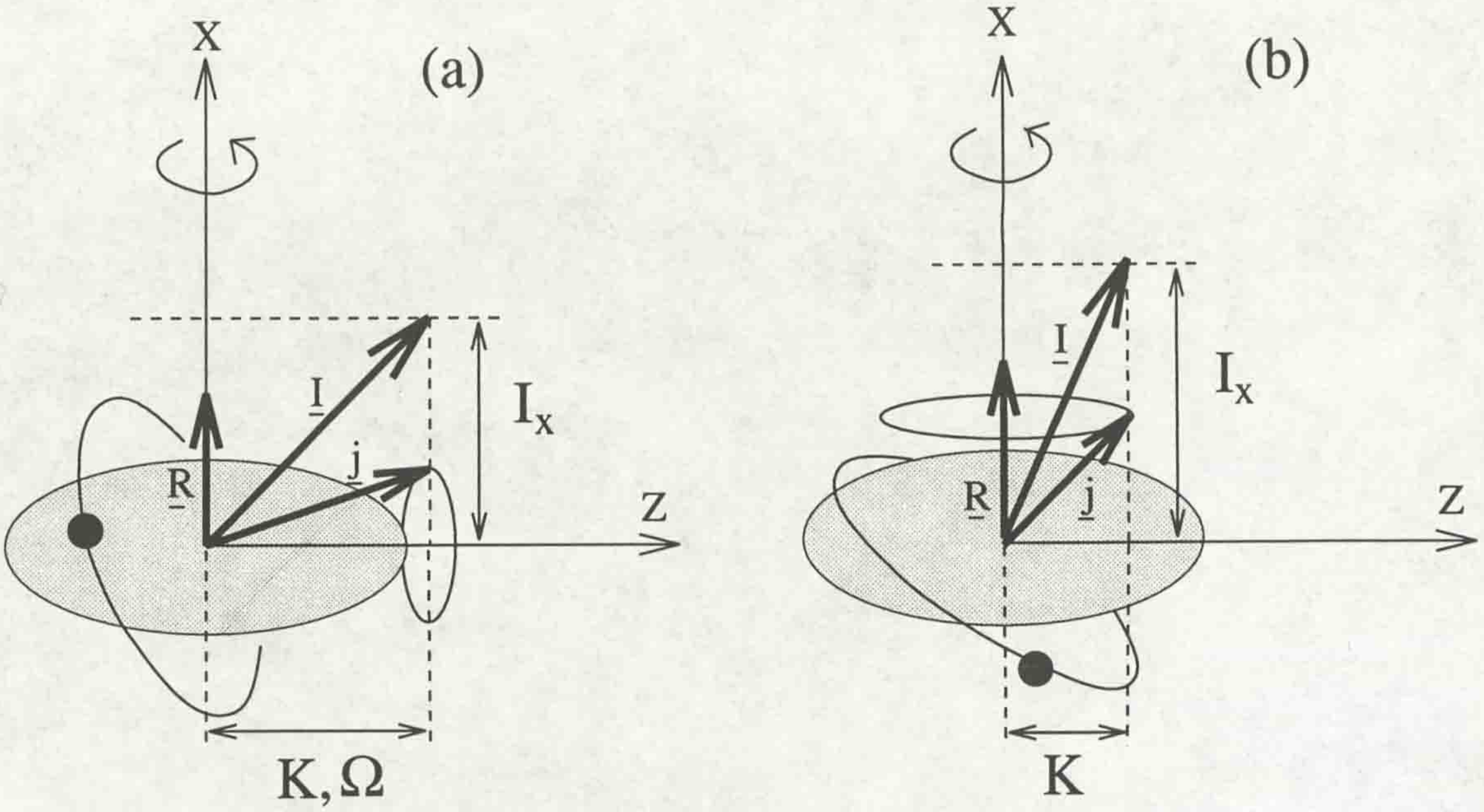

Figure 2.2: *Deformation aligned (DAL),(a), and rotationally aligned (RAL), (b), single particles.*

$$\underline{I} = \underline{R} + \underline{j} \tag{2.7}$$

Where $\underline{R}$ is the total angular momentum of the core and $\underline{j}$ is the total angular momentum of the single particle. K is the projection of the total angular momentum of the nucleus onto the symmetry axis, this quantity is not conserved in both mechanisms. I_x is the projection of total angular momentum onto the rotational axis (x), this quantity is conserved in both methods and is therefore a good quantum number. Ω is the projection of the single particle angular momentum onto the symmetry axis defined by the single particle orbital, the single particle symmetry axis changes when the method of alignment changes.

The DAL mechanism is present at low frequencies where the Coriolis force is weak. As the frequency increases the Coriolis force becomes strong enough to break a pair of nucleons and align them to the rotational axis. High-j orbitals are more sensitive to coriolis effects as can be seen in the equation below.

$$E_{Cor} = \frac{\hbar^2}{\mathcal{J}} \underline{I}.\underline{J} \tag{2.8}$$

E_{Cor} is stronger for high-j nucleons, therefore experimentally we expect to see backbending due to alignment of high-j nucleons first. $\mathcal{J}$ is the moment of inertia of the

system and is inversely proportional to the angular frequency of the nucleus, introduced in section 2.2. It can be seen in figure 2.2 that when a nucleon changes from DAL to RAL there is an increase in aligned angular momentum, I_x. Because of this gain in alignment (the nucleus has gained angular momentum) the nucleus is able to reduce its angular frequency, hence the 'backbend' shape in both the alignment plots and spectra and the violation of the $I(I+1)$ rule. The transition from the DAL to the RAL system is described in reference [FS72].

2.3 Introduction to The Cranked Shell Model

Nuclear theory has to be fine tuned in order to reflect experimental phenomena as described in section 2.2. If the experimental data cannot be explained by current theory the first step is to re-examine the nuclear force.

The nuclear Hamiltonian has been kept as 'true' as possible, but, without using mathematical 'tricks and shortcuts' the solution for one particle in a simple potential involves vast derivations. Therefore the force must be simplified, the Hamiltonian is divided into a series of functions:

$$\hat{H} = [\text{one body term}] + [\text{two body term}] + [\text{three body term}] \text{ ..etc...}$$

These terms increasingly deal with the effects of interactions involving more nucleons. The shell model deals with the one body term, the potential and kinetic energy of a single nucleon interacting with rest of the nucleus as a whole (equation 1.22). This Hamiltonian was improved by the introduction of a residual interaction, pairing (equation 1.41). To reproduce experimental results with greater accuracy a two-body nuclear Hamiltonian is introduced. An aspect of the two body term is described by the cranked shell model (CSM) [BF86].

2.4 The Cranked Shell Model

The rotation referred to in chapter 1 is defined by the rotation of individual nucleons. The cranking model introduces the idea of an additional rotation, in the rotation of the nucleus as a whole. The addition of nuclear rotation introduces centrifugal and Coriolis forces that will effect nucleon orbitals and hence, the behaviour of the nucleus as a whole.

The Hamiltonian of equations 1.22 and 1.23, will be referred to as $\hat{H}_o$ where subscript o indicates the non-rotational Hamiltonian. $\hat{H}_o$ (equation 1.22) uses V_{ws}, this can be replaced with any of the potentials described in chapter 1. $\hat{H}_o$ will be used as a basis for the cranking Hamiltonian, $\hat{H}^\omega$. The transition from a non-rotating to a rotating nucleus involves the combining of Hamiltonians, therefore the wave functions have to be modified. The single particle wave functions are non-rotational (ψ') and therefore have to be changed. The unitary operator, R is used to create a rotational wave function, ψ (equation 2.9).

$$\psi = R(\omega t)\psi' \tag{2.9}$$

where $R(\omega t) = exp(\frac{-\omega t j_x}{\hbar})$

The x axis, as before, is defined as the axis of rotation. Substituting the new rotational wave functions into the time dependent Schrödinger equation we get equation 2.10 and the single particle Hamiltonians (h^ω) can be extracted, equation 2.11.

$$i\hbar\frac{d\psi}{dt} = H\psi \tag{2.10}$$

$$h^\omega = h_o - \omega j_x \tag{2.11}$$

and the total Hamiltonian is written:

$$\hat{H} = \hat{H}_o - \omega J_x \qquad where \;\; J_x = \sum_{i=1}^{A} j_{xi} \tag{2.12}$$

Solutions to the Hamiltonian are found using the Hartree-Fock method, a self consistent procedure.

2.4.1 Pairing in the Cranked Shell Model

Pairing is now incorporated into the single particle cranking Hamiltonian, the final Hamiltonian will represent quasiparticle rather than single particle states. Using equations 1.41 (labelled below as $\hat{H}_o^{PAIR}$) and 2.12, the cranking Hamiltonian, including pairing (for quasiparticles) is written in equation 2.13 below,

$$\hat{H}^\omega_{TOTAL} = \hat{H}_o^{PAIR} - \omega J_x = \hat{H}_o - \Delta(P^+ + P^-) - \lambda N \tag{2.13}$$

therefore, the total Hamiltonian including pairing can be written,

$$\hat{H}^\omega_{TOTAL} = \hat{H}^\omega + \hat{H}_{PAIR} \tag{2.14}$$

This Hamiltonian is known as the Hartree-Fock Bogolyubov (HFB) Hamiltonian. This model assumes the nucleus consists of independently moving quasiparticles. Figure 2.3 illustrates the effect pairing and the CSM has on energy levels in the nucleus. The Hamiltonian can be solved using a method devised by Frauendorf and Bengtsson where input parameters are manipulated to obtain solutions consistent with experimental values. For a complete description of the cranked shell model see reference [BF86].

2.4.2 Band Crossings in the Cranked Shell Model

In order to use the CSM calculations with any success the diagrams produced must be understood [BF79a, BF79b]. Figure 2.4 is an example of the output from CSM calculations. The parameters for these CSM calculations are discussed in section 6.2.1. The calculated quasiparticle routhians are single particle energy levels calculated in the rotating (cranking) frame. In the cranked shell model band crossings are restricted. If two levels have the same symmetries they cannot cross, they repel each other. From this phenomenon it can be derived that only two good quantum numbers remain, these two remaining symmetries are parity and signature, discussed in section 2.4.3.

If a level is occupied (A for example) the conjugate level ($-A$) is free, therefore half the levels are always occupied. The conjugate level is the reflection of the level about $e' = 0$ resulting also in a signature change of $\alpha \rightarrow \ -\alpha$. A quasiparticle excitation arises when a level at e' is occupied freeing its conjugate partner, resulting in a change of energy (an excitation). All quasiparticle configurations for a particular nucleus can be obtained by exciting nucleons into different routhians.

Band crossings are identified by the repulsion of quasiparticles (routhians) with the same π and α. One routhian originates in the $e' < 0$ region of the diagram and the other from the $e' > 0$ region. The frequency at which the repulsion, band crossing, takes place is referred to as the crossing frequency, ω_c. Such a crossing is identified by (a) in figure 2.4. For a band crossing to take place the routhian that the quasiparticle is to 'cross' into at the frequency ω_c must be unoccupied at the particular crossing frequency, due to the Pauli exclusion principle. If the routhian is already occupied the band crossing cannot take place and the crossing is said to be 'blocked'.

The total routhian energy and the x component of the total angular momentum

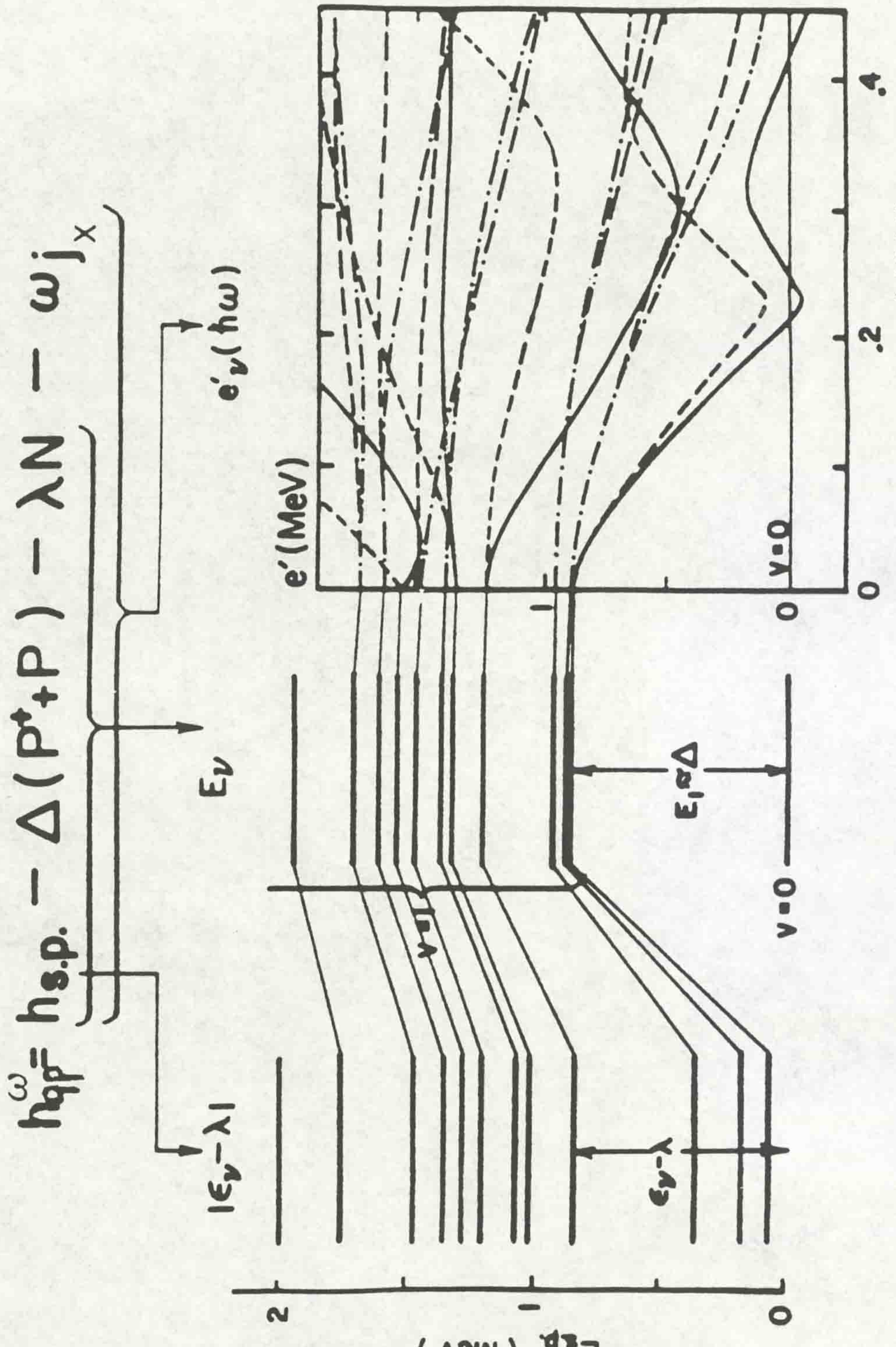

Figure 2.3: *Energy levels in a nucleus after Pairing and the Cranked Shell Model calculations*

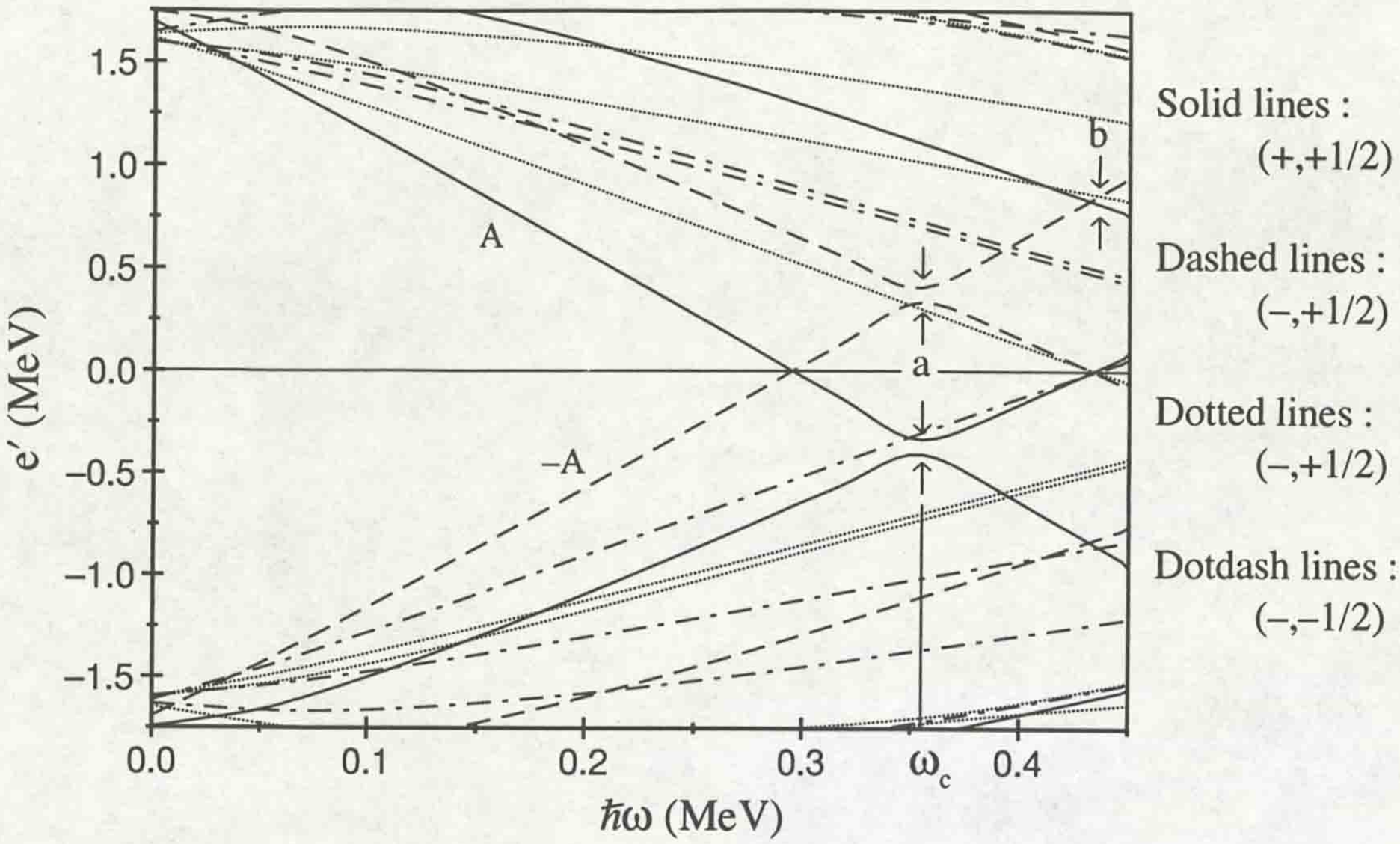

Figure 2.4: *Quasiparticle energy versus frequency diagram output from CSM calculations*

are E' and I_x respectively. These quantities are related in equation 2.15.

$$\frac{dE'}{d\omega} = -I_x \tag{2.15}$$

When relating the experimental measurements to theory only the relative quantities can be measured. The excitation energy, $e'(\omega)$ is such a quantity and is defined in equation 2.16. The projection of the angular momentum onto the x axis (axis of rotation) is called the aligned angular momentum, i_x. i_x is a relative quantity that can be obtained from experimental data (equation 2.17).

$$e' = E'_{exc}(\omega) - E'_{gs}(\omega) \tag{2.16}$$

$$i(\omega) = I^x_{exc}(\omega) - I^x_{gs}(\omega) \tag{2.17}$$

The subscripts gs and exc represent the ground and excited bands respectively. From equation 2.17 it can be seen that the alignment is the differential of the quasiparticle routhian with respect to x (equation 2.18) and is the slope of the routhian.

$$-\frac{de'}{d\omega} = < \psi | j_x | \psi > = i_x \tag{2.18}$$

The strength at which the two bands of the band crossing interact, the interaction strength, is equal to half the distance of closest approach. A sharp gain in alignment

represents a weak interaction and a smooth gain represents a strong interaction [FS72]. From figure 2.4 it can be seen that two levels with the same symmetries cannot cross, they repel each other. Therefore the quantum numbers responsible for the repulsions are the only true symmetries remaining. The two remaining symmetries conserved are parity and signature. It can be seen in figure 2.4 that if the π and α of the bands are different the routhians can cross, (b).

In the case of even-even nuclei the ground state configuration is characterised by all the $e' > 0$ levels being unoccupied. Such a state is called the quasiparticle vacuum. The last quasiparticle of nuclei with an odd number of protons or neutrons will occupy the lowest energy (first available) $e' > 0$ level and is referred to as a single quasiparticle excitation. Odd-odd nuclei have an excited quasineutron and quasiproton implying a ground state spin $\neq 0$ (the lowest energy $e' > 0$ level is occupied in the case of both the unpaired neutron and proton). The ground state of an odd-odd nucleus is described as a two quasiparticle excitation.

2.4.3 Parity and Signature

If the properties of the nucleus are invariant with respect to a rotation of 180° about an axis perpendicular to the axis of symmetry it implies that such a rotation is part of the intrinsic (not the rotational) degrees of freedom. Axially symmetric nuclei (such as ^{157}Er) display rotational invariance, where the rotation takes place about the axis of rotation (x).

Parity(π) describes the behaviour of the spatial wavefunction of a particle. The parity operator causes a reflection of all co-ordinates through the origin. If the system is left unchanged by the operator, the wavefunctions can be described:

$$|\psi(r)|^2 = |\psi(-r)|^2 \longrightarrow \psi(-r) = \pm\psi(r)$$

Stationary states of the wavefunctions must have even or odd parity. The parity of a state is given by equation 2.19.

$$\pi = (-1)^N \tag{2.19}$$

where N is the shell number used in the labelling of Nilsson orbitals. Caution must be taken when reading labels on Nilsson diagrams. Due to mixing of states from the onset of deformation, the labels are only strictly valid at $\omega = 0$ and at deformations where the degeneracy in Ω is removed. The parity of a quasiparticle configuration is

given by the product of the individual parities (see equation below).

$$\pi_{total} = \prod_{\mu} \pi_{\mu}$$

Signature(α), reflects the properties of a nucleon under rotation of 180° about the x axis (rotational axis). Signature, α is defined in equation 2.20 where $R_x(\pi)$ is a rotation of 180° about the axis of rotation.

$$R_x(\pi)\psi_\alpha = e^{-i\pi j_x}\psi_\alpha = e^{-i\pi\alpha}\psi_\alpha \tag{2.20}$$

The quantity α describes the effect of rotation of the nucleus on the pairing correlation. Classically the total angular frequency of the particle will depend on the frequency of the nucleus and the sign of the signature. The Coriolis force acting upon a particle is proportional to its angular frequency, therefore the Coriolis effects will depend on the signature of the nucleon. Signature, α, can be calculated using the following formula.

$$I = \alpha \ mod \ 2 \tag{2.21}$$

Where I = total angular momentum of the configuration. Signature is additive, therefore

$$\alpha_{total} = \sum_{\mu} \alpha_{\mu}$$

A full discussion and explanation of α and π is given in references [AG74], [BMV2] and [SJ87].

An octupole deformed nucleus, 'pear' shape, is not rotationally invariant about the axis of rotation. It has been determined experimentally that both parity and signature are violated in such nuclei [WN84], verifying that these two symmetries are a consequence of rotational invariance.

2.5 The Strutinsky Shell Correction Including Pairing and Cranking

To incorporate the liquid drop model and the HFB CSM, the strutinsky shell model has to be extended, the correction given in equation 1.28 must be adapted [RS80]. The pairing interaction is dependent on the density of states in the nucleus and is to be included in the correction.

The correction due to pairing is an oscillatory term and is calculated using ideas similar to those describing the shell correction in section 1.5. The liquid drop model parameters are adjusted to reproduce experimental masses (the effect of the pairing force is included in the model) therefore an oscillatory term reflecting the shell structure of the nucleus is required for the pairing correction, equation 2.22.

$$\delta U_{pair} = P - \overline{P} \tag{2.22}$$

P is the pairing energy calculated using the normal distribution of states in the shell model. $\overline{P}$ is the pairing energy calculated a smooth density of states function.

When cranking (rotation) is included, a term representing the change in energy with frequency must be added, equation 2.23.

$$\delta U_{CSM} = [< \psi^{\omega}|H^{\omega}|\psi^{\omega} > - < \psi^{\omega}|H^{\omega}|\psi^{\omega} >^{\omega=0}]_{CSM} \tag{2.23}$$

Equation 2.23 describes the change in energy of the CSM calculations at $\omega \neq 0$ compared to calculations when there is no rotation present in the system ($\omega = 0$). The complete Strutinsky shell correction is written

$$W_{total} = U_{LDM} + \delta U_{shell} + \delta U_{pair} + \delta U_{CSM} \tag{2.24}$$

The above equation has the same form as equation 1.28, where the δ terms reflect the correction to the liquid drop model due to the shell structure (bunching of levels and shell gaps).

2.6 Comparison of CSM Calculations to Experimental Results

CSM calculations are made in a rotating frame of reference. To compare the experimental routhians with theory, results have to be transferred into the rotating frame. Rotational frequency can be calculated as follows.

$$\hbar\omega = \frac{dE}{dI} = \frac{E_i - E_f}{I_x(I_i) - I_x(I_f)} \simeq \frac{E_\gamma}{\Delta I_x} \tag{2.25}$$

experimentally

$$I_x(I) = \sqrt{(I + \frac{1}{2})^2 - K^2} \tag{2.26}$$

For stretched quadrupole transitions the following approximation can be made.

$$\hbar\omega \simeq \frac{E_\gamma}{2} \tag{2.27}$$

The CSM provides Hamiltonians in the form of single-particle excitation energy routhians. To enable a true comparison with theory a reference representing the core has to removed from the experimental results leaving the single particle effects. Calculations can be made for either single particles or quasiparticles, depending on whether pairing correlations are a valid assumption in the region being studied. It has been discussed earlier (section 2.2) that valence nucleons provide the nucleus with an identity, for example its deformation, therefore the removal of a reference should not 'wash-out' any interesting nuclear effect. The experimental routhian, before the removal of a reference is given in equation 2.28.

$$E'(I) = \frac{1}{2}(E_i - E_f) - \omega(I).I_x(I) \tag{2.28}$$

The choice of reference is generally a ground state band in an even-even nucleus. The final experimental energy routhians, $e'(\omega)$ and the alignment, $i_x(\omega)$, are given below.

$$e'(\omega) = E'(\omega) - E'_{ref}(\omega) \tag{2.29}$$

$$i_x(\omega) = I_x(\omega) - I_x^{ref}(\omega) \tag{2.30}$$

where

$$I_x^{ref}(\omega) = (\mathcal{J}^0 + \omega^2\mathcal{J}^1)\omega \tag{2.31}$$

$\mathcal{J}^0$ and $\mathcal{J}^1$ are Harris parameters [SH65]. The Harris parameters enable good, two parameter, fits to rotational energy levels in nuclei. The parameters are fitted to the reference band. The energy of this band ($E'_{ref}(\omega)$) can be obtained from equation 2.32.

$$E'_{ref}(\omega) = -\int I_x^{ref} d\omega \tag{2.32}$$

It can then be found that

$$E'_{ref}(\omega) = \frac{1}{2}\omega^2\mathcal{J}^0 - \frac{1}{4}\omega^4\mathcal{J}^1 + \frac{1}{8\mathcal{J}^0} \tag{2.33}$$

At high frequencies structural changes may have an effect on the usefulness of the reference band, therefore an excited single or quasiparticle band can be used as a reference, improving the accuracy at these frequencies. Such an addition to the reference is shown in equation 2.34.

$$I_x^{ref}(\omega) = i_x^{ref}(excitedband) + (\mathcal{J}^0 + \mathcal{J}^1\omega^2)\omega \tag{2.34}$$

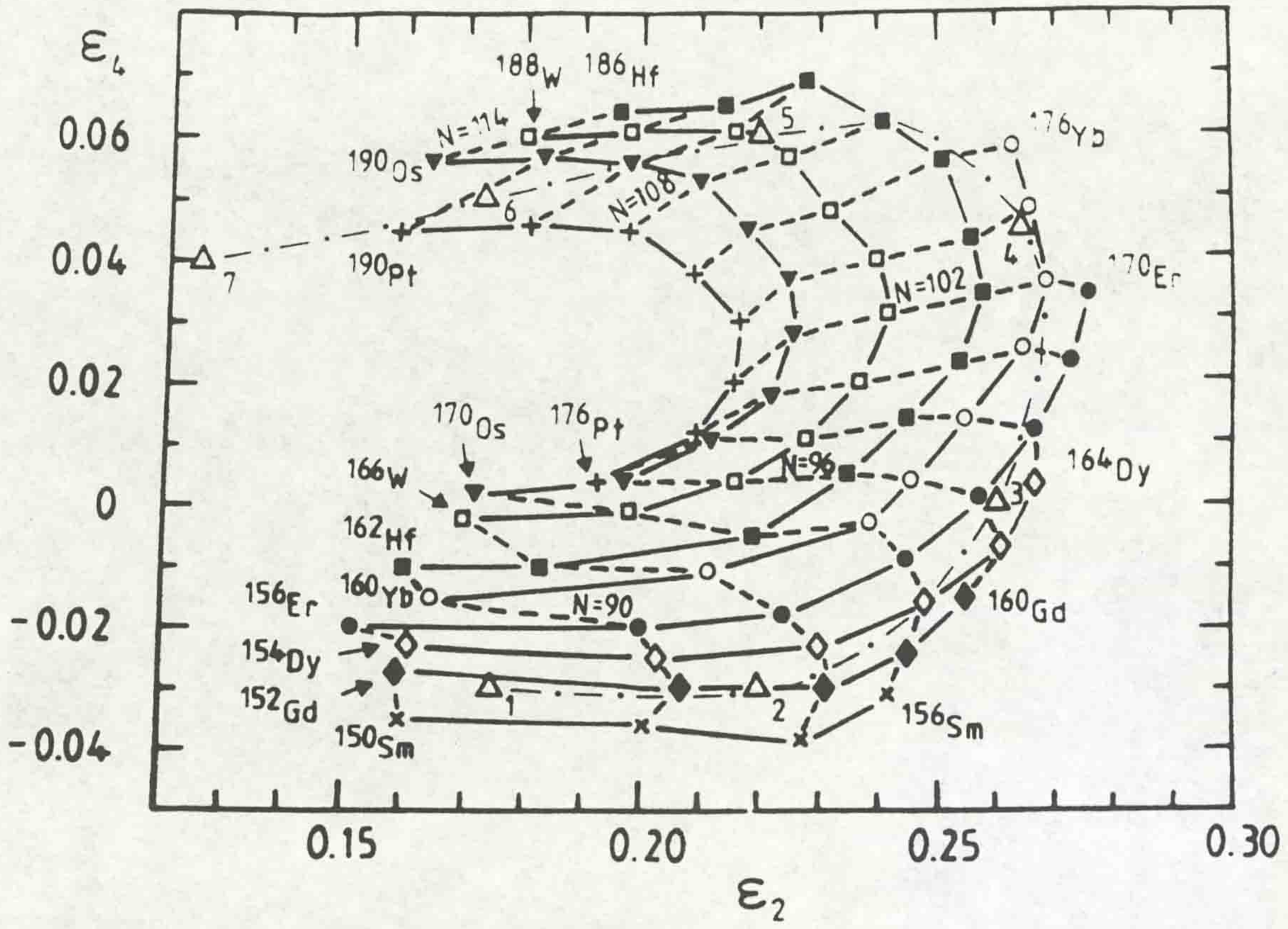

Figure 2.5: *Theoretical ground state deformations of even-even nuclei isotopes [FH93].*

2.7 Nuclear Shapes and Angular Momentum

The ground state of a nucleus can have its overall shape (triaxiality, deformation) generated by one of two methods.

- the polarisation effects of nucleons (this leads to deformed nuclei)
- pairing correlations (pairing likes to keep the nucleus in a spherical shape)

Nuclei near closed shells are near spherical in shape because of pairing correlations. Nuclei far from closed shells have a deformed shape due to polarisation effects of the valence nucleons. In the rare earths the near spherical shaped nuclei are in the $N = 82 - 86$ region. The deformed prolate shaped nuclei are in the $N \geq 92$ region. The nuclei in the $87 \leq N \leq 92$ region are referred to as transitional nuclei, the ground state shape changes rapidly with N. Figure 2.5 illustrates these shape changes. The method the nucleus uses to generate angular momentum is also very important in defining the shape of the nucleus. Angular momentum can be generated by collective rotation or single particle excitation.

2.7.1 Collective Nuclear Shape

For purely collective rotation the axis of rotation is perpendicular to the symmetry axis. This implies that the nucleons have polar orbits. Purely collective nuclei have a triaxiality, γ, of $0°$ and $-60°$, describing collective prolate and oblate nuclei respectively. A prolate collective nucleus favours low-j orbitals (see section 2.2.1). Collective rotation is described in section 2.2.

2.7.2 Non-Collective/Single Particle Shape

Non-collective rotation cannot exist, the energy generated by single particles is referred to as a single particle excitation. For single particle excitations the symmetry axis of the nucleon aligns with that of the rotational axis of the nucleus. Oblate single particle configurations favour high-j orbitals (see section 2.2.1). Fully aligned orbitals have an equatorial path. Angular momentum is increased by rearranging the nucleons into fully aligned orbitals. A non-collective nucleus has a triaxiality of 60^o and -120^o, oblate and prolate shapes respectively.

Triaxiality is discussed in section 1.2.1, figure 1.1 illustrates collective and non-collective states. The collective nuclear shape generally describes the core and the ground state of the nucleus whereas single particle states can be used to describe the valence nucleons of an excited nucleus. As the nucleus gains angular momentum the nucleons are able to align their angular momentum with the axis of symmetry, rather than the axis of rotation.

2.7.3 Band Termination

When the rotation of the nucleus increases single particles align the symmetry axis of their orbitals with the axis of rotation of the nucleus. The alignment of single particles implies one nucleon will occupy an energy level (state). When a nucleon is aligned it has the maximum spin possible for the state, therefore, due to the Pauli exclusion principle only one nucleon can occupy an energy level. The alignment of nucleons involves the breaking of pairs in the nucleus, a change from a collective to a single particle (non-collective) structure.

The nucleons involved in observed band terminating states are generally the valence nucleons only, as it costs a lot of energy to break a pair of nucleons in the core. When the valence nucleons have aligned fully with the axis of rotation the band

is said to terminate [WN93]. A band terminating state is that with the maximum amount of angular momentum possible for a given configuration and therefore the valence nucleons are single-particle in nature. The total angular momentum (spin) of a fully aligned state is the sum of the individual single particle angular momentum.

These fully aligned (band terminating) states have a triaxiality of $\gamma = 60°$ or $\gamma = -120°$, the symmetry axis is the same as the axis of rotation (non-collective). This band terminating process is therefore associated with a shape change, for example, a transition from a collective prolate to a non-collective oblate structure. The experimental results will reflect the change in mechanism used to generate angular momentum, showing an abrupt transition from a regular rotational (collective) structure to a single particle (a seemingly random distribution of gamma-ray energies) structure at the onset of the terminating sequence. An example of such a transition is given in figure 2.6.

Band termination can only be observed over a narrow band of nuclei. The number of particles outside the last closed shell must be large enough to allow for collective rotation at low spin. If the number of valence nucleons is too large the band terminating configuration will be at such a high spin that it will be almost impossible to observe, the excitation energy of such a state would be so high that the probability of fission before forming the state would be almost unity.

The $N \sim 90$ region fulfills the requirements of band termination.

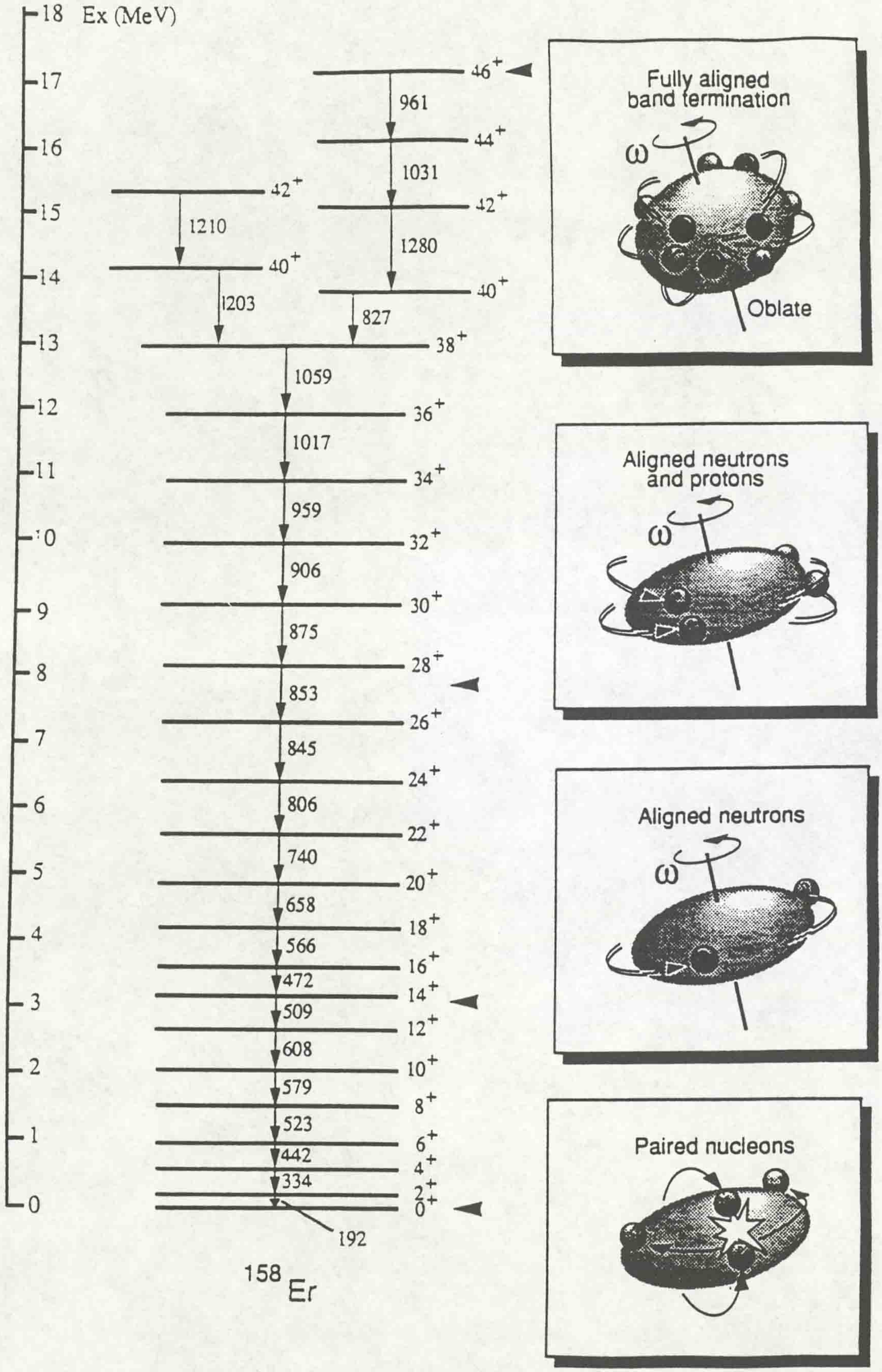

Figure 2.6: *A classic example of band termination, the yrast band of* ^{158}Er

Chapter 3

Electromagnetic Properties of the Nucleus

A distribution of electric charge will produce an electromagnetic field and the distribution is assigned a multipole moment. Multipole moments form an infinite power series, this converges quickly and only the first few terms are found to be important. In general, the nature of the nucleus is such that it will acquire, if possible, a symmetric structure and therefore lower terms of multipole moments characterise the electromagnetic properties of the nucleus.

3.1 Electromagnetic Moments

In the case of this analysis magnetic dipole and electric quadrupole moments are relevant, these multipole moments will be covered in this work.

3.1.1 Magnetic Dipole Moment

Magnetic fields in a nucleus can be generated by two mechanisms, orbiting charged particles (protons) and by the intrinsic spin of the nucleon (each nucleon generates its own field). The magnetic dipole moment for a single nucleon is calculated using equation 3.1.

$$\mu_{nucleon} = \mu_{orbital} + \mu_{spin} \tag{3.1}$$

$\mu_{orbital}$ is the contribution of magnetic moment from the orbital angular momentum of the nucleon and μ_{spin} is the contribution from the intrinsic angular momentum.

These terms are calculated using equations 3.2.

$$\mu_{orbital} = g_l l \mu_N \qquad \mu_{spin} = g_s s \mu_N \tag{3.2}$$

Where $\mu_N = \frac{e\hbar}{2m}$ = the nuclear magneton, g_l and g_s are the orbital and spin angular momentum g-factors respectively. An expression of the magnetic dipole moment of a single nucleon can therefore be written:

$$\mu = \mu_N(g_l l + g_s s) \tag{3.3}$$

The magnetic dipole moment of the nucleus describes the charge distribution. and therefore it was expected that the orbital magnetism would be generated by the protons only. $g_l = 1$ and 0 were predicted for the proton and neutron respectively (g_l in units of the nuclear magneton). Historically it was found that $\mu_{neutron}$ had a non zero value and μ_{proton} had a value larger than 1. This led to the introduction of the concept that nucleons are non point-like particles, the neutron and proton magnetic moments are consistent with those of particles with an internal structure due to charged particles in motion.

In order to calculate the total magnetic dipole moment of the nucleus, the single particle magnetic moments are added together and expressed as a sum of two terms (equation 3.4).

$$\mu = \mu_N \sum_{i=1}^{A} g_{l_i} l_i + g_{s_i} s_i \tag{3.4}$$

μ is the expectation value of the nuclear magnetic moment, the projection of the magnetic moment onto the symmetry axis. The method of summing together all the single particle magnetic moments is complicated, μ is the total projection of all the nucleons onto the symmetry axis, the relative orientations of each single particle, $\mu_{nucleon}$, are not known. Initially, to simplify calculations, it was assumed that only the valence nucleons would contribute to the nuclear dipole moment. By separating like nucleons into two groups (as in section 2.2), the nuclear magnetic moment, μ (contribution from the valence nucleons only) can be written:

$$\mu = \mu_I - \mu_R \tag{3.5}$$

Subscripts I and R represent the complete nucleus and the core respectively.

The calculation of magnetic moments of heavy nuclei is not trivial. Exact nuclear wave functions cannot be obtained, therefore we are forced to use approximate models

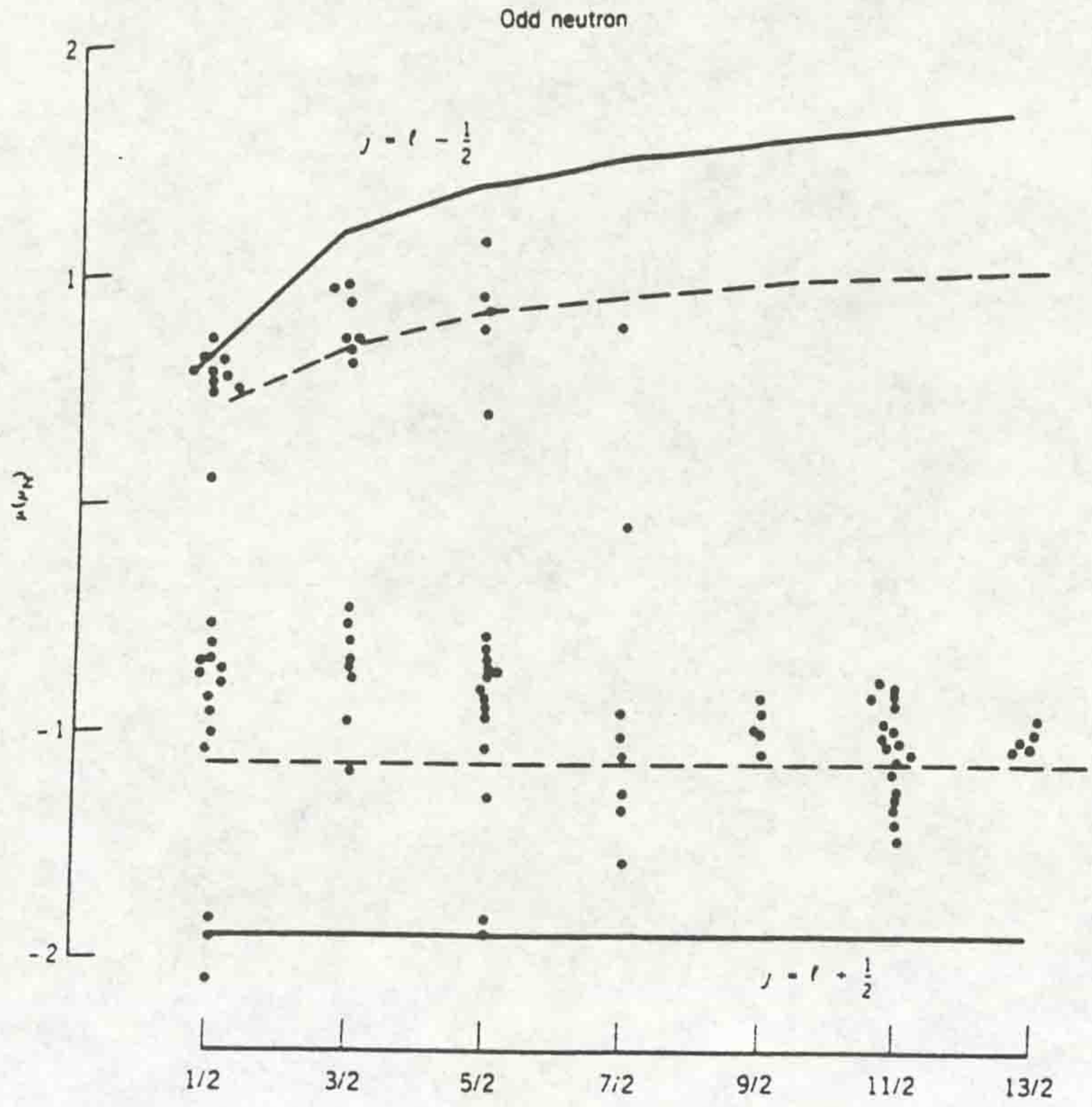

Figure 3.1: *Plot of the magnetic dipole moment, μ, against the angular momentum of a nucleus, I. Theoretical calculations (solid lines) are compared to experimentally measured μ.*

such as the shell model. One can obtain the following expression for calculating the g-factor of a single nucleon [CT90].

$$g_{j=l\pm\frac{1}{2}} = g_l \pm \frac{g_s - g_l}{2l+1} \tag{3.6}$$

The following orbital and spin g-factors are used in equation 3.6.

Protons	Neutrons
$g_l^\pi = 1$	$g_l^\nu = 0$
$g_s^\pi = 2\mu_p$	$g_s^\nu = 2\mu_n$

These g-factors are defined by $j = l \pm \frac{1}{2}$ the total angular momentum possible for a given l and s, corresponding to the shells of the spherical shell model. Figure 3.1 is a plot of μ against I of experimentally measured magnetic dipole moments and theoretical calculations (Schmidt lines). The large deviations between experimental and theoretical results can be partly explained by the fact that the calculations are model dependent.

The spherical shell model, based on degenerate j-shells, has been used. When the nucleus becomes deformed most of the degeneracy of the $j-$shell is removed, ie. the orbitals split into Ω components where $-j < \Omega < +j$. As phenomena such as deformation, quasi-particles and cranking have been introduced to successfully model experimental results, as described in chapter 2, it seems reasonable to incorporate these ideas and also assume that the Ω of the particle will affect the g-factor. In the case of heavy nuclei, the core is important. The spin dependent components of the core partially align the spins of the valence nucleons (spin polarisation) effecting the μ of each valence particle [CT90]. A new expression for the nuclear magnetic dipole moment is obtained by modifying equation 3.5 to include j-shell degeneracy and spin polarisation effects(μ_{sp}). This expression is written in equation 3.7, in units of the the nuclear magneton μ_N.

$$\mu = \mu_I - \mu_R + \mu_{sp} \tag{3.7}$$

The term μ_R describes the magnetic moment of the collective core and is calculated using the method described in equations 3.2. The nuclear magnetic dipole moment now has the form written below.

$$\mu = g_R I + (g_K - g_R)\frac{K^2}{I+1} \tag{3.8}$$

Where the g-factor of the core $g_R \simeq \frac{Z}{A}$, Z and A are the number of protons and the atomic mass number respectively (experimentally g_R is found to be smaller). K is the band-head, introduced in section 2.2. g_K, the intrinsic spin factor accounting for the spin polarisation effect, is written in equation 3.9 below [PS92a].

$$g_k = g_l + \left[\frac{(g_s - g_l)}{\Omega}\right] < s_z > \tag{3.9}$$

$g_s = k g_s^{free}$

$k =$ quenching factor $\simeq 0.7$ (conventional choice for normal deformations).

By calculating the reduced matrix element an expression for the strength of the magnetic dipole transition, $B(M1; I \rightarrow I-1)$ abbreviated to $B(M1)$ in this work, can be calculated [CT90]. The expression is written in equation 3.10.

$$B(M1) = \frac{3}{4\pi}(g_K - g_R)^2 K^2 | < IK10|I-1K > |^2 \mu_N^2 \tag{3.10}$$

The $< IK10|I-1K >$ term is a Clebsch Gordan coefficient (an explanation of these coefficients is given in references [BW91] and [RG75]).

3.1.2 Electric Quadrupole Moment

The electric quadrupole moment is dependent on the charge density of the nucleus. Information about the nuclear shape and deformation is obtained from its measurement. For example, if the nucleus has spherical symmetry, the quadrupole moment vanishes. The electric quadrupole moment is the measure of the nucleus' deviation from spherical symmetry.

Initially it was assumed that as a result of the pairing force (see sections 1.6 and 2.4.1) the nucleus would have a spherical core and would not contribute to the electric quadrupole moment of the nucleus. Results of measured electric quadrupole moments in rare earth nuclei have been larger than those expected from calculations, implying the core plays an important role in the identity of the nuclear electric quadrupole moment.

The electric quadrupole moment operator, $\hat{Q}$, is defined in equation 3.11 below.

$$\hat{Q} = e \sum_{k=1}^{A} g_l^{(k)} (3z_k^2 - r_k^2) \tag{3.11}$$

e is the electric charge. z_k and r_k are position co-ordinates of the nucleon k. Charge distribution in the nucleus is purely from the protons, therefore $g_l^{(\pi)} = 1$ and $g_l^{(\nu)} = 0$ respectively. The electric quadrupole moment, Q, is defined as the expectation value of $\hat{Q}$ in the nuclear substate $M = I$ and can be calculated using equation below.

$$Q = Q_0 \frac{3K^2 - I(I+1)}{(I+1)(2I+3)} \tag{3.12}$$

The term Q_0 is the maximum expectation value of the intrinsic quadrupole moment. Q_0 is defined in the intrinsic frame of reference and is equal to zero for a spherically symmetric system (Q_0 is different to the spectroscopic quadrupole moment measured in the laboratory frame of reference).

As with the magnetic dipole moment calculations, from the reduced matrix elements an expression for the strength of electric quadrupole transitions, $B(E2; I \rightarrow I-2)$ written as $B(E2)$ in this work, can be determined [CT90], equation below.

$$B(E2) = \frac{5}{16\pi} Q_0^2 | < IK20|I-2K > |^2 (eb)^2 \tag{3.13}$$

$b = 1$ barn $= 10^{-28}$ m^2. The $< IK20|I-2K >$ term is a Clebsch Gordan coefficient.

3.1.3 $B(M1; I \rightarrow I-1)/B(E2; I \rightarrow I-2)$ Ratios

$B(M1; I \rightarrow I-1)/B(E2; I \rightarrow I-2)$ ratios of reduced transition probabilities (abbreviated to $B(M1)/B(E2)$) will be described in this work. These branching ratios measure the competition between competing $\Delta I = 1$ and 2 transitions. Electric and magnetic radiation are sensitive to different properties of the nucleus(see below). The ratios of the magnetic and electric properties give information as to the structure of the nucleus.

$M1$ - dipole transition
- sensitive to intrinsic structures (configuration of nucleons)

$E2$ - quadrupole transition
- gives information on the collectivity of the nucleus (deformation)

A method of coupling quasi-particles g-factors together, vectorally, described in references [FD82] and [FD87], is written below. This expression is derived assuming the strong coupling limit and $K \neq \frac{1}{2}$.

$$< I, I||M1||I-1, I-1 >= \sqrt{\frac{3}{8\pi}} K \left[(g_1 - g_R) \left(\sqrt{1 - \frac{K^2}{I^2}} - i_1 \pm \frac{\Delta e'}{\hbar\omega} \right) - (g_2 - g_R) \frac{i_2}{I} \right]. \tag{3.14}$$

The strong coupling limit is the assumption that the two quasiparticles (subscript 1 and 2) will couple to one of the following

$$K = K_> = \Omega_1 + \Omega_2$$
$$K = K_< = |\Omega_1 - \Omega_2|$$

$\sqrt{\frac{3}{8\pi}} K$ is an approximate term substituted for the Clebsch Gordon coefficient. The transition probability, B(M1) is proportional to the square of equation 3.14. This equation can be modified for a three quasi-particle structure by assuming a configuration consisting of two rotationally aligned quasi-particles coupled to a third aligned to the symmetry axis. This assumption for a three quasi-particle configuration is valid in the majority of cases [FD82]. Theoretical branching ratios calculated using equation 3.14 are referred to as the semi-classical formalism of Dönau and Frauendorf.

When calculating the theoretical $B(E2)$ value the following equation is used to calculate the intrinsic quadrupole moment $Q_\circ$:

$$Q_\circ = \frac{3}{\sqrt{5\pi}} Z R_\circ^2 \beta_2 (1 + 0.16\beta_2) \tag{3.15}$$

Where $R_\circ$ is the nuclear radius given in equation 1.3. The deformation parameter, β_2, is introduced in section 1.2.1.

3.1.4 Comparison of Experimental Results and Calculations

Experimentally measurable quantities using a spectrometer such as Eurogam are intensities and energies of transitions. Therefore an expression for the experimental $B(M1)/B(E2)$ ratios has to be derived in terms of these quantities.

The probability of decay via a quadrupole or dipole transition, the transition probability, is given in equation 3.16 [WB79].

$$T_{if}(L) = \frac{1}{\tau_\gamma} = \frac{\mu_o c^2}{4\pi} \frac{8\pi(L+1)}{[L(2L+1)!!]^2} \frac{1}{\hbar} \left(\frac{E_\gamma}{\hbar c}\right)^{2L+1} B_{if}(L) \tag{3.16}$$

L is the multipole order, subscript if signifies a transition from an initial state i to a final state f. Due to the nature of the ratios being studied, $B_{if}(L) = B(M1)$ and $B(E2)$ for dipole and quadrupole transitions respectively, expressions of these quantities are given in equations 3.10 and 3.13. τ_γ is the lifetime.

Equation 3.16 is derived using Fermi's golden rule [JC82], this expression is dependent on the density of final states available to a transition. The transition probability is the probability of a decay per unit time, therefore the ratios of the intensities measured for competing transitions will yield the same value of the ratio of the transition probabilities.

The ratio of intensities is given by substituting equations 3.10 and 3.13 into equation 3.16, as shown in equation 3.17.

$$\frac{Int(M1)}{Int(E2)} = \frac{T_{if}(1)}{T_{if}(2)} = 3.49 \frac{(g_k - g_R)^2}{Q_0^2} K^2 \frac{|<IK10|I-1K>|^2}{|<IK20|I-2K>|^2} \frac{E_\gamma(M1)^3}{E_\gamma(E2)^5} \mu_N^2 \tag{3.17}$$

An expression for the theoretical B(M1)/B(E2) ratios can be derived from equations 3.10 and 3.13, by substituting in equation 3.17, the following expression for the experimental B(M1;I→I−1)/B(E2;I→I−2) can be derived.

$$\frac{B(M1; I \to I-1)}{B(E2; I \to I-2)} = 0.697 \, \frac{Int(M1)}{Int(E2)} \, \frac{E_\gamma(E2)^5}{E_\gamma(M1)^3} \tag{3.18}$$

3.2 Gamma-ray Angular Distributions

Gamma-rays of different multipolarity have different distributions of emission probabilities in space.

The A(c,d)B* type of reaction is of interest for this analysis, for example, in this case ^{116}Cd(^{48}Ca,5n)^{157}Er* where the * denotes an excited nucleus. The target nuclei have randomly oriented magnetic states (isotropic).

The exited states populated by the compound reaction, have spins oriented perpendicular to the beam axis, the system has cylindrical symmetry. Following the compound reaction the nuclear state is said to be aligned, ie. the population of magnetic substates is different. These two assumptions are made in the derivation of gamma-ray angular correlation theory [RG75].

Equation 3.19 is an expression of the angular distribution of a gamma-ray transition. The equation is a description of a transition composed of mixed multipolarities of order L and L' ($L' \equiv L+1$), from an initial state to a final state with total angular momentum J_i and J_f respectively. To simplify the angular distribution formula it is assumed that only the lowest two multipoles contribute significantly to the transition. Odd values of k (Legendre polynomial order) disappear due to axial and reflection symmetry.

The angular distribution function of a gamma-ray transition is written

$$W(\theta) = \sum_{k=even} P_k(cos\theta)B_k(J_i)[R_k(LLJ_iJ_f)+2R_k(LL'J_iJ_f)\delta+R_k(L'L'J_iJ_f)\delta^2]\left[\frac{1}{1+\delta_2}\right] \tag{3.19}$$

This equation can be simplified

$$W(\theta) = \sum_{k=even} A_k P_k(cos\theta) \tag{3.20}$$

The terms used in equations 3.19 and 3.20 are defined as follows:

$P_k(cos\theta)$ - Legendre polynomial

$$A_k = B_k(J_i)[R_k(LLJ_iJ_f) + 2R_k(LL'J_iJ_f)\delta + R_k(L'L'J_iJ_f)\delta^2]\left[\frac{1}{1+\delta_2}\right]$$

where $B_k(J_i)$ is a statistical tensor for the initial state J_i and is the term devoted to the population of the initial state J_i.

$$B_k(J_i) = \sum_{M_i} W(M_i)(-1)^{J_i-i}(2J+1)^{\frac{1}{2}}(J_iJ_iM_i - M_i|k0)$$

$W(M_i)$ is the relative population of the magnetic substates of J_i. When the Legendre polynomial order $k = 0$ $B_k(J_i) = 1$, when k is odd $B_k(J_i) = 0$.

R_k is an angular coefficient and is written

$$R_k = (-1)^{1+J_i-J_f+L'-L-k}\hat{J}_i\hat{L}\hat{L}'(LL'1-1|k0)xW(J_iJ_iLL'|kJ_f)$$

where $\hat{J}_i\hat{L}\hat{L}' = [(2J_i+1)(2L+1)(2L'+1)]^{\frac{1}{2}}$

The term δ, the multipole mixing ratio, is defined as the ratio of the reduced matrix elements of the two electromagnetic multipole operators [RG75] and is given by

$$\delta = \frac{< J_i||T^{\omega'}_{L'}||J_f >}{< J_i||T^{\omega}_{L}||J_f >}\left[\frac{2L+1}{2L'+1}\right]^{1/2} \tag{3.21}$$

Equations 3.19 and 3.20 have been derived assuming a detector the size of a single point in space. But detectors have a finite size and the response of a detector depends on the size of the detector face. The detector must be in a position such that its symmetry axis passes through the radiation source, the target. The following equation is the angular distribution function with the finite size correction, Q_k.

$$W(\theta) = \sum_{k=even} A_kQ_kP_k(cos\theta) \tag{3.22}$$

Q_k is a solid angle factor, an attenuation coefficient. A description of the coefficient and a table of values is given in [EM74].

Equation 3.22 is expanded for dipole and quadrupole transitions ($k = 0, 2$, and 4).

$$W(\theta) = A_0[1 + a_2Q_2P_2(cos\theta) + a_4Q_4P_4(cos\theta)] \tag{3.23}$$

where $a_2 = \frac{A_2}{A_0}$ and $a_4 = \frac{A_4}{A_0}$.

The values of k run evenly from 0 to $2L$, where L is the highest order multipole. The mixtures of electric and magnetic transitions of the same multipolarity cannot be observed due to conservation of parity. But mixtures of electric and magnetic transitions can be observed as long as parity is conserved. In the case of this analysis $M1/E2$ mixtures are observed. Angular momentum is also conserved. Due to the conservation of the quantities above the following selection rules can be derived for electromagnetic transitions in the nucleus. $\Delta\pi$ indicates a change in parity, $\Delta\pi = -1 \Rightarrow$ change and $+1 \Rightarrow$ no change.

$$|J_i - J_f \leq L, L' \leq |J_i + J_f|$$
$$\text{EL} \quad - \quad \Delta\pi \quad = \quad (-1)^L$$
$$\text{ML} \quad - \quad \Delta\pi \quad = \quad (-1)^{L+1}$$

A stretched transition has the maximum change in angular momentum possible for the multipole order, for example, a stretched $E2$ transition has a ΔJ of $2\hbar$.

3.2.1 Angular Correlation Ratios

In the present work quadrupole and dipole transitions are being investigated. These transitions have unique spatial probability distributions, therefore measurements of **coincident** gamma-rays at different angles should yield different results depending on the multipolarity of the transition.

Intensities of different transitions at particular angle are not directly comparable, as the intensities are dependent on the initial population of the level as well as the angular distribution, therefore angular correlation ratios are measured.

The intensity of a gamma-ray is measured at two different angles and the ratio of these two measurements is calculated. Due to the unique spatial emission probabilities of electromagnetic multipoles all quadrupoles should have the same ratios regardless of gamma-ray energy, and the same for dipoles. The ratios are therefore calibrated on known transitions. The ratios of unknown transitions are then measured and compared to known multipoles.

In order to measure the angle at which the γ-ray is emitted it has to be defined relative to a reference, another γ-ray (reference γ). This technique is the DCO (Directional Correlations of $\gamma-$rays from Oriented states) method [KK73]. For the purpose of this analysis a $\gamma-$ray detected in a detector in the 90° detector ring of Eurogam (see chapter 4) was used as the reference.

The angular correlation ratios given below were measured in this work.

$$\frac{Intensity\ of\ gamma\ at\ 134°}{Intensity\ of\ gamma\ at\ 90°} = \frac{Int[134° - 90°]}{Int[90° - 90°]} \tag{3.24}$$

$Int[134° - 90°]$=sum of the detectors at 134° in coincidence with a detector at 90°

$Int[90° - 90°]$=sum of the detectors at 90° in coincidence with another detector at 90°

In this analysis known transitions have been calibrated such that angular correlation values of ≥ 1 are taken as stretched quadrupoles and ratios ≤ 0.8 are taken as stretched dipole transitions. These values are consistent with other angular correlation measurements using Eurogam, for example, see [EP94] and [EP93].

This method of measuring angular correlation ratios gives information on the multipole order only. Eurogam Phase I is not sensitive to the polarisation of $\gamma-$rays and therefore differences between electric and magnetic transitions cannot be distinguished. It must also be noted that pure $\Delta J = 0$ non-stretched dipoles cannot be determined from stretched $\Delta J = 2$ transitions, see [PT73] for an explanation of these ambiguities. It is assumed throughout this work that levels within rotational structures are connected by stretched electric quadrupole transitions, $E2$'s. Previous polarisation experiments in the rare earth region have shown that similar rotational structures are electric by nature. An example of polarisation measurements in the neighbouring ^{158}Er nucleus is given in [JS82].

3.2.2 Linear Polarisation

Initially aligned states will generally decay resulting in linearly polarised $\gamma-$rays. The Klein-Nishina formula [GFK2] gives the cross-section of scattering of incident photons through an angle θ. This formula shows that the cross-section is largest for scattering normal to the electric vector, $\underline{\mathrm{E}}$. Polarisation experiments enable the parities of states left ambiguous after angular correlation measurements to be determined.

The complete angular correlation function is written in equation 3.25 given below [PT73], this equation is composed of two terms, the first is equivalent to equation 3.22 and the second term represents the polarisation. The polarisation term has a different sign depending on whether the transition is electric or magnetic.

$$W(\theta,\psi) = \sum_{k=even} A_k Q_k [P_k(cos\theta) + (-1)^{\pi'} cos\psi K_k(LL') P_k^2(cos\theta)] \qquad (3.25)$$

The polarisation occurs at two angles in ψ separated by 90°. The term $\pi' = 0$ and 1 for electric and magnetic L' transitions respectively. $K_k(LL')$ are polarisation coefficients defined in [LF59].

Experimental measurements are not usually made of the whole function, as linear polarisation experiments are difficult to perform [PG72]. Generally the following ratio, $P(\theta)$, is measured [JS82].

$$P(\theta) = \frac{W(90°,0°) - W(90°,90°)}{W(90°,0°) + W(90°,90°)} \qquad -1 \leq P(\theta) \leq 1 \qquad (3.26)$$

Using the above ratio, if the $\gamma-$ray is unpolarised $P(\theta) = 0$.

Chapter 4

Experimental Techniques

4.1 "Creating" ^{157}Er

To produce high spin states in ^{157}Er a heavy ion fusion–evaporation reaction was used. This reaction uses a target nucleus and a projectile, the projectile and target nuclei fuse together, forming a compound nucleus. The projectile must have enough energy to overcome the Coulomb barrier of the target nucleus for this fusion to occur. The 20MV tandem Van de Graaff generator at Daresbury Laboratory, Warrington, UK (section 4.3) was used to produce a beam of nuclei accelerated to a sufficient energy to overcome the Coulomb barrier.

The ^{114}Cd(^{48}Ca,5n)^{157}Er reaction was used. The projectile (^{48}Ca) was accelerated to an energy of 210 MeV and ^{157}Er was formed via the 5n reaction channel (five neutrons were emitted after the formation of the compound system, to create ^{157}Er).

Particle emission will occur until the excitation energy remaining in the system is within a nucleon binding energy ($\sim$ 8 MeV) of the yrast line [JGSS]. In these reactions neutrons, protons, alpha particles are emitted and fission may occur , but for the formation of ^{157}Er only the 5n channel is of interest.

The "cooling" of the system after the ejection of particles is continued via gamma decay. Due to the high density of states at this excitation energy ($\sim$ 8 MeV above yrast) there is a continuum of statistical gamma rays. When the nucleus de–excites to an energy 2–3 MeV above the yrast line the level density is small enough for discrete gamma-rays to be emitted; see figure 4.1.

The target used consisted of 2 stacked 500μg/cm^2 ^{114}Cd foils. A thin target was used to reduce Doppler broadening of the high spin states. All the γ–rays are fully

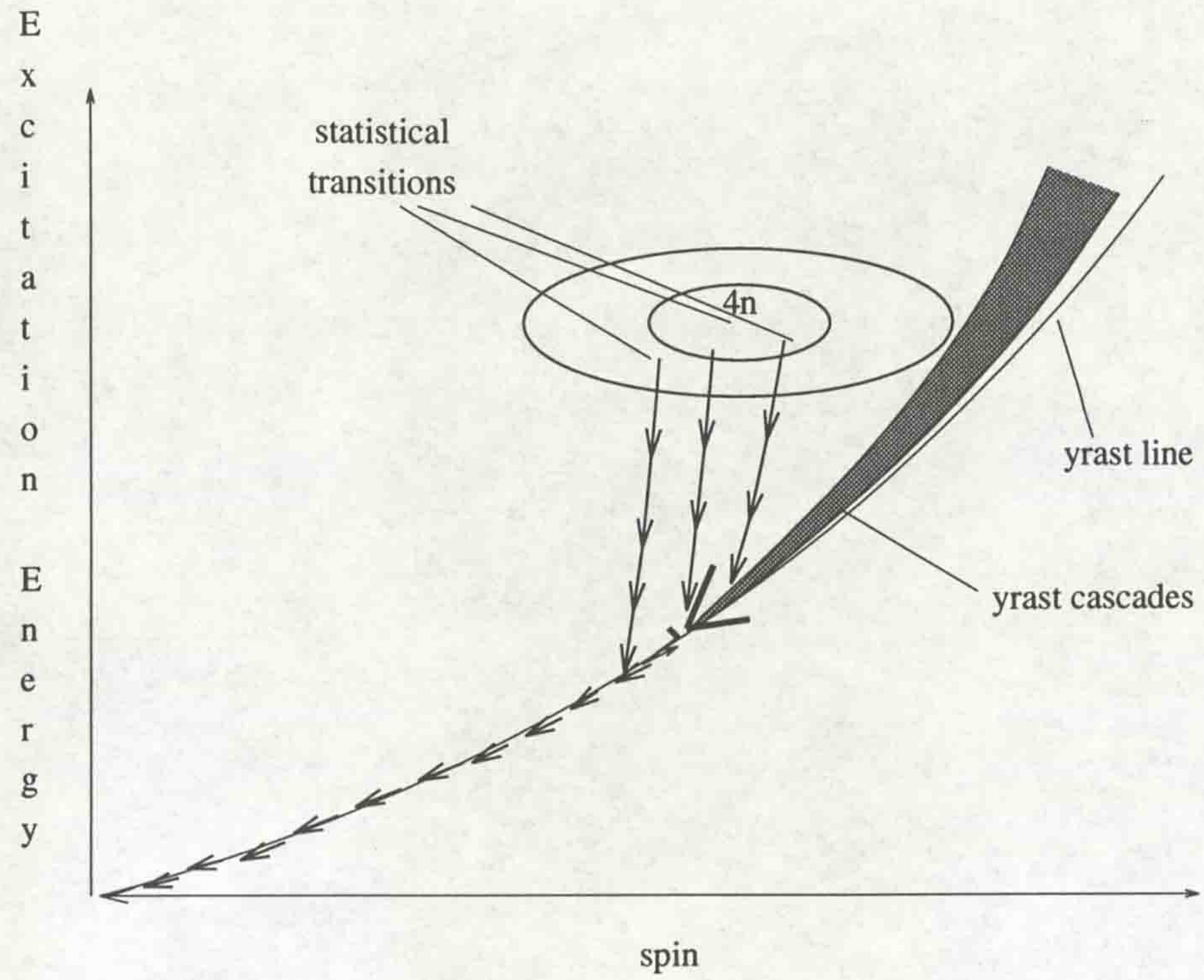

Figure 4.1: *Diagram illustrating the modes of de–excitation of a compound nucleus [HT92].*

Doppler shifted , preventing the transitions with the very short lifetimes from being 'smeared' by the Doppler broadening in a thick target.

The gamma–rays emitted by the de–exciting nucleus were detected using a multi-detector system, an escape suppressed array. A discussion of methods of detection will follow.

4.2 Detection of Gamma–Rays

Before a detailed description of the detector system used, the interaction of gamma-rays, with reference to detector systems, will be described [GFK2].

4.2.1 Gamma–Ray Interaction Mechanisms

The three major types of interaction that play an important role in the detection of gamma–rays, are;

- photoelectric absorption
- Compton scattering
- pair production

A brief description of each mechanism follows.

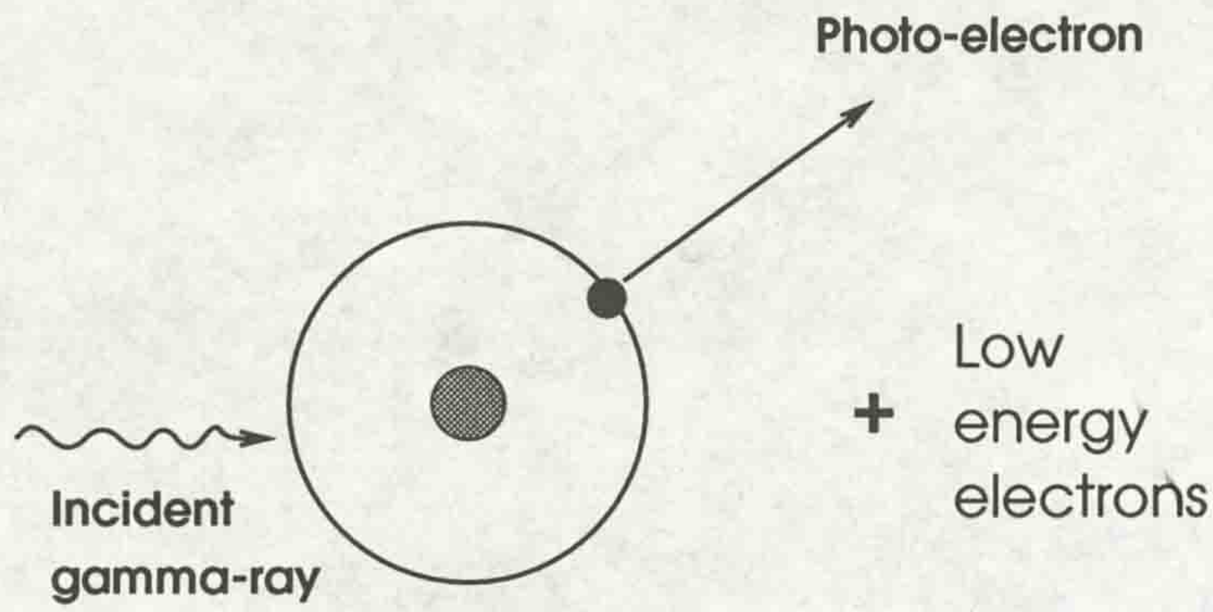

Figure 4.2: *Photoelectric Absorption.*

Photoelectric Absorption

This mechanism can only take place with a bound electron. The photon undergoes an interaction with an atom, the photon is absorbed and a photoelectron is ejected from one of the atom's bound shells.

$$E_{photoelectron} = h\nu - E_{bindingenergy} \tag{4.1}$$

The photo-electron carries most of the gamma–ray energy. One or more low energy electrons are also excited with total energy equal to the binding energy of the original photo-electron (see figure 4.2). Therefore if no photons escape from the detector, the total energy collected is that of the incident gamma–ray.

An approximate expression for photoelectric absorption (Γ) is given in equation 4.2 below.

$$\Gamma \propto \frac{Z^n}{E_\gamma^{7/2}} \tag{4.2}$$

where n is in the range 4–5 for gamma–rays. From equation 4.2 it can be seen that it is desirable to have a detector material with a high Z (atomic number) to increase the probability of detecting a gamma–ray.

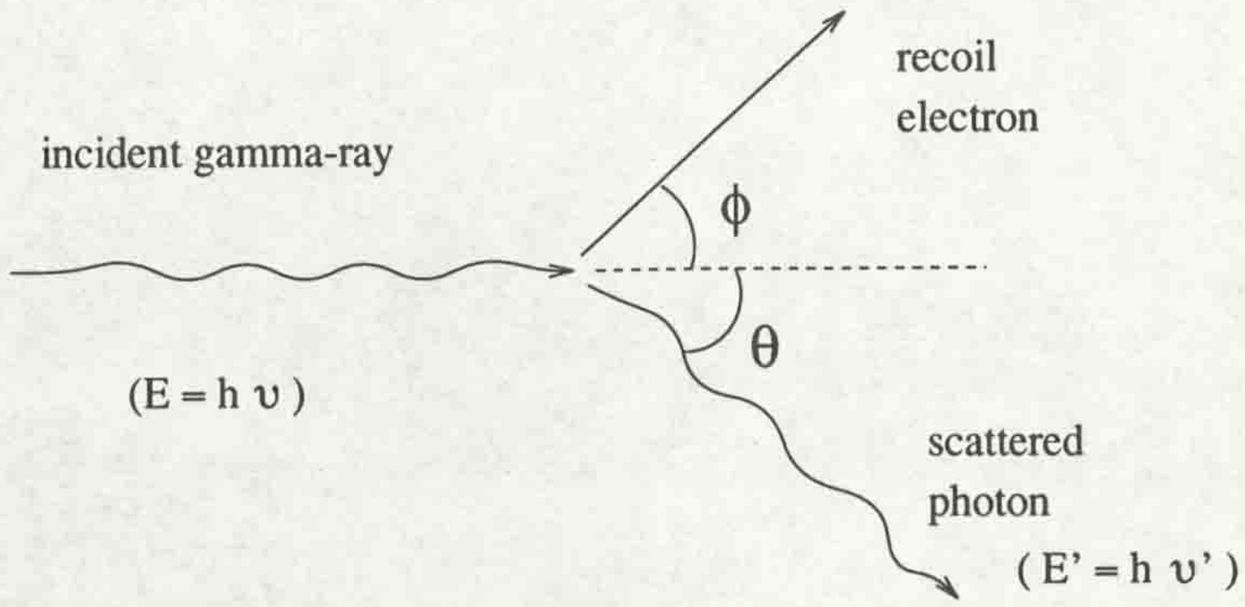

Figure 4.3: *Compton Scattering.*

Compton Scattering

Compton scattering is an interaction between the incident gamma–ray and an electron in the absorbing material. The gamma–ray, incident on the electron, transfers a portion of its energy to the electron (assumed initially to be at rest) and is then scattered, because all angles of scattering are possible the energy transferred to the electron can vary from zero to a large fraction of the gamma–ray energy. The energy of the scattered photon (see figure 4.3) is written:

$$h\nu' = \frac{h\nu}{1 + \frac{h\nu}{m_o c^2}(1 - cos\theta)} \tag{4.3}$$

$m_o c^2$= rest mass of electron

$0 \leq \theta \leq \pi$

In practice, all values of θ occur and a continuum of energies can be transfered to the electron ($E_{el} = h\nu - h\nu'$). A single gamma–ray can undergo multiple scattering, which does not cause any problems if the scattering is confined to a single detector. The methods used to overcome the problem of Compton scattering out of a detector will be discussed in section 4.4.2.

The angular distribution of scattered gamma–rays is predicted by the Klein-Nishina formula [GFK2] for the differential scattering cross-section.

Pair Production

To conserve angular momentum this process occurs in the field of a nucleus of the absorbing material. An electron-positron pair is created at the point of disappearance of the incident gamma-ray. A γ–ray energy of at least 1.02 MeV (mass of two

electrons) is required for this mechanism, equation 4.4. Any energy in excess of this minimum value is shared by the electron-positron pair.

$$E_{electron} + E_{positron} = h\nu - 2m_o c^2 \tag{4.4}$$

The positron and electron travel a few millimetres before losing all the energy to the absorber. The time for the positron to slow down and annihilate is so small that it appears in coincidence with the original pair production interaction.

Summary

Figure 4.4 summarises the areas in which the three reaction mechanisms (photo-electric absorption, Compton scattering and pair production) dominate.

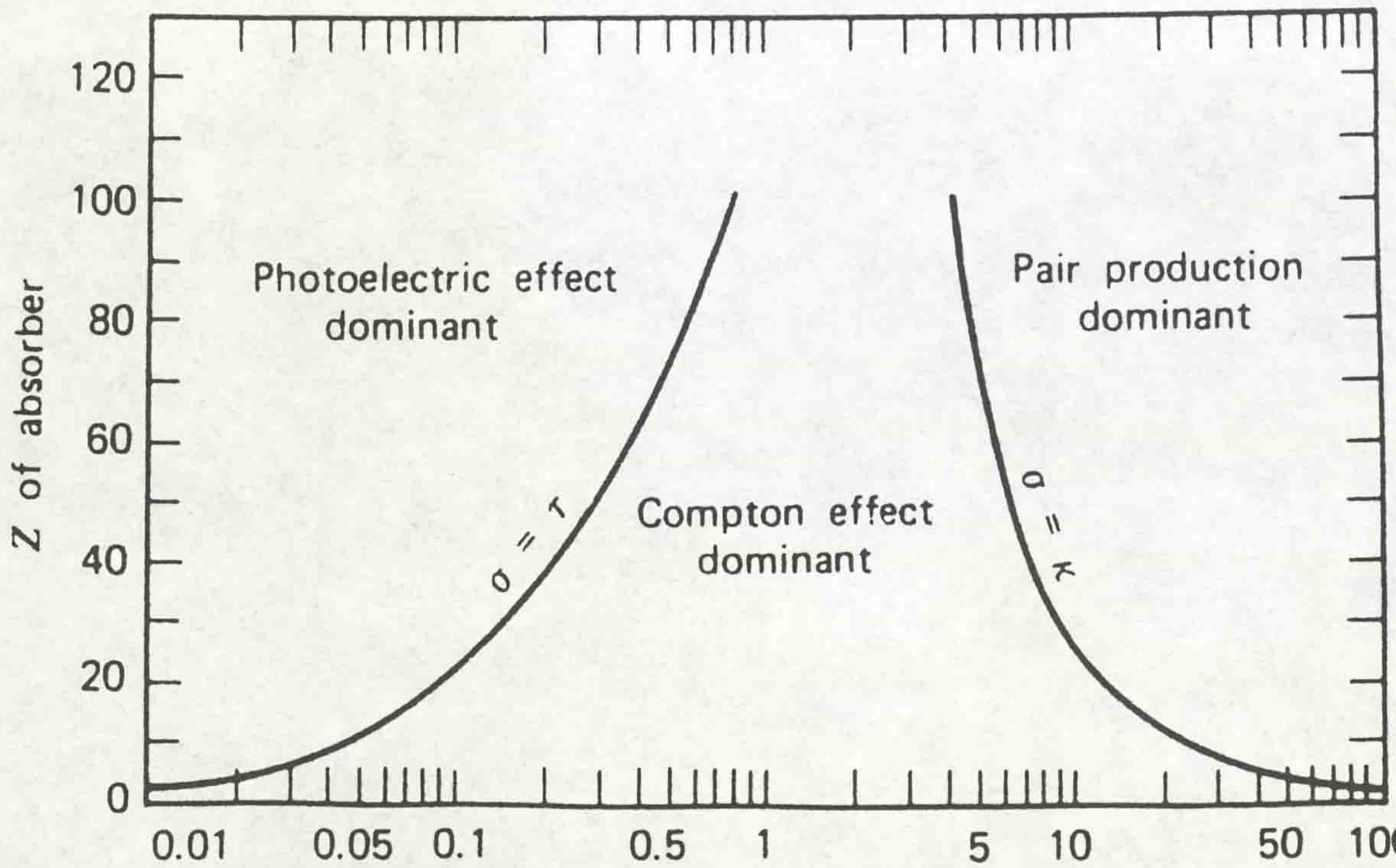

Figure 4.4: *Relative importance of the three major reaction mechanisms plotted as a function of Z of absorber and gamma-ray energy [RE55].*

4.3 The Tandem Van de Graaff

The simplest method to accelerate a charged particle (ion) is to 'drop' it through a constant potential difference (PD). Van de Graaff accelerators (VDG), see general references such as [KK87]), exploit this technique. Traditional VDG's have the ion source (source of charged particles) inside the high voltage (HV) terminal of the accelerator, this creates many practical problems, the tandem VDG is a solution to this problem. Following is a description of the Nuclear Structure Facility (NSF) at Daresbury, Warrington, U.K., utilised for this analysis. Figure 4.5 shows a picture of the Daresbury NSF. For comprehensive details of the NSF, including design considerations, see reference [JL82].

A beam of ions are produced in the ion source located outside the accelerator. Negative ions are accelerated from the ion source towards the positive HV terminal at the centre of the VDG. Two strippers are located within the HV terminal, the first is gas (argon) and the second is foil (carbon). The strippers remove electrons from the ion, leaving the atoms positively charged. The number of protons in excess of the number of electrons is referred to as the charge state of the ion. A quadrupole triplet magnet for charge state selection is also housed inside the HV terminal. The positive ions are accelerated through a constant PD, created by the VDG, towards ground. The target used in the experiment is connected to ground, with the help of bending magnets (see references [KK87] and [JL82]) the beam of positive ions strikes the target. As the beam drops through the PD it gains a kinetic energy proportional to the PD and the charge state of the ions.

A laddertron was designed and built to charge the tandem NSF VDG, this has the same function as the belt in a simple VDG. The rings of the laddertron are insulated from each other and charged inductively. A stable gas, SF_6 (sulphur hexafluoride), is enclosed in a pressure tank within the accelerator body, this inhibits sparking and breakdown. Throughout the VDG the beam is carried through an accelerator tube consisting of titanium electrodes bonded to ceramic isolation rings.

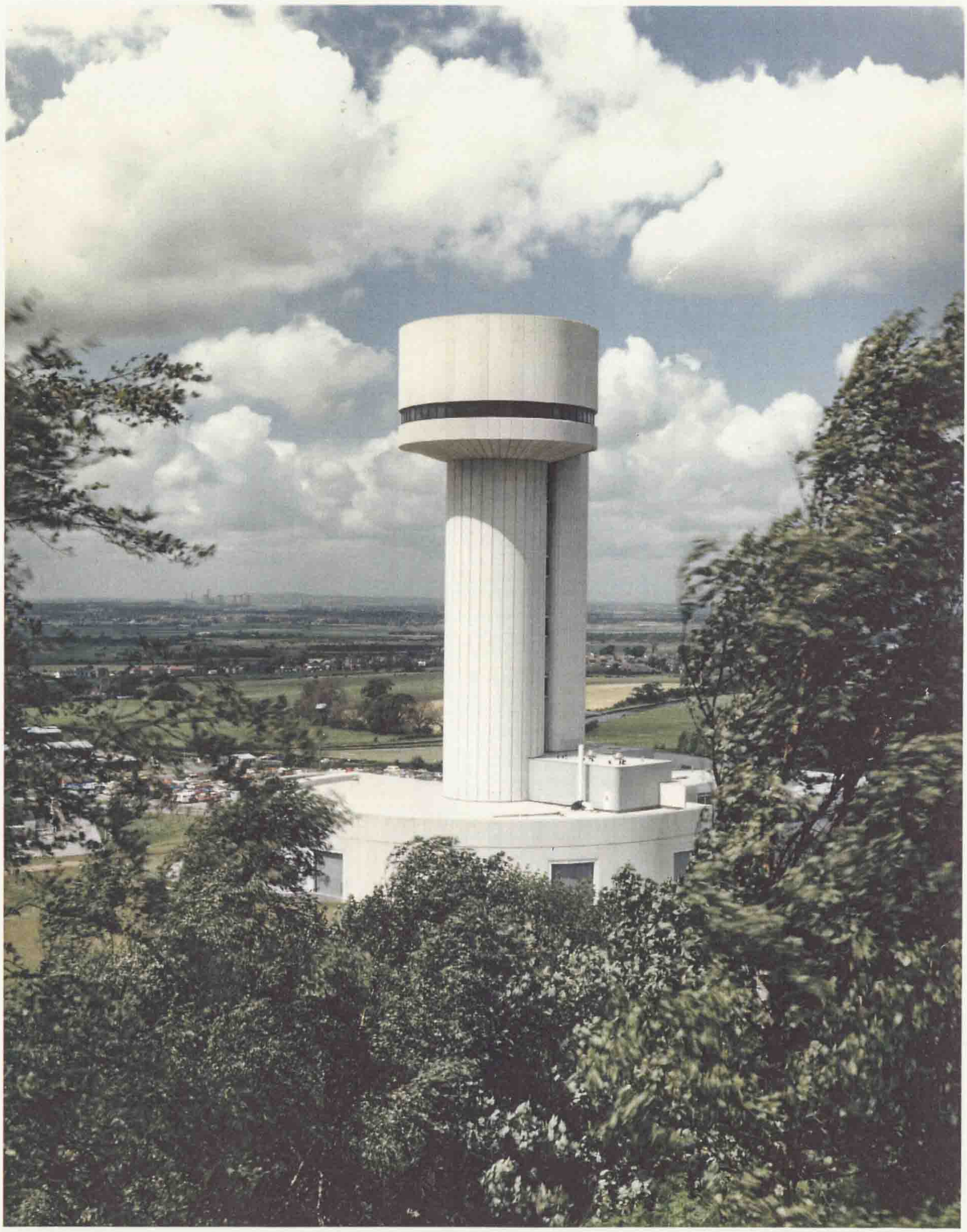

Figure 4.5: *The Nuclear Structure Facility, Daresbury, Warrington, U.K.*

4.4 Eurogam

Eurogam phase I, the United Kingdom and France gamma-ray microscope, was used in the collection of data. This spectrometer is a high-efficiency escape-suppressed germanium detector array and consists of 45 Compton-suppressed HP-Ge detectors, this will be increased to 30 phase I HP-Ge detectors and 24 clover detectors [PJ94] in phase II.

An overview of Eurogam and its design considerations is given in reference [PN90].

4.4.1 Germanium Detectors

Semi-conductor materials are used as radiation detectors [GFK2], because they have a large number of charge carriers for an incident gamma-ray resulting in excellent energy resolution. N-type germanium detectors have been used as these are more resilient to neutron damage than P-type.

The depletion depth (active volume) is a limiting factor on the performance of semi-conductor detectors. A germanium crystal of normal purity has a depletion depth of about 3mm. As a result of improved manufacturing techniques Eurogam detectors have been constructed using high purity germanium (HP-Ge), these detectors have a depletion layer of 1cm and above. The thermal noise of the detector is reduced considerably by keeping the crystal at liquid nitrogen temperatures, reducing the number of thermally excited electrons.

4.4.2 Suppression Shields

Compton scattering of gamma rays results in a Compton continuum in the recorded spectrum (see section 4.2.1 Compton Scattering). The continuum is due to the escape of a scattered photon from the detector, resulting in only a fraction of the incident gamma-ray energy being detected. The energy detected will add to the continuum, not to the full energy peak, increasing the background. To overcome this problem the veto (anti-coincidence) principle is applied, using a suppression shield [PN82]. If an event in the suppression shield is detected the output from the associated Ge detector is ignored, ie. if the shield has detected an event it implies that a scattered photon has escaped and the total energy of the initial gamma-ray has not been deposited in the germanium detector.

The use of suppression shields increases the ratio of full energy peak to Compton continuum, since it "cleans up" the spectrum. Escape of the annihilation photons produced by pair production are also suppressed.

4.4.3 Eurogam Ge Detectors

The Ge detectors are each made from one tapered HP-Ge crystal $\sim$ 70mm in length. The first 30mm of the crystal is tapered to an angle of 5.7°. Resolution is not lost from this tapering as the portion removed is almost inactive in an un-tapered detector. Tapered Ge detectors can be pushed closer to the target, increasing efficiency.

4.4.4 Eurogam BGO Suppression Shields

Each HP-Ge detector has an associated bismuth germanate (BGO) suppression shield. This material has been proved efficient for suppression during the operation of previous spectrometers, for example TESSA3 [JSS88]. BGO is an inorganic scintillator, which has poor energy resolution but excellent timing, essential for an anti-coincidence device. Due to its high density, BGO shields need only a small volume for efficient suppression [SF92] and therefore increase the number of Ge detectors that can be fitted around the target at optimum distance (the interaction region).

The suppression shield consists of 10 optically isolated BGO crystals, 190mm in length, each with a separate photo-multiplier.

4.4.5 Eurogam BGO Suppressed Ge Detectors

Eurogam has 45 detectors, each Ge detector has a BGO suppression shield [CB92], see Figure 4.6. The detectors are grouped in a sphere around an interaction region approximately 40cm in diameter, in which the target chamber is housed.

4.4.6 The Eurogam Array

The Eurogam array can be seen in Figure 4.7. The flat end of the array support is positioned closely to the Daresbury Laboratory recoil separator, down stream of the accelerated beam. The detectors are grouped in repeating segments of six. Eurogam phase 1 has 45 detectors, the central Ge detector in each group of six detectors was

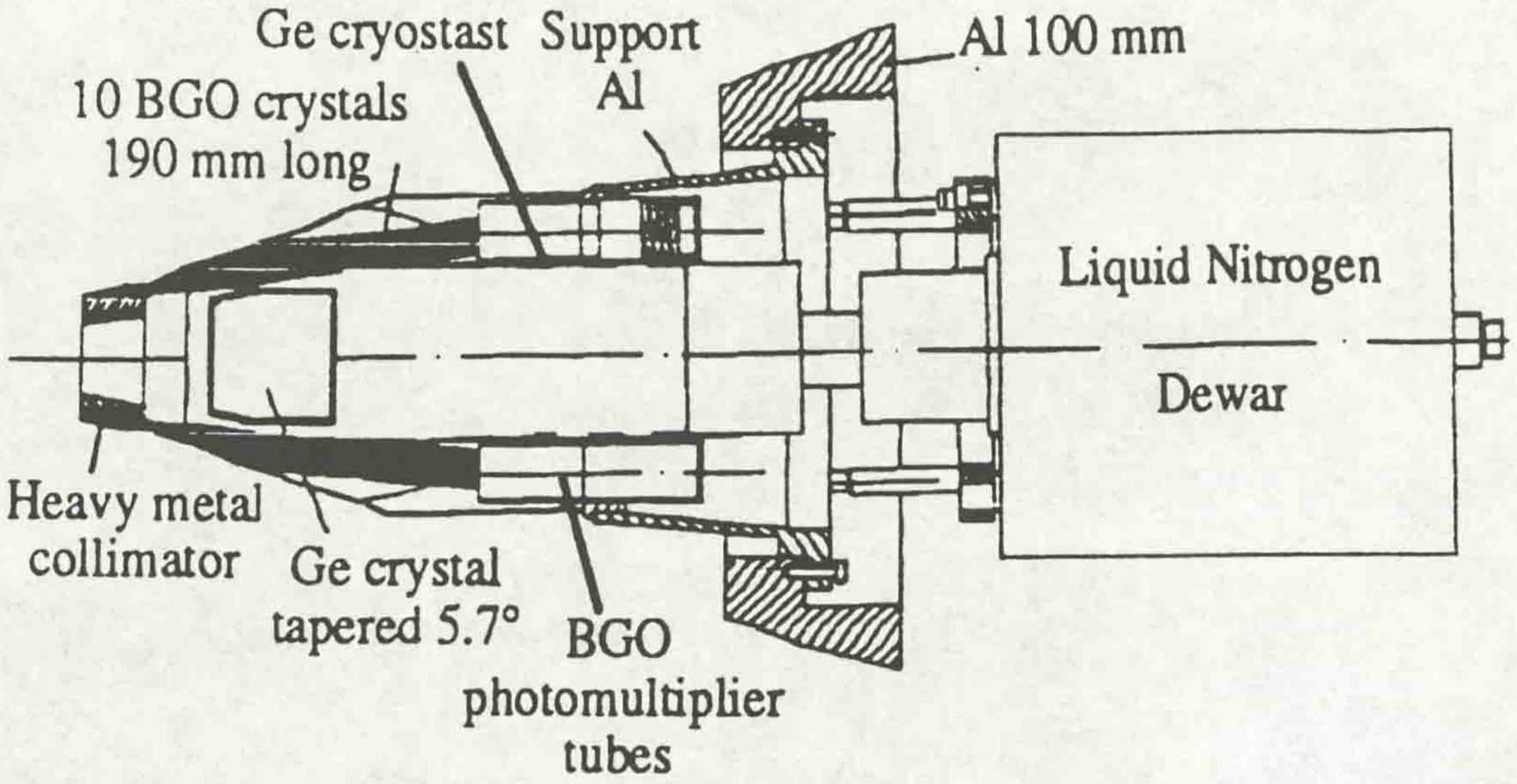

Figure 4.6: *Composite Ge BGO detector system used on the Eurogam array [GM92].*

omitted (the central detector has a different shaped BGO shield to that the other five in the group).

4.5 Eurogam electronics and Data Acquisition

NIM electronics have been used for previous spectrometers, one Ge channel occupies a large fraction of a crate. This method of processing the output of Ge detectors and Compton shields is not practical for the number of Eurogam detectors used. A new electronic and data acquisition system has been devised ([VP92] and [GM92]) with the following features:

- VXI crates for all electronics and master trigger
- VME crates for software handling (event builder)
- high data rates for transfer between VXI–VME
- network link to control all processes
- network of work stations (UNIX) to control the experiment and data acquisition.

A diagram illustrating the incorporation of these features into Eurogam, is shown in figure 4.8.

It was decided to put six Ge channels (one channel per detector) on a single Ge

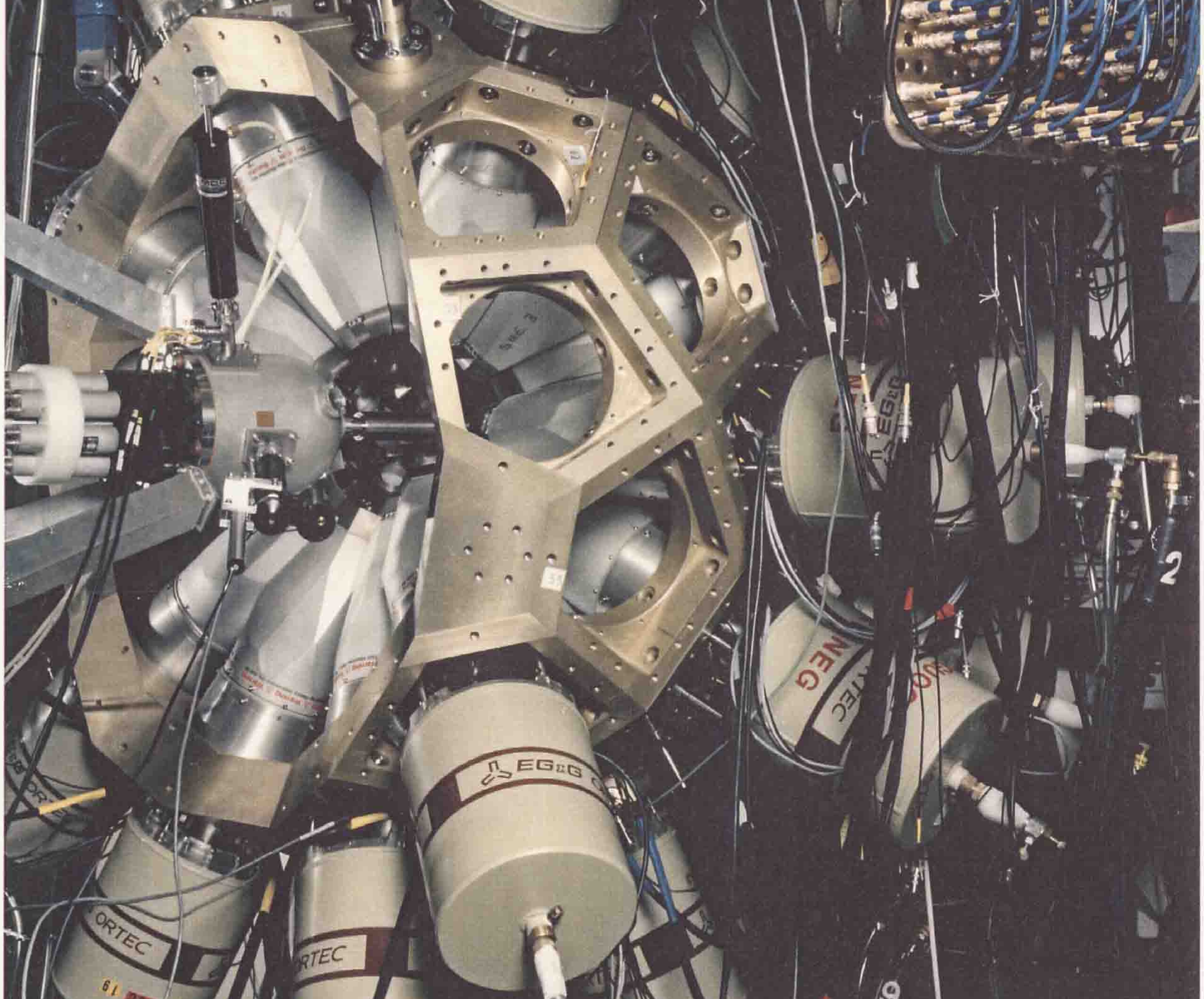

Figure 4.7: *The Eurogam array.*

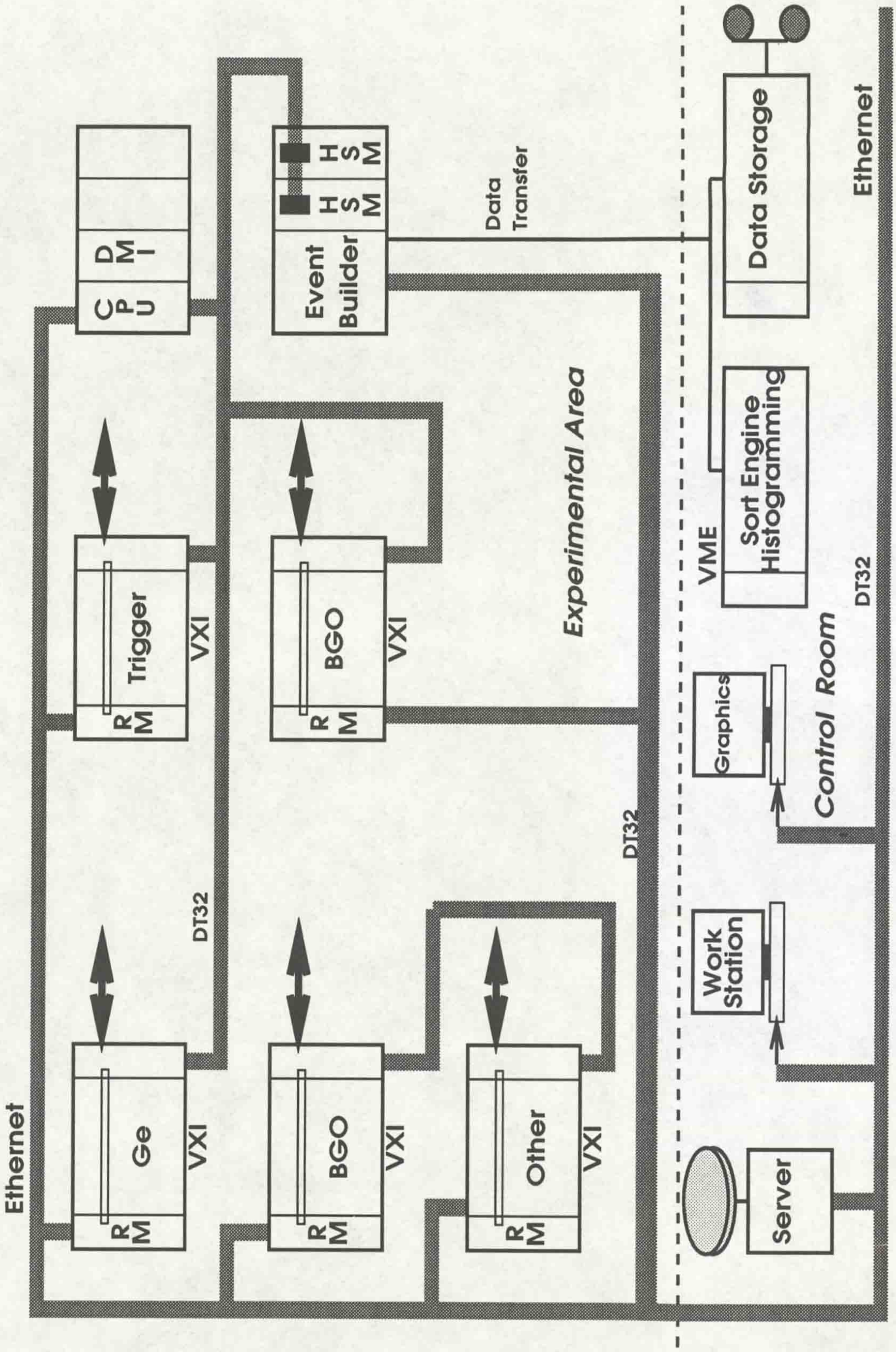

Figure 4.8: *Block diagram of Eurogam electronics and data acquisition system [EG90].*

VXI card, and sixty channels (ten channels per shield) on a BGO VXI card. The BGO and Ge cards are interleaved in order to apply the BGO anti-Compton veto signal to its respective Ge.

Eurogam data rates are of the order of 10^4 events per second (unsuppressed).

4.5.1 Ge Detectors

Each Ge signal is processed in a single channel of the Ge VXI card (see Figure 4.9), each signal will be processed for time and energy analysis.

ENERGY The pulse shaper processes the signal, the ADC converts the pulse into the following energy ranges;

0–20 MeV, 2.5 keV per channel

0– 4 MeV, 0.5 keV per channel.

TIME for relative timing between detectors a CFD (constant fraction discriminator) and two TAC's (time to amplitude converter) are required. The signal passes through the CFD, starting the TAC (to be stopped by the local trigger). The CFD also increments the VXI analogue sum-bus if an event has occurred (this increases the multiplicity reading).

The second TAC is also started from the CFD output, this is used for on card ballistic deficit correction, also, its information is used by the event builder to identify pulse pile-up and charge trapping effects.

The Ge VXI card has a local trigger, this stops the TAC, provides gates to the ADC and manages pile–up detection.

4.5.2 BGO Shields

A diagram of a BGO channel can be seen in Figure 4.10.

The sum of the signals from any or all of the BGO elements is used for processing, a ten bit hit pattern is created to indicate which of the crystals have detected an event. The ADC converts the BGO signal into a digitised energy, only one energy

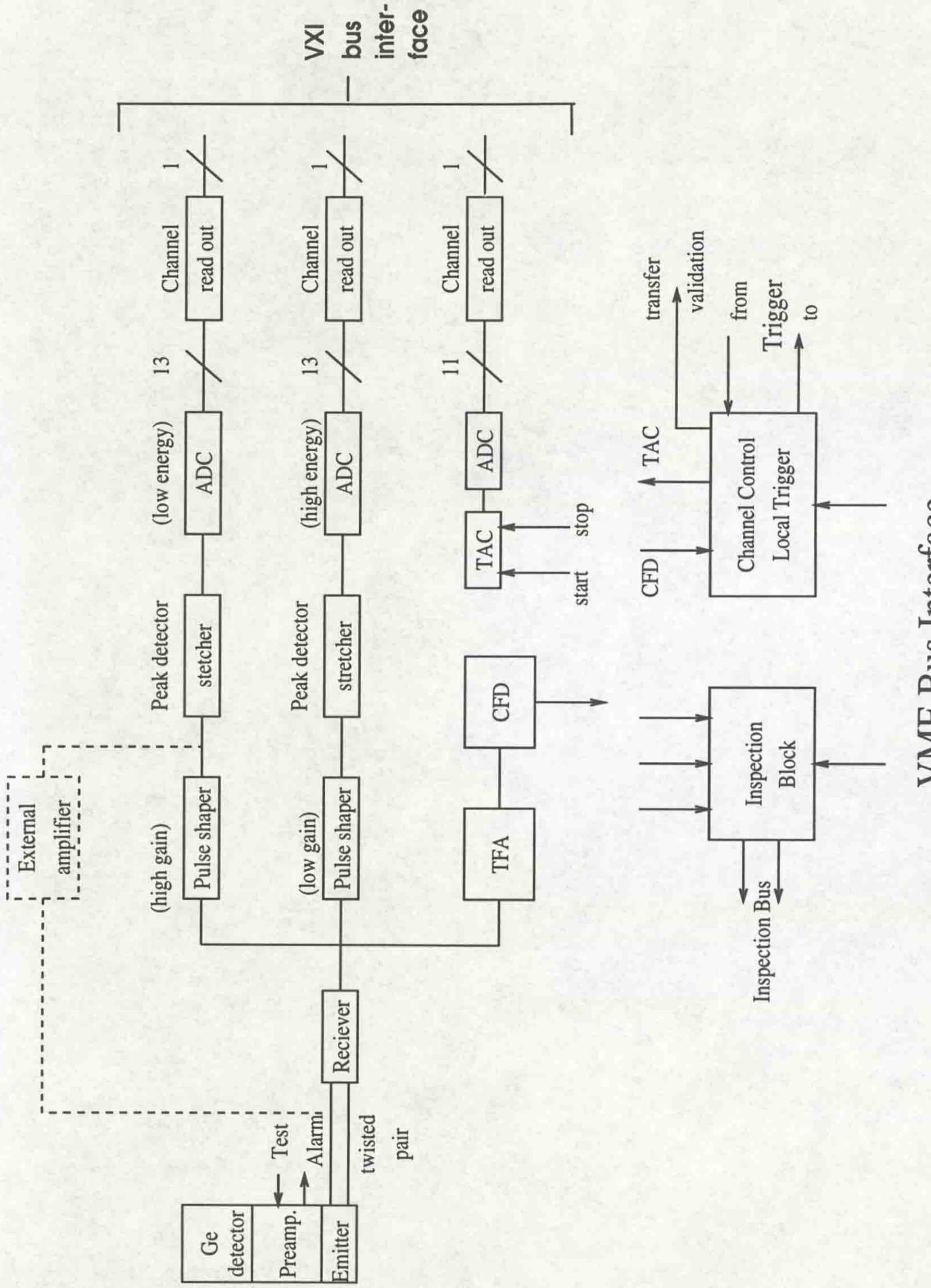

Figure 4.9: *A Ge channel (six are stored on a single VXI card) [EG90].*

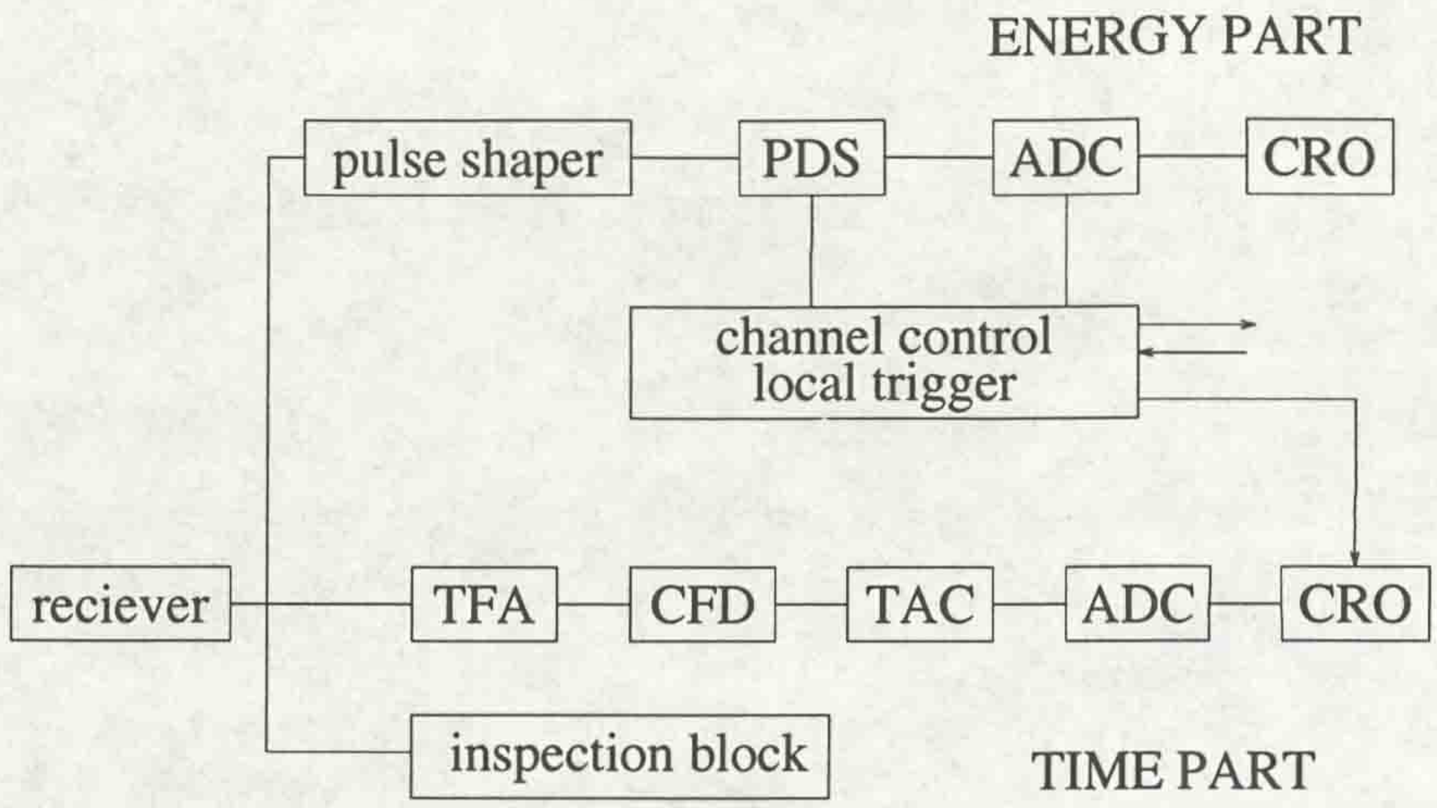

Figure 4.10: *BGO channel [EG90].*

range is necessary, 0-20MeV, 10 keV per channel. Relative time and multiplicity is generated in a similar way to that of the Ge detectors [EG90].

4.5.3 Triggers

There are two levels of hardware triggering incorporated in the main trigger control unit, these are the fast trigger and the validation signal [IL92].

FAST TRIGGER : issued to the Ge and BGO cards, this trigger needs to be very fast as it enables event processing to begin. This trigger also starts an "inhibit" pulse that stops any VME activity in the VXI crates during the processing of an event (common dead time mode).
In the event of a fast trigger not arriving, the data processing channels are reset to accept the next event.
The Ge multiplicity, obtained from the VXI analogue sum-bus, is used as the fast trigger.

VALIDATION SIGNAL : this trigger operates on a slower time scale and is used by the local trigger sections of Ge and BGO cards. This signal has to arrive to enable readout of the digitised events, if it does not arrive, the event is abandoned.

These triggers share a VXI card (the main trigger unit) referred to as the 'Master Trigger'.

4.5.4 Data Handling

Following is a brief description of how data from Eurogam is transferred from the electronics of the array to a medium and format accessible for analysis.

Data Readout

Data readout is carried out at the card, crate and system level [VP92]. At the card and crate level FIFO (first in, first out) devices are used.

Each card has control logic to organise the output from each individual channel. In each VXI (data acquisition) crate there is a read out controller card (ROCO). At the system level a high speed memory (HSM) is used as the readout mechanism, this being part of the event builder. Due to the data transfer needs of Eurogam a point-to-point cable bus, DT32 [JA92], has been devised for reading data from the ROCO to the event-builder.

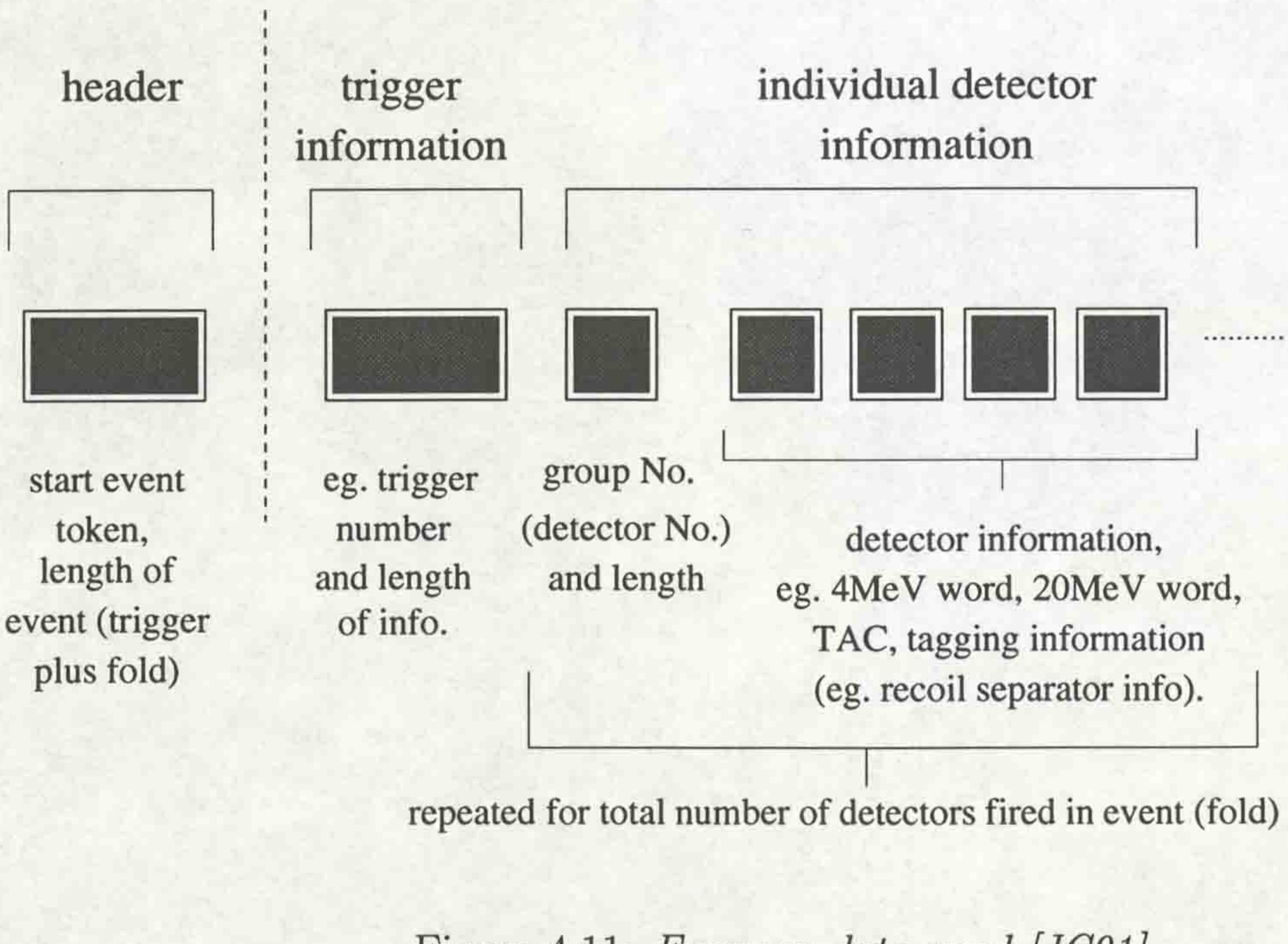

Figure 4.11: *Eurogam data word [JC91].*

The Histogrammer

Eurogam is able to independently histogram, in real time, the data as it is being collected. The Eurogam histogram unit (EHU) has been specifically designed for this purpose. The EHU spies on the DT32 bus, ie. the data is sampled before it reaches the event builder.

The Event Builder

The primary function of the event builder is to reorganise event by event data into a standard format (see Figure 4.11) for data storage.

In the event builder the data word can be tailored to the particular needs of an experiment. Other functions of the event builder are Compton suppression and total sum energy calculations (from both the Ge and BGO data words) [JC91].

Storage

Exabyte video tapes are used to store the data, they have a high storage capacity per tape, this is necessary due to the huge data sets collected.

Figure 4.12 shows a schematic diagram of the Eurogam data acquisition system.

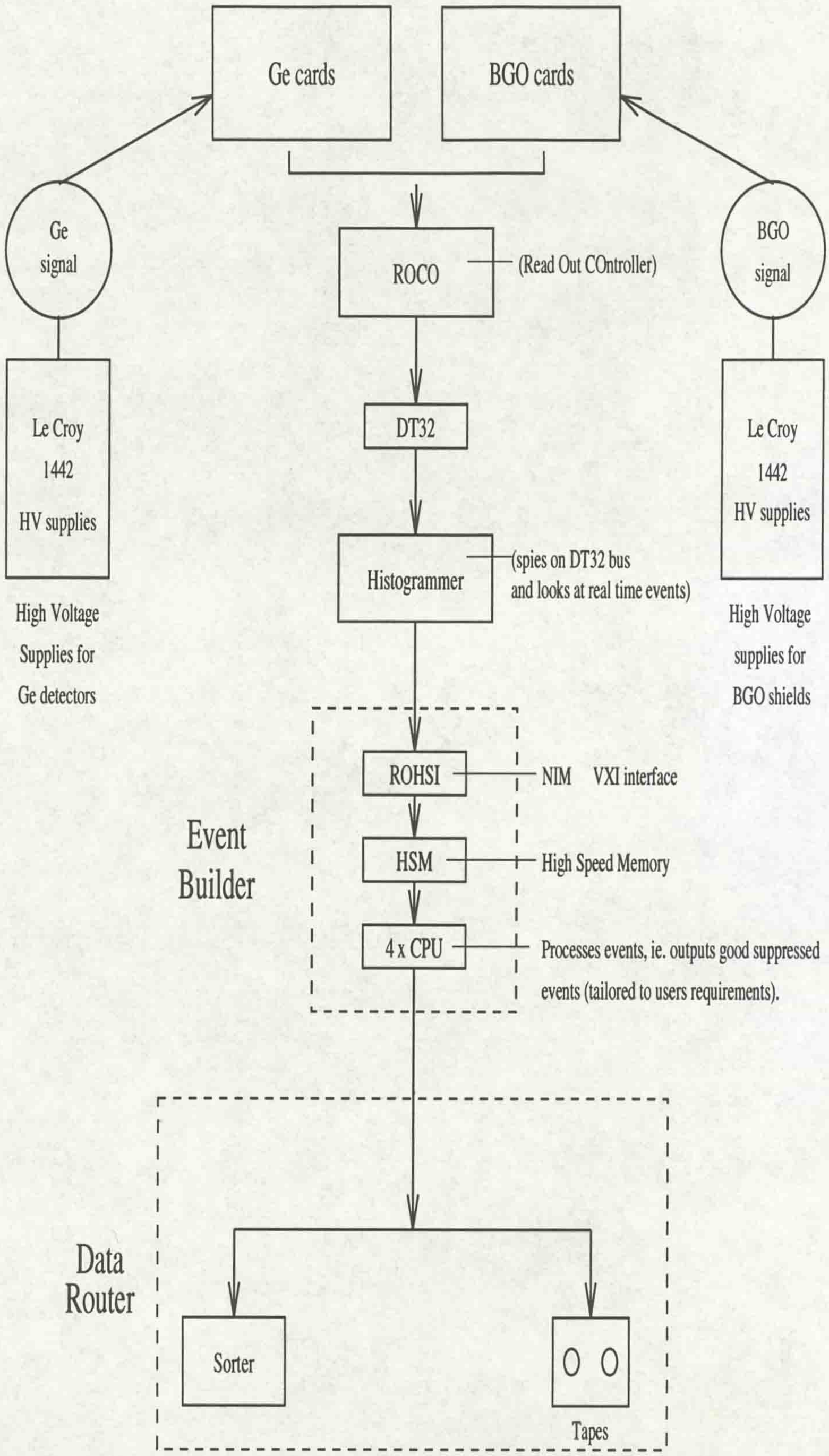

Figure 4.12: *Schematic diagram of the Eurogam data acquisition system [RC92].*

Chapter 5

Results

The high spin results for ^{158}Er are also included in this chapter, section 5.4. (the 4n channel of the experiment used to populate ^{157}Er) in order that comparisons can be made at high spin between the neighbouring nuclei ^{157}Er and ^{158}Er. Figure 5.1 shows the ^{157}Er level scheme known previously to this work [JS89]. This scheme was the starting point of this analysis.

5.1 Experimental Method

The nucleus ^{157}Er was populated to high spin by the reaction ^{114}Cd(^{48}Ca,5n). The 210 MeV beam of ^{48}Ca was provided by the tandem Van de Graaff accelerator at the Nuclear Structure Facility, Daresbury Laboratory. The target consisted of two stacked thin foils of ^{114}Cd, each of thickness 500 μg cm^{-2}. Gamma-rays were detected by the Eurogam spectrometer (see section 4.4) with 44 escape suppressed germanium detectors [CB92]. These hyper-pure germanium detectors (HP-Ge) had an average measured relative efficiency of $\sim$ 70%, relative to a 76 mm x 76 mm NaI (Tl) detector for 1.33 MeV γ-rays. A total of 8 x 10^8 suppressed coincident events were collected when at least six un-suppressed Ge detectors were in prompt coincidence (within 50 ns). After unpacking the higher fold events, the data yielded a total of 5.2 x 10^9 triple (γ^3) and 4.1 x 10^9 quadruple (γ^4) γ-ray coincidence events see section A.1.

Throughout the analysis the (γ^3) and (γ^4) data were used to produce γ–γ coincidence matrices which themselves were in coincidence with one or two γ-rays being used to select a particular structure of interest (see appendix A).

The Ge detectors were calibrated using a ^{152}Eu γ-ray source and relative efficien-

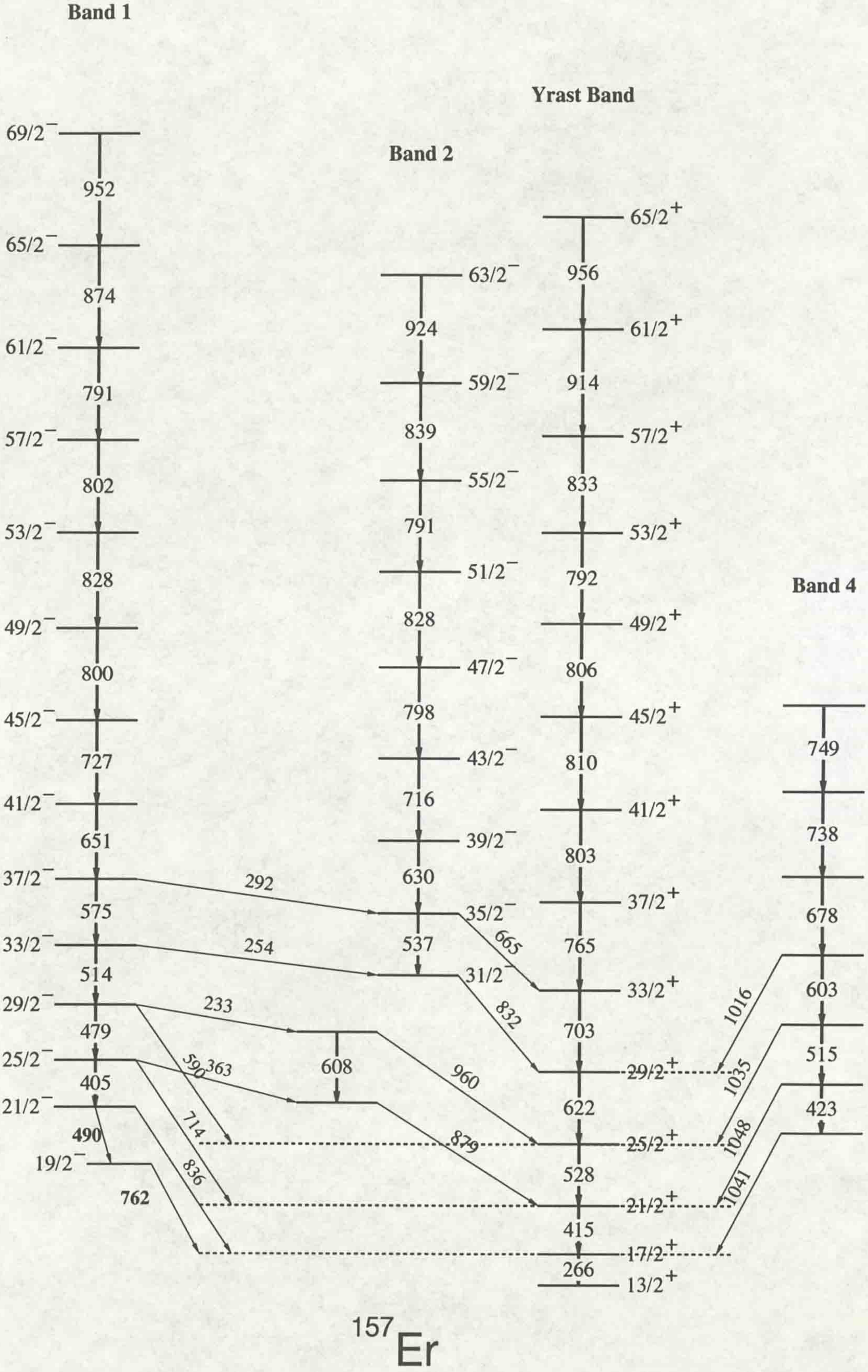

Figure 5.1: *The original ^{157}Er level scheme as deduced by Simpson et al., [JS89].*

cies established by intensity measurements of transitions below and in coincidence with high spin members of the yrast band in ^{158}Er [JS94]. A detailed description of the calculation of the efficiency of the Eurogam array is given in section 5.1.1. The gains of the Ge detectors were adjusted off-line to align the Doppler shifted γ-rays from the recoiling nuclei. The relative intensities of the transitions were extracted from the $\gamma - \gamma$ and $\gamma - \gamma - \gamma$ coincidence data to give a quantitative measure of the population of the band as a function of spin, see section 5.1.2.

In order to determine the multipole order of new transitions and confirm those previously known in ^{157}Er, the angular correlation of emitted γ-rays has been measured, see section 3.2. The angular correlation ratios have been evaluated for almost every transition in ^{157}Er. The ESCL8R analysis package (see section A.2.5 and [DR93]) with its excellent background subtraction and fitting facilities was utilised. The 10 Eurogam detectors at 94° and 86° ($\simeq$ 90°) and 9 detectors at 134° with respect to the beam axis were used in these measurements. Angular correlation ratio values $\geq$ 1.0 are taken as evidence as stretched quadrupole transitions (the measured in-band quadrupole transitions are assumed to be stretched E2s) and values $\leq$0.8 are taken for evidence as stretched dipole transitions. Indeed, the average value obtained for the previously known stretched quadrupole transitions in the yrast bands of ^{157}Er [JS89] is 1.7 and the corresponding average value for known stretched dipole transitions is 0.5. The angular correlation measurements are given in table B.1. and plotted against spin for all the observed bands in figure 5.5. Some of the very weak in-band transitions were observed in the $[134°, 90°]$ but not in the $[90°, 90°]$ coincidence spectra. These data were therefore consistent with stretched quadrupole transitions, such assumptions have been made previously, for example see reference [JS87].

5.1.1 Efficiency Measurements

The intensities of transitions measured with Eurogam have to be corrected for the efficiency of the spectrometer. The efficiency, ε, of a germanium detector can be approximated to the expression given below in equation 5.1, where c is a constant. The efficiency ε is approximately constant for a given detector type, therefore it is assumed all germanium detectors in the array have the same efficiency.

$$\varepsilon = cE_{\gamma}^{-x} \tag{5.1}$$

Equation 5.1 can be written in the form given in equation 5.2, a linear relationship,

and the value of x can be extracted.

$$\ln \varepsilon = -x \ln(E_\gamma) + c \tag{5.2}$$

This equation is only valid at $E_\gamma \geq 200$ keV.

The efficiency of the Eurogam detectors during the ^{157,158}Er experiment was calculated using available γ-γ matrices, giving an accurate value for the efficiency of the germanium detectors for coincidence data (the array responds differently when detecting gamma-rays from a source than from compound nucleus reaction). Transitions in the yrast band of ^{158}Er were measured. A gate was set at the top of the band and transitions below were measured, see figure 5.2.

If the array was perfect (100% efficient) each transition measured below the gate would be of equal intensity, but, due to the efficiency of the array this is not the case, hence this is a direct method of measuring the efficiency of ^{157,158}Er coincidence data.

The results of these measurements can be seen in figure 5.3. The value derived for x is written below.

$$x = 0.587 \pm 0.057$$

5.1.2 Intensity Measurements

Intensity measurements of transitions in the level scheme are made in order to ensure the transitions are placed correctly in the scheme.

The ordering of transitions in the level scheme is based on coincidence relationships and the general trend of increasing intensity with decreasing spin within a structure such as a rotational band. In a coincidence gated spectrum the intensities of the in-band transitions which are fed by the gate are expected to be constant. The transitions above the gate are expected to have intensities decreasing as spin increases, this is due to successive side feeding at higher levels. Therefore by utilising these two observable effects the transitions can be placed in the correct order in the level scheme.

The intensities for each transition are corrected for efficiency, I_{ABS}. This correction is valid for $E_\gamma \geq 200$keV.

$$I_{ABS} = \frac{Number\ of\ counts\ in\ peak}{E_\gamma^{-0.587}} \tag{5.3}$$

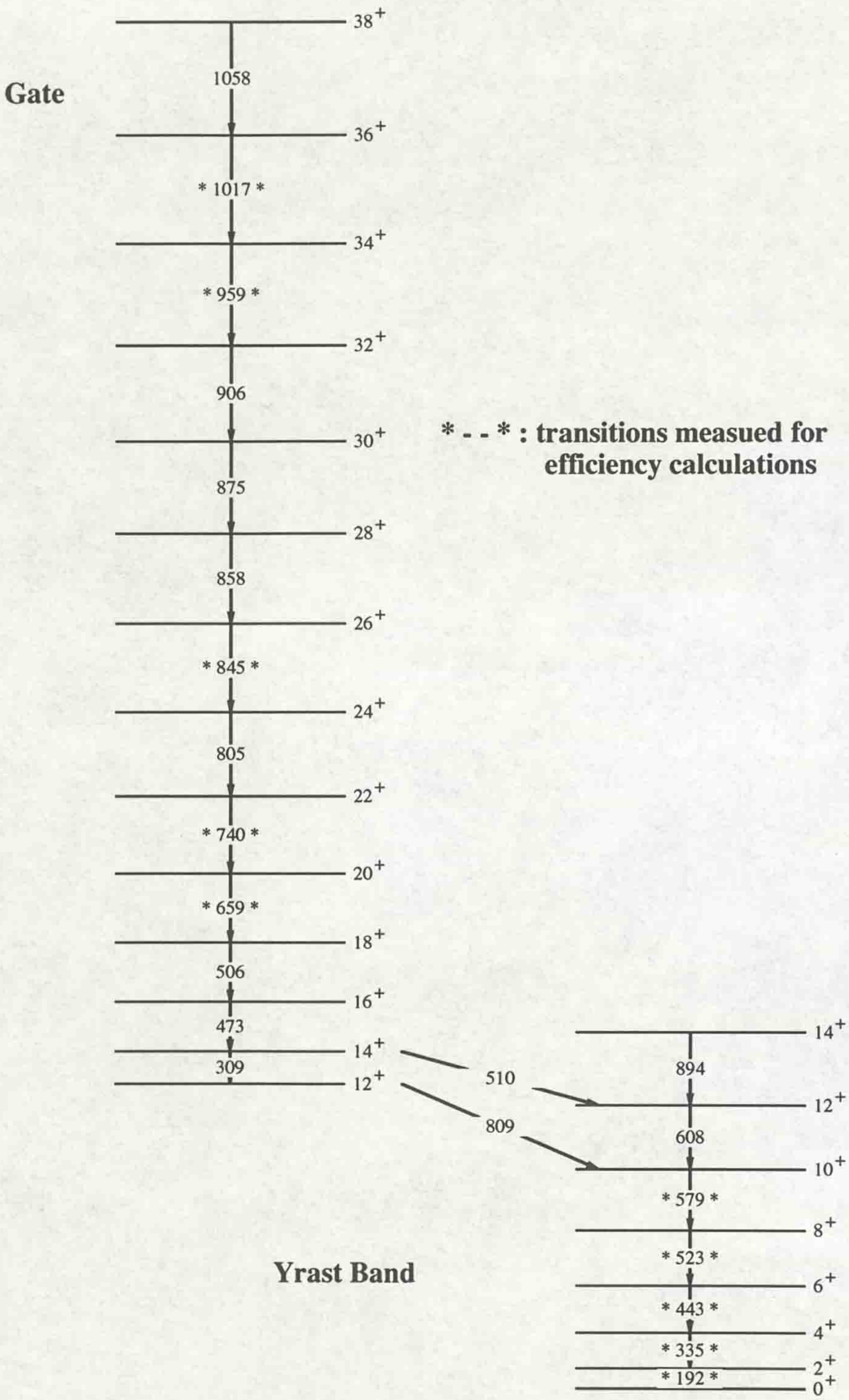

Figure 5.2: ^{158}Er *Yrast band, with gate and transitions used for efficiency calculation.*

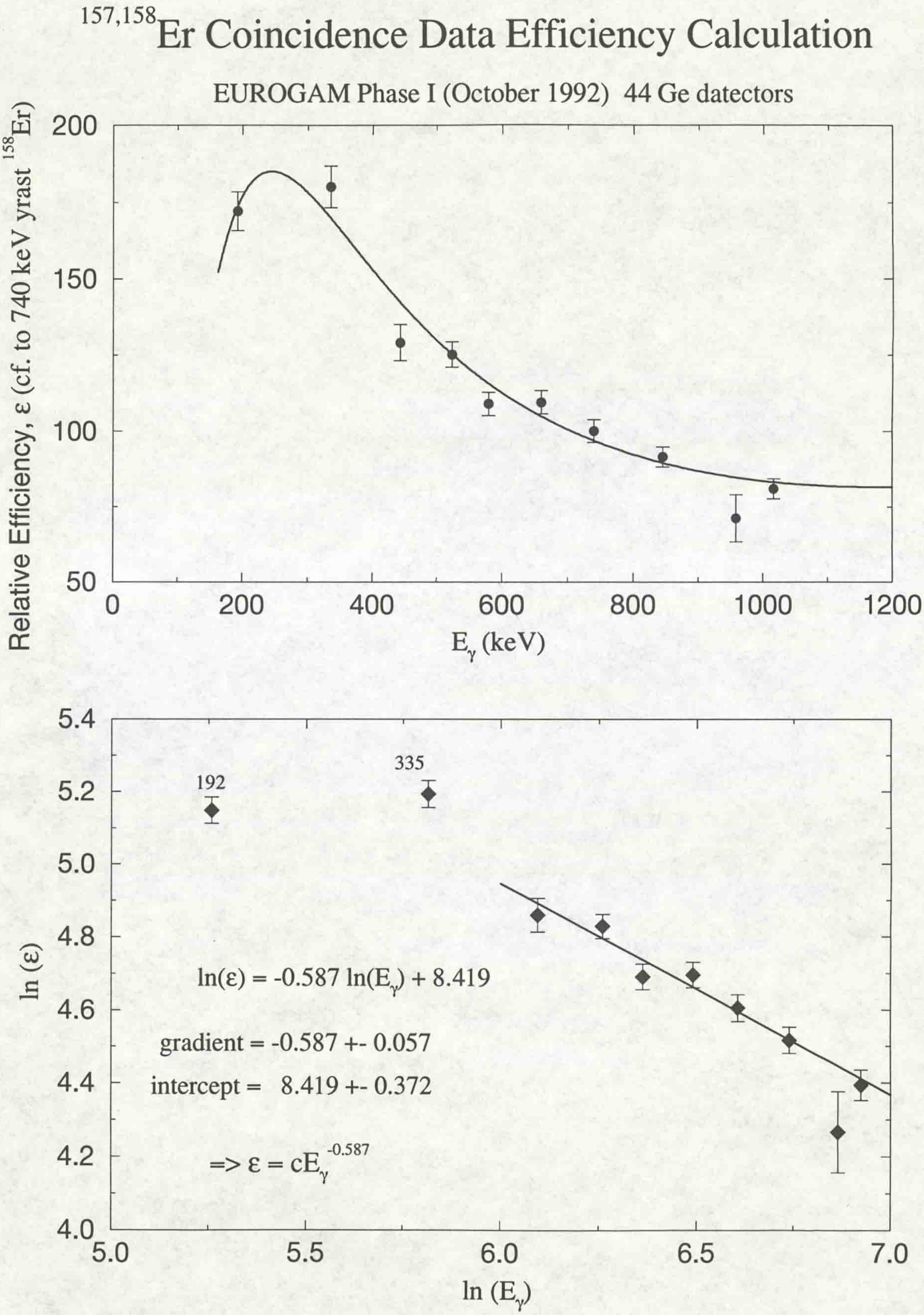

Figure 5.3: *Graphs illustrating the method used to calculate the efficiency.*

5.2 ^{157}Er Results

The level scheme of ^{157}Er obtained from this work is shown in figure 5.4. Previous work on this nucleus [JS89] has established the (parity, signature) = $(+,+\frac{1}{2})$ band up to $\frac{65}{2}^+$ and the lowest energy negative parity bands, $(-, +\frac{1}{2})$ and $(-,-\frac{1}{2})$, up to $\frac{69}{2}^-$ and $\frac{63}{2}^-$, respectively. In addition, a further band, see section 5.2.5, was observed up to $E_x = 5013$ keV. Figure 5.5 shows angular correlation ratios plotted against gamma-ray energy.

The known contaminants present in all the spectra shown in this section are denoted by $\star$.

The excitation and γ-ray energies, relative γ-ray intensities, angular correlation ratios and spin parity assignments for ^{157}Er are given in table B.1.

5.2.1 Positive Parity States, $(+,+\frac{1}{2})$ and $(+,-\frac{1}{2})$ Bands.

The lowest energy positive parity band $(+,+\frac{1}{2})$, which is yrast at low spin, $I \leq 20\hbar$, has been extended up to $(\frac{85}{2}^+)$. This band has a maximum intensity of ~40% of the ^{157}Er reaction channel. The intensity of the transitions between $\frac{37}{2}^+$ and $\frac{57}{2}^+$ were very similar which meant that unambiguous determination of the order of the γ-rays was not possible. The order shown in figure 5.4 is the most plausible, consistent with the measured intensities, and agrees with the previous assignment [JS89]. The order produces a smooth and large gain in aligned angular momentum which is well understood in terms of quasiparticle alignments, discussed in the following chapter. The γ-rays in the band have angular correlation ratios consistent with them being stretched E2 transitions, see table B.1. The spectrum of transitions in coincidence with the 1080 keV ($\frac{73}{2}^+ \rightarrow \frac{69}{2}^+$) transition is shown in figure 5.6. The $\frac{69}{2}^+$ state (10054 keV) is observed to be fed by a second sequence of transitions, 598, 1072 and 1039 keV, see figure 5.7. These figures show transitions coincident with a $\gamma-$ray from a matrix selected by pairs of $\gamma-$rays in the (+,+1/2) sequence (ie. a gate on the (+,+1/2) quadruples matrix).

The 598 keV transition has an angular correlation ratio consistent with it being a stretched dipole transition and the 1072 and 1039 keV transitions are consistent with being stretched E2's, see appendix A and figure 5.5. The 598 keV transition is assigned to be an M1 transition therefore implying a (+,−1/2) structure.

The $\frac{71}{2}^+$ state is also fed by an 891 keV transition; the angular correlation ratio

^{157}Er

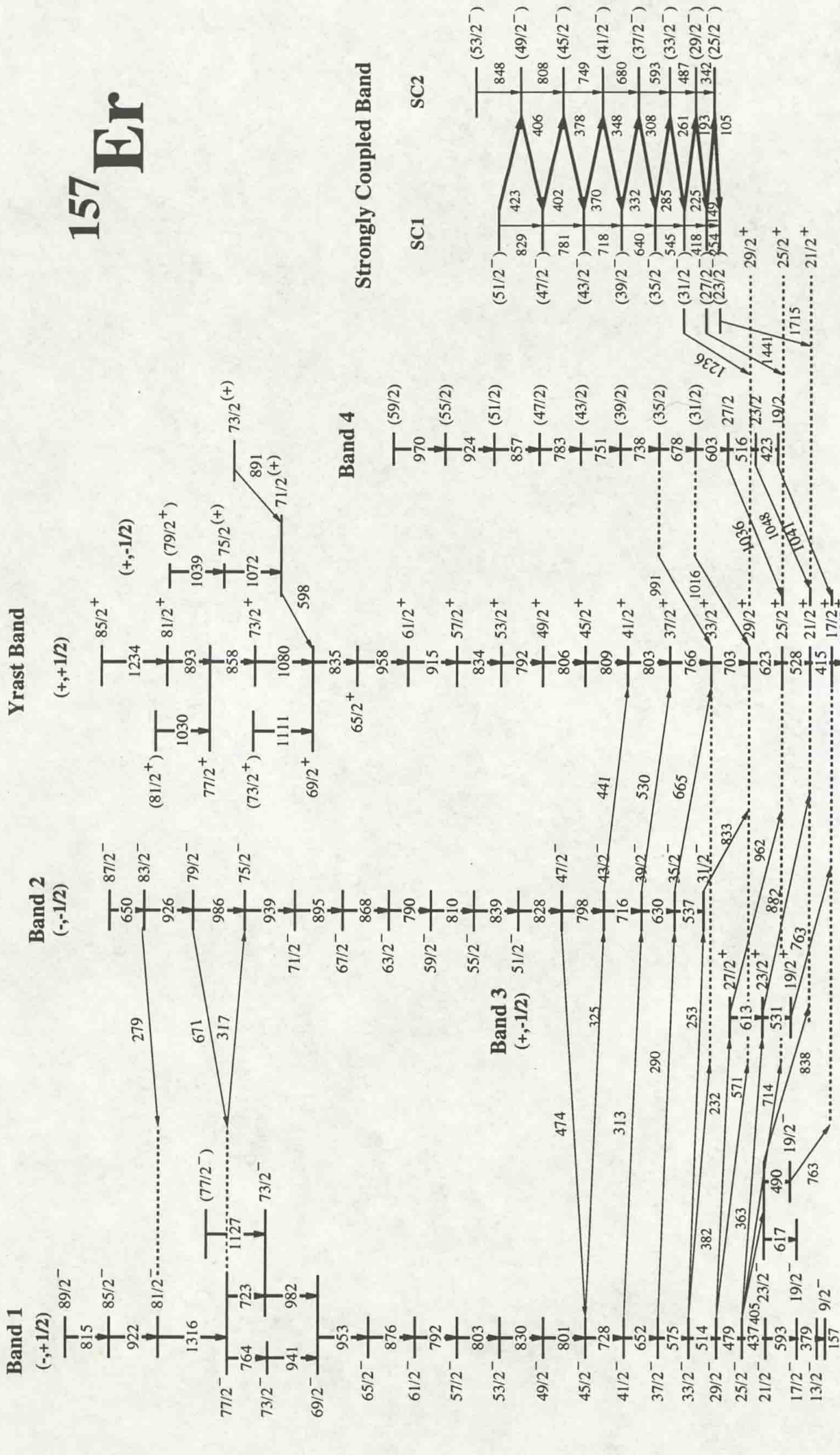

Figure 5.4: *The deduced level scheme for* ^{157}Er.

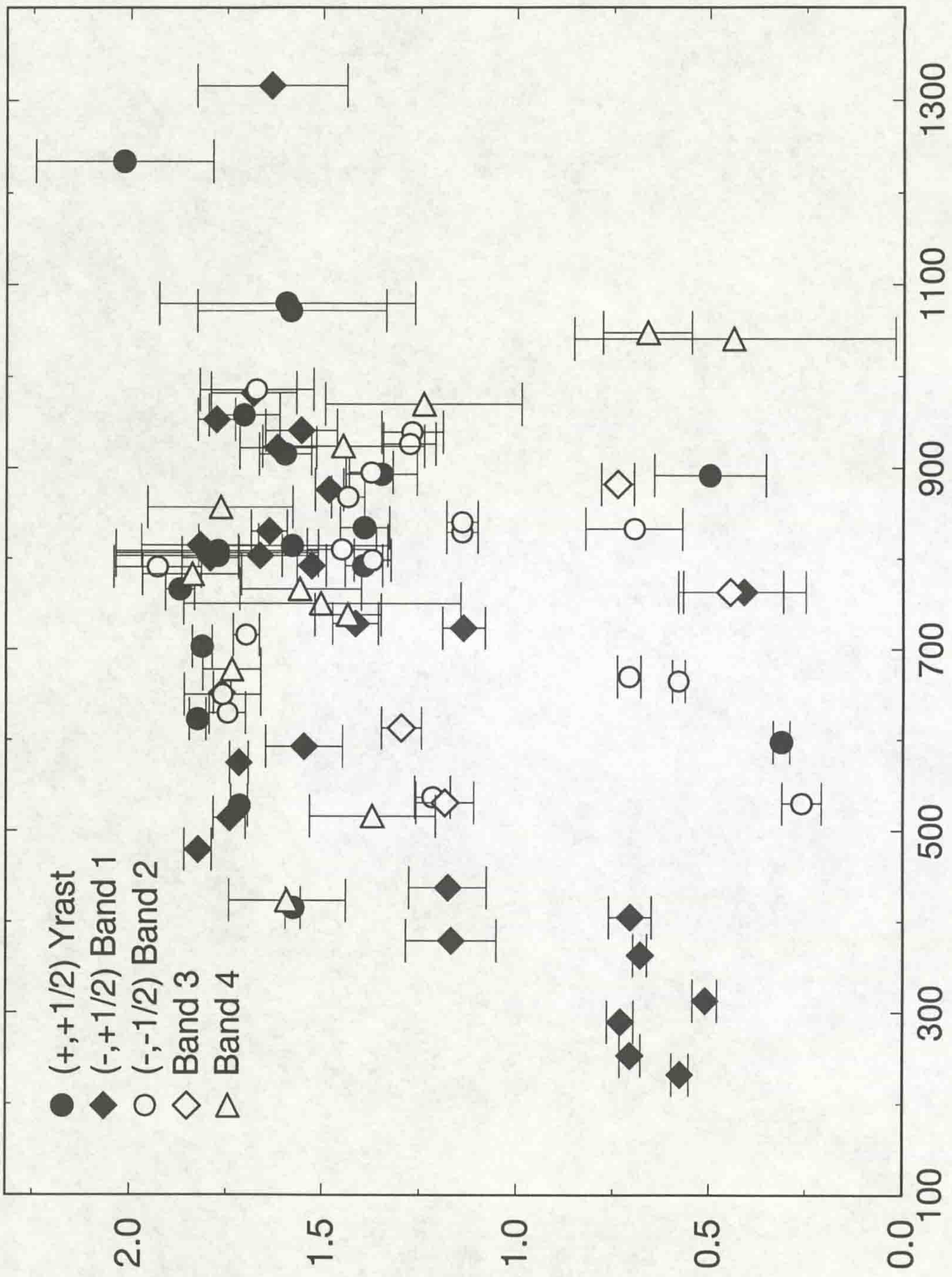

Figure 5.5: *Measured ^{157}Er angular correlation ratios.*

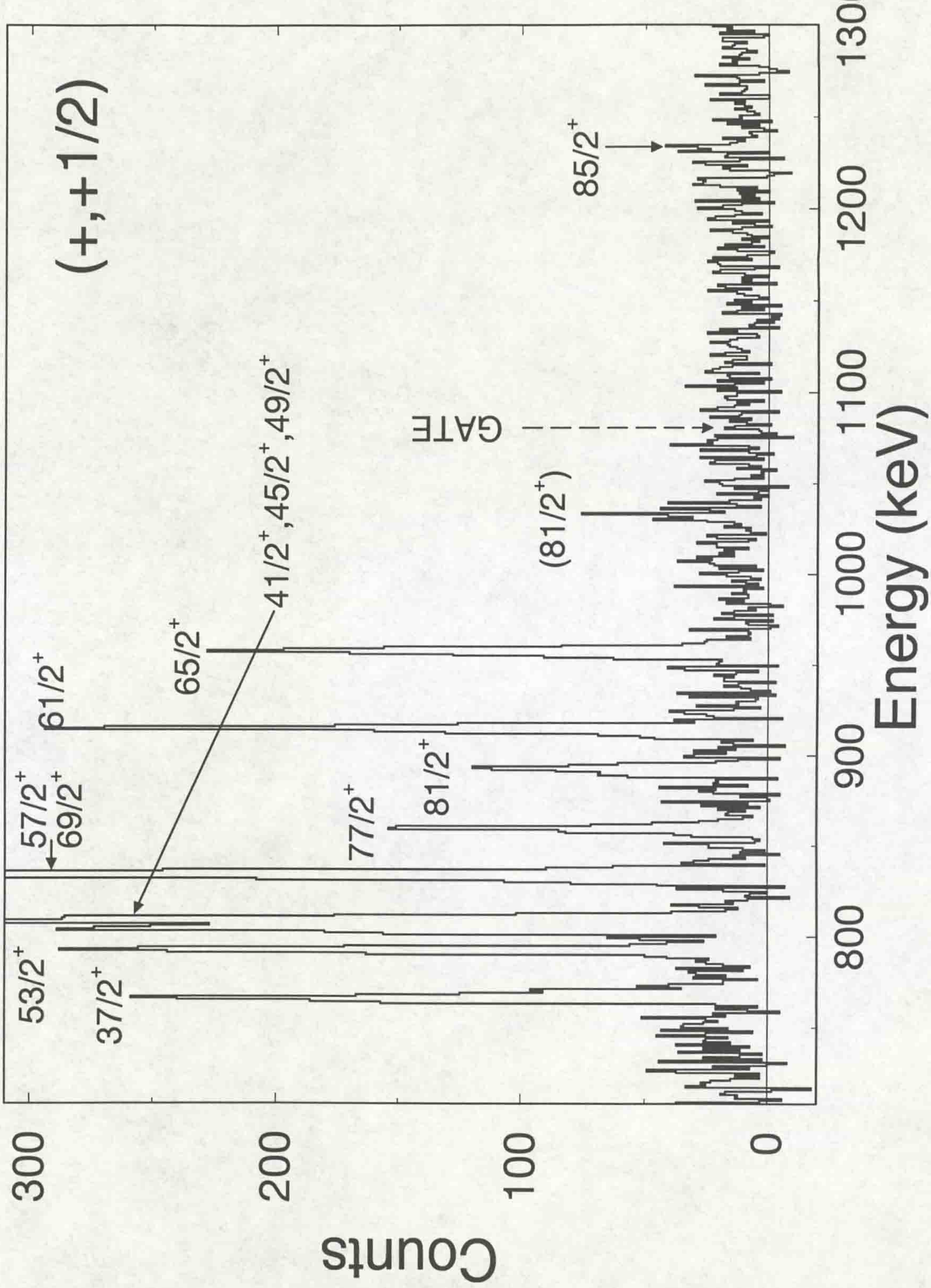

Figure 5.6: *(+,+1/2) Yrast band spectrum. Transitions in coincidence with the 1080 keV* $\frac{73}{2}^+ \rightarrow \frac{69}{2}^+$ *γ−ray.*

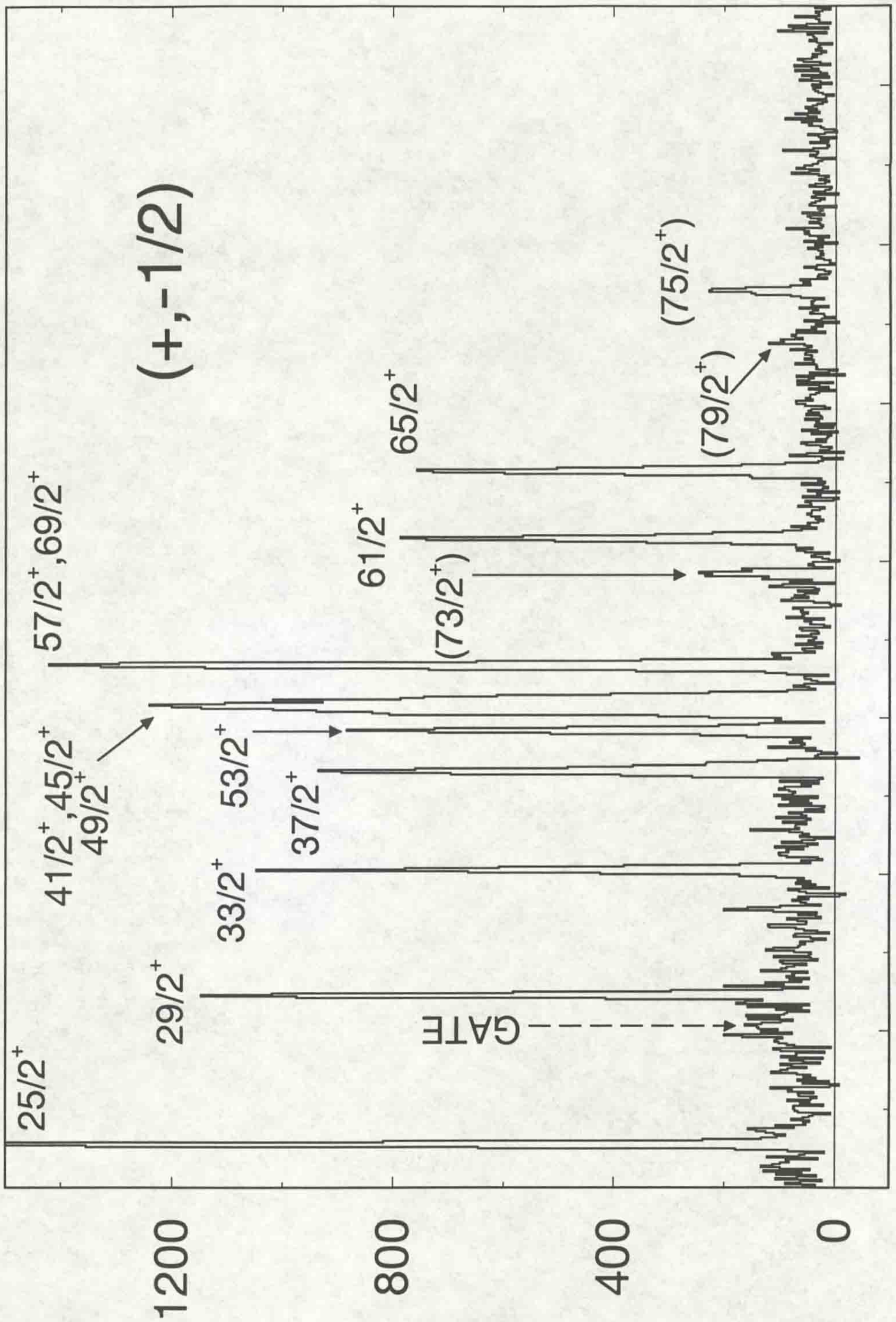

Figure 5.7: *(+,−1/2) Yrast branch spectra. Transitions in coincidence with the 598 keV* $(\frac{71}{2}^{+}) \rightarrow \frac{69}{2}^{+}$ *γ−ray.*

of this transition is consistent with that of a stretched dipole. The $\frac{69}{2}^+$ state is fed by a 1111 keV γ-ray, which has a measured angular correlation ratio consistent with that of a stretched quadrupole transition, and the $\frac{77}{2}^+$ state is fed by a 1030 keV transition. This transition is too weak for the multipolarity to be determined.

5.2.2 The band based on the 358.4 keV ($\frac{9}{2}^-$) level : Band 1 $(-,+\frac{1}{2})$.

The $(-,+\frac{1}{2})$ sequence, band 1, which has a maximum intensity of ~30% of the ^{157}Er reaction channel, was established previously [JS89] between the $\frac{25}{2}^-$ and $\frac{69}{2}^-$ states. This work confirms these states and extends the $(-,+\frac{1}{2})$ band to both higher and lower spin. The majority of the intensity of this band decays to the low spin yrast $(+,+\frac{1}{2})$ states from decays out of the states between $\frac{25}{2}^-$ and $\frac{45}{2}^-$. The decay path involves many intermediate states.

A sequence of weak (~2% of the band intensity) stretched E2 transitions has been established extending the band down to the $\frac{9}{2}^-$ state. These low-spin transitions can be seen in figure 5.8. This figure shows the spectrum in coincidence with a sum of the 157, 379, 437 and 593 keV γ-rays gated on a matrix selected by single $\gamma-$rays in the (−,+1/2) sequence (triples matrix).

Band 1 has been extended to an excitation energy of 14683 keV and spin $\frac{89}{2}^-$, see figure 5.9. This figure shows the 1316 keV $\frac{81}{2}^- \rightarrow \frac{77}{2}^-$ transition in coincidence with the 479, 575 and 728 keV in−band transitions. All the in−band γ-rays have angular correlation ratios consistent with them being stretched E2 transitions.

A decay path of two γ-rays (E_γ = 982 and 723 keV) was observed in parallel with the 941 and 764 keV γ-rays establishing two $\frac{73}{2}^-$ states.

5.2.3 The band based on the 2663.8 keV ($\frac{31}{2}^-$) level : Band 2 (−,−1/2)

The lowest energy $(-,-\frac{1}{2})$ sequence, band 2, has been observed up to $\frac{87}{2}^-$. This band has a maximum intensity of ~21% of the intensity of the ^{157}Er reaction channel. This band was established previously [JS89] to $\frac{63}{2}^-$. This work has reordered the γ-rays above $\frac{51}{2}^-$ and added further transitions in the sequence at higher spin. All the in-band γ-rays have angular correlation ratios consistent with them being stretched E2 transitions. The spectrum in figure 5.10 which is in coincidence with the 716, 868

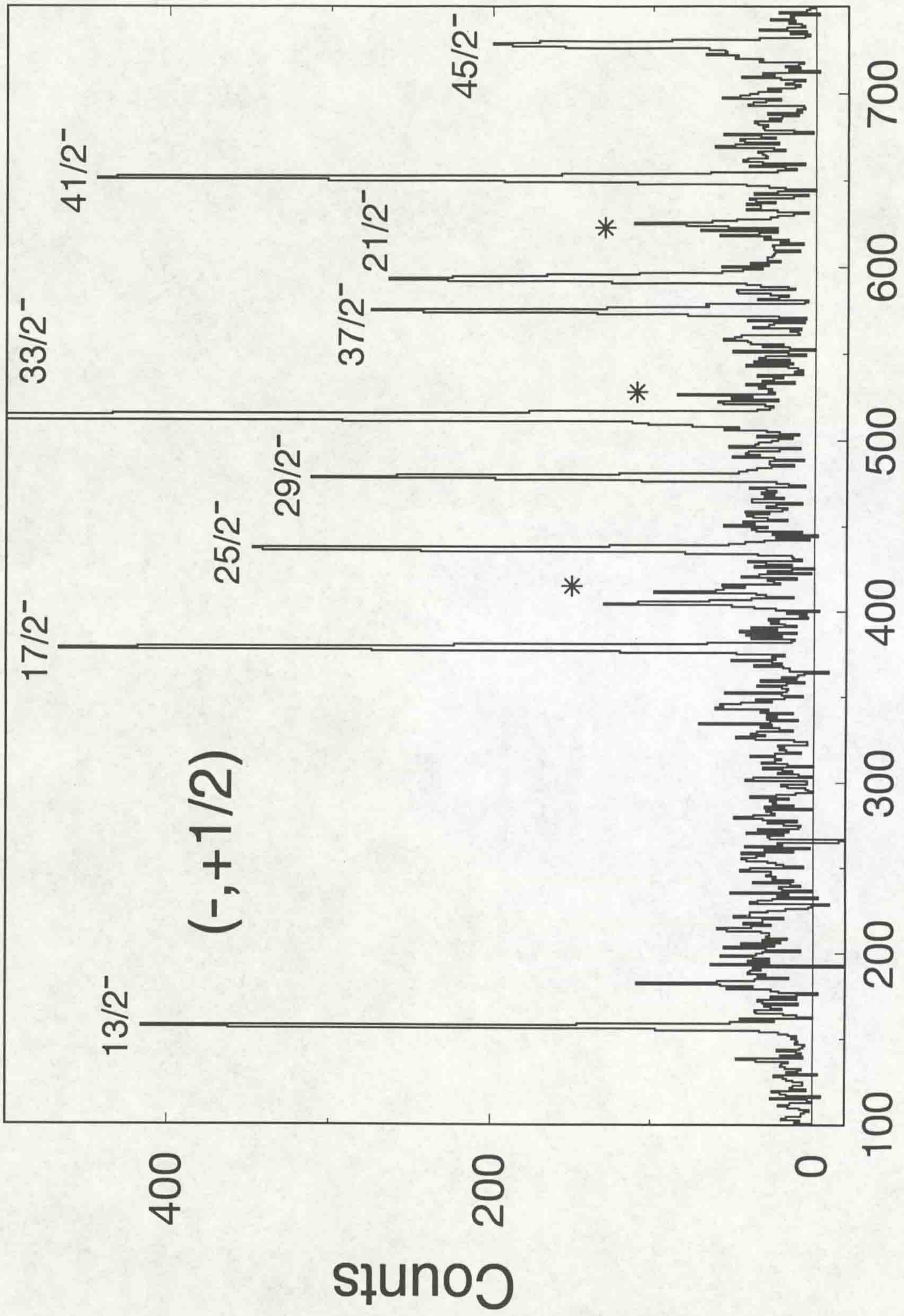

Figure 5.8: *Low-lying structure (band 1) spectrum. Transitions in coincidence with the sum of the 157, 379, 437 and 593 $\gamma-$rays.*

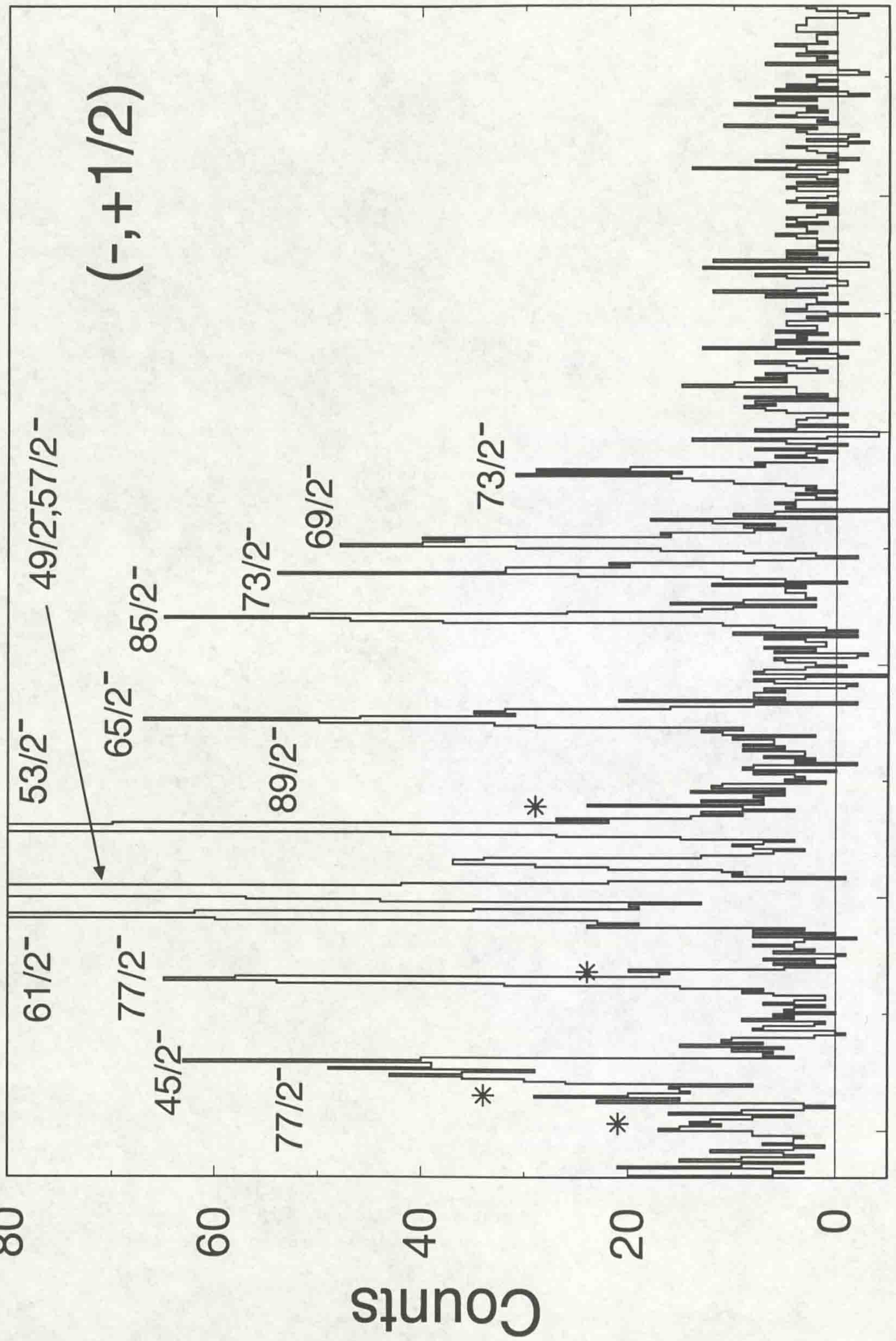

Figure 5.9: *(−,+1/2)Band 1 spectrum. Transitions in coincidence with the 1316 keV* $\frac{81}{2}^- \rightarrow \frac{77}{2}^-$ *γ−ray.*

and 895 keV γ-rays shows the high spin transitions in this sequence. This spectrum was created from a matrix selected by pairs of $\gamma-$rays in the $(-,-1/2)$ sequence.

The decay of this band to the yrast $(+,+\frac{1}{2})$ states via the 665 and 833 keV dipole transitions is confirmed [JS89] and an additional decay, 530 keV, from the $\frac{39}{2}^-$ state to the $\frac{37}{2}^+$ is observed. The angular correlation ratio of this γ-ray is consistent with that of a dipole transition, see table B.1 and figure 5.5. Transitions of energy 279, 671, 317 keV between bands 2 and 1 were observed at high spin.

5.2.4 The band based on the 1030.3 keV $(\frac{19}{2}^+)$ level : Band 3

A sequence of two stretched E2 transitions, 531 and 613 keV, were observed to populate a state at 1030 keV. All the states in this sequence decay via dipole transitions to the low spin states of the yrast band. The states in this band are populated mainly by decays from band 1.

5.2.5 Band 4

A sequence of six γ-rays based on a state at 1306 keV and extending up to an excitation energy of 5013 keV was observed previously [JS89]. The lowest spin states of this band are connected to the low spin yrast states by a series of high energy transitions. All these γ-rays are observed in this work, see figure 5.11. This spectrum shows the transitions in coincidence with the sum of the 423, 750, 738 and 970 keV γ-rays gated on a matrix created by a matrix selected by pairs of $\gamma-$rays in the band.

Angular correlation measurement of the 603 keV γ-ray is consistent with it being a dipole transition. An assignment of a dipole to this transition would split the sequence into two bands. A sequence of two γ-rays in one band and seven γ-rays, in the other. However, this assignment is not easily understood in terms of the alignment properties of the bands which favour the 603 keV transition as being a stretched quadrupole transition making band 4 a smooth sequence. This transition has finally been assigned as a stretched quadrupole, reasons for this decision are given in section 6.3.5.

The total intensity of this band is $\sim$8% of the ^{157}Er reaction channel. The angular correlation ratios are consistent with all the in-band γ-rays being stretched E2 transitions and the 1041 and 1048 keV linking transitions to the yrast states being dipoles.

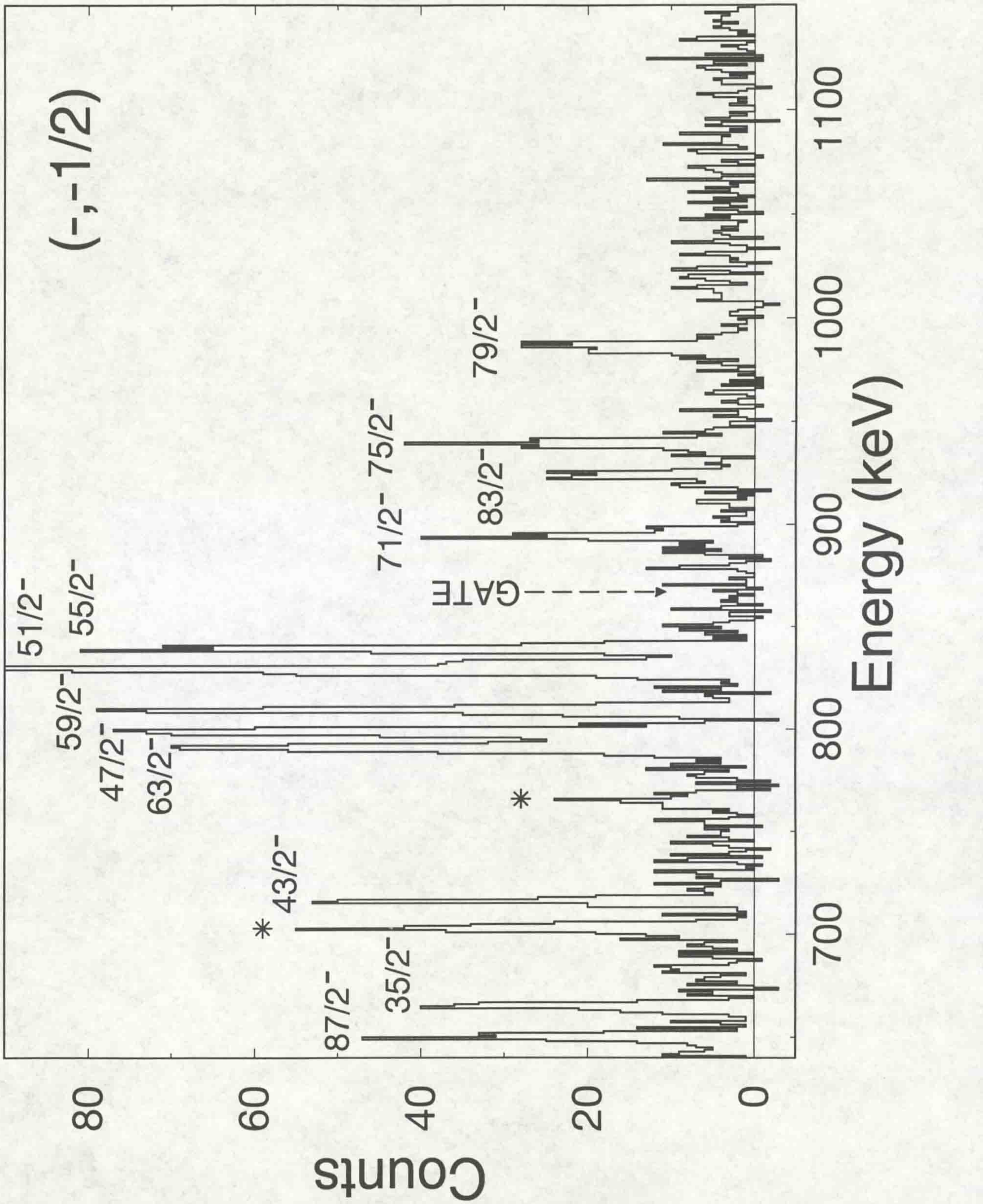

Figure 5.10: *(−,−1/2)Band 2 spectrum. Transitions in coincidence with the 868 keV* $\frac{67}{2}^- \rightarrow \frac{63}{2}^-$ *transition.*

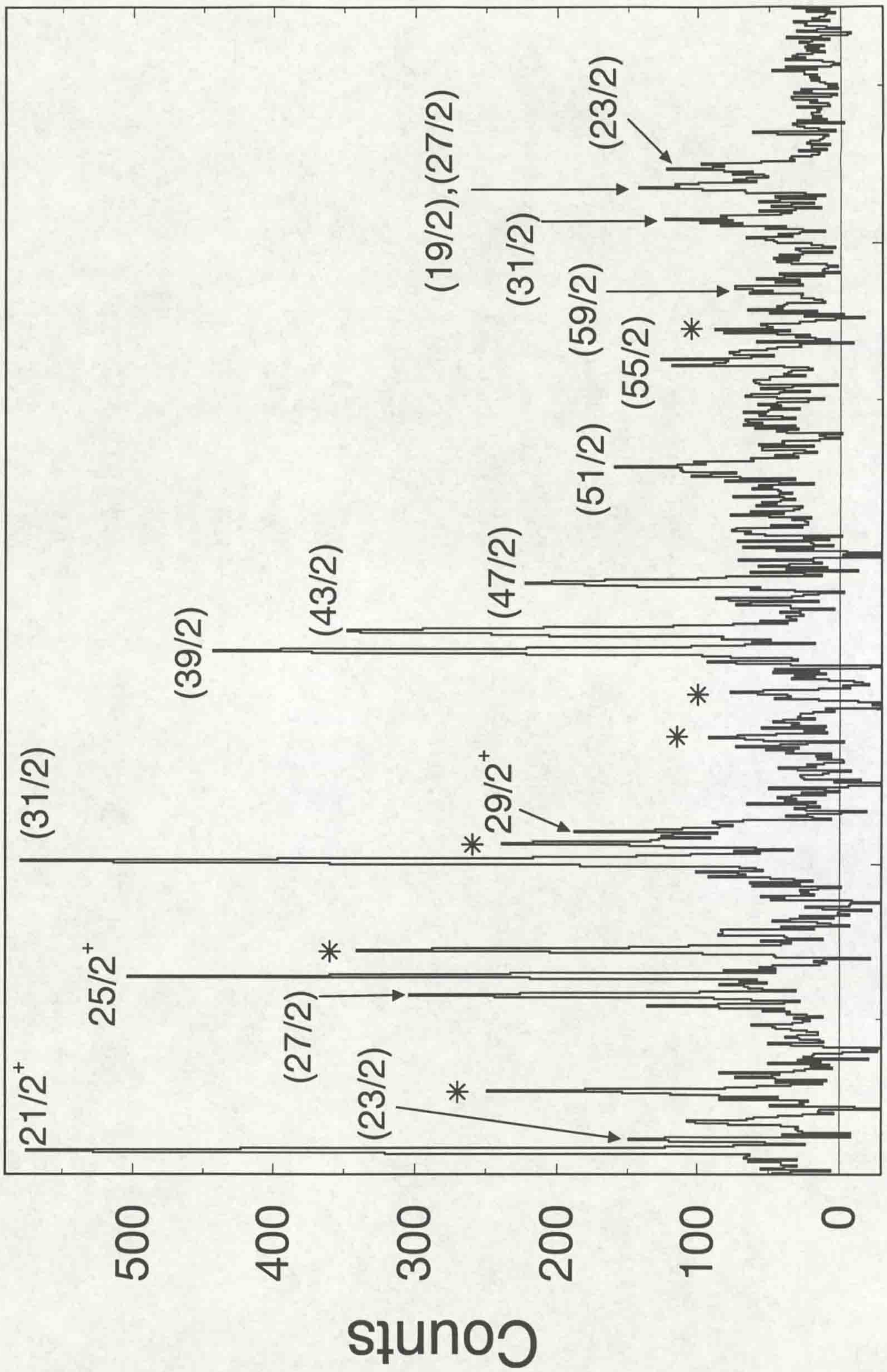

Figure 5.11: *Band 4 spectrum. Transitions in coincidence with the 423, 750, 738 and 970 KeV $\gamma-$rays.*

5.2.6 The Strongly Coupled Band

^{157}Er is the lightest of the erbium nuclei in which such a strongly coupled band has been observed. A strongly coupled sequence with a very low intensity (its maximum being $\sim$ 1.0% of the ^{157}Er reaction channel) has been observed, see figures 5.4 and 5.12. The spectrum is a sum of gates on transitions in the strongly coupled band gated on a matrix selected by single $\gamma-$rays in the band. The inter-band, M1, transitions are denoted by $\diamond$ and the quadrupole, E2, transitions by $\bullet$.

The main decay path of this sequence is via the 1236, 1441 and 1715 keV transitions to the $\frac{29}{2}^+$, $\frac{25}{2}^+$ and $\frac{21}{2}^+$ yrast states, respectively. Since this band is very weak it has not been possible to reliably obtain angular correlation ratios. The spin and parity assignments shown are based on the assumption that the in-band transitions are stretched quadrupole E2's, the inter connecting transitions are M1's and the 1236, 1441 and 1715 keV γ-rays are dipole E1 transitions. These assignments are consistent with the observation of similar strongly coupled bands in the neighbouring Er nuclei [MR94b].

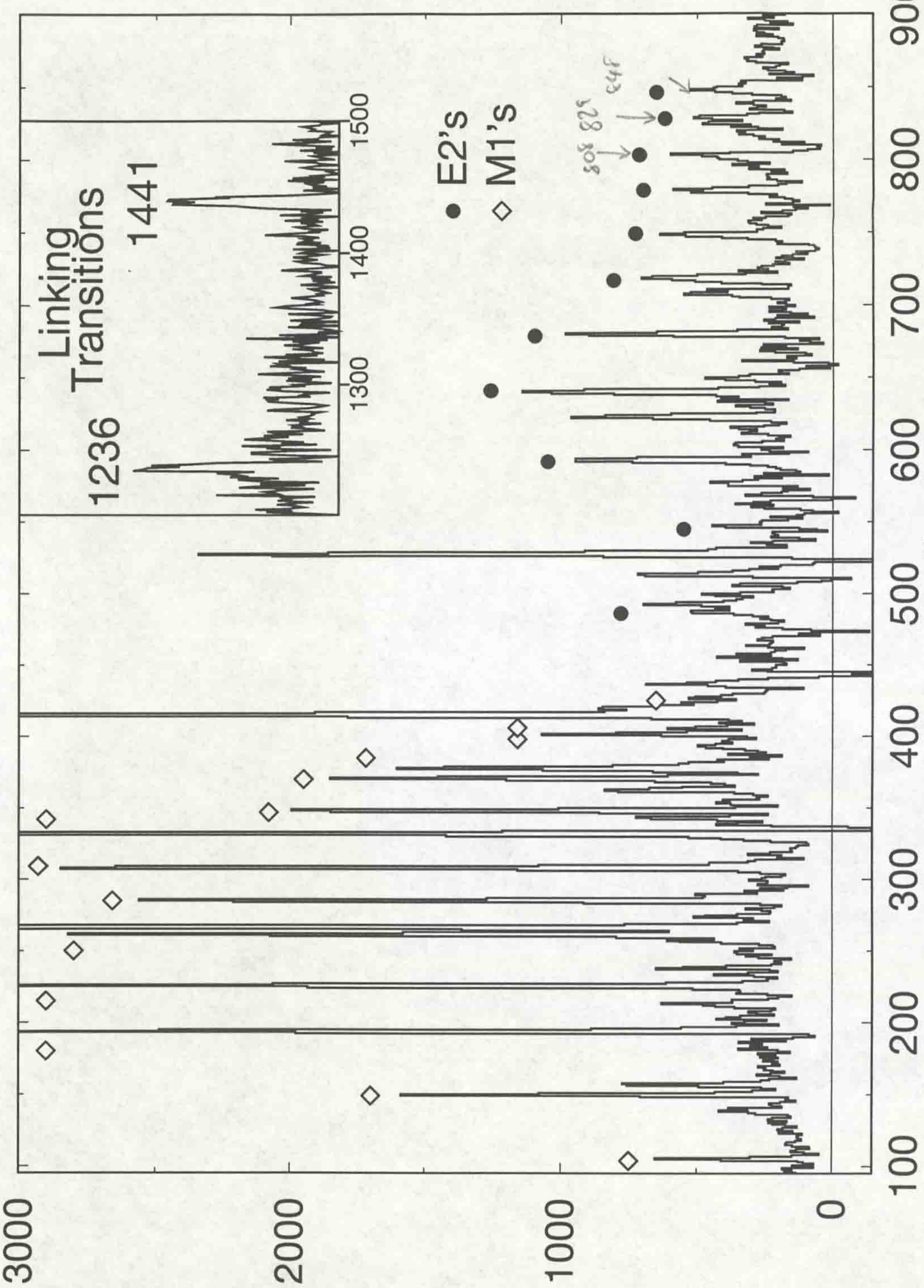

Figure 5.12: *Strongly Coupled Band spectrum. Transitions in coincidence with the sum of the 225, 261, 285 and the 370 keV $\gamma-$rays.*

5.3 Summary of ^{157}Er Results

Figure 5.13 shows the new high spin structures discovered in ^{157}Er during this analysis. Table 5.1 below is a summary of the strength and spin range of the bands.

Table 5.1

Band	% of ^{157}Er Reaction Channel	Spin Range
yrast(+,+1/2)	≃40	$\frac{13}{2}^+ \rightarrow (\frac{85}{2}^+)$
(+,−1/2)	-	$(\frac{71}{2}^+) \rightarrow (\frac{79}{2}^+)$
Band 1(−,+1/2)	≃30	$\frac{13}{2}^- \rightarrow \frac{89}{2}^-$
Band 2(−,−1/2)	≃21	$\frac{31}{2}^- \rightarrow \frac{87}{2}^-$
Band 3	-	$\frac{19}{2}^+ \rightarrow \frac{27}{2}^+$
Band 4	≃8	$\frac{19}{2} \rightarrow (\frac{57}{2})$
Strongly Coupled Band	≃1	$(\frac{23}{2}^-) \rightarrow (\frac{53}{2}^-)$

Notes for Table

The (+,−1/2) branch of the yrast band has no entry for the % of reaction channel as it is included in the (+,+1/2) entry (the measurement of these values are made at low spin in order to prevent inaccuracies due to the feeding out of bands).

Band 3 has not an entry in the % of reaction channel as it is fed by Band 1.

The strongly coupled band is not separated in the table above, this is because in both cases the bands are too strongly linked to obtain separate reaction channel intensities.

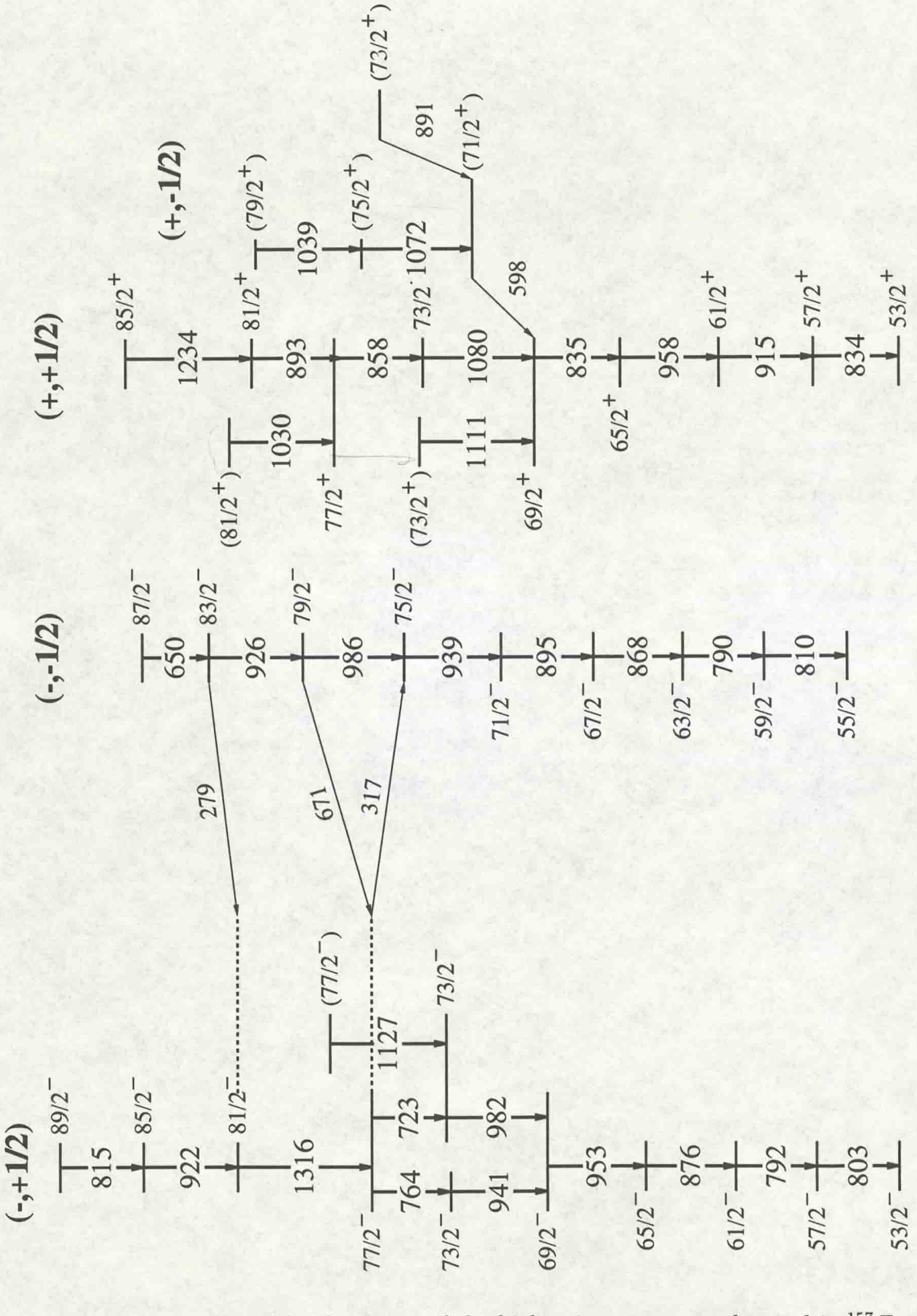

Figure 5.13: *The partial level scheme of the high spin structures observed in* ^{157}Er.

5.4 ^{158}Er Results

The interpretation of ^{157}Er high spin results is closely related to that of the even-even neighbouring nuclei ^{158}Er. The high spin bands observed in this nucleus will therefore be included in this chapter for clarity. The ^{158}Er nucleus was populated during the same experiment as the ^{157}Er described in this analysis. The reaction was ^{48}Ca(^{114}Cd,4n)^{158}Er (^{157}Er was formed via the 5n channel). This 4n channel was the major reaction channel and therefore yielded higher statistics, the relative intensity of the ^{157}Er reaction channel compared to the ^{158}Er channel is 80%. This analysis, was carried out by J.Simpson and M.A.Riley [JS94]. The extraction of angular correlation ratios (section 3.2.1) was carried out as part of the work for this thesis. The angular correlation ratios have been used to verify the high spin transitions.

Figure 5.14 shows the level scheme deduced from the analysis of the above experiment. The experimental methods used are described in section 5.1 and appendix A.

The results of the high spin structure, I$\geq$28, of ^{158}Er are reported below. As with ^{157}Er the bands will be labelled by parity and signature. Figure 5.15 shows the angular correlation ratios measured made for these high spin transitions, these values are given in table B.2. A transition assumed to be a dipole has been observed at high spin in this data, 939 $47^- \rightarrow 46^+$ transition, linking the (+,0) and (−,1) bands. This transition is very weak and the angular correlation ratio is very small, coincident measurements confirm that the placing of the $\gamma-$ray in the level scheme is correct.

A spectrum illustrating the quality of the data is shown in figure 5.16. This spectrum shows the transitions in coincidence with the favoured single particle sequence of the (+,0) band.

5.4.1 (+,0) Band

Previous work on this nucleus [MR84a, PT85] observed this band branching into two decay sequences above (I^π) 38^+. It can be seen in figure 5.17 that the right hand branch has been increased to a spin range of $30^+ \rightarrow 46^+$. The spins labelled with subscript 2 indicate the weaker of the two branches (note that the strong band crosses the weak band). It can be seen that the main decay path runs from 28^+ to 46^+ via the 827 ($40^+ \rightarrow 38^+$) transition. The 38^+ to 46^+ sequence is built on a series of irregular energy $\gamma-$rays, implying a single particle structure.

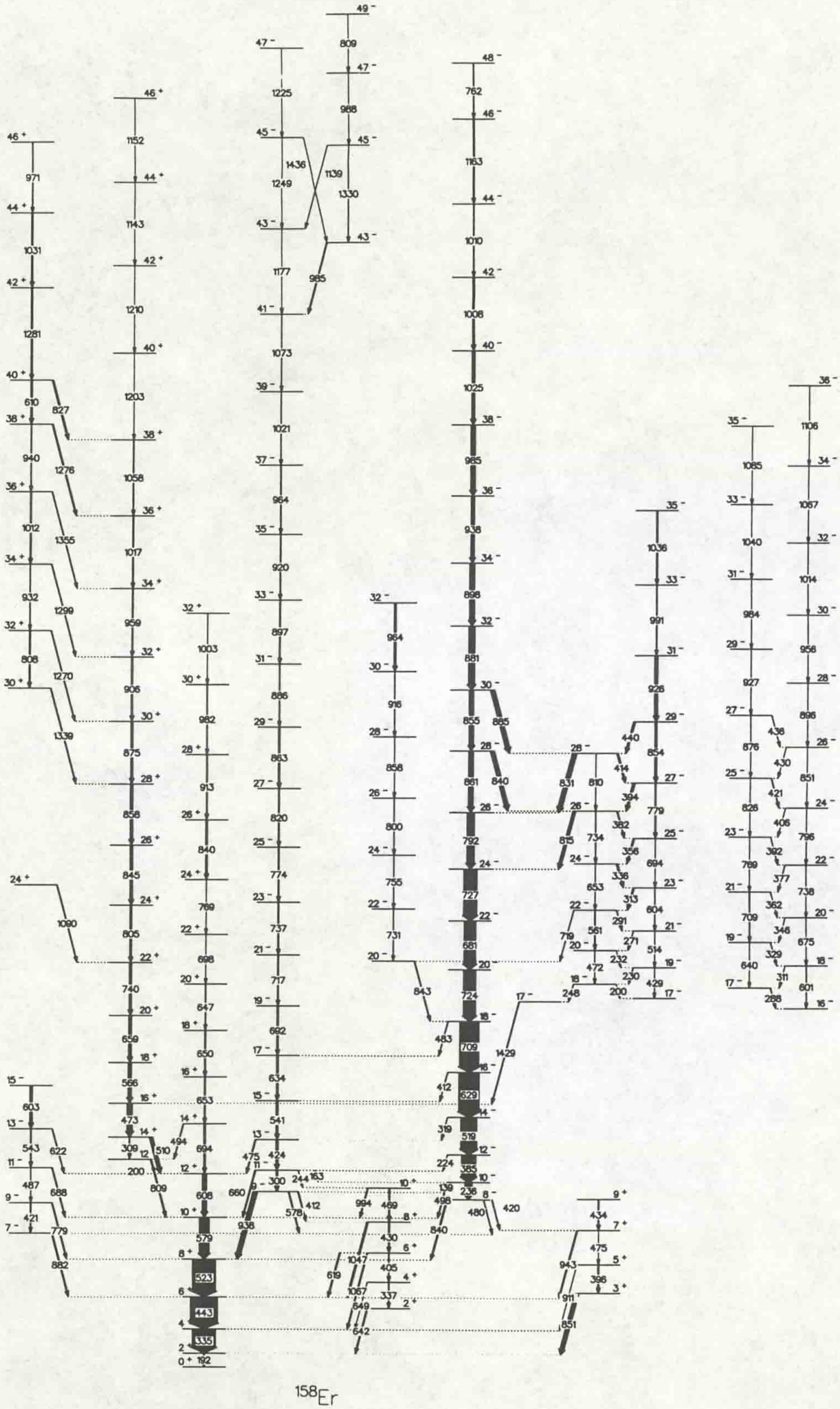

Figure 5.14: *The ^{158}Er level scheme deduced by J.Simpson and M.A.Riley [JS94].*

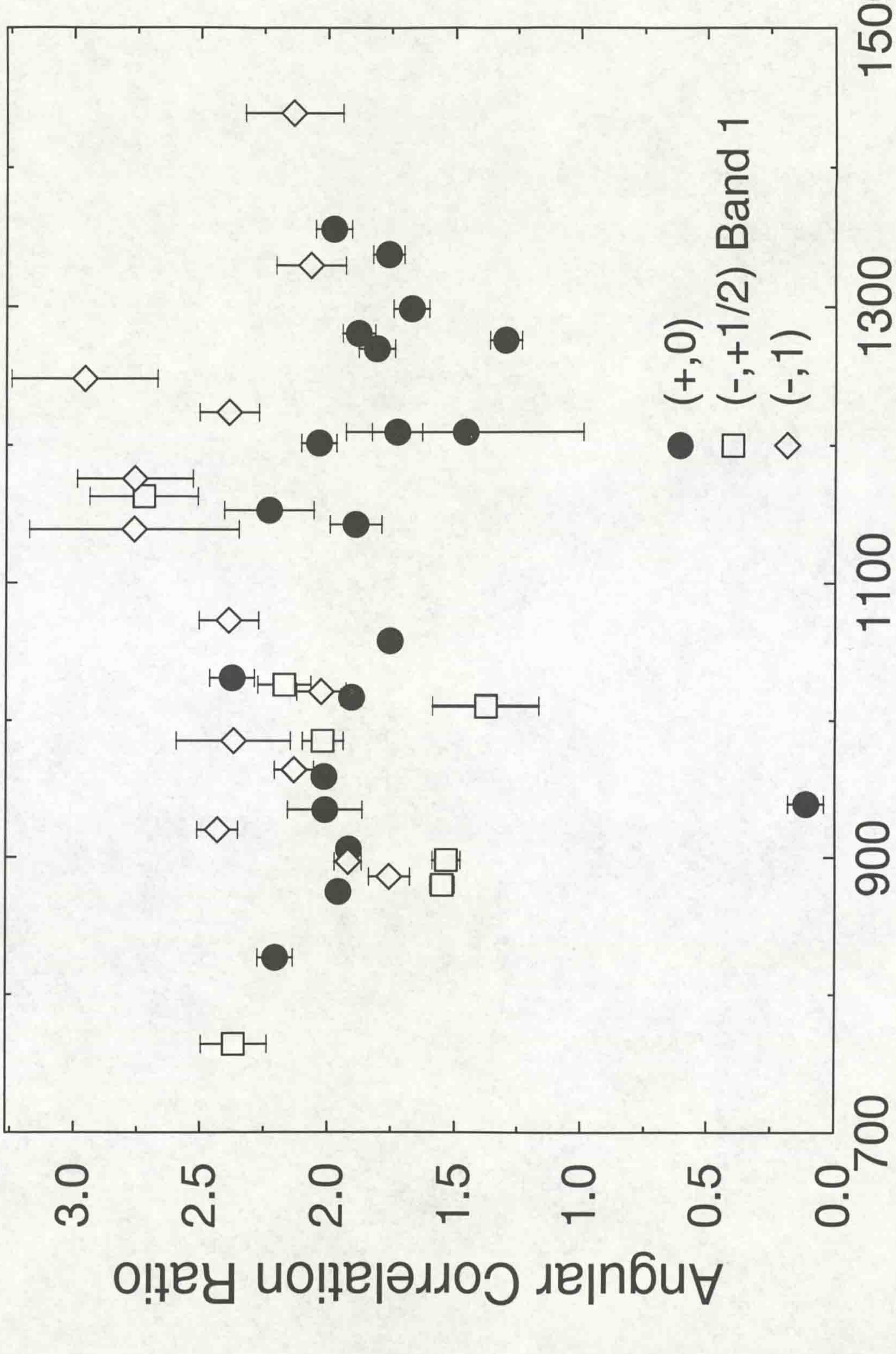

Figure 5.15: *The angular correlation ratios measured for the high spin structure of* ^{158}Er.

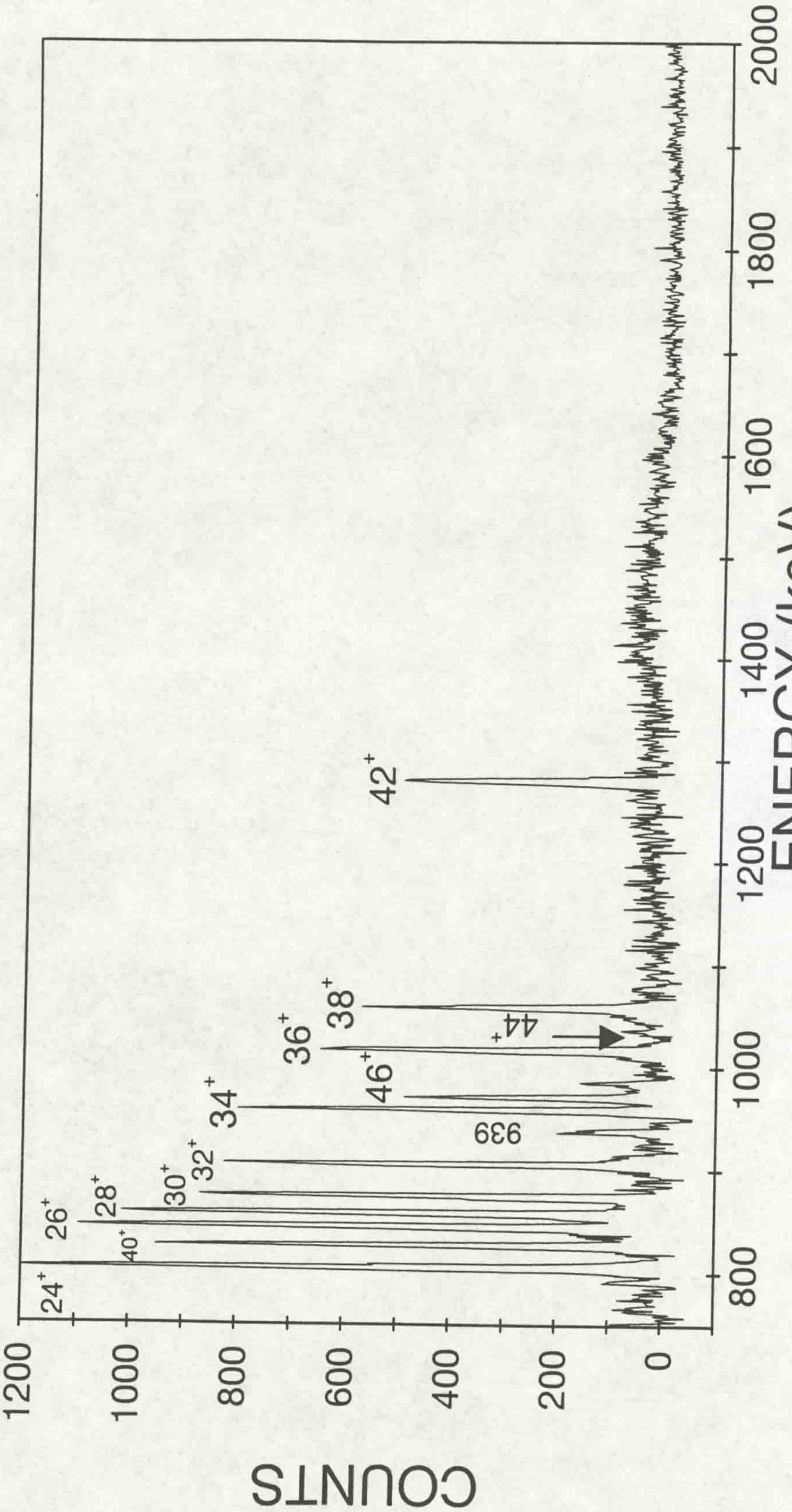

Figure 5.16: *(+,0) sequence. Spectrum with transitions coincident with the 1031keV ($44^+ \rightarrow 42^+$) $\gamma-ray$ [JS94].*

The other weaker branch has been extended up to (50_2^+) and has been interpreted as the continuation of the collective sequence [PT85, JS94].

5.4.2 (−,0) Band

This band has been extended to 48^-, see figure 5.17. Above 40^- an irregular sequence of $\gamma-$ray energies is observed to continue above the collective structure [PT85]. This sequence at the top of the band gains energy relative to a rigid rotor reference.

5.4.3 (−,1) Band

This band has been observed to branch into two decay sequences linked by high energy $\gamma-$rays, see figure 5.17. The favoured decay path is the sequence of irregular energy $\gamma-$rays observed up to (49^-), indicating a single particle structure. The 809 keV transition is assumed to be an E2 although an accurate angular correlation measurement could not be made of this transition. The 939 keV transition ($47^- \rightarrow 46^+$) has been observed in the data and has been interpreted as a stretched dipole transition linking the (+,0) and (−,1) bands.

5.4.4 Summary of ^{158}Er Results

A partial level scheme is shown in figure 5.17, this illustrates the region of high spin relevant to this analysis.

The spectrum shown in figure 5.16 is in coincidence with the $44^+ \rightarrow 42^+$ yrast band transition from a matrix selected by a single $\gamma-$ray (triples matrix).

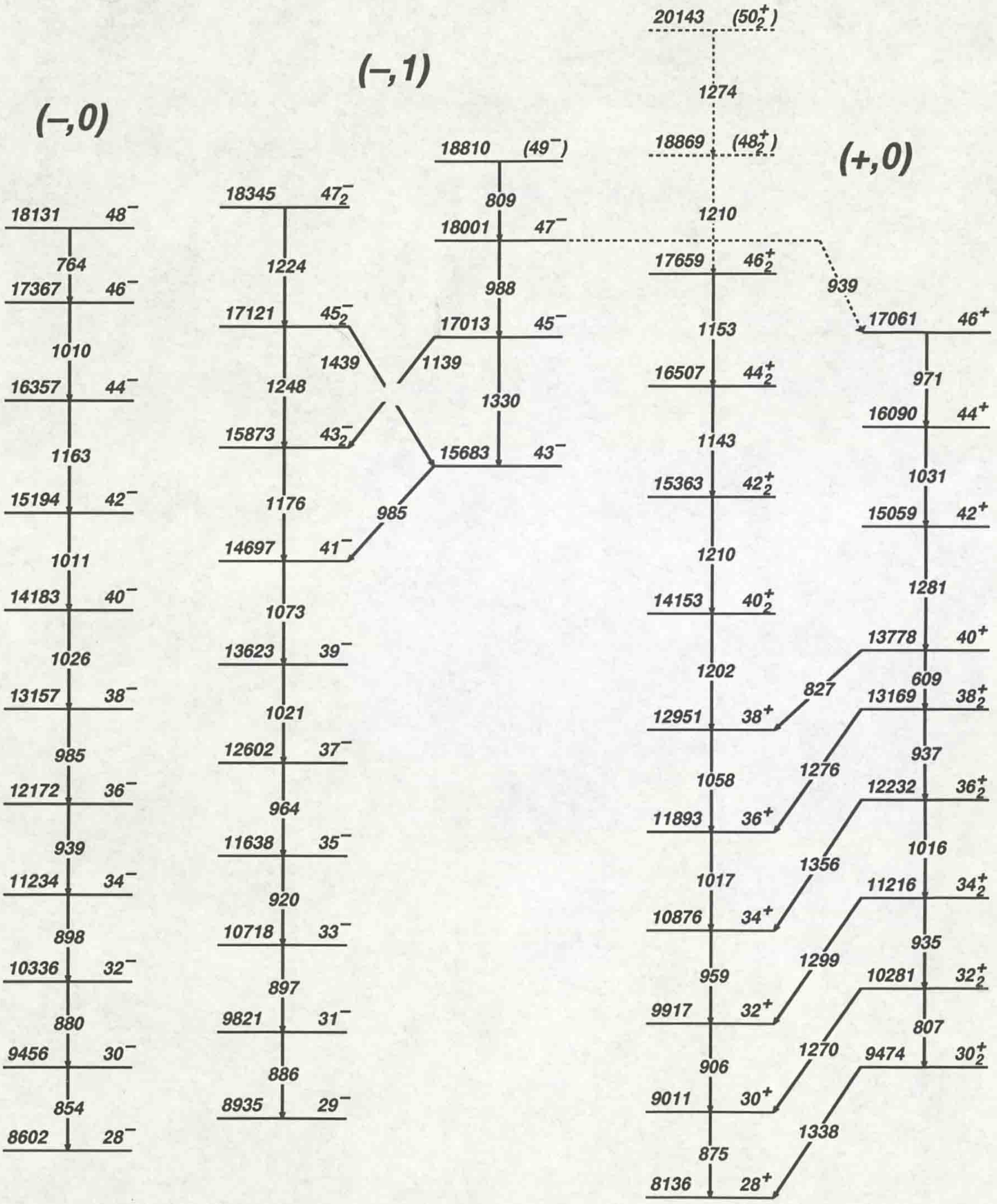

Figure 5.17: ^{158}Er *partial level scheme illustrating the high spin structures observed in the data [JS94].*

Chapter 6

Low Spin Interpretation

The interpretation is divided between two chapters, interpretation of the low spin structure of ^{157}Er and the high spin structure. This chapter is concerned with the theoretical interpretation of the low spin results of this analysis. The low spin (I) region has been defined for this analysis as $\frac{9}{2} \leq I \simeq \frac{61}{2}$, units of I are $\hbar$.

6.1 Low Spin Structure of ^{157}Er and Neighbouring nuclei

In the previous work [JS89] CSM calculations (see section 2.4) were successful in the interpretation of the low spin structure observed in ^{157}Er. This model describes the independent particle motion in a rotating deformed potential.

The CSM will be used to assign quasi particle configurations to the bands and characterise observed band crossings. This method of comparing experimental data to CSM calculations is used in the lower spin regions only, as at high rotational frequency the single particle structure becomes yrast.

By studying the level scheme and Nilsson diagrams, figures 7.2 and 7.3, assumptions can be made of the structure of the nucleus. It can be seen from the ^{157}Er level scheme, figure 5.4 that the low spin structure of consists of rotational bands. This implies that the nucleus is a deformed collective structure (see sections 1.2.1 and 2.2). ^{157}Er has 89 neutrons, 7 valence neutrons outside the ^{146}Gd core (the N=82 shell gap), it can be seen from the Nilsson diagram that there is a high density of low lying, low Ω, levels for prolate deformation. Therefore it is assumed that the ground state deformation of ^{157}Er is prolate.

6.1.1 Quasiparticle Systematics

A wide study of the transitional rare earth nuclei ($87 \leq N \leq 92$) has been made. The prolate deformation of these nuclei increases with the number of valence neutrons outside the N=82 closed shell. Therefore the study of alignment, band-crossing and the corresponding crossing frequencies in this region offer information on the orbitals available and the deformation of the nuclei. Examples of these systematics are given in, ^{154}Gd [JM89], ‘^{156}Dy [MR88], ^{157}Ho [DR92], ^{159,160}Er [JS89], ^{159,160}Yb [TB87], ^{162}Hf [CB88, HH88] and ^{165,166}W [JS92].

Band crossings and alignments were observed in Er and Yb isotopes [EG73, MR84b] and with the aid of blocked orbitals in neighbouring odd nuclei were assigned unambiguous quasiparticle configurations. A systematic increase in the proton crossing frequency (A_pB_p) between ^{157}Er, ^{158}Er, ^{159}Er and ^{160}Er [MR84b, JS87] was observed and described as a direct result of the increase in quadrupole deformation with neutron number. This effect is described in detail in [JS87], the theoretical description of the change in deformation is given in references [BF79a, BF79b].

6.2 Cranked Shell Model Calculations

The CSM calculates quasiparticle energies, e', in the rotating frame as a function of rotational frequency, $\hbar\omega$. To identify the quasiparticles contributing to a rotational band and characterise band crossings, experimental alignments and routhians are extracted from the data.

6.2.1 Parameters used in CSM Calculations

A modified oscillator potential was used in the calculations performed for this work and a description of the parameters chosen for the calculations is given below, the values are listed in table 6.1.

$\underline{\epsilon_2,\epsilon_4}$

values for β_2 and β_4 were extrapolated from [WN90]. This reference includes the equilibrium deformations, β_2 and β_4, for even-even isotopes of nuclei in the range Gd-Os (Z=62→76). Figure 6.1 shows the calculated and experimental values . It can be seen from this figure that there is a straight line relationship in the region ^{156}Er to ^{160}Er. Therefore an approximate value for the deformation parameters can

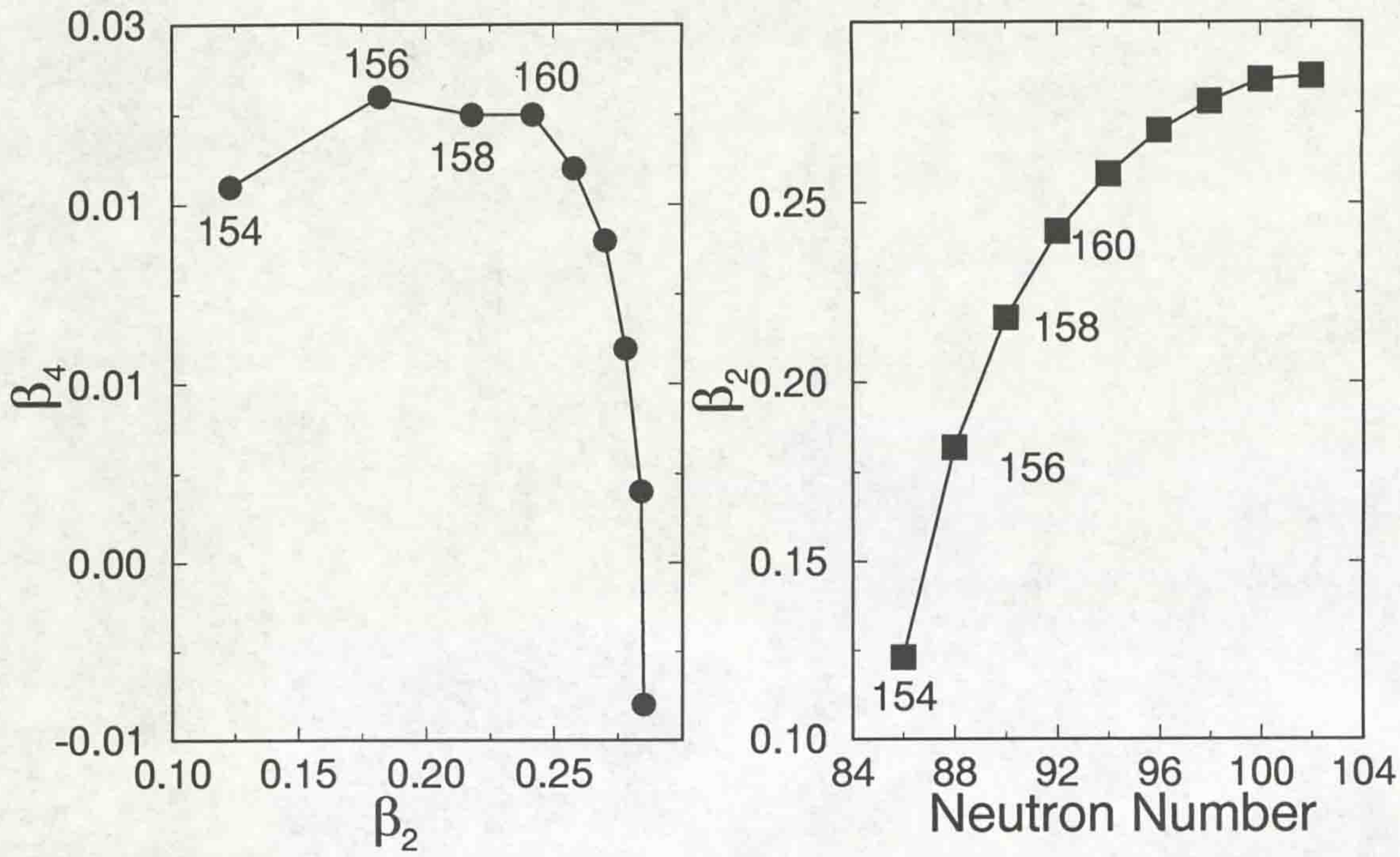

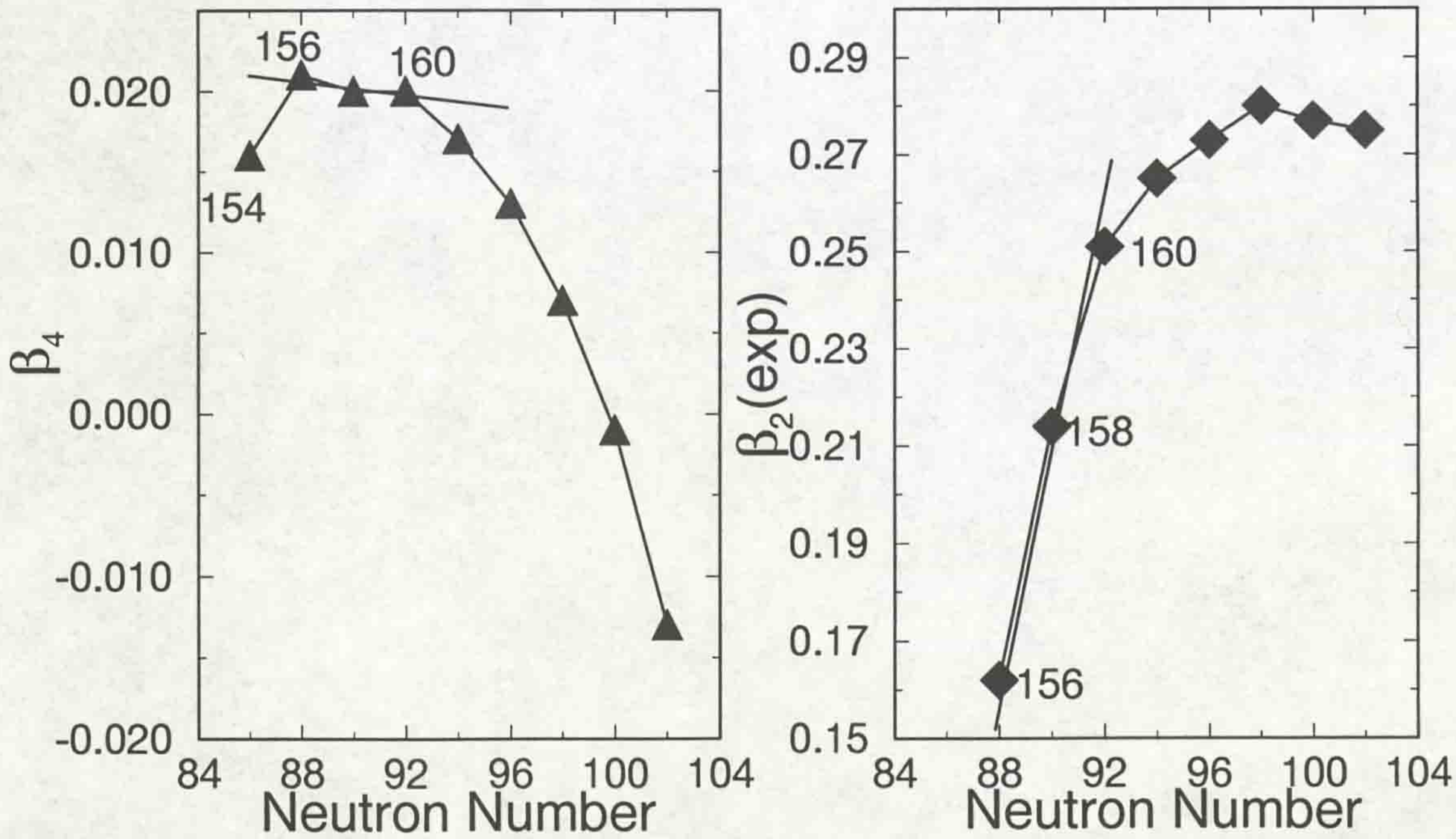

Figure 6.1: *The deformation parameters, β_2 and β_4, given in* [*WN90*].

be obtained by taking the mean of the ^{156}Er and ^{158}Er values. The deformation parameters for ^{157}Er are $\beta_2 = 0.188$ and $\beta_4 = 0.021$. To change these deformation parameters into ϵ_2 (quadrupole deformation) and ϵ_4 (hexadecapole deformation) used in the calculations, the formulae given in equations 6.1 and 6.2 were used (as derived in [RB89])

$$\epsilon_2 \simeq 0.944\beta_2 - 0.122\beta_2^2 + 0.154\beta_2\beta_4 - 0.199\beta_4^2 \tag{6.1}$$

$$\epsilon_4 \simeq -0.852\beta_4 - 0.141\beta_4^2 + 0.122\beta_2\beta_4 + 0.295\beta_2^2 \tag{6.2}$$

yielding $\epsilon_2 \simeq 0.173$ and $\epsilon_4 \simeq -0.018$ used in the CSM calculations.

γ, triaxiality

A triaxiality of $\gamma = 0.0°$ corresponding to a collective prolate nuclear structure has been used.

Δ_p and Δ_n

The neutron and proton pairing gap were chosen so that the calculations reproduced band crossings at the correct energy (method used in reference [JS89]). The values satisfying this criterion were $\Delta_n = 1.69$ and $\Delta_p = 0.75$ MeV.

λ

The Fermi energy, λ, is different for protons and neutrons. An approximate value of λ obtained using the Nilsson diagram plotted in reference [LS78] is input into the calculations.

An approximate value of the energy of the Fermi surface is taken from the Nilsson diagram. This energy is given in units of $\frac{e_i}{\hbar\omega_o}$. $\hbar\omega_o$ is calculated using the formulae given in equation 1.25. The values of $\hbar\omega_o$ and the estimated Fermi levels used in the calculations are

Protons:	$\hbar\omega_o =$	7.94 MeV	$\lambda_p = 42.34$ MeV
Neutrons:	$\hbar\omega_o =$	7.26 MeV	$\lambda_n = 51.02$ MeV.

These initial estimates of the Fermi surface are used by the CSM calculations to place the Fermi level at an approximate energy. An accurate value of the Fermi surface is then calculated using equation 6.3.

$$\lambda = \frac{dE}{dN} \tag{6.3}$$

The proton and neutron Fermi surfaces are calculated to reproduce the correct proton and neutron numbers respectively.

Table 6.1 Parameters used in CSM calculations

quadrupole deformation	ϵ_2	=	0.173	hexadecapole deformation	ϵ_4	=	-0.018
π pair gap	Δ_p	=	1.69 MeV	ν pair gap	Δ_n	=	0.75 MeV
π Fermi level	λ_p	=	42.34 MeV	ν Fermi level	λ_n	=	51.02 MeV
triaxiality	γ	=	0.00°				

6.3 Interpretation of Experimental Results Using the Cranked Shell Model

Figures 6.2 and 6.3 show the results of the CSM calculations made for ^{157}Er used in this analysis. The routhian labels used in the figures correspond to quasiparticle orbitals given in table 6.2 (over-page). The labelling convention used was proposed in [LR80].

The band crossings shown in the figures are labelled by the pair of particles that align. The AB and BC neutron crossings and the A_pB_p proton crossing are indicated. It should be noted that the BC and A_pB_p crossings both occur at the same frequency, $\hbar\omega \simeq 0.4$ MeV in these calculations. A large gain in alignment is expected, experimentally, at this frequency to reflect the alignment of both the neutron and proton pairs.

To compare the CSM calculations with the experimental data the results have to be transferred from the laboratory to the rotating frame of reference, see section 2.6, equations 2.30 and 2.31 are used. The Harris parameters chosen for the calculations were:

$$\mathcal{J}_\circ = 32.1 \text{ MeV}^{-1}\hbar^2 \qquad \mathcal{J}_1 = 34.0 \text{ MeV}^{-3}\hbar^4$$

These parameters have been chosen because they give a constant alignment as a function of rotational frequency for the yrast band $(-,+1/2)$ in the neighbouring ^{157}Ho nucleus [MR88]. The configuration of this reference band is ABB_p, in which the AB, BC and A_pB_p crossings are blocked. This configuration is therefore an excellent reference for investigating the quasiparticle structure of ^{157}Er above the AB neutron crossing.

Figure 6.4 shows the alignment plot of the ^{157}Er data, using the ordering of transitions given in the level scheme, figure 5.4. The interpretation of these low spin structures will be made with reference to this figure.

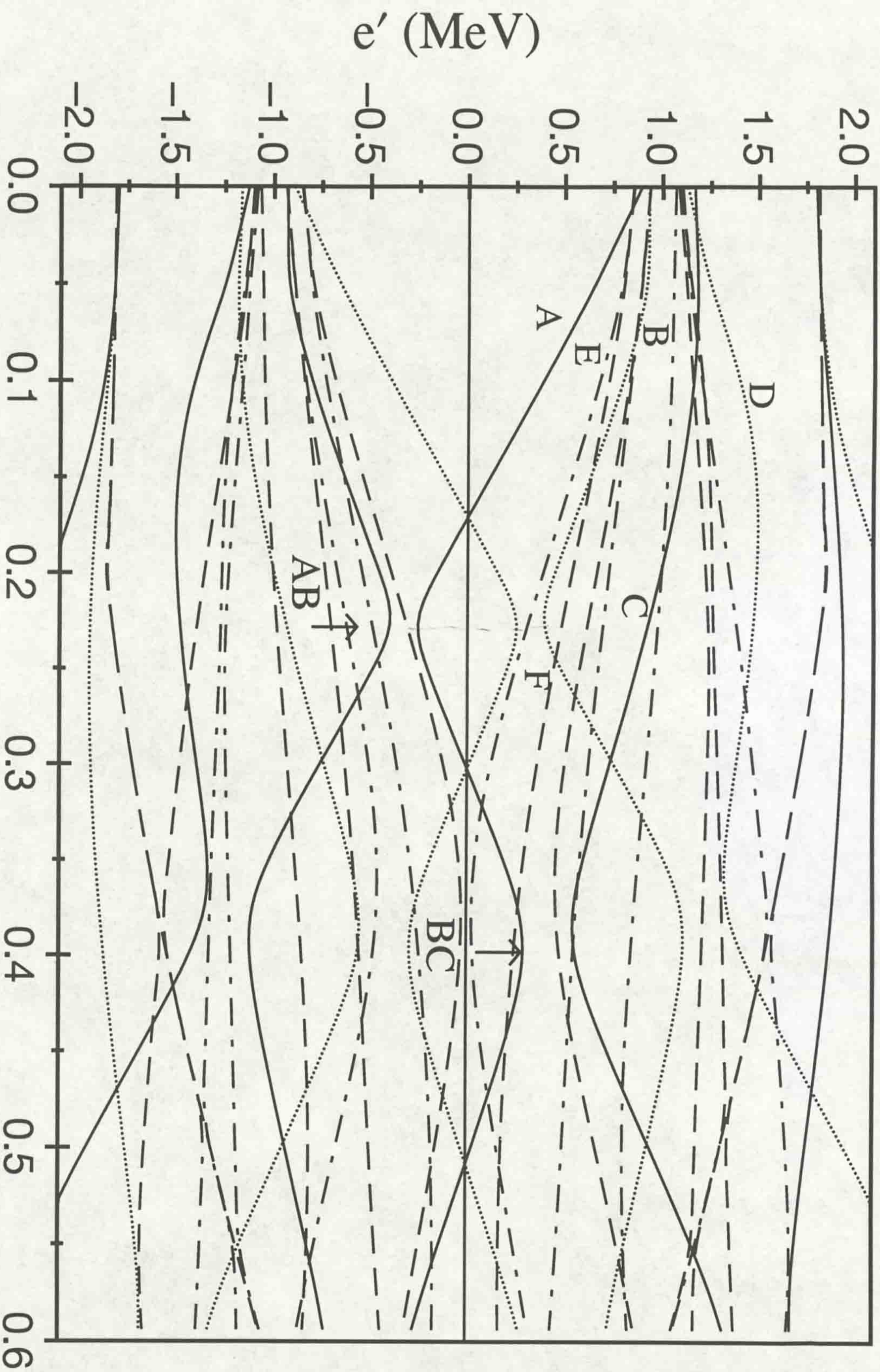

Figure 6.2: *The quasineutron routhians calculated using the CSM. Solid lines=(+,+1/2), Dotted=(+,−1/2), Dot-dash=(−,+1/2), Dashed=(−,−1/2)*

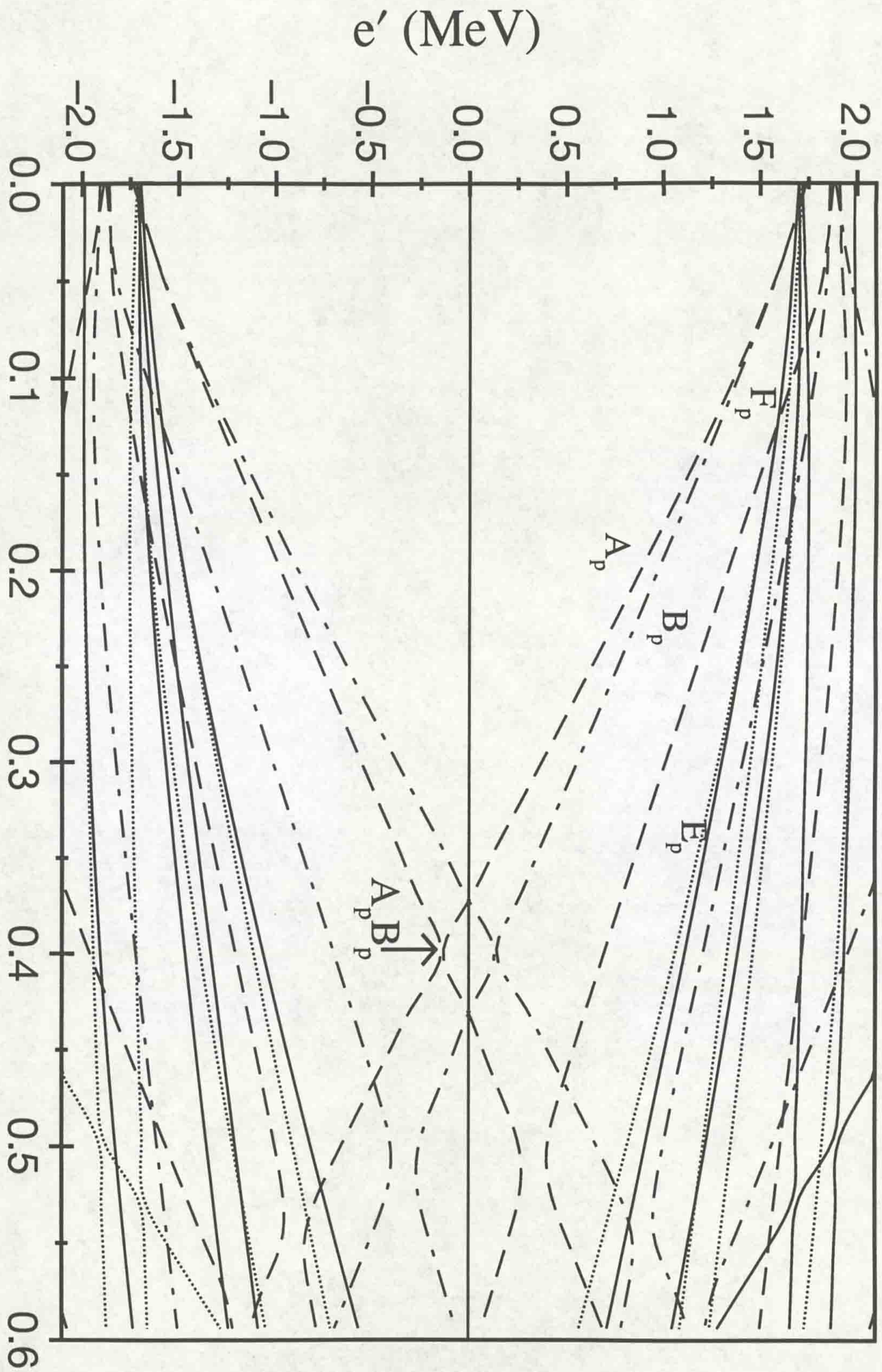

Figure 6.3: *The quasiproton routhians calculated using the CSM. Solid lines=(+,+1/2), Dotted=(+,−1/2), Dot-dash=(−,+1/2), Dashed=(−,−1/2)*

Table 6.2 Labelling of CSM routhians used in this analysis.

Nilsson Orbital $\hbar\omega = 0$	Label $[\alpha]$ (quasiparticle)
$\nu i_{\frac{13}{2}}$ $[651]$ $\frac{3}{2}^+$	**A** $[+\frac{1}{2}]$, **B** $[-\frac{1}{2}]$
$\nu i_{\frac{13}{2}}$ $[660]$ $\frac{1}{2}^+$	**C** $[+\frac{1}{2}]$, **D** $[-\frac{1}{2}]$
$\nu f_{\frac{7}{2}}$ $[521]$ $\frac{3}{2}^-$	**E** $[+\frac{1}{2}]$, **F** $[-\frac{1}{2}]$
$\pi h_{\frac{11}{2}}$ $[523]$ $\frac{7}{2}^-$	$\mathbf{A}_p$ $[-\frac{1}{2}]$, $\mathbf{B}_p$ $[+\frac{1}{2}]$
$\pi g_{\frac{7}{2}}$ $[404]$ $\frac{7}{2}^+$	$\mathbf{E}_p$ $[-\frac{1}{2}]$, $\mathbf{F}_p$ $[+\frac{1}{2}]$
$\pi h_{\frac{9}{2}}$ $[541]$ $\frac{1}{2}^-$	$\mathbf{X}_p$ $[+\frac{1}{2}]$, $\mathbf{Y}_p$ $[-\frac{1}{2}]$

6.3.1 (+,+1/2): Yrast Band

At low spin this band has the single quasineutron configuration, A with an alignment, i_x, of 3.2 $\hbar$. At a rotational frequency of $\simeq$ 0.4 MeV/$\hbar$ the band experiences a large gain in alignment, $\simeq 8.4\hbar$. This gain is a direct result of the alignment of both the BC neutron pair and the A_pB_p proton pair, ie. the BC and A_pB_p band crossings [MR84b, JS89]. The band now has the five quasiparticle configuration $ABCA_pB_p$.

This band does not experience the AB neutron crossing [JM89] indicated in figure 6.2. This is because the yrast band has the initial configuration A and therefore this crossing is blocked.

6.3.2 Band 3

This is a sequence of two quadrupole transitions. The band has the alignment characteristics of it being the un-favoured positive parity quasineutron configuration, B. The average alignment of this band is $2\hbar$.

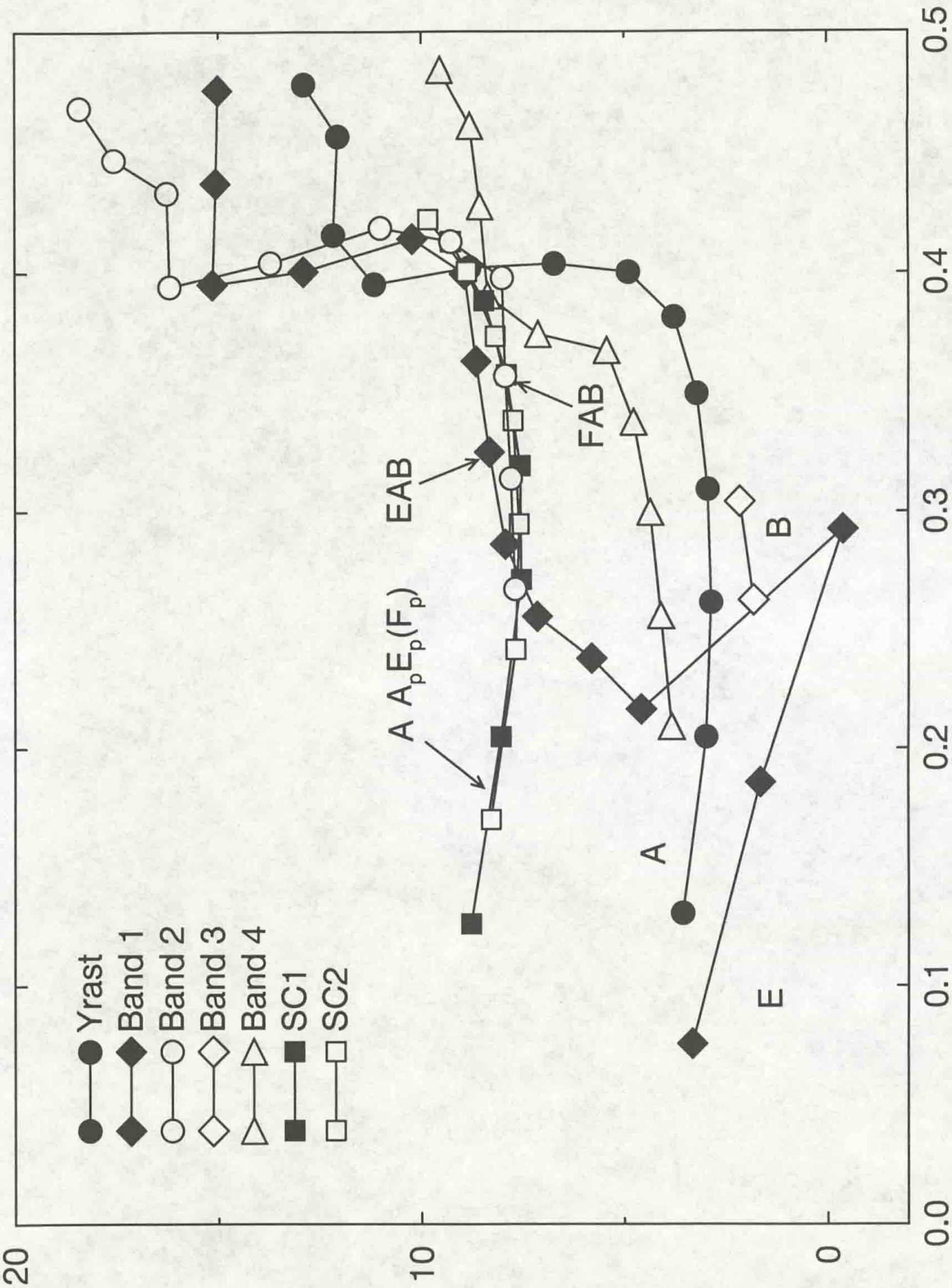

Figure 6.4: *Experimental alignment against rotational frequency for the bands observed in* ^{157}Er.

6.3.3 (−,+1/2): Band 1

This band has been extended down to a spin of $\frac{9}{2}^-$ in this work. This low spin region has been interpreted as the lowest energy, negative parity single quasineutron configuration, E. The band has an initial alignment of $3.5\hbar$. At a rotational frequency $\simeq 0.22$ MeV/$\hbar$ a gain in alignment is observed, $\simeq 6.9\hbar$. This is interpreted as the AB neutron crossing. The values of gain in alignment and band crossing frequency at the AB crossing are difficult to evaluate (see figure 6.4) and therefore the values quoted are approximate. The band now has the three quasineutron configuration EAB. At a frequency $\simeq 0.40$ MeV/$\hbar$ the band experiences another dramatic gain in alignment, this is a result of the alignment of the A_pB_p protons. The BC neutron crossing is blocked. The band now has the five quasiparticle configuration EABA_pB_p.

6.3.4 (−,−1/2): Band 2

The alignment of this band implies that the low spin single quasiparticle configuration has not been observed. If this band was extended to lower spin it is expected to have the quasineutron configuration F. This band has an initial alignment of $7.7\hbar$. F is the lowest energy negative parity negative signature orbital. This band has an alignment similar to that of band 1 within the AB neutron and the BC/A_pB_p crossing frequency region, it is opposite in signature and therefore assigned the three quasiparticle configuration FAB. At 0.4 MeV/$\hbar$ the band experiences a gain in alignment interpreted as the A_pB_p proton crossing. An approximate value of gain in alignment of $8.4\hbar$ has been determined. The band now has the five quasiparticle configuration FABA_pB_p.

6.3.5 Band 4

The nature of this band is uncertain. In previous work [JS89] it was suggested that this band is most likely a rotational band based on a gamma vibration excitation of the yrast band. This band has an initial alignment of $3.9\hbar$ and experiences a gain of $3.6\hbar$ at a rotational frequency of $\simeq 0.37$Mev/$\hbar$.

It is assumed in this analysis that 603keV transition is a stretched quadrupole and not a stretched dipole as suggested by the angular correlation ratios, see figure 5.5 and table B.1. If the 603keV transition is a stretched dipole band 4 would be split into two separate bands, referred to as bands 4 and 5 in this section. Figure 6.5 shows the alignment plot of band 4 compared to the yrast band (top) and the

scenario if band 4 was split into two bands by the 603 (if it were a dipole), bands 4 and 5, (bottom). It can be seen from this figure that the single band scenario is more convincing from these alignment systematics. Figure 6.6 shows a routhian plot with the single band at the top and the two bands scenario at the bottom, compared to the strongly coupled band. It can be seen from this diagram that if the sequence was two bands (band 4 and 5) the strongly coupled band is more favoured, which clearly from its intensity it is not. Band 4 has an intensity of $\simeq 8\%$ of the ^{157}Er reaction channel and the strongly coupled band ≤ 1.0 % (introduced in section 6.3.6). Therefore the sequence is more likely a single band which is in agreement with [JS89].

6.3.6 High-K (Strongly Coupled) Band

Angular correlation measurements for this structure were not made due to its low intensity ($\leq 1.0\%$ of ^{157}Er reaction channel). From the spectrum shown in figure 5.12 it can be see that the structure consists of two sequences, strong low energy and weak higher energy $\gamma-$rays. This is typical of a high-k structure (strongly coupled band). This high-k band consists of two rotational bands (weaker sequence of $\gamma-$rays) linked by dipoles (high intensity lower energy $\gamma-$rays), similar bands have been observed in Gd, Dy and Ho [JM89, MR88, DR92]. From figure 6.4 it can be seen that these two bands have approximately the same alignment and have very little signature splitting (discussed in section 6.4). One band has the E_p and the other the F_p configuration. The assignment of the configuration is discussed in detail in section 6.4.

At low frequency the alignment of these bands is consistent with a three quasi-particle configuration. The AB neutron crossing is not observed, therefore the band must contain either or both these orbitals. At a rotational frequency of $\simeq 0.4\text{MeV}/\hbar$ there appears to be evidence that the band is about to experience a gain in alignment. Unfortunately the band has not been extended high enough in spin to observe the band crossing. The A_pB_p proton crossing is not expected to be observed as it is blocked, however, the BC neutron crossing is expected.

The assignment of the configuration AA_pE_p/F_p is discussed in detail in section 6.4.

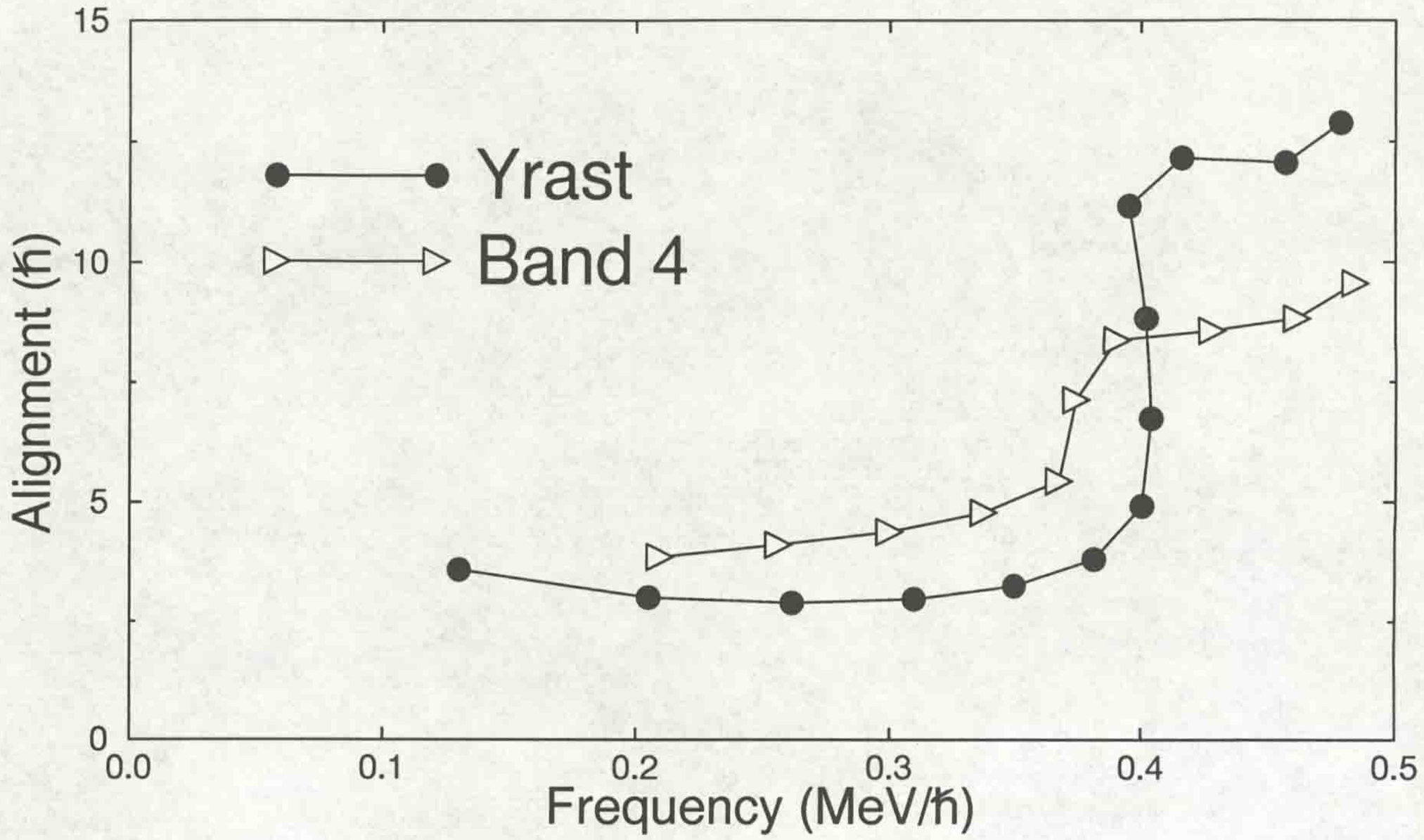

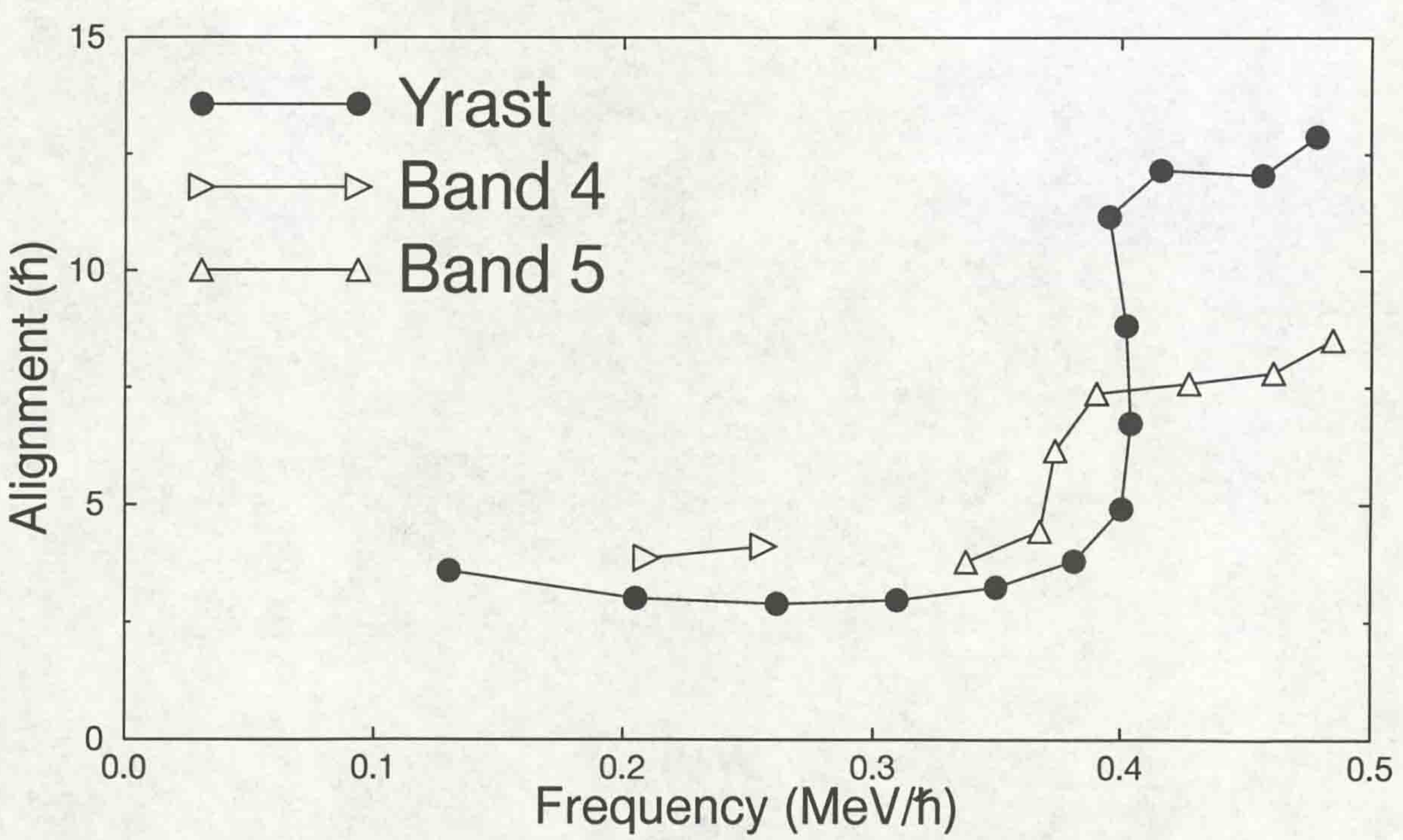

Figure 6.5: *Comparison of alignment of the yrast band to the single band 4, top plot and band 4 split into two bands (4 and 5), bottom plot*

.

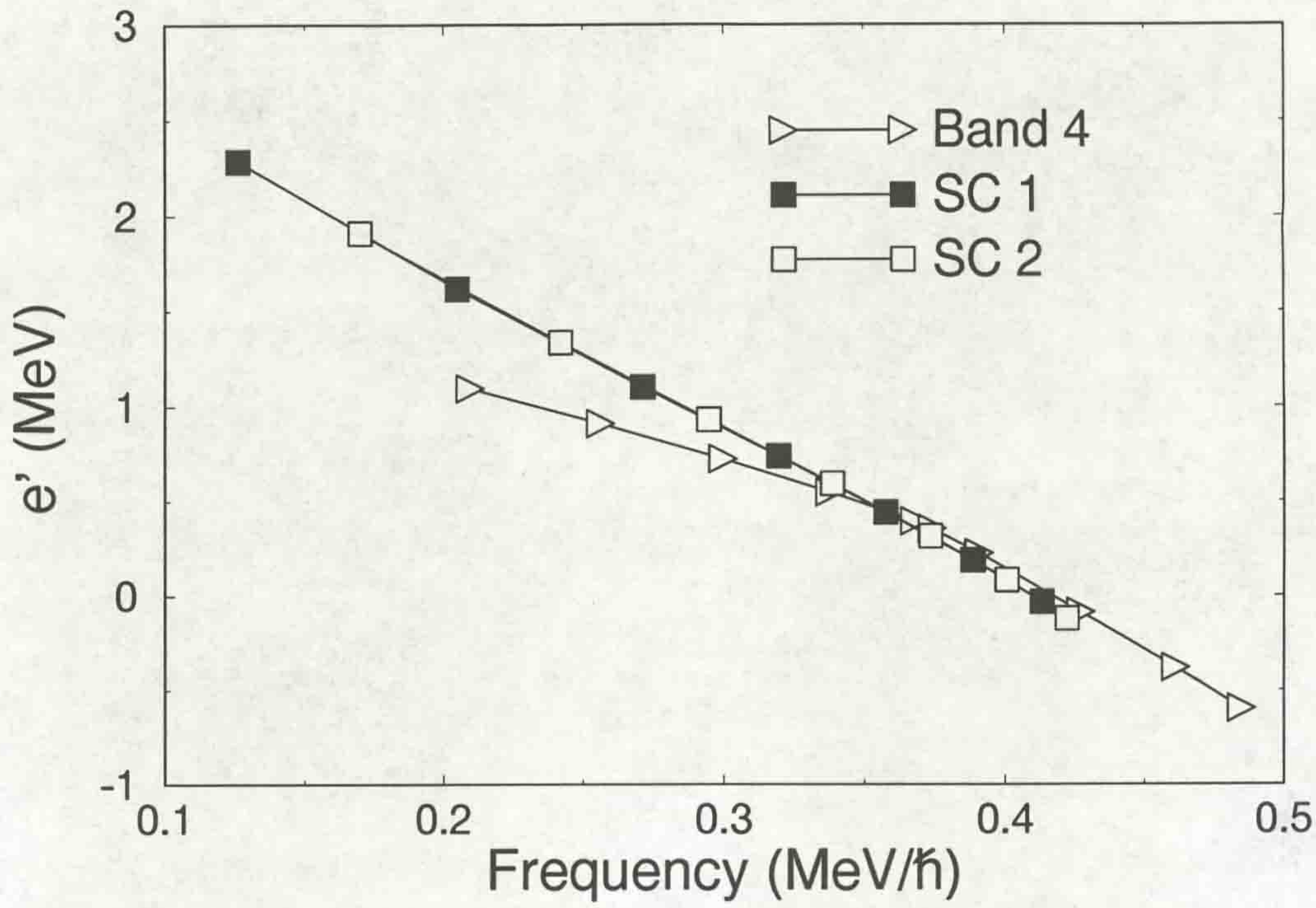

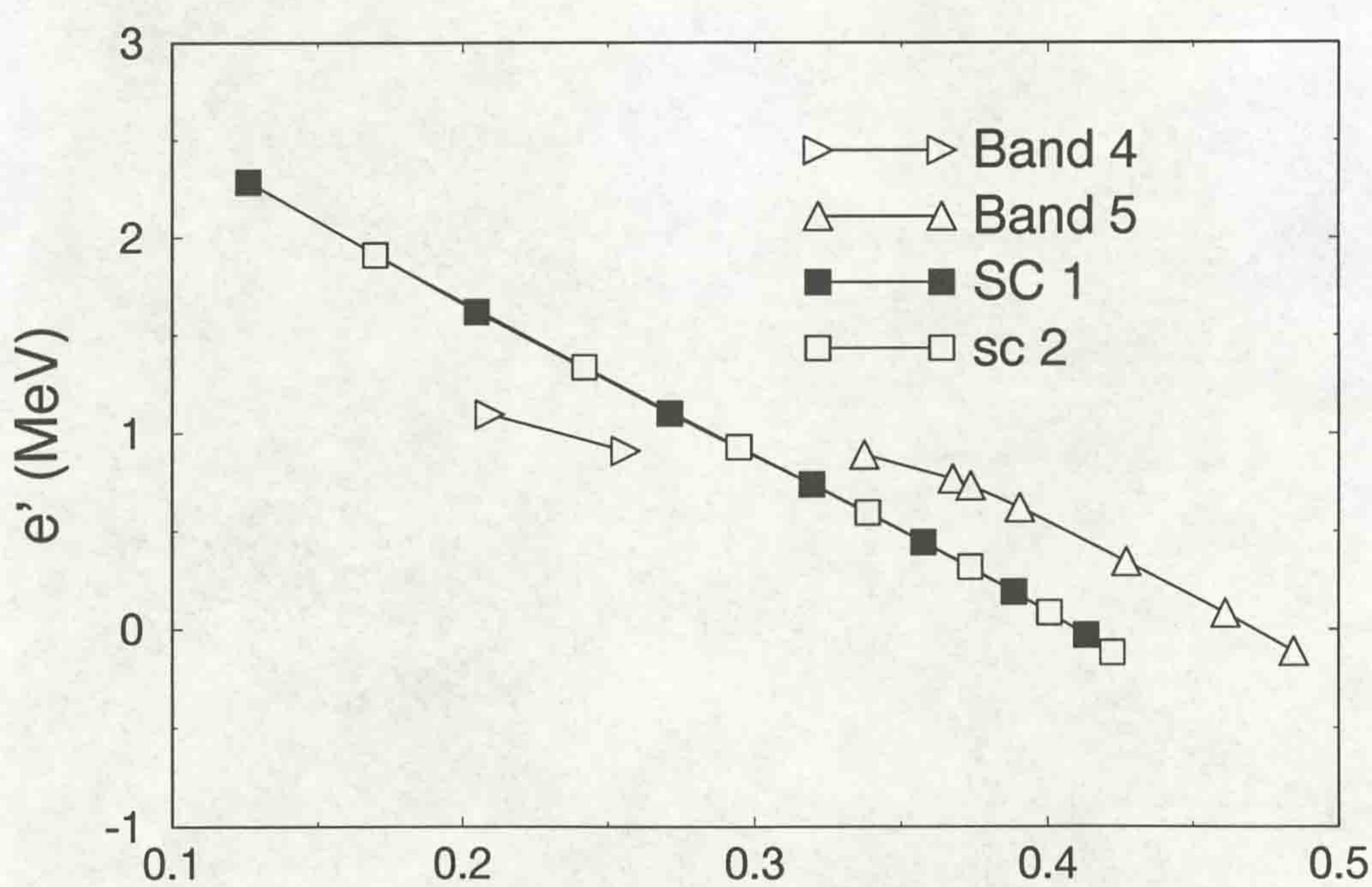

Figure 6.6: *Comparison of routhians of the strongly coupled band to the single band 4, top plot and band 4 split into two bands (4 and 5), bottom plot*

.

6.3.7 Summary of ^{157}Er Band Crossing Systematics

A summary of band crossing systematics is given in table 6.3 below. The frequencies, ω and ω_c (band crossing frequency), are given in units of MeV/$\hbar$. The change in alignment, Δi_x, is in units of $\hbar$. The quasiparticle configurations refer to the orbital detailed in figures 6.2 and 6.3 and in table 6.2. Band 4 has not been included in this table as its identity has not been determined.

Table 6.3

Band		Yrast	3	1	2	SC
initial ω		0.13	0.26	0.08	0.27	0.13/0.17
initial i_x		3.2	1.8	3.4	7.7	8.8/8.3
configuration		A	B	E	-	$AA_pE_p(F_p)$
AB	ω_c	•	-	0.22	-	•
crossing	Δi_x	•	-	†6.9	-	•
configuration		A	-	EAB	FAB	$AA_pE_p(F_p)$
BC	ω_c	0.40	-	•	•	?
crossing	Δi_x	*8.4	-	•	•	?
A_pB_p	ω_c	0.40	-	0.40	0.40	•
crossing	Δi_x	*8.4	-	6.6	†8.4	•
configuration		$ABCA_pB_p$	-	$EABA_pB_p$	$FABA_pB_p$	-

- indicates the band was not observed within the frequency region of the crossing.

• indicates the crossing is blocked.

⋆ this value is the total for both the A_pB_p and the BC crossings.

† accurate values for these entries have not been determined

The experimental routhians are plotted in figure 6.7, the AB, BC and A_pB_p band crossings are indicated.

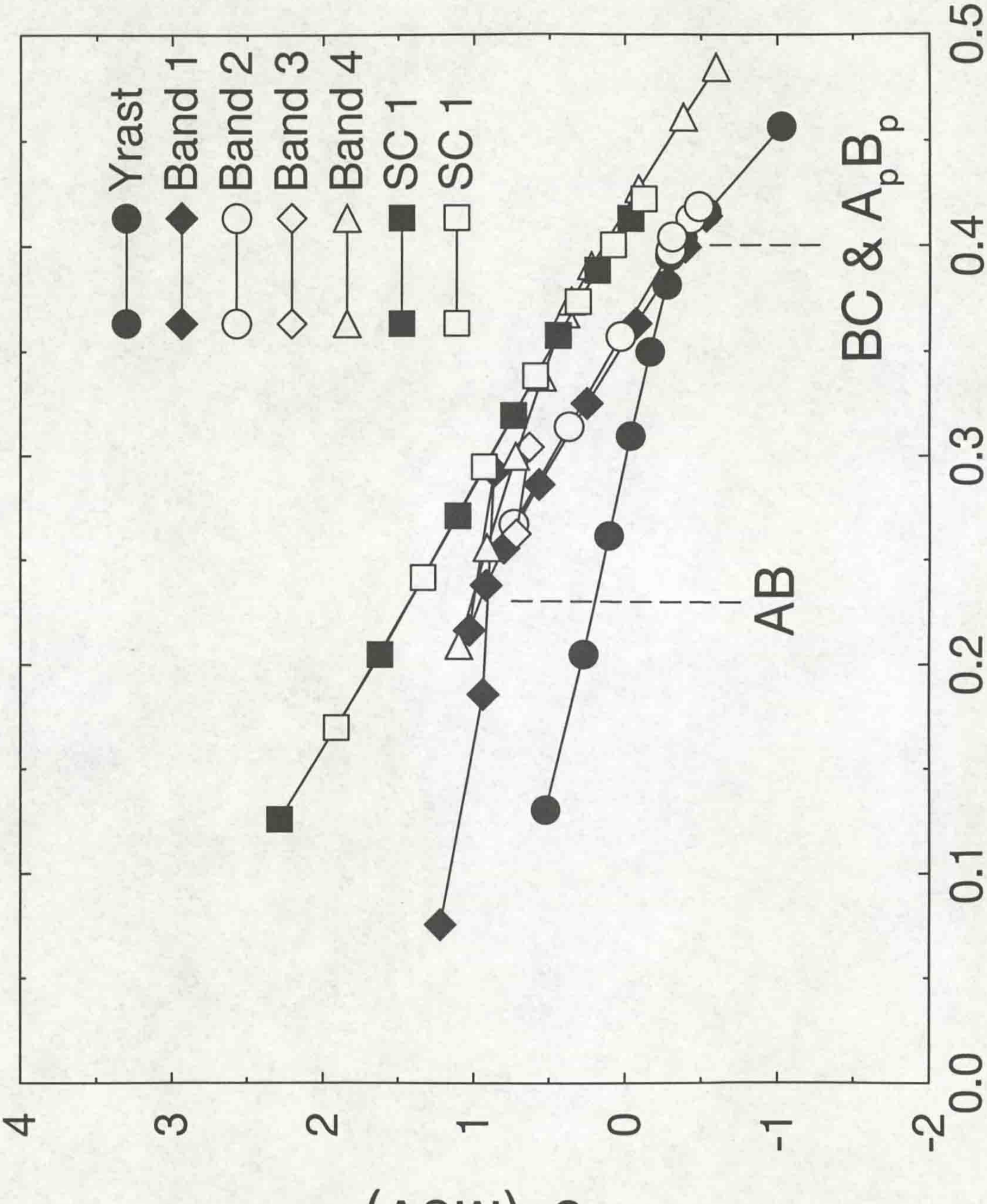

Figure 6.7: *Experimental routhians of the bands observed in* ^{157}Er.

6.4 Interpretation of the High-K Band

^{157}Er is the lightest of the erbium nuclei in which a strongly coupled band has been observed. Figure 6.8 shows a partial level scheme of this strongly coupled band. From arguments given in section 6.3.6 this structure must be composed of a three quasiparticle configuration, containing either an A or a B neutron. The strongly coupled nature of the band means that it must be based on a high Ω orbital (M1 transition strength is proportional to K^2, equation 3.10). The orbitals available in this region [MR94b] are given in table 6.4.

Table 6.4

Nilsson Orbital $\hbar\omega = 0$	Label [α] (quasiparticle)	g–factor (orbital)	Alignment, i_x ($\hbar$)
$i_{\frac{13}{2}}$ [651] $\frac{3}{2}^+$	**A** [$+\frac{1}{2}$], **B** [$-\frac{1}{2}$]	−0.21	5.8, 3.8
$f_{\frac{7}{2}}$ [521] $\frac{3}{2}^-$	**E** [$+\frac{1}{2}$], **F** [$-\frac{1}{2}$]	−0.24	3.0
$h_{\frac{11}{2}}$ [505] $\frac{11}{2}^-$	**X** [$+\frac{1}{2}$], **Y** [$-\frac{1}{2}$]	−0.23	0.5
$h_{\frac{11}{2}}$ [523] $\frac{7}{2}^-$	$\mathbf{A}_p$ [$-\frac{1}{2}$], $\mathbf{B}_p$ [$+\frac{1}{2}$]	1.13	3.0
$g_{\frac{7}{2}}$ [404] $\frac{7}{2}^+$	$\mathbf{E}_p$ [$-\frac{1}{2}$], $\mathbf{F}_p$ [$+\frac{1}{2}$]	0.70	1.0
$h_{\frac{9}{2}}$ [541] $\frac{1}{2}^-$	$\mathbf{X}_p$ [$+\frac{1}{2}$], $\mathbf{Y}_p$ [$-\frac{1}{2}$]	0.76	5.0

(apart from A and B quasineutrons signature partners have the same alignment)

Similar bands have been observed in Gd [JM89] and Dy [MR88] which are based on the X and Y quasiparticles. The smaller deformation of ^{157}Er means that these orbitals are farther from the Fermi surface and hence unlikely to be observed. Therefore it seems more likely that the strongly coupled band is based on a high-Ω proton orbital as is observed in ^{157}Ho [DR92].

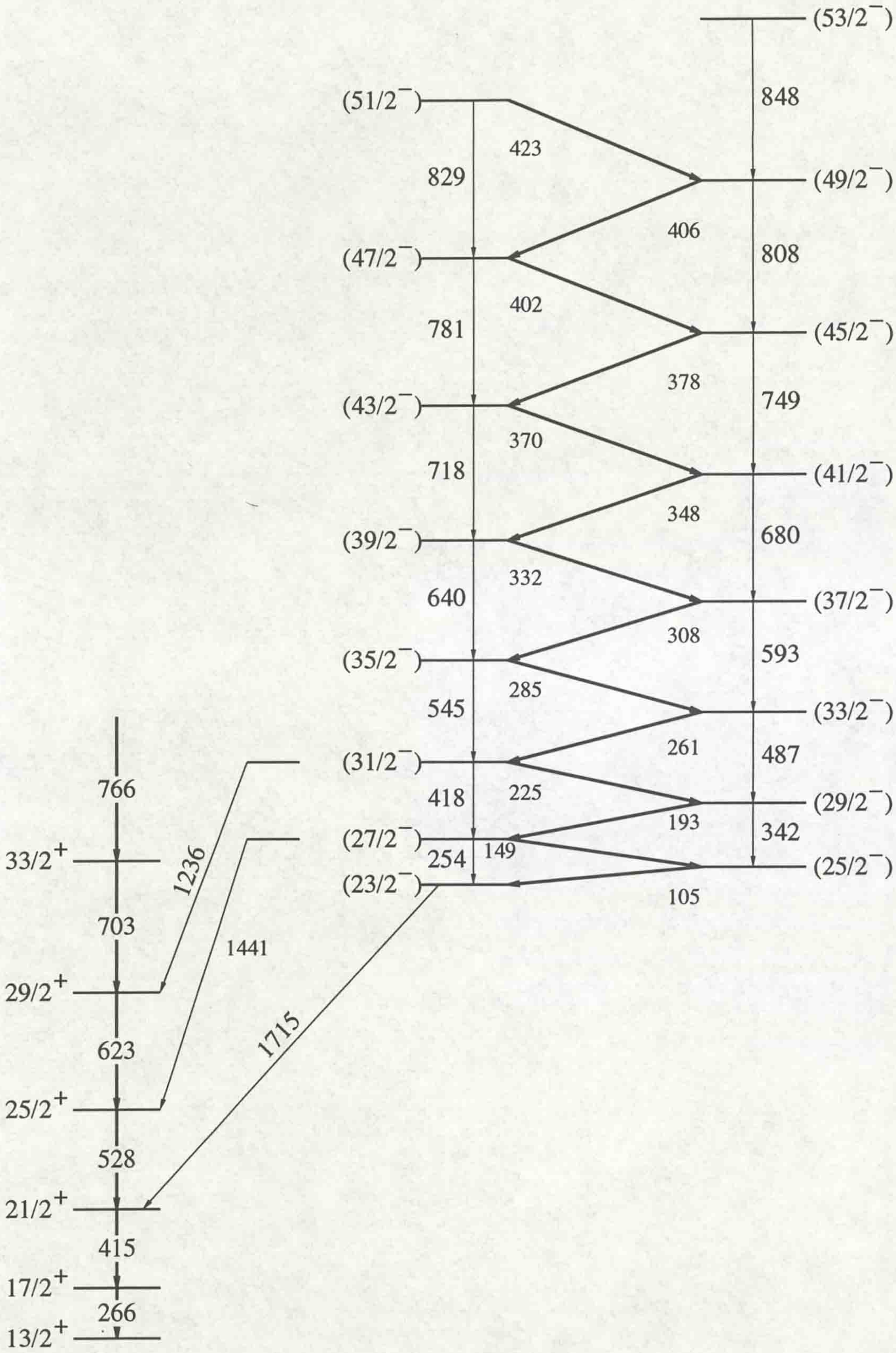

Figure 6.8: *Partial level scheme of the strongly coupled band observed in* ^{157}Er.

The proton orbitals available are the A_p/B_p and E_p/F_p, these are based on the $h_{\frac{11}{2}}[523]\frac{7}{2}$ and the $g_{\frac{7}{2}}[404]\frac{7}{2}$ orbitals, respectively. The signature splitting from this band observed in the data does not exceed 10keV, see figure 6.9. This gives better agreement with the signature splitting of the [404] orbitals.

From the CSM calculations it can be seen in figure 6.2 that the quasineutron A is lower in energy than B, therefore it is more likely that the configuration with the A neutron will have a higher intensity and be observed.

6.4.1 B(M1;I→I−1)/B(E2;I→I−2) Calculations

To obtain a quantitative idea of which configuration the strongly coupled band is most likely to be built on B(M1;I→I−1)/B(E2;I→I−2) transition probabilities are calculated. These transition probabilities and the calculations of theoretical and experimental values are introduced in sections 3.1.3 and 3.1.4.

Parameters used in the theoretical calculations

The deformation parameter used was $\beta_2 = 0.188$. The choice of this value is discussed in section 6.2.1. The quasiparticles and the associated alignments and g-factors given in reference [DR92] have been used, these values are written in table 6.4. The alignment for the quasiparticles were obtained from alignment systematics in the region compiled by M.A.Riley, [MR94a]. These alignment values for different nuclei in the region are given in table 6.5. All the values of alignment given in table 6.5 are in units of $\hbar$. $\mathcal{J}_\circ = 19.0\ \mathrm{MeV}^{-1}\hbar^2$ and $\mathcal{J}_1 = 90.0\ \mathrm{MeV}^{-3}\hbar^4$ Harris parameters were used. Calculation of AB alignment:

$$A_pAB - AB = A_p = 12.6 - 9.6 \tag{6.4}$$

$$A_pAB - AB = E_p = 10.6 - 9.6 \tag{6.5}$$

The configurations considered are given below.

- A $A_pE_p(F_p)$
- A $A_pX_p(F_p)$
- ABX

Although the band found experimentally is very weak, it was possible to extract nine B(M1)/B(E2) ratios, these measurements can be seen in table 6.6. Comparison has been made with the predicted and experimental B(M1)/B(E2) values, these are plotted in figure 6.10. It can be seen that good agreement is found between experiment and the A $A_pE_p(F_p)$ configuration. This reinforces the assignment of this configuration

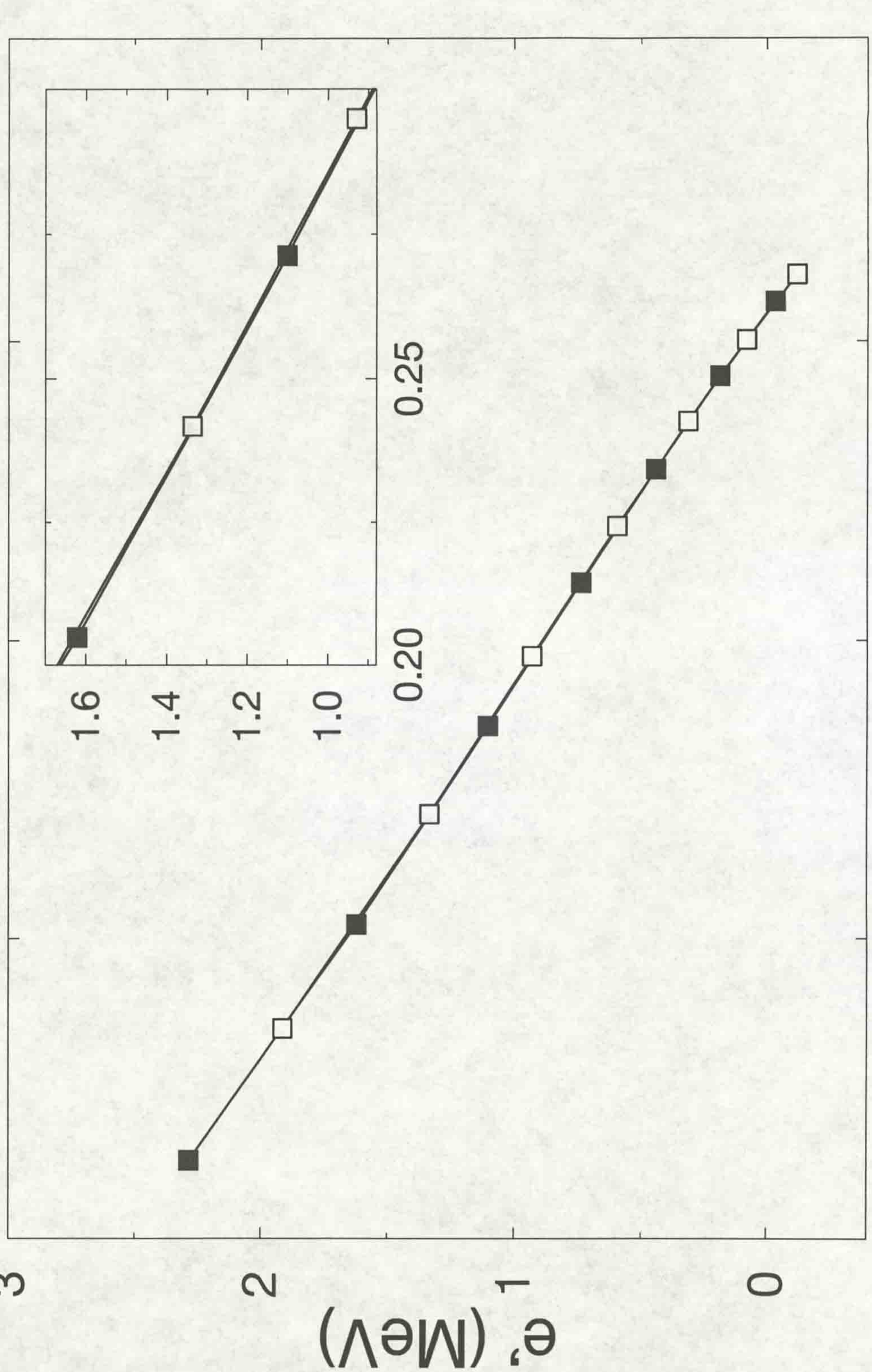

Figure 6.9: *A routhian plot of the strongly coupled band observed in* ^{157}Er *to illustrate the signature splitting.*

to the band previously based on alignment systematics and signature splitting (see section 6.3.6 and beginning of section 6.4).

Table 6.5 Alignment systematics in light erbium nuclei

Quasi-particle(s)	^{157}Er	^{158}Er	^{159}Er	^{160}Er	^{157}Ho	^{159}Tm	average	value taken
AB	-	10.1	-	9.1	-	-	9.6	9.6
EAB	-	-	10.9	-	-	-	10.9	10.9
A	5.2	-	6.4	-	-	-	5.8	5.8
AE	-	7.5	-	-	-	-	7.5	7.5
X								•0.5
E/F	-	-	3.0	-	-	-	3.0	3.0
A_p	-	-	-	-	3.9	3.3	3.6	*3.0
E_p/F_p	-	-	-	-	2.3	1.1	1.7	*1.0
X_p	-	-	-	-	5.8	-	-	5.8
A_pAB	-	-	-	-	12.7	12.5	12.6	12.6
E_pAB	-	-	-	-	10.6	10.5	10.6	10.6

• the alignment of this quasiparticle has been determined from comparison of alignment systematics in the region.

* the alignment values for these quasiparticles when coupled to multi-quasiparticle configurations were calculated.

Table 6.6 Measured reduced transition probabilities.

I ($\hbar$)	B(M1;I$\rightarrow$ I-1)/B(E2;I$\rightarrow$ I-2) $(\frac{\mu_N}{eb})^2$
$\frac{29}{2}$	3.8(0.6)
$\frac{33}{2}$	4.9(0.6)
$\frac{25}{2}$	3.7(0.4)
$\frac{37}{2}$	3.5(0.4)
$\frac{39}{2}$	3.6(0.6)
$\frac{41}{2}$	2.9(0.6)
$\frac{43}{2}$	3.1(0.6)
$\frac{45}{2}$	3.5(0.6
$\frac{47}{2}$	2.5(0.5)

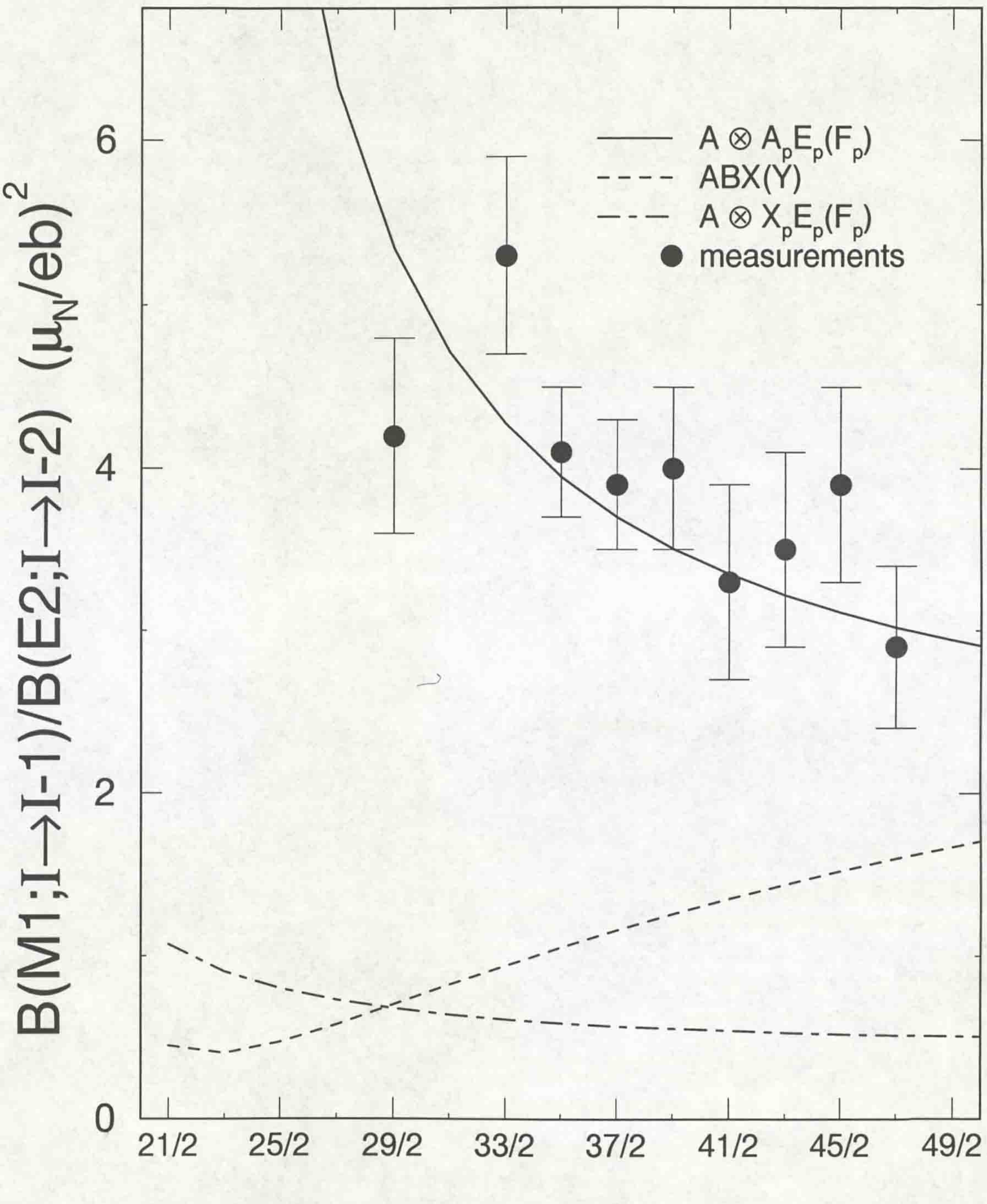

Figure 6.10: *Ratios of the reduced transition probabilities B(M1)/B(E2) as a function of spin, experimental and theoretical calculations.*

6.4.2 High-K Structures in $^{157-160}$Er

A series of high-k structures (strongly coupled bands) have been observed in the light erbium isotopes $^{157-160}$Er, N=89-92 [MR94b]. Figure 6.11 shows the partial level schemes of these structures. Not all of the bands have been fixed to the main level scheme of the respective nucleus, the ^{157}Er which is firmly anchored by the 1236, 1441 and 1715 keV transitions. Angular correlation data is not available for all these bands and the spin assignments for these bands have made by comparison to bands of known spin in this region.

Proposed quasiparticle configurations have been tested using the same methods used in the ^{157}Er strongly coupled band analysis. B(M1;I→I-1)/B(E2;I→I-2) measurements have been made where possible and band systematics (alignment, band-crossings and blocking arguments). Table 6.7 lists the quasiparticle configurations and the evidence for these assigned to the bands.

Table 6.7 Quasi-particle configurations assigned to the high-k structures in light erbium nuclei

Band	Configuration	Evidence
^{157}Er Band 1	A⊗$A_pE_pF_p$	i_{3qp} evidence of BC crossing B(M1)/B(E2) ratios
^{158}Er Band 1	AB⊗$A_pE_pF_p$ or AB⊗$B_pE_pF_p$	i_{AB} no A_pB_p crossing
Band 2	AB⊗$X_pE_pF_p$	i_{AB} evidence of A_pB_p crossing (strong interaction)
^{159}Er Band 1	A⊗$A_pE_pF_p$ (ABC⊗$A_pE_pF_p$)	no AB or A_pB_p crossing BC crossing
Band 2	EAB⊗$A_pE_pF_p$	i_{3qp} no A_pB_p crossing
^{160}Er Band 1	AX(Y)	BC crossing
Band 2	AB⊗$A_pE_pF_p$	i_{AB} no A_pB_p crossing

i_{3qp} - alignment consistent with a 3 quasiparticle configuration.

i_{AB} - alignment consistent with it an A and B neutron configuration.

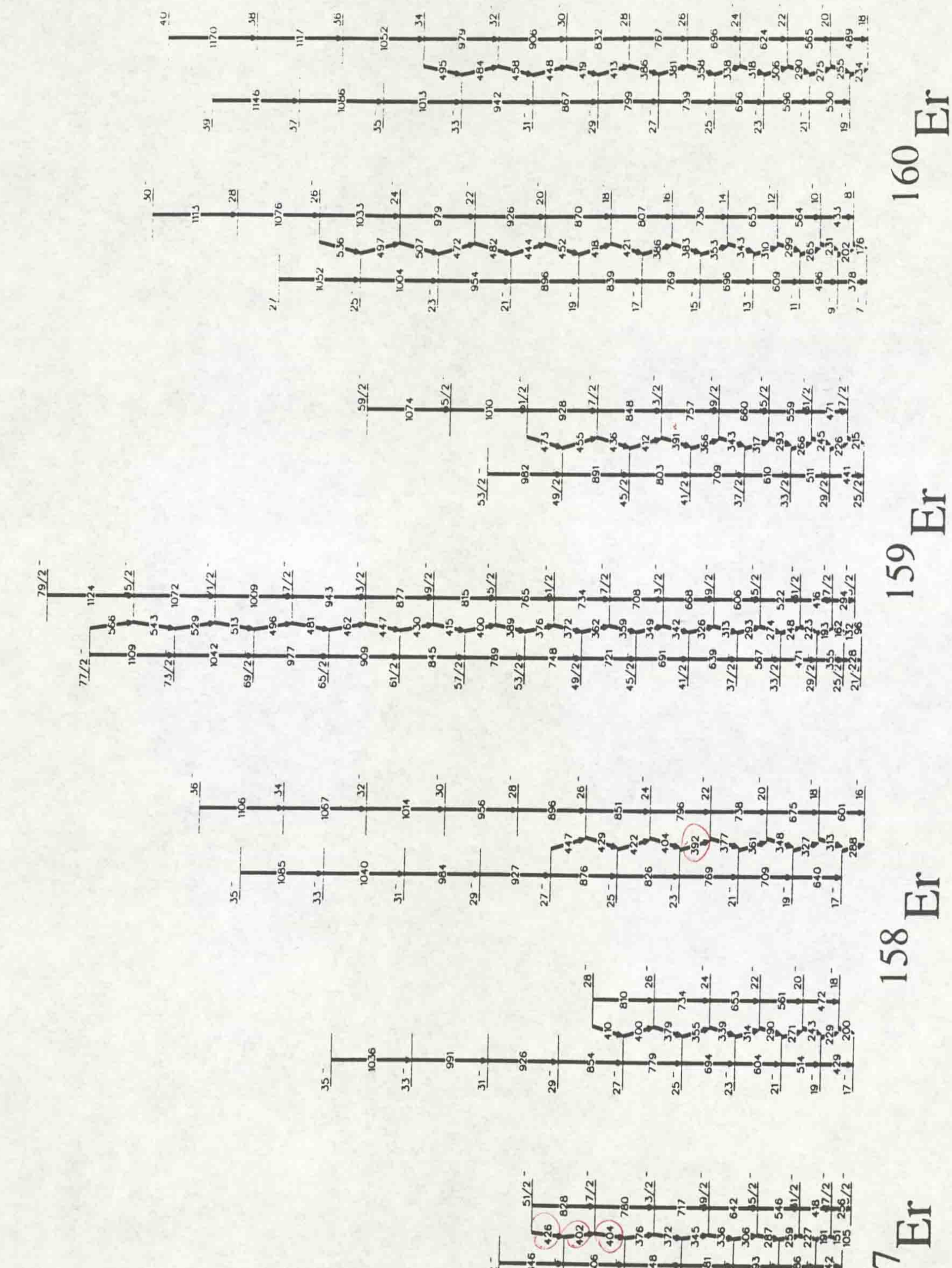

Figure 6.11: *Strongly coupled bands observed in light erbium nuclei [MR94b].*

Branching ratios were calculated for possible configurations of the bands and the experimentally measured values. The assignment of $AA_pE_p(F_p)$ for both ^{157}Er and ^{159}Er agrees very well with the theoretical calculations see section 6.4.1 and [MR94b].

The orbitals these structures are based on are assumed using the systematics of the transitional rare-earth nuclei given in section 6.4. It can be seen from table 6.7 that apart from ^{160}Er band 1 the high-k bands in the light erbium region are built on 2 quasiproton configurations. Band 1 of ^{160}Er is assigned the AX(Y) configuration, this is similar to the strongly coupled band structures observe in Gd [JM89] and Dy [MR88].

Chapter 7

High Spin Interpretation

7.1 Introduction

The nucleus has two methods of generating spin. Spin can be generated by the summed contributions of individual nucleons with their angular momentum vectors aligned in the same direction, single particle excitation. Spin can also be generated by the collective rotation of the deformed system (see section 2.2). These two methods of spin generation have different nuclear shapes (section 2.7) described by the triaxiality, γ. Figure 7.1 illustrates these two mechanisms of generating angular momentum. The competition between prolate and oblate shapes for N=90 isotones ^{158}Er, ^{160}Yb, ^{156}Dy, ^{157}Ho and ^{159}Tm is discussed in [MR86a].

The neighbouring even-even nucleus, ^{158}Er, which has a rotational, collective structure at low spin (prolate shape), experiences a shape transition at spin I$\simeq 40\hbar$, where the yrast line of the nucleus exhibits a single particle structure (oblate shape) [JS94]. Similar shape changes are expected in ^{157}Er and the intention of this analysis is to search for evidence of these changes and the predicted end of the single particle alignment sequence, band termination.

The high spin study of this work is based on the observation and interpretation of fully aligned states in ^{157}Er, these states are then compared to those observed in ^{158}Er.

The valence nucleons of ^{157}Er are counted with respect to the ^{146}Gd core, which has 64 protons and 82 neutrons. ^{157}Er has 4 valence protons and 7 valence neutrons. Nilsson diagrams for protons and neutrons are shown in figures 7.2 and 7.3 respectively. These figures are plots of single particle energies as a function of quad-

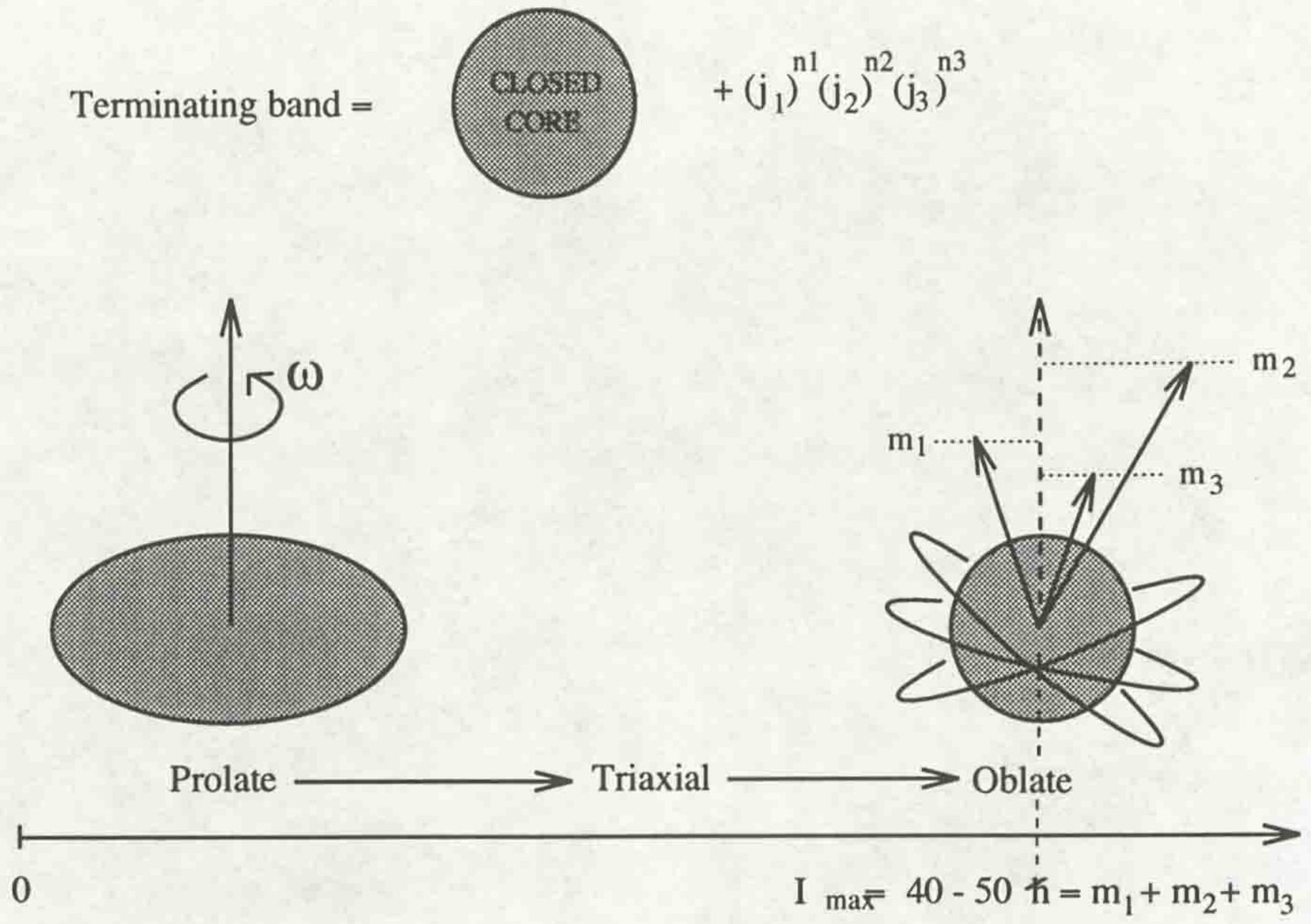

Figure 7.1: *Classical picture of band Termination. Evolution of nuclear shape with spin [IR86].*

rupole deformation, ε. Positive and negative values of ε indicate prolate and oblate nuclear shapes respectively. On inspection it can be seen in the neutron Nilsson diagram, just above the N=82 shell gap, the single particle process is more energetically probable for oblate deformations, since the high Ω components of the $f\frac{7}{2}$, $h\frac{9}{2}$ and $i\frac{13}{2}$ shells are low in energy. For a sufficient number of valence neutrons a prolate ground state deformation where the angular momentum is generated by collective rotation is more likely because of the high density of low Ω orbitals corresponding to prolate deformation.

In the rotating prolate system, as the angular momentum increases coriolis forces will increase. With increasing I the valence nucleons align their angular momentum vectors with the axis of rotation resulting in a loss of collectivity and a nucleus with axial symmetry about the nuclear axis of rotation. The reduction in pairing correlations at high spin enhances this alignment effect. Eventually all the valence nucleons align to the maximum spin available for the configuration, this maximum I configuration is called the band termination state. In this region band termination states are low-lying, the last spin units (the final alignment of the valence nucleons) are energetically cheap. If the energy of a band is plotted against spin it is expected that the curve will be down-sloping as termination is reached. The plots used in this work are referred to as rigid rotor plots, since the energy is plotted minus rigid rotor

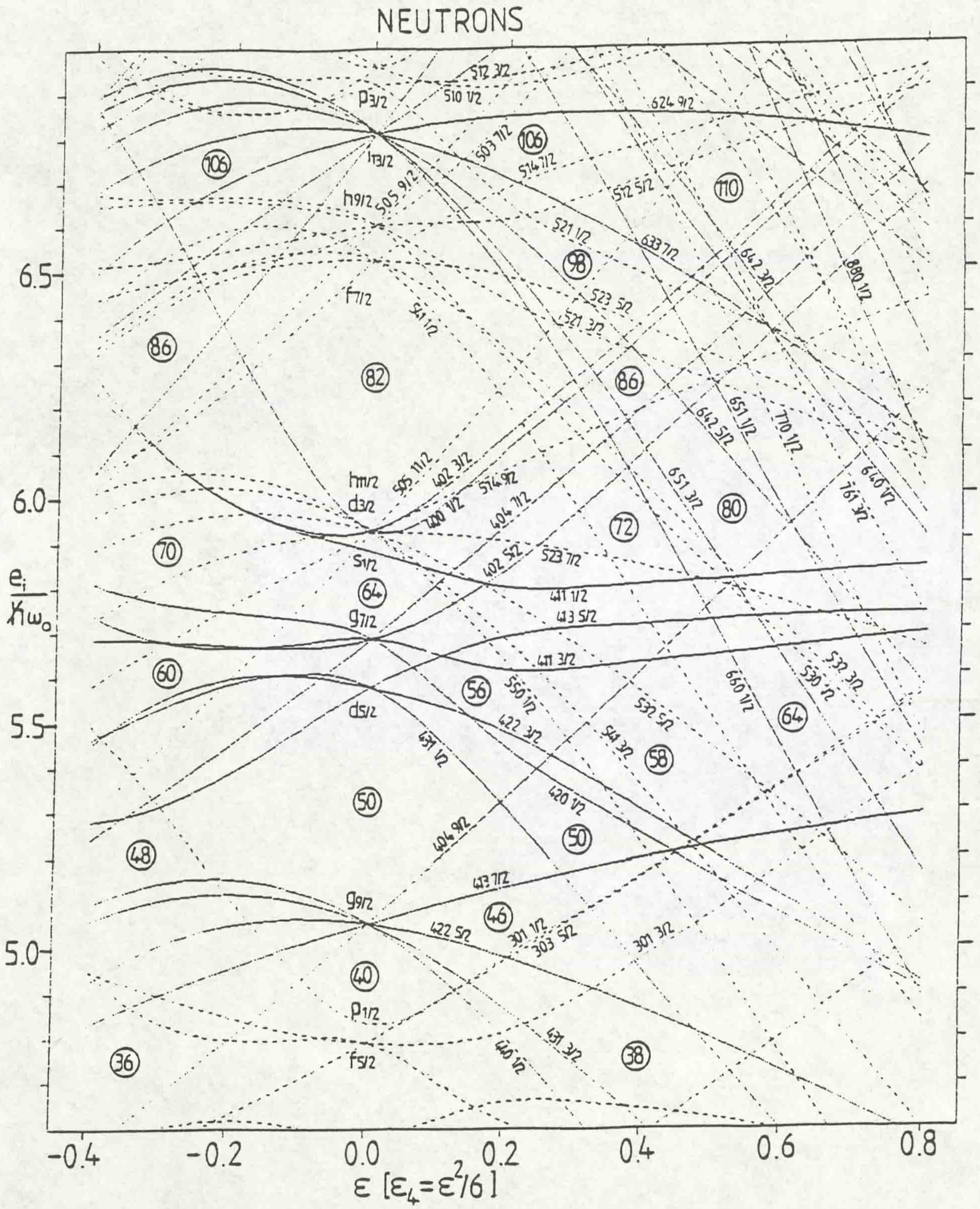

Figure 7.2: *Nilsson Diagram, neutron single particle energy levels as a function of quadrupole deformation, ε.*

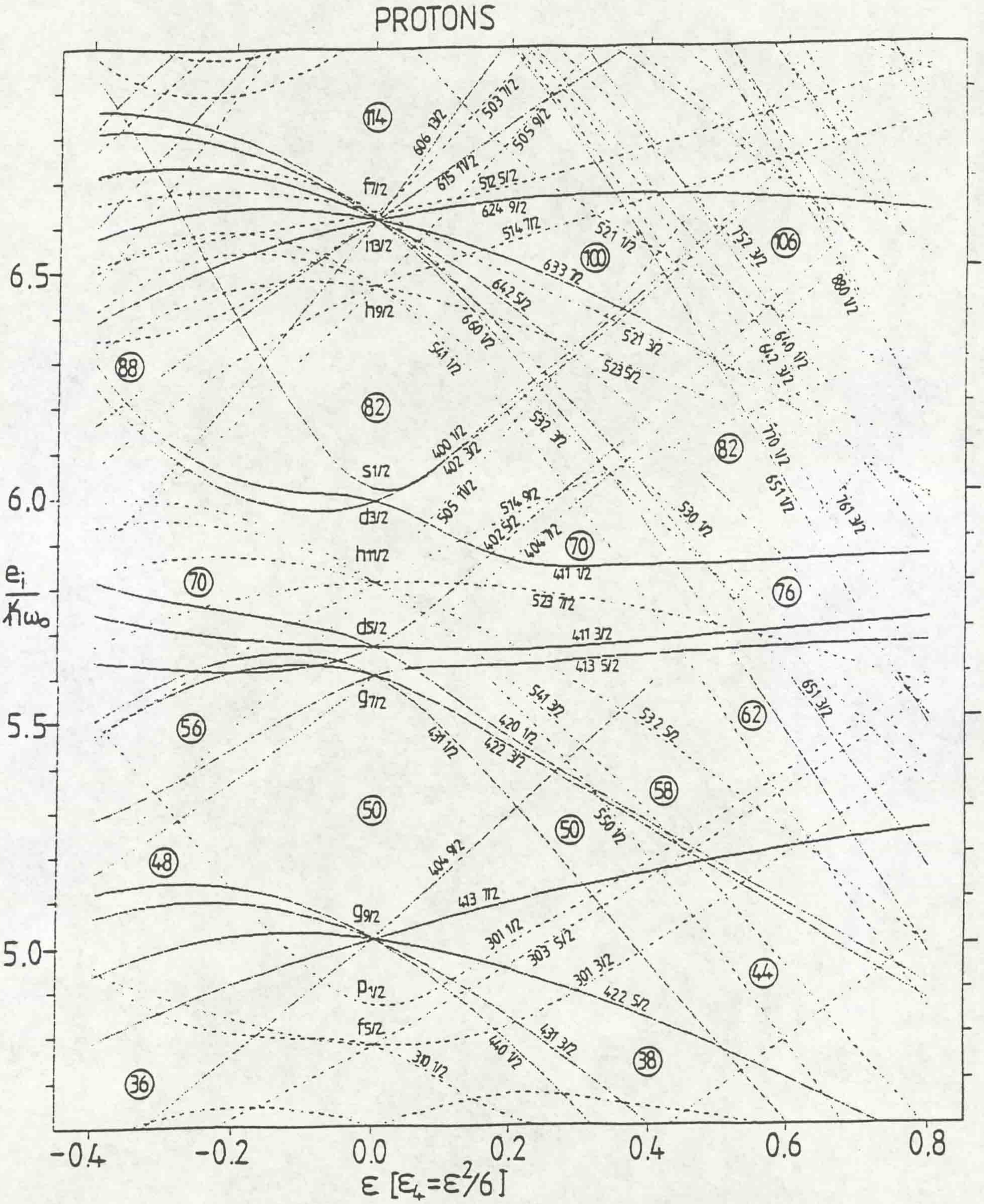

Figure 7.3: *Nilsson Diagram, proton single particle energy levels as a function of quadrupole deformation, ε.*

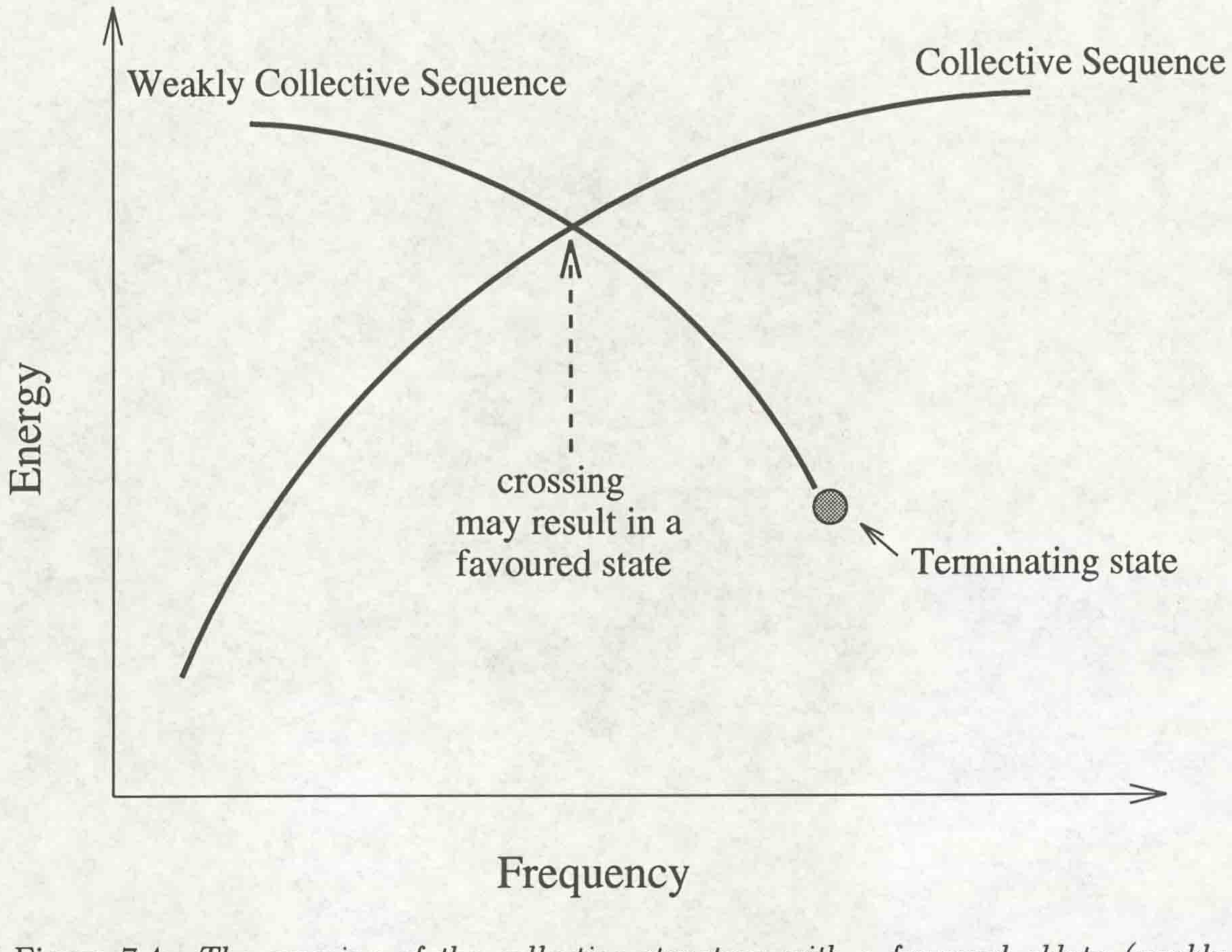

Figure 7.4: *The crossing of the collective structure with a favoured oblate (weakly collective structure) configuration. The state where these two structures cross will be favoured in energy, and a perturbation in the energy of the state is expected.*

energy.

The transition from a collective prolate ellipsoid to a weakly collective structure is manifested by the end of the rotational sequence followed by a structure more characteristic of single particle excitations, such as a non-uniform sequence of energies (referred to as a single particle sequence in this text).

Energetically favoured states have been observed in single particle sequences at a spin lower than the final band terminating state. These favoured states can be understood as a crossing or perturbation of a rotational sequence by favoured single particle states. Figure 7.4 illustrates the "crossing" of these two nuclear facets. An example of such a crossing and the continuation of the collective sequence and the single particle sequence has been observed in the yrast band of ^{158}Er [JS94].

Light rare-earth transitional nuclei, N$\simeq$ 88 – 90, have a small number of nucleons outside the ^{146}Gd core and were therefore considered as suitable candidates for

band termination. Band terminating (oblate) states were later observed in ^{156}Er and ^{158}Er, see references [FS85] and [PT85], in the odd erbium nucleus ^{155}Er [FB87] and neighbouring odd nucleus ^{157}Ho [DR92].

7.2 Band Termination Spectroscopy

Figure 7.5 shows the single particle orbitals available for single particle alignment with an oblate deformation.

Band termination spectroscopy carried out on ^{158}Er has been understood by nucleon configurations built on the aligned proton configuration $\pi(h\frac{11}{2})^4_{16^+}$. This notation indicates a proton configuration of four h$\frac{11}{2}$ protons coupled to a spin of 16 $\hbar$ with positive parity. The individual valence protons have aligned angular momentum of $\Omega = \frac{11}{2}, \frac{9}{2}, \frac{7}{2}$ and $\frac{5}{2}$, see figure 7.5. Calculations made for ^{158}Er, introduced in section 7.3 later, have also predicted a favoured state with a proton configuration of $\pi(h\frac{11}{2})^4_{8^+}$, two protons are anti-aligned ($\Omega = \pm\frac{11}{2}$), this configuration is also indicated in figure 7.5. An oblate 41^+ state has been predicted in ^{158}Er, a favoured state in the positive parity unfavoured signature band, but has not been observed.

The configurations, labelled by the occupation of particles outside the ^{146}Gd core, are characterised in a simple manner, ie. by the number of valence particles in intruder orbitals.

The fully aligned prolate orbitals remain the same for all the favoured states observed in ^{158}Er and therefore the valence neutron configuration is of main interest when assigning configurations to favoured and band terminating states.

Initially, due to the absence of theoretical calculations for single particle states in ^{157}Er, it was assumed that ^{157}Er would act like ^{158}Er with one less neutron. Therefore the observed phenomena (favoured and band terminating states) could be explained by the manipulation of the favoured and terminating configurations calculated for ^{158}Er, ie. by the removal of a neutron. This method proved to be a very useful guide in the interpretation of observations made in the initial stages of analysis.

Five favoured oblate states were observed in ^{158}Er, the spin and parity (I^π) are $40^+, 46^+, 43^-, 48^-$ and 49^- the nature and energies of these states are described in section 5.4. Table 7.1 (following Nilsson diagrams) lists the oblate configurations, the predicted 41^+ state is also included but is not observed in the data. These configurations are described pictorially in figure 7.6 [JS93] the spins of the configurations are

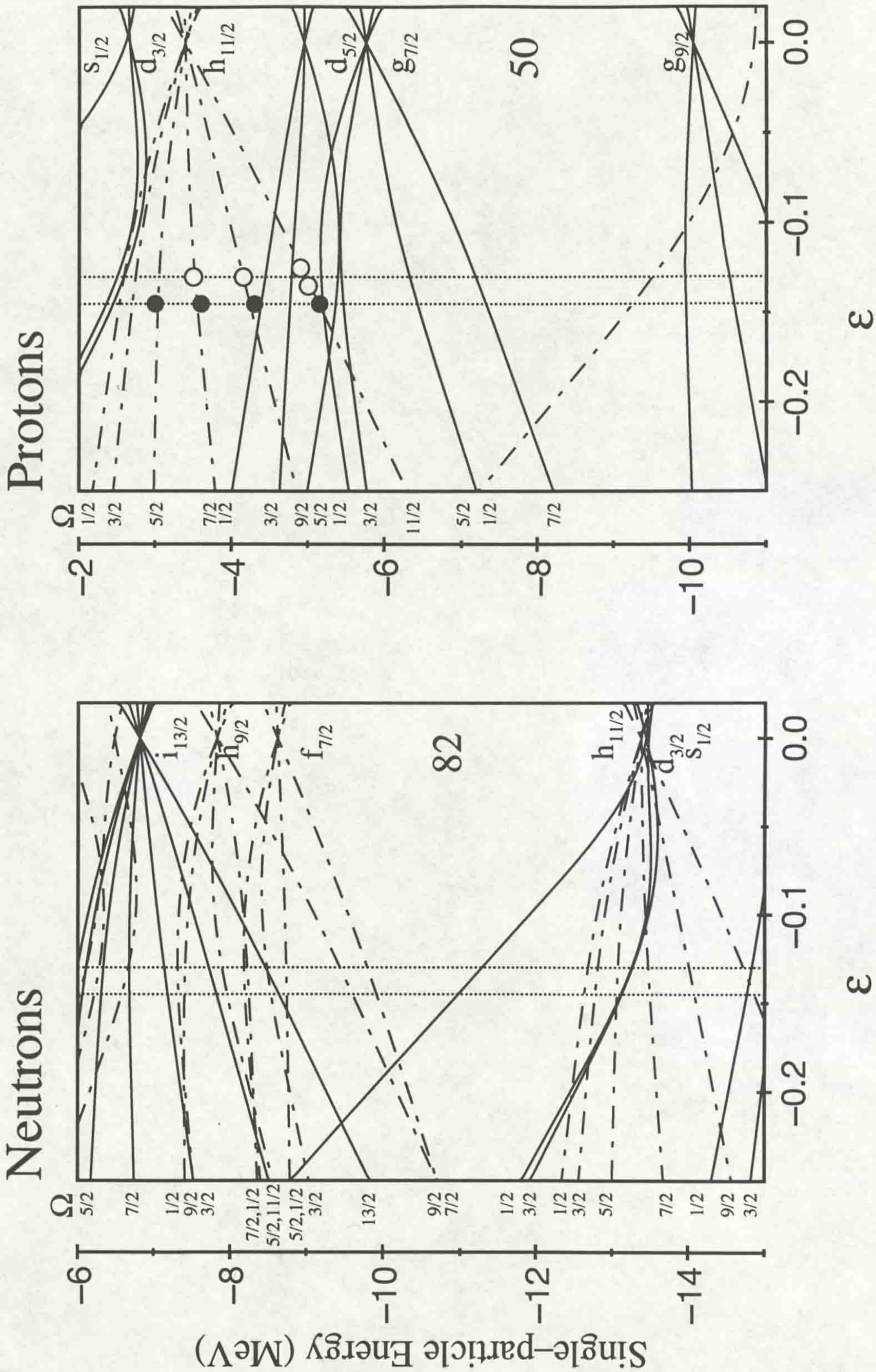

Figure 7.5: *Proton and Neutron Nilsson energy levels corresponding to oblate deformation. Erbium oblate deformation in region between dotted lines. Two possible proton configurations indicated by • and ∘. Orbitals above N=82 gap are relevant to the neutron configurations.*

indicated, the orbitals are in the energy order as found in the Nilsson diagram. By removing neutrons from these configurations predictions of favoured oblate states in ^{157}Er were made.

Table 7.1 oblate states in ^{158}Er

I^{π}	Proton Configuration	Neutron Configuration
40^{+}	$[\pi(h_{11/2})^4]_{16^+}$	$[\nu(i_{13/2})^2(h_{9/2},f_{7/2})^6]_{24^+}$
46^{+}	" "	$[\nu(i_{13/2})^2(h_{9/2},f_{7/2})^6]_{30^+}$
43^{-}	" "	$[\nu(i_{13/2})^3(h_{9/2},f_{7/2})^5]_{27^-}$
49^{-}	" "	$[\nu(i_{13/2})^3(h_{9/2},f_{7/2})^5]_{33^-}$
48^{-}	" "	$[\nu(i_{13/2})^3(h_{9/2},f_{7/2})^5]_{32^-}$
41^{+}	" "	$[\nu(i_{13/2})^2(h_{9/2},f_{7/2})^6]_{25^+}$

7.3 Nilsson-Strutinsky Calculations

To interpret the experimental observations Nilsson-Strutinsky calculations were performed by I. Ragnarsson [IR94].

In the calculations different bands are formed by fixing a configuration and tracing the lowest energy states as a function of spin. The formalism for these calculations is described in detail in [IR86, BR85]. The method allows collective and non-collective states to be treated in the same way. The Nilsson parameters employed are those used in [TB90]. Pairing correlations are neglected in the calculations, which is reasonable given the very high spins under consideration. Figures 7.7-7.10 show the predictions from these calculations for the positive and negative parity configurations [IR94], the $\gamma = 60°$ states are indicated by small circles or squares. From the diagrams it can be seen there are more than one possible configuration for each parity and signature group. The configuration expected to be observed experimentally at a particular spin is the one that is yrast, lowest in energy.

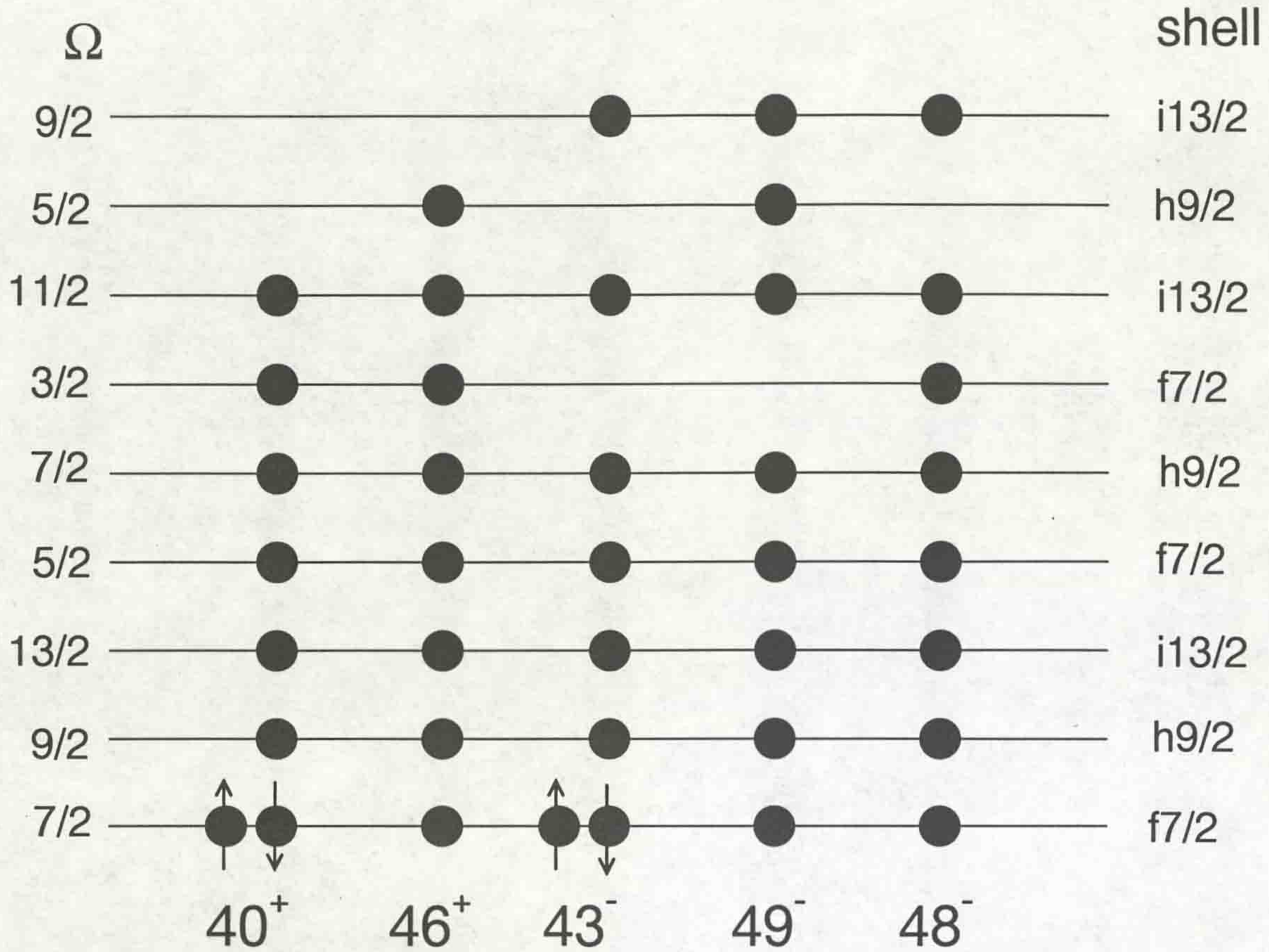

Figure 7.6: *Simple 'ball' diagram illustrating the oblate neutron configurations observed in* ^{158}Er *[JS94]. Occupation of an orbital is identified by a* •.

It should be noted on the figures that some data points are missing, this is because these spins yielded unphysical results for particular configurations. The shells available to the valence nucleons are (the same as those discussed earlier):

protons	$h_{11/2}$	negative parity
neutrons	$f_{7/2}$	negative parity
	$h_{9/2}$	negative parity
	$i_{13/2}$	positive parity

An example of the labels used to identify the configurations is $(f_{7/2}, h_{9/2})^5$. These labels do not specify which particles are $f_{7/2}$ or $h_{9/2}$ because these two subshells are strongly mixed. Negative superscripts indicate a hole in the shell.

It can be seen in figures 7.7-7.10 that configurations close to their limiting angular momentum are favoured in energy compared with the rigid rotor energy. The calculations predict band terminating states and other oblate states at a spin lower than

that of the terminating state. The band terminating states are themselves particularly favoured. Within the terminating sequence it is possible to form aligned oblate states at a lower spin if the spin vectors of a pair of particles are in opposite direction (in this analysis two anti-aligned $f_{7/2}$ neutrons coupled to $\Omega = \frac{7}{2}$ and $-\frac{7}{2}$), these states are also relatively favoured in energy.

From Nilsson-Strutinsky calculations a plot of the single neutron and proton energies, e_i, for oblate shape $\varepsilon_2 = -0.14$, versus the spin projection on the symmetry axis m_i can be made. see figure 7.13. The value used for the oblate deformation is determined from the comparison of theoretical predictions with experimental results and is discussed later. The sloping Fermi surfaces indicate the occupation of orbitals for the fully aligned proton 16^+ state and neutron $\frac{57}{2}^-$ states and the oblate neutron $\frac{45}{2}^-$ state. The $\frac{45}{2}^-$ configuration is plotted as this corresponds to a favoured state, not fully aligned, indicating the anti-aligned $f_{7/2}$ neutrons. These configurations will be discussed in the following sections.

7.4 Phenomena Observed in ^{157}Er and it's Interpretation

In figure 7.11 the excitation energy of the states in ^{157}Er, relative to a rigid rotor reference, is plotted as a function of spin. The sequence of the bands can be seen in figures 5.4 and 5.13. The excitation energies (E_x), $\gamma-$ray energies (E_γ) and angular correlation ratios are given in table B.1.

Figure 7.12 shows the high spin data on an expanded scale and two important features can be seen. Firstly, particularly favoured states are observed is some of the sequences. Secondly, the negative parity states show down-sloping behaviour compared to the rigid rotor energy. This is a characteristic of weakly collective bands approaching termination [IR86, MR86a].

7.4.1 (+,+1/2) sequence

The calculations for the (+,+1/2) states, figure 7.7, predict that between $30 \leq I \leq 40$, the yrast (+,+1/2) states are the collective configuration $\pi(4^{-1}5^5)\ \nu(5^56^2)$, ($\varepsilon_2 = 0.15$, $\gamma = -7°$ at $\frac{61}{2}^+$). This configuration has a smooth rotational behaviour which is in contrast to the experimental data where, above the $\frac{69}{2}^+$ state, irregular behaviour is

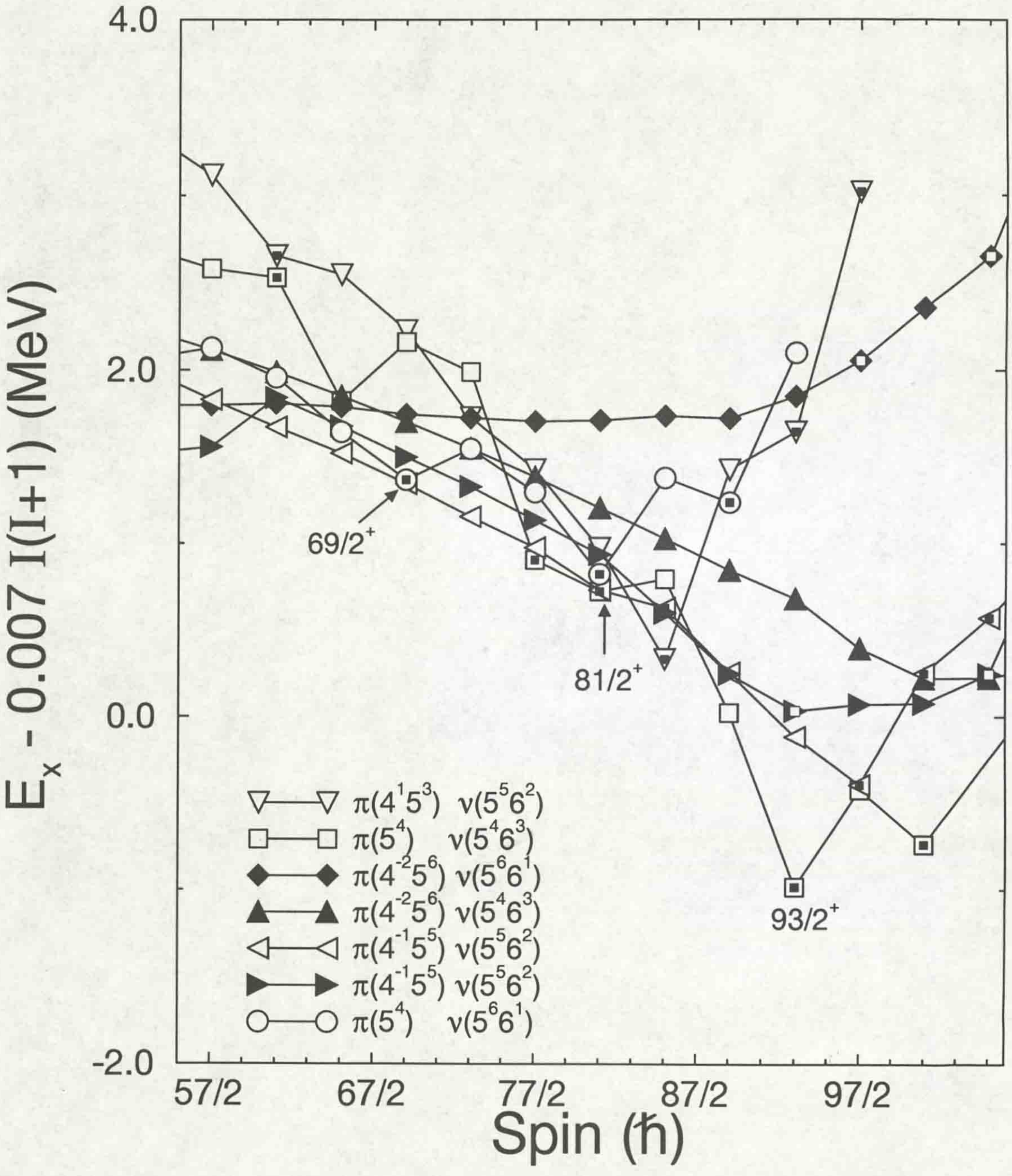

Figure 7.7: *Excitation energy minus a rigid rotor reference as a function of spin for the calculated (+,+1/2) states.*

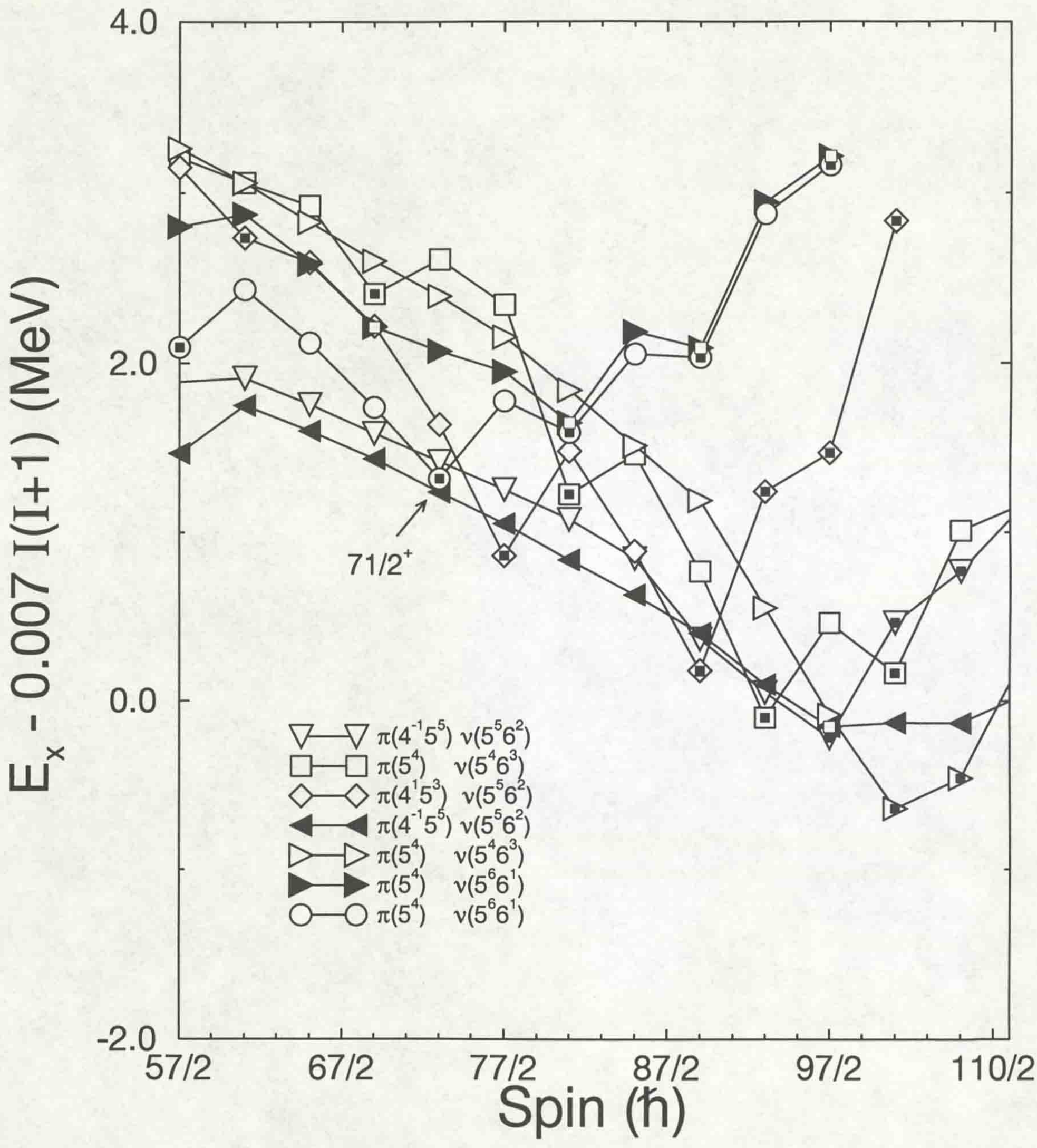

Figure 7.8: *Excitation energy minus a rigid rotor reference as a function of spin for the calculated (+,−1/2) states.*

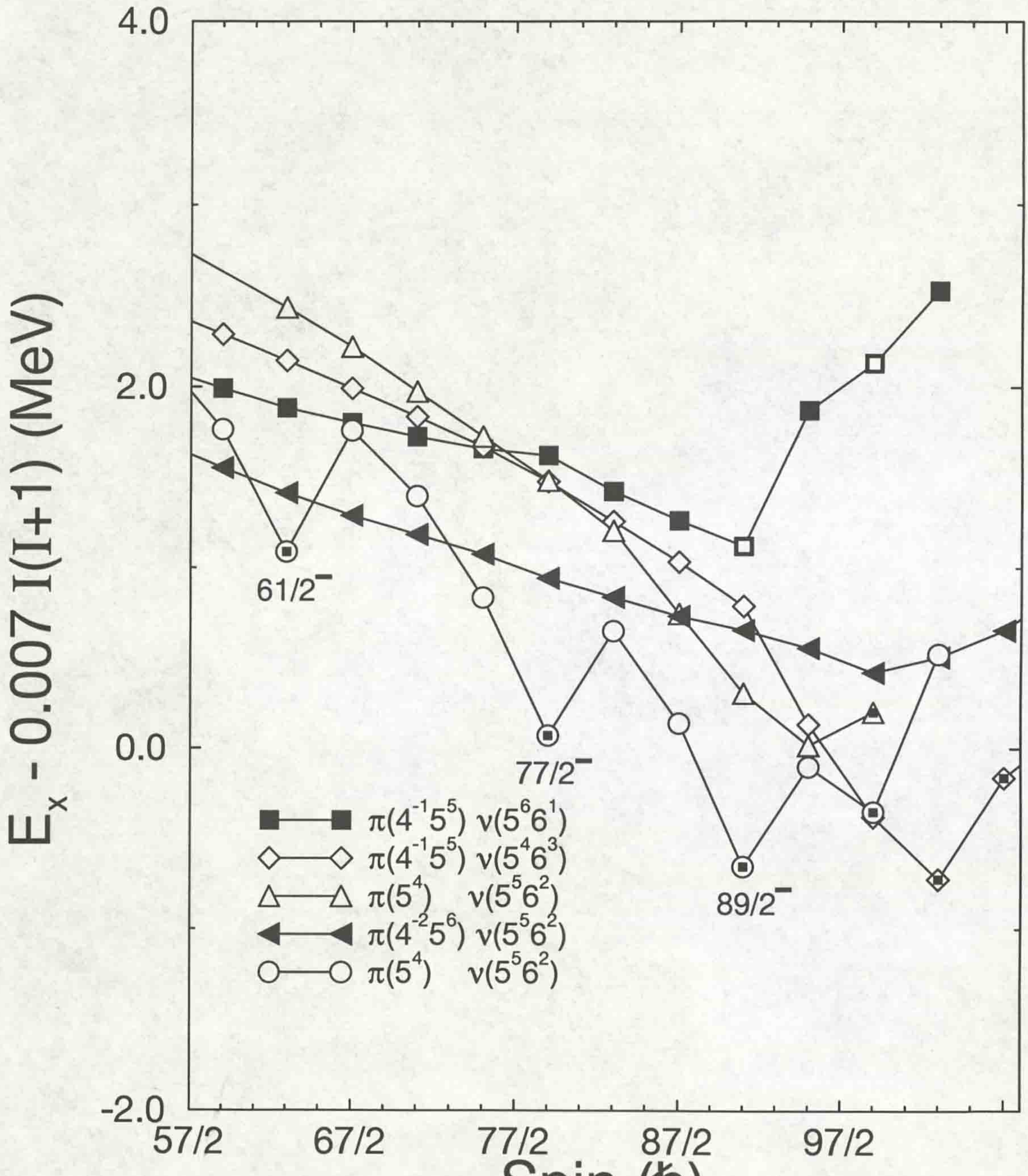

Figure 7.9: *Excitation energy minus a rigid rotor reference as a function of spin for the calculated (−,+1/2) states.*

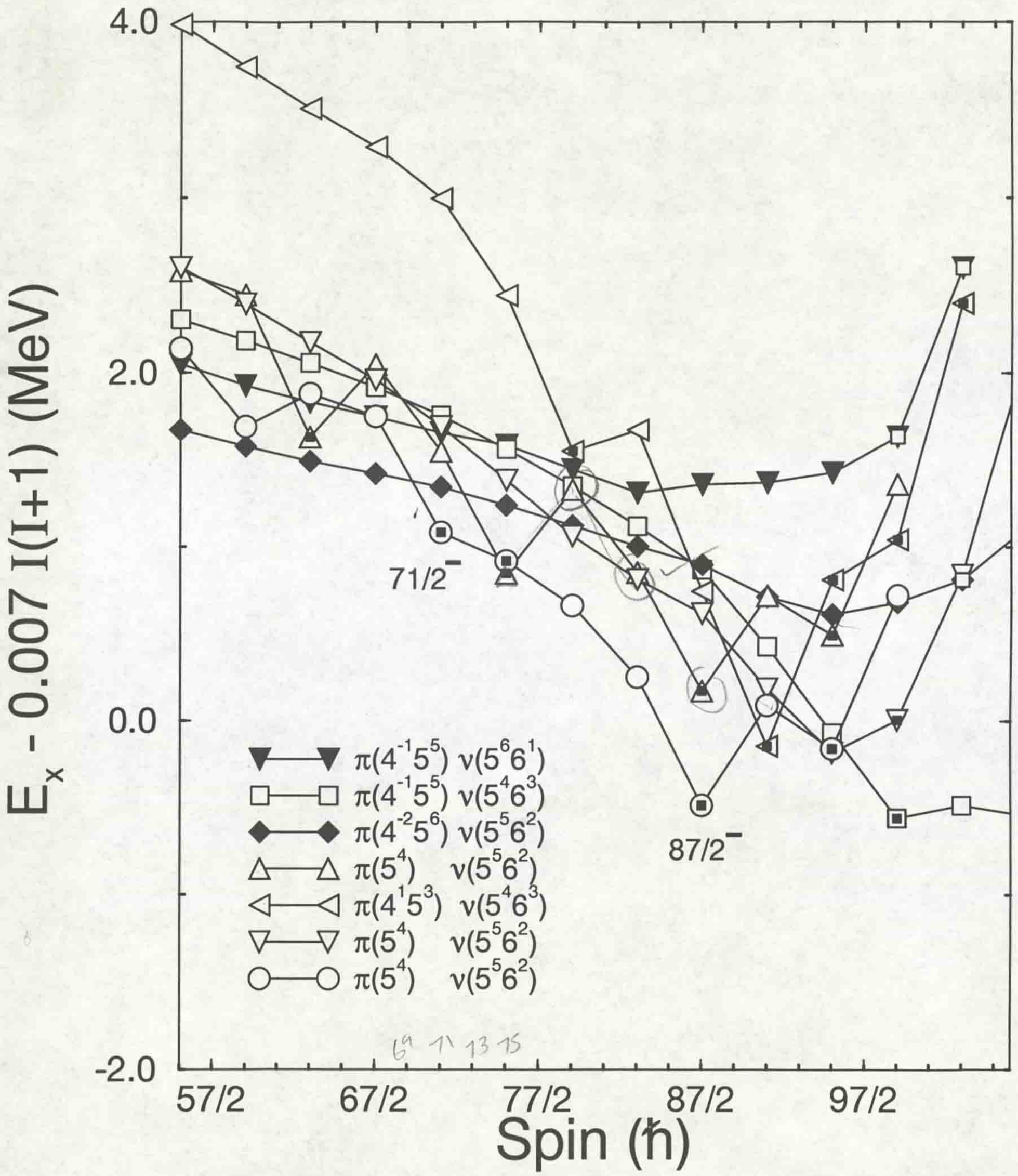

Figure 7.10: *Excitation energy minus a rigid rotor reference as a function of spin for the calculated (−,−1/2) states.*

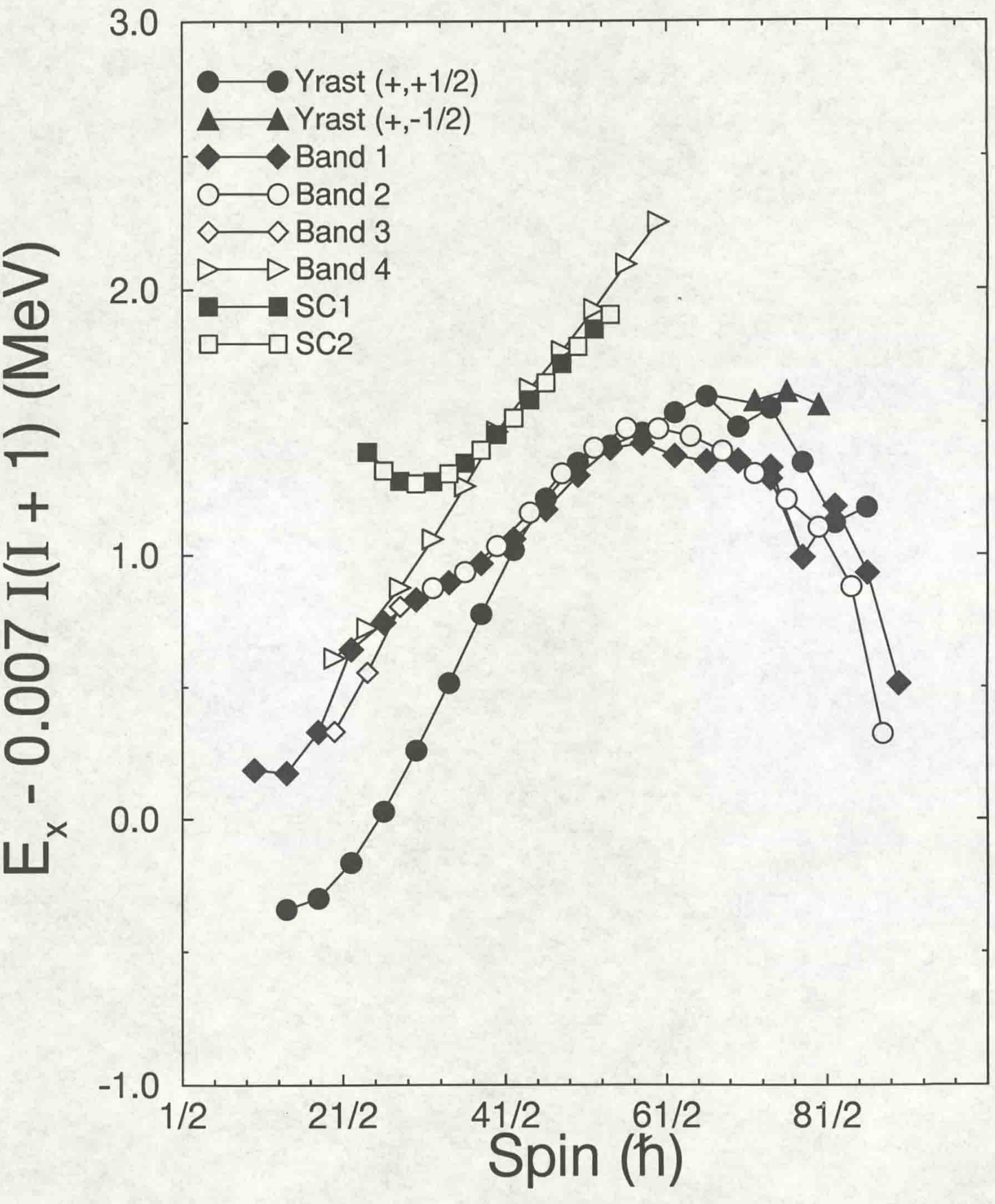

Figure 7.11: *Excitation energy, E_x, minus a rigid rotor reference as a function of spin, for all states observed in ^{157}Er.*

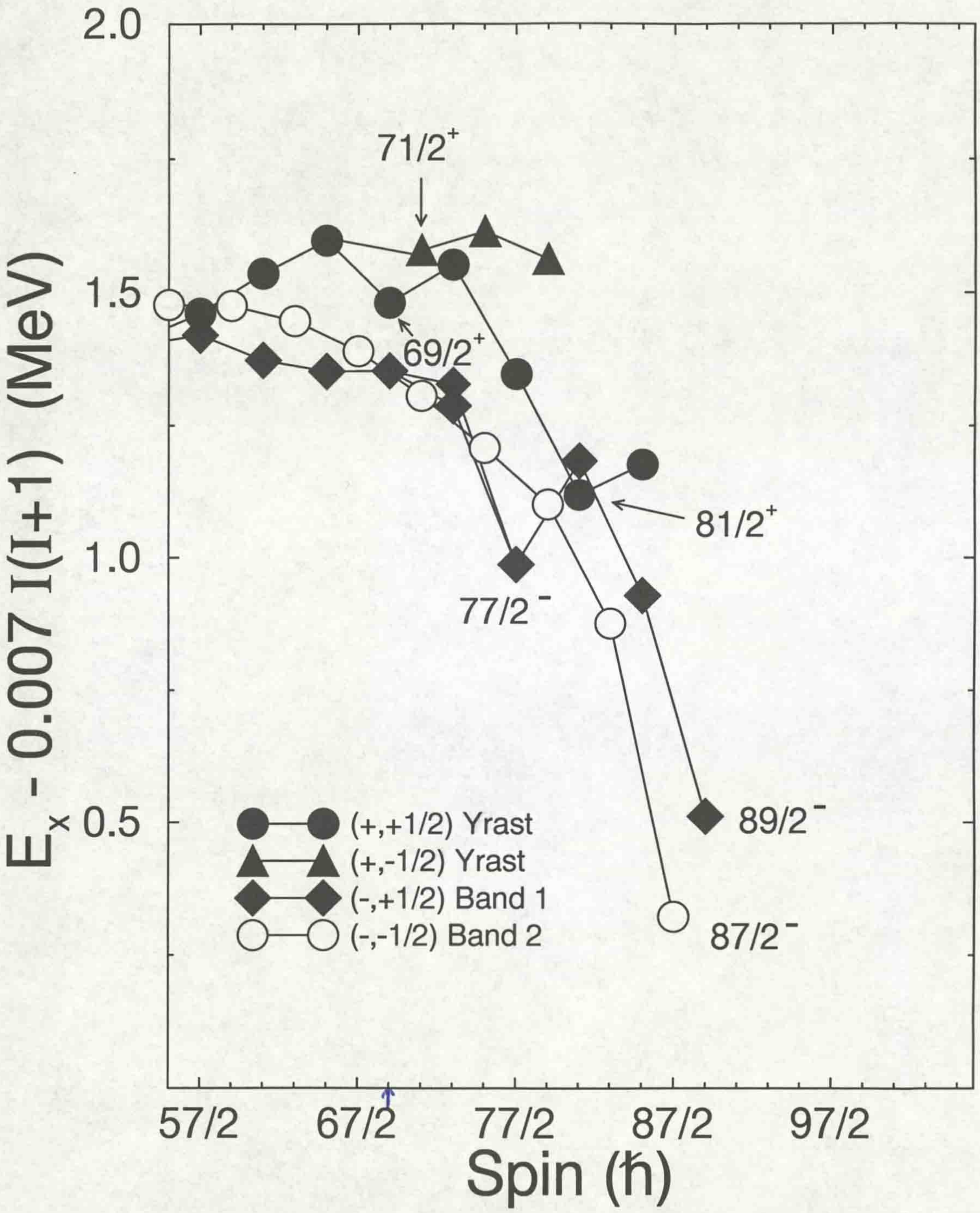

Figure 7.12: *Rigid rotor plot for states above* $I=\frac{55}{2}$ *observed in* ^{157}Er.

observed and there is fragmentation into several decay paths. The strongest sequence has energetically favoured states at $\frac{69}{2}^+$ and $\frac{81}{2}^+$. This sequence follows closely the predicted behaviour of the $\pi(5^4)\ \nu(5^6 6^1)$ configuration, open circles in figure 7.7, which also has favoured states at $\frac{69}{2}^+$ and $\frac{81}{2}^+$. In this spin region this configuration is weakly collective and has a low lying oblate state at $\frac{69}{2}^+$ (with the specific single particle occupation $[\pi(h_{11/2})^4]_{16^+} \otimes [\nu(i_{13/2})(h_{9/2}, f_{7/2})^6]_{37/2^+}$) and a fully aligned band terminating state at $\frac{81}{2}^+$ ($[\pi(h_{11/2})^4]_{16^+} \otimes [\nu(i_{13/2})(h_{9/2}, f_{7/2})^6]_{49/2^+}$). In the $\frac{69}{2}^+$ state two $f_{7/2}$ neutrons are coupled to spin 0 ($\Omega = \frac{7}{2}^+, -\frac{7}{2}^+$), see figure 7.13. Therefore, it seems likely that the observed structure is this terminating sequence. The prediction of several configurations being close to yrast near spin 40 may explain the complicated decay path observed above $\frac{69}{2}^+$.

The yrast structure above spin 40 is predicted to be a competition between the $\pi(4^1 5^3)\ \nu(5^5 6^2)$ and the $\pi(5^4)\ \nu(5^4 6^3)$ configurations [IR94]. The $\pi(4^1 5^3)\ \nu(5^5 6^2)$ configuration has a favoured yrast state at $\frac{85}{2}^+$ and the $\pi(5^4)\ \nu(5^4 6^3)$ configuration, with three $i_{13/2}$ neutrons, has a terminating spin of $\frac{93}{2}^+$. The observed state at $\frac{85}{2}^+$ may belong to one of these configurations.

7.4.2 (+,−1/2) sequence

The calculations, figure 7.8, predict several (+,−1/2) configurations competing for yrast status between 30 ≤I≤ 40. One configuration, $\pi(5^4)\ \nu(5^6 6^1)$, has an oblate energetically favoured state at $\frac{71}{2}^+$ ($[\pi(h_{11/2})^4]_{16^+} \otimes [\nu(i_{13/2})^1(h_{9/2}, f_{7/2})^6]_{39/2^+}$). This is consistent with the favoured state observed experimentally at $\frac{71}{2}^+$ with the assumption that the dipole γ-ray at 598 keV is an M1 transition. If this interpretation is correct then this is the first observation of the un-favoured signature, positive parity terminating sequence in the N = 90 nuclei. The corresponding favoured oblate state in the positive parity odd spin sequence in ^{158}Er at 41^+ has not been observed to date [JS94].

7.4.3 (−,+1/2) sequence

In contrast to the positive-parity states, the calculations for the negative- parity states figures 7.9 and 7.10 show a clear crossing between an yrast low spin collective configuration and a weakly collective terminating configuration at $\sim 35\ \hbar$. The (−,+1/2) calculations predict that the collective configuration $\pi(4^{-2}5^6)\ \nu(5^5 6^2)$, ($\varepsilon_2 = 0.175$,

$\gamma = 5°$ at $\frac{65}{2}^-$), is the yrast $(-,+1/2)$ sequence up to $\sim \frac{69}{2}$ where it is crossed by the weakly collective $\pi(5^4)\ \nu(5^56^2)$ terminating sequence. This configuration has a favoured oblate state at $\frac{77}{2}^-$ ($[\pi(h_{11/2})^4]_{16^+} \otimes [\nu(i_{13/2})^2(h_{9/2}, f_{7/2})^5]_{45/2^-}$) and a maximum spin band termination state at $\frac{89}{2}^-$ ($[\pi(h_{11/2})^4]_{16^+} \otimes [\nu(i_{13/2})^2(h_{9/2}, f_{7/2})^5]_{57/2^-}$). Figure 7.13 shows these states in terms of the single particle energies as a function of the spin projection on the symmetry axis. The favoured states observed experimentally are interpreted as these states. Below $\frac{77}{2}^-$, the $\pi(5^4)\ \nu(5^56^2)$ sequence was not identified in the experimental data. Hence, the favoured oblate $\frac{61}{2}^-$ state, which has the four $h_{11/2}$ protons coupled to spin 8^+, was not observed. However, in the neighbouring nucleus ^{158}Er, such a state was identified at 32^+ where the terminating sequence was established below the crossing point [JS94].

7.4.4 $(-,-1/2)$ sequence

This experimental data does not have any clear favoured states in the $(-,-1/2)$ sequence but does show significant downs-loping above $\sim \frac{71}{2}^-$, figure 7.11. The calculations, figure 7.10, predict that at $\sim \frac{71}{2}^-$ the collective configuration $\pi(4^{-2}5^6)\ \nu(5^56^2)$, ($\varepsilon_2 = 0.173$, $\gamma = 7°$ at $\frac{67}{2}^-$) is crossed by the $\pi(5^4)\ \nu(5^56^2)$ sequence. This latter sequence has oblate states at $\frac{71}{2}^-$, $\frac{75}{2}^-$ and a very favoured band terminating state at $\frac{87}{2}^-$ ($[\pi(h_{11/2})^4]_{16^+} \otimes [\nu(i_{13/2})^2(h_{9/2}, f_{7/2})^5]_{55/2^-}$). Therefore, the high spin structure of this sequence is interpreted as this terminating sequence and the observed $\frac{87}{2}^-$ state as the terminating state.

The configurations and oblate deformations (ε_2) of the favoured and terminating states observed in ^{157}Er compared to ^{158}Er are given in table 7.2. These states can also be obtained by rotating the Fermi surface indicating the orbitals occupied, see figure 7.13.

7.5 Comparison of ^{157}Er and ^{158}Er Band Termination Spectroscopy

The oblate states identified in ^{157}Er and ^{158}Er are summarised in table 7.2. The spin and parity of the state, the neutron configuration and the predicted deformation is given. It should be noted that although the predicted $\frac{71}{2}^+$ oblate state has been observed in ^{157}Er, the corresponding 41^+ state has not been observed in ^{158}Er.

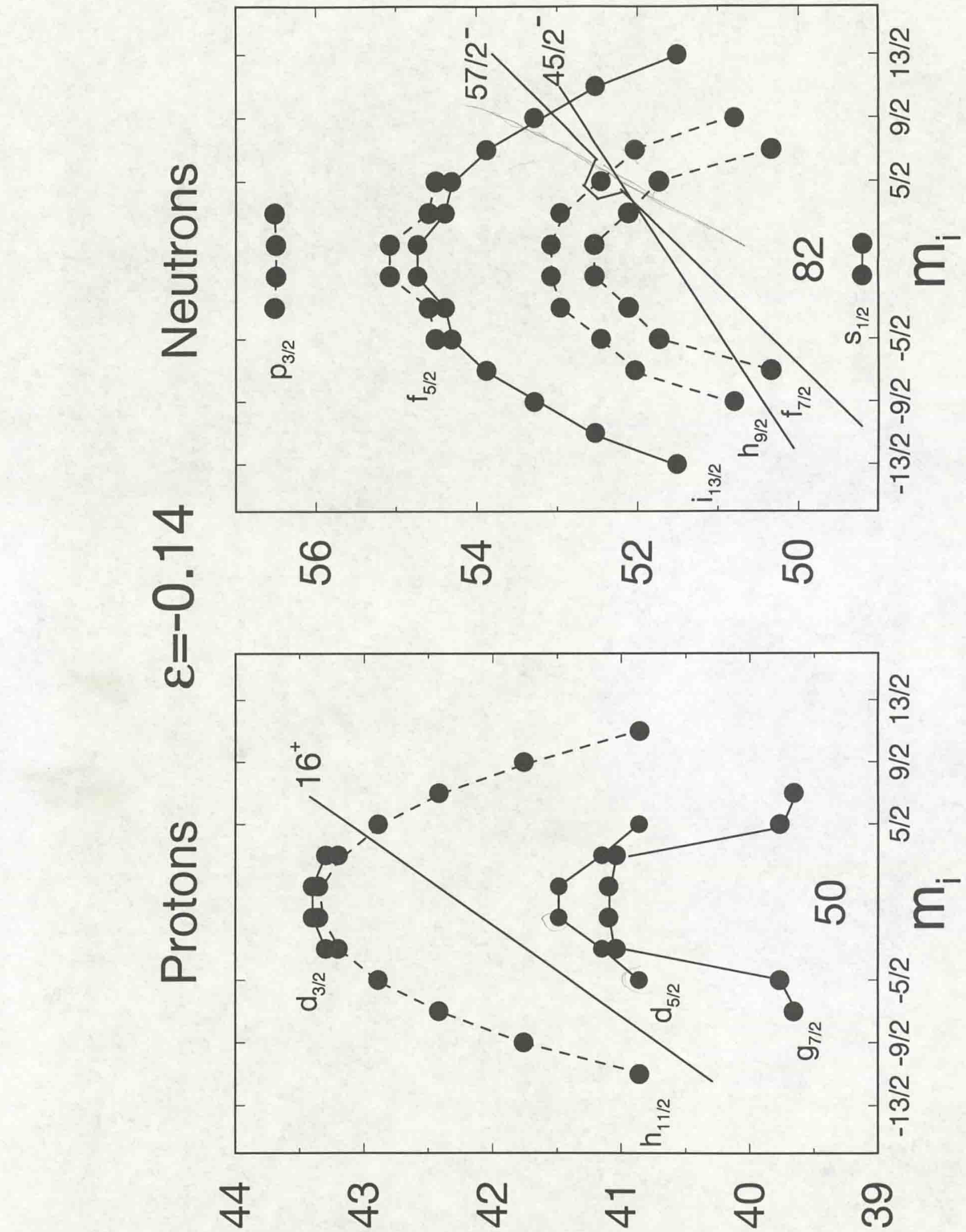

Figure 7.13: *Single proton and neutron energies e_i for oblate shape $\varepsilon = -0.14$ vs. the spin projection onto the symmetry axis m_i. The sloping Fermi surfaces indicate the occupation of orbitals for the fully aligned proton 16^+ and neutron $\frac{57}{2}^-$ states and the oblate neutron $\frac{45}{2}^-$ state.*

Table 7.2 Oblate States observed in ^{157}Er and ^{158}Er

^{157}Er			^{158}Er		
I^π	Neutron Configuration	ε_2	I^π	Neutron Configuration	ε_2
$\frac{69}{2}^+$	$[\nu(i_{13/2}), (h_{9/2}, f_{7/2})^6]_{37/2+}$	-0.131	40^+	$[\nu(i_{13/2})^2(h_{9/2}, f_{7/2})^6]_{24+}$	-0.146
$\frac{81}{2}^+$	$[\nu(i_{13/2}), (h_{9/2}, f_{7/2})^6]_{49/2+}$	-0.114	46^+	$[\nu(i_{13/2})^2(h_{9/2}, f_{7/2})^6]_{30+}$	-0.136
$\frac{77}{2}^-$	$[\nu(i_{13/2})^2, (h_{9/2}, f_{7/2})^5]_{45/2-}$	-0.144	43^-	$[\nu(i_{13/2})^3(h_{9/2}, f_{7/2})^5]_{27-}$	-0.151
$\frac{89}{2}^-$	$[\nu(i_{13/2})^2, (h_{9/2}, f_{7/2})^5]_{57/2-}$	-0.114	49^-	$[\nu(i_{13/2})^3(h_{9/2}, f_{7/2})^5]_{33-}$	-0.136
$\frac{87}{2}^-$	$[\nu(i_{13/2})^2, (h_{9/2}, f_{7/2})^5]_{55/2-}$	-0.130	48^-	$[\nu(i_{13/2})^3(h_{9/2}, f_{7/2})^5]_{32-}$	-0.137
$\frac{71}{2}^+$	$[\nu(i_{13/2}), (h_{9/2}, f_{7/2})^6]_{39/2+}$	-0.135	41^+	$[\nu(i_{13/2})^2(h_{9/2}, f_{7/2})^6]_{25+}$	-0.150

It can be seen that the equivalent states in ^{157}Er are related to those in ^{158}Er by the removal of one $i_{13/2}$ neutron in each case. This is illustrated in figure 7.14. Black circles represent the ^{158}Er favoured and fully aligned configurations and white circles the ^{157}Er configurations. This vindicates the initial assumption of this analysis, ^{157}Er should act as ^{158}Er with one less neutron.

The predicted deformations for these states are given in table 7.2 they all have a similar oblate deformation, $\varepsilon_2 \sim -0.14$. These values of oblate deformation were obtained from the theoretical calculations and the numerical accuracy of these deformations is ~ 0.01.

In total eleven single particle states have now been observed giving the full spectrum of states that can be formed by these favoured orbitals. The difference in energy of these pure, single-particle states corresponds to a change in the occupation of specific neutron orbitals and therefore can be used to build up a detailed spectrum of states at this oblate deformation. This difference in energy is referred to as a single particle exchange. Such an exchange can be seen in figures 7.13 and 7.14, for example, to go from the favoured $\frac{77}{2}^-$ state to the fully aligned $\frac{89}{2}^-$ state the $f_{7/2,\Omega=-7/2}$ neutron has to be exchanged for a $h_{9/2,\Omega=-5/2}$ neutron, a particle exchange. Therefore the difference in the excitation energies of these two states will give the energy needed to

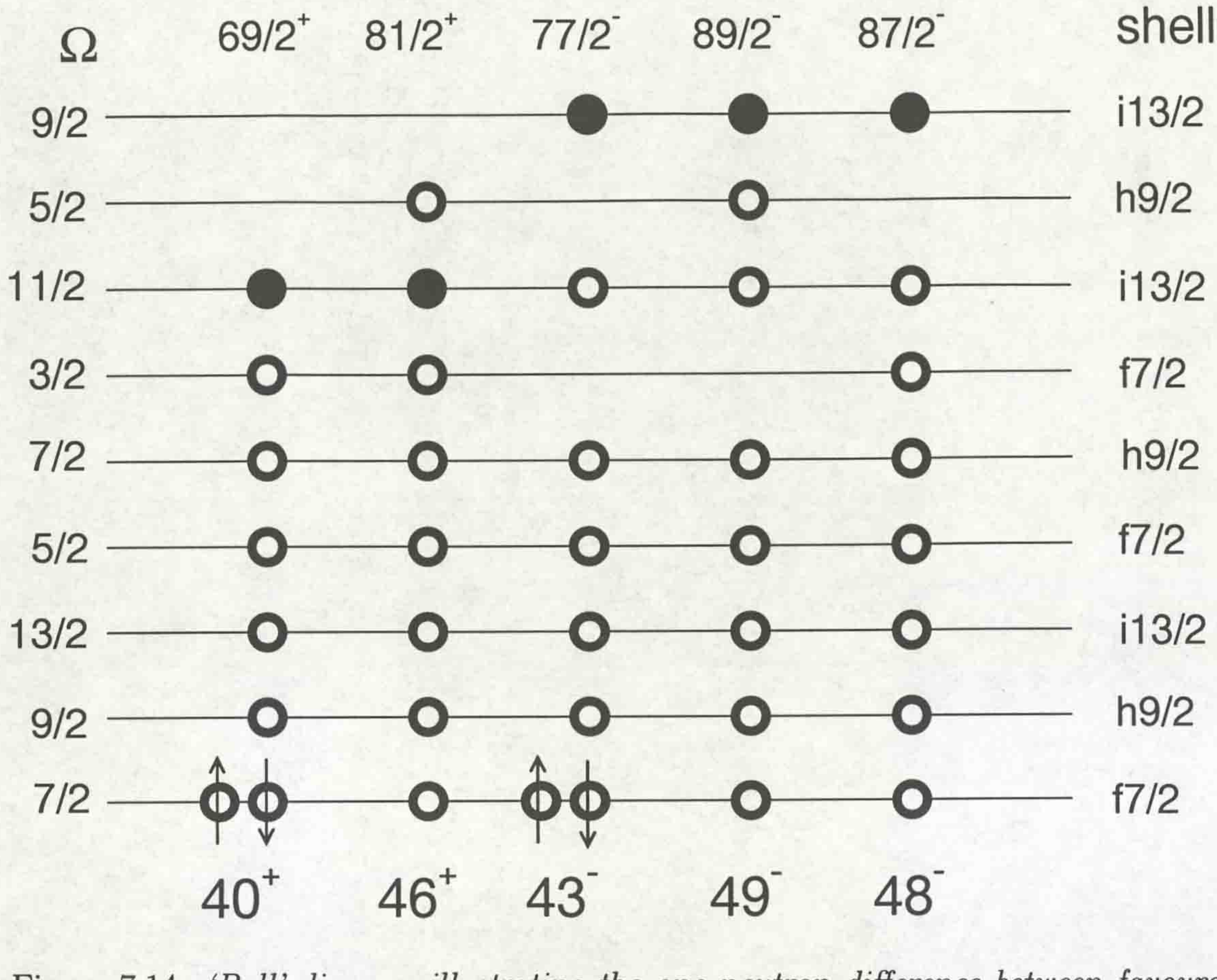

Figure 7.14: *'Ball' diagram illustrating the one neutron difference between favoured and single particle states in* ^{157}Er *and* ^{158}Er.

move a neutron between two different orbitals.

It is interesting to compare the particle exchange values (energy difference between states) with the calculations and with the energy difference for the same particle exchange in different configurations. This is summarised in table 7.3 which also gives values for the single particle states observed in ^{157}Ho [DR92]. The uncertainty of the theoretical calculation for excitation energies is $\sim$ 100 keV.

The largest differences between the calculated and experimental numbers for ^{157}Er are only around 400 keV, comparing this to the numerical uncertainty in the theoretical calculations this shows a reasonable agreement. The particle exchange $\nu(\mathrm{h}_{9/2,\Omega=5/2}) \rightarrow \nu(\mathrm{f}_{7/2,\Omega=-7/2})$, is established in five sequences in the three nuclei considered. The energy differences are all very similar indicating a very stable oblate mean field.

Table 7.3 Theoretical and experimental Particle exchange energies of ^{157}Er and the neighbouring odd nucleus ^{157}Ho.

Particle Exchange		Experiment (keV)	Theory (keV)
$^{157}\mathrm{Er} - \mathrm{E}_x(\frac{81}{2}^+) - \mathrm{E}_x(\frac{69}{2}^+)$	$\nu(\mathrm{h}_{9/2,\Omega=5/2}) \rightarrow \nu(\mathrm{f}_{7/2,\Omega=-7/2})$	2830.6	2680
$^{157}\mathrm{Er} - \mathrm{E}_x(\frac{89}{2}^-) - \mathrm{E}_x(\frac{77}{2}^-)$	.. ..	3051.1	2840
$^{158}\mathrm{Er} - \mathrm{E}_x(46^+) - \mathrm{E}_x(40^+)$	.. ..	3284	2864
$^{158}\mathrm{Er} - \mathrm{E}_x(49^-) - \mathrm{E}_x(43^-)$	.. ..	3127	2932
$^{157}\mathrm{Ho} - \mathrm{E}_x(\frac{87}{2}^-) - \mathrm{E}_x(\frac{75}{2}^-)$	.. ..	3318	
$^{157}\mathrm{Er} - \mathrm{E}_x(\frac{89}{2}^-) - \mathrm{E}_x(\frac{87}{2}^-)$	$\nu(\mathrm{h}_{9/2,\Omega=5/2}) \rightarrow \nu(\mathrm{f}_{7/2,\Omega=3/2})$	806.8	463
$^{158}\mathrm{Er} - \mathrm{E}_x(49^-) - \mathrm{E}_x(48^-)$	.. ..	679	450

Particle exchange values are very useful for refining the parameters used in the calculations. These energies can be used to check the energy spacings (differences) between calculated orbitals and parameters can be changed accordingly.

Chapter 8

Summary of ^{157}Er Results

The level scheme of ^{157}Er has been extended to very high spin using high fold coincidence γ-ray data from the Eurogam spectrometer.

8.1 Low Spin Structure in ^{157}Er

For spins up to $\sim 30\hbar$ the rotational bands observed are interpreted as multi quasiparticle excitations within the framework of the cranked shell model.

Band crossings interpreted as AB and BC neutron and A_pB_p proton alignments have been observed in these data.

The negative parity positive signature band (band 1) has been extended down to a spin of $\frac{9}{2}$. The extension of this band has been assigned the single quasiparticle configuration E.

Evidence of an un-favoured signature partner to the yrast band has been observed, band 3.

8.2 High-K Band in ^{157}Er

A new strongly coupled sequence has been established which represents the first quasiparticle configuration involving a high-K orbital observed in ^{157}Er. This structure is similar to other high-K bands observed in the light erbium nuclei.

This structure was interpreted as a three quasi-particle configuration involving the high-K $[404]_{\frac{7}{2}}$ proton orbital. This configuration was confirmed by comparing experimental and theoretical B(M1;I$\rightarrow$I+1)/B(E2;I$\rightarrow$I+2) reduced transition probabilities,

using the semi-classical Dönau and Frauendorf formalism.

8.3 Band Termination Spectroscopy in ^{157}Er

Above spin $30\hbar$ the yrast structure changes from that corresponding to a prolate nucleus rotating collectively about an axis perpendicular to its symmetry axis to a regime where the spin of the yrast states is produced by the alignment of all or most of the available valence nucleons along the symmetry axis of a weakly deformed oblate shape. Particularly favoured states are observed which have been identified as specific single particle configurations by comparison with cranked Nilsson-Strutinsky calculations. Particularly favoured states (I^{π}) $\frac{69}{2}+$, $\frac{81}{2}+$, $\frac{71}{2}+$ $\frac{77}{2}-$, $\frac{89}{2}-$ and $\frac{87}{2}-$ have been observed. If the interpretation of the $\frac{71}{2}^{+}$ state is correct it is the first observation of the un-favoured signature positive parity terminating sequence observed in the N$\simeq$90 nuclei. These states are found to be related by simple single particle excitations to states observed in the neighbouring nuclei ^{158}Er and ^{157}Ho. These data provide the complete spectrum of single particle states for the lowest lying valence orbitals above the ^{146}Gd closed core. Figure 8.1 shows the high spin rigid rotor plot for ^{157}Er and the corresponding Nilsson-Strutinsky calculations.

Fully aligned, band terminating states have been firmly established in ^{157}Er at $\frac{81}{2}^{+}$, $\frac{87}{2}^{-}$ and $\frac{89}{2}^{-}$. An $\frac{85}{2}^{+}$ state has been observed in the yrast band, this feeds the oblate $\frac{81}{2}^{+}$ band terminating state. The yrast structure above spin 40 has a competition between two configurations, the $\frac{85}{2}^{+}$ may belong to one of these configurations. A transition feeding this state has not been observed.

Transitions feeding the fully aligned $\frac{89}{2}^{-}$ and $\frac{87}{2}^{-}$ states of the $(-,+1/2)$ and $(-,-1/2)$ bands respectively have not been observed. For example, it can be seen in figure 5.10 that the band terminating $\frac{87}{2}^{-}$ state has a high intensity ($\simeq$ 33% of the band intensity), therefore if the state was was fed by a single transition it should have a large enough intensity to be measured.

A possible explanation of why these feeding transitions have not been observed is that the fully aligned state is not fed by a single $\gamma-$ray transition, but many so that the intensity is fragmented and the individual transitions too small to be detected. It is also possible that the feeding transitions may have large energies because a pair of nucleons may have to be broken in the core and the resulting single particle will be excited over the shell gap (neutron or proton). But high energies have been measured

in this data, therefore if the excited state above the fully aligned state is a single high energy $\gamma-$ray it should have been observed.

The feeding mechanism of band termination states has been looked for in ^{158}Er. Figure 5.16 shows the top of the (+,0) band in ^{158}Er. The fully aligned 46^+ state is strong, it can clearly be seen that there are no strong transitions feeding this terminating state that would indicate the continuation of the band. A 939 keV stretched dipole transition has been observed feeding from the (−,1) band to the fully aligned 46^+ state of the (+,0) band.

8.4 Future Study

An experiment has been recently performed aimed at the measurement of linear polarisation of transitions in ^{157}Er using Eurogam Phase II. This experiment should prove that these high spin state are stretched electric quadrupoles, as the angular correlation measurements give the multipole order of the transition only, but offers no information on whether the transition is electric or magnetic.

To verify that the high spin structures in ^{157}Er is showing a shape transition from a collective to a non-collective structure lifetime measurements [PS79] should be performed.

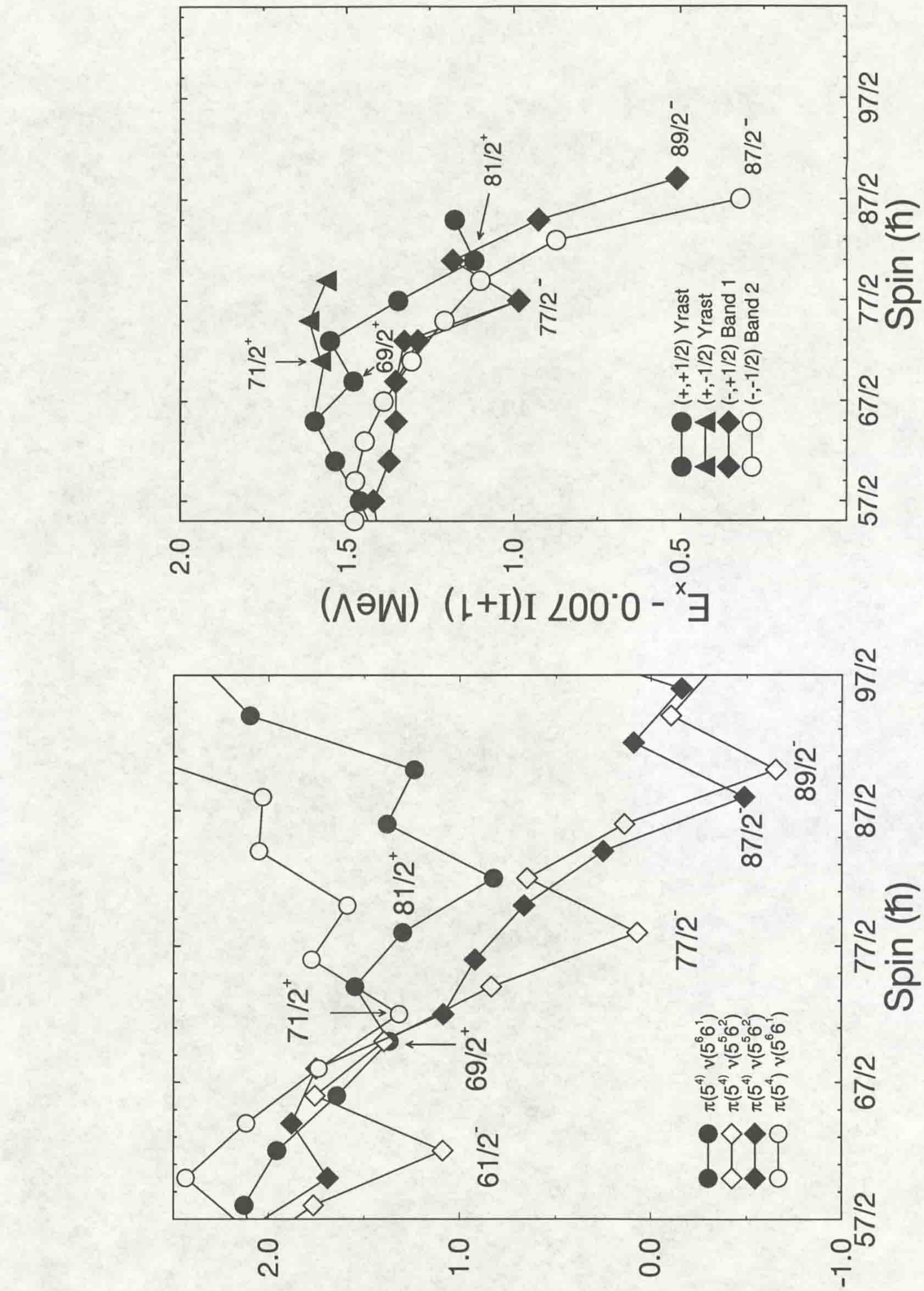

Figure 8.1: *Experimentally observed favoured and terminating states (top) in comparison to the theoretically calculated sequences (bottom).*

Appendix A

Data Analysis Methods

A.1 ^{157}Er Data Collected Using Eurogam

The total number of events collected from the Er experiment, using Eurogam, was 8x10^8 events (this includes all the reaction channels). Figure A.1 shows the fold distribution of the data, where a distinction is made between fold and real fold. The fold is the number the number of Ge detectors that detected a gamma ray in the event (written at the beginning of the event). The real fold is defined as the number of Ge words remaining after all the gamma–ray energy, E_γ=0 keV words have been removed.

A.1.1 Event Format

The data (in event form) collected had the following format:

- fold (number of detectors in the event)
- TAC

the following information is stored in the event for each Ge detector:

- detector number (used to identify individual detectors)
- energy (0 – 4 MeV range)
- energy (0 – 20 MeV range)

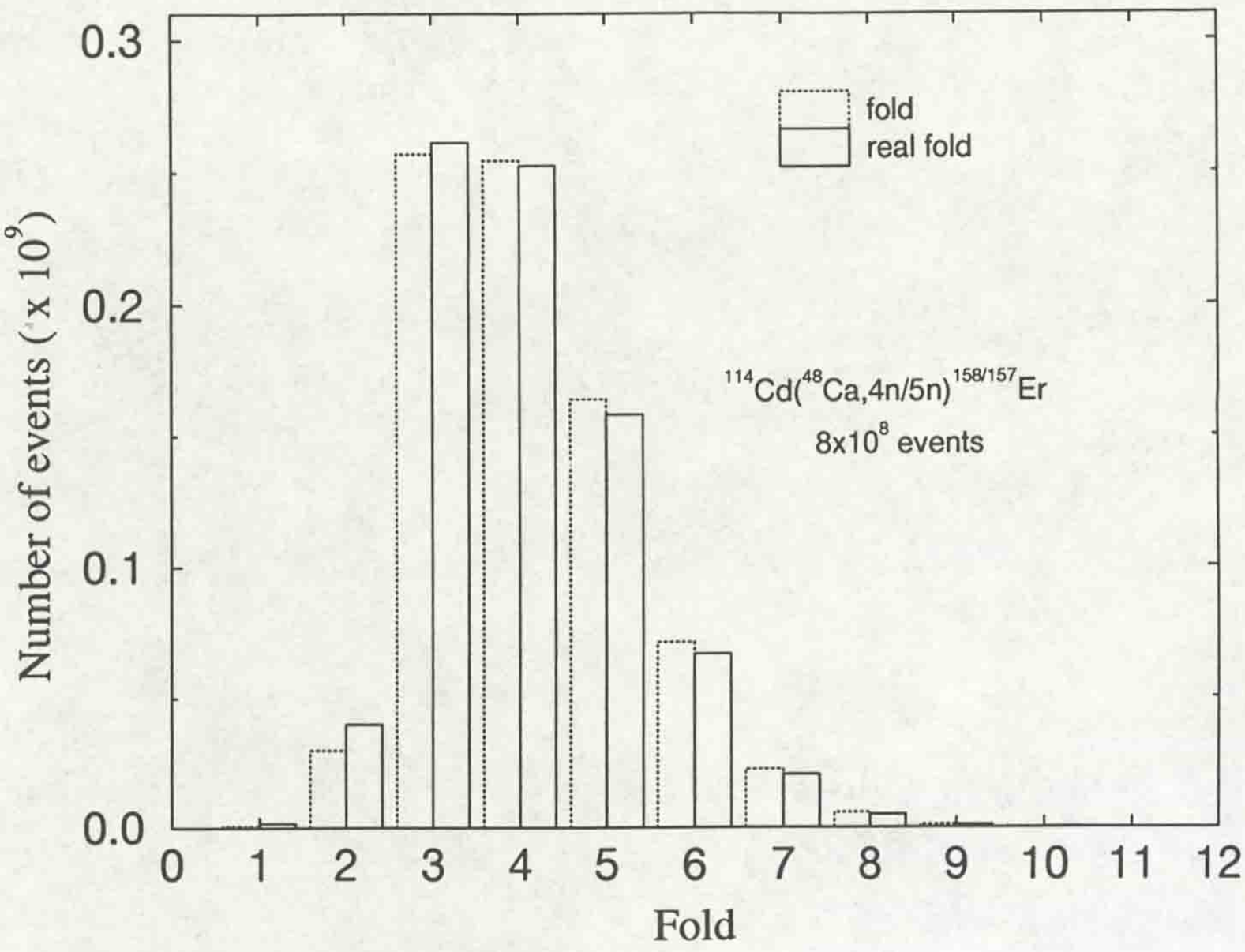

Figure A.1: *Fold distributions of the Er data from* ^{157,158}*Er Eurogam experiment, October 1992*

A.1.2 Data Distributions

Figure A.2 shows the unfolded distributions of the recorded data. The unfolded distributions of double, triples, quadruples, etc., can be explained as follows:

unfolded doubles – all combinations of detected gamma–ray energy, E_γ, pairs in the event

unfolded triples – all combinations of detected E_γ triples in the event

unfolded quadruples – all combinations of detected E_γ quadruples in the event

etc.,

It can be seen from figure A.2, as the fold increases the number of triples (and higher) is greater than the number of doubles, as predicted for such high multiplicity gamma-ray spectrometers such as Eurogam. The results reported in this work show that selectivity has not been lost due to the absence of an inner BGO ball. The BGO ball has previously been used because it "cleans" doubles data by enabling the user to select single reaction channels, this is equivalent to the data acquired from triples analysis (discussed in section 3.2.2.) using Eurogam, but, as can be seen the number

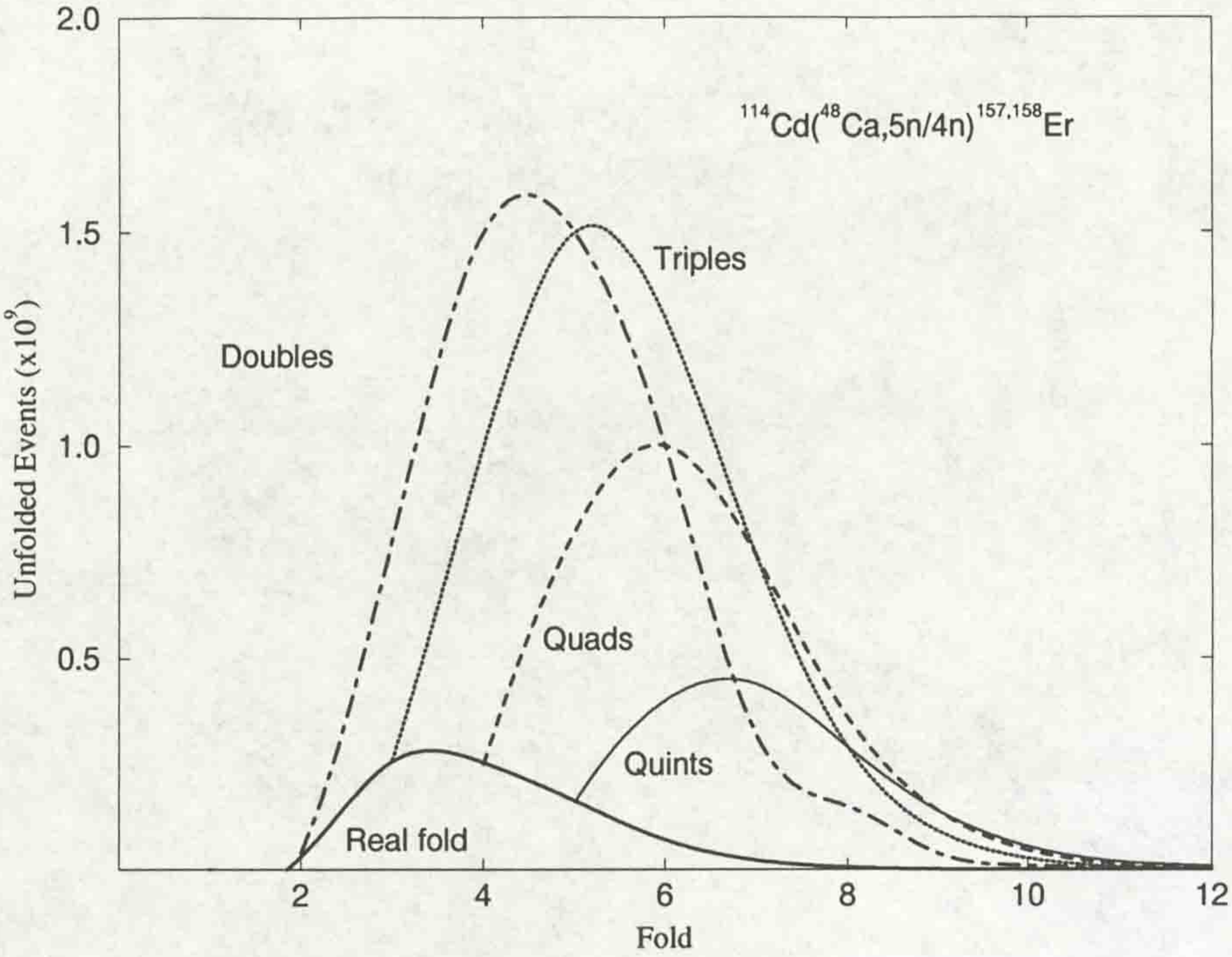

Figure A.2: *Distribution of γ^n events as a function of fold.*

of triples (and higher), data sets are large enough to create clean matrices, ie. single reaction channel data only, with high statistics.

A.2 Matrices

Two dimensional, 4k x 4k (4096 x 4096) channel, symmetric (except for angular correlation matrices, see section A.2.6) matrices are used in this analysis. The calibration used is 0.5 keV per channel, the energy range of the matrices is therefore 0-2.047 MeV.

The matrix itself can be described as a grid, with each element of the matrix corresponding to the number of times a particular combination of 2 gamma-ray energies has been detected.

A method describing how a matrix is incremented follows.

The matrices used in this analysis are essentially two dimensional arrays. A matrix element is a single element in the array and is located by two co-ordinates (x and y).

If an event has two gamma-rays detected by detectors Ge1 and Ge2 with energies $E_{\gamma 1}$ and $E_{\gamma 2}$ respectively, the matrix element ($E_{\gamma 1}$,$E_{\gamma 2}$) is incremented, indicating detection of energies $E_{\gamma 1}$ and $E_{\gamma 2}$ in coincidence. To symmeterise the matrix the element ($E_{\gamma 2}$,$E_{\gamma 1}$) is also incremented. The process described is referred to as "sorting" the

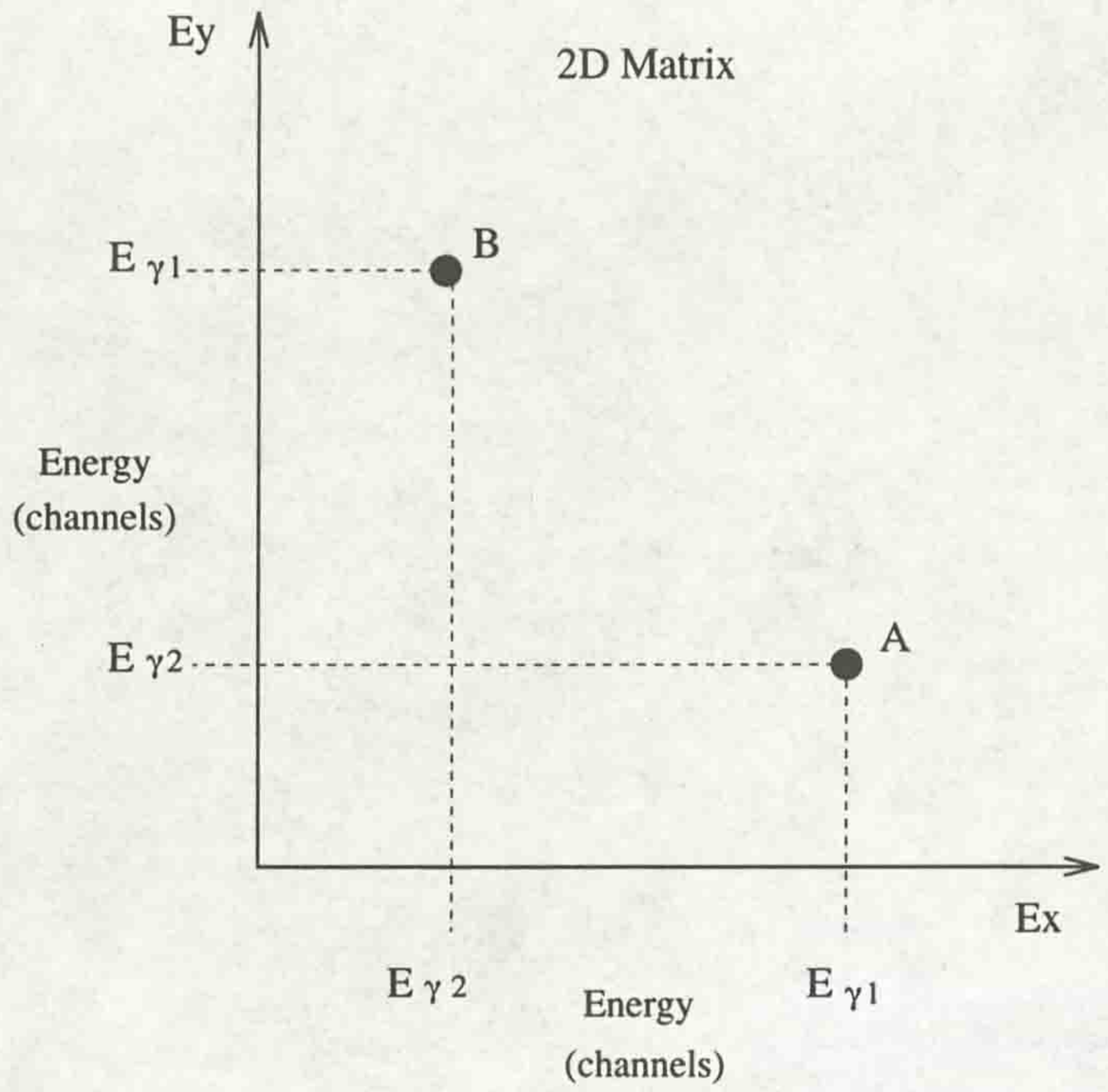

Figure A.3: *diagram illustrating the updating of a two dimensional matrix.*

data, described in figure A.3.

A.2.1 Doubles (γ-γ) Matrices

In the case of doubles matrices, the matrices are incremented using the same method described in the beginning of section A.2 above. Using Eurogam, high fold data is collected, for each event every combination of pairs of γ-ray energies are used to increment the matrix. The maximum fold obtainable in a single event, using the Er data, is 44, as 44 Ge detectors were collecting data for the erbium experiment, this corresponds to a spin of $88\hbar$ and is therefore highly unlikely.

A.2.2 Triples (γ-γ-γ) Matrices

As Eurogam has no inner BGO ball for reaction channel selection, a doubles matrix contains all reaction channels. To reduce the background and select a particular reaction channel or structure of interest, triples matrices are used. This method of creating matrices is based on coincidences between $\gamma-$rays, genuine coincidence events are correlated but the background is not, hence the background is reduced.

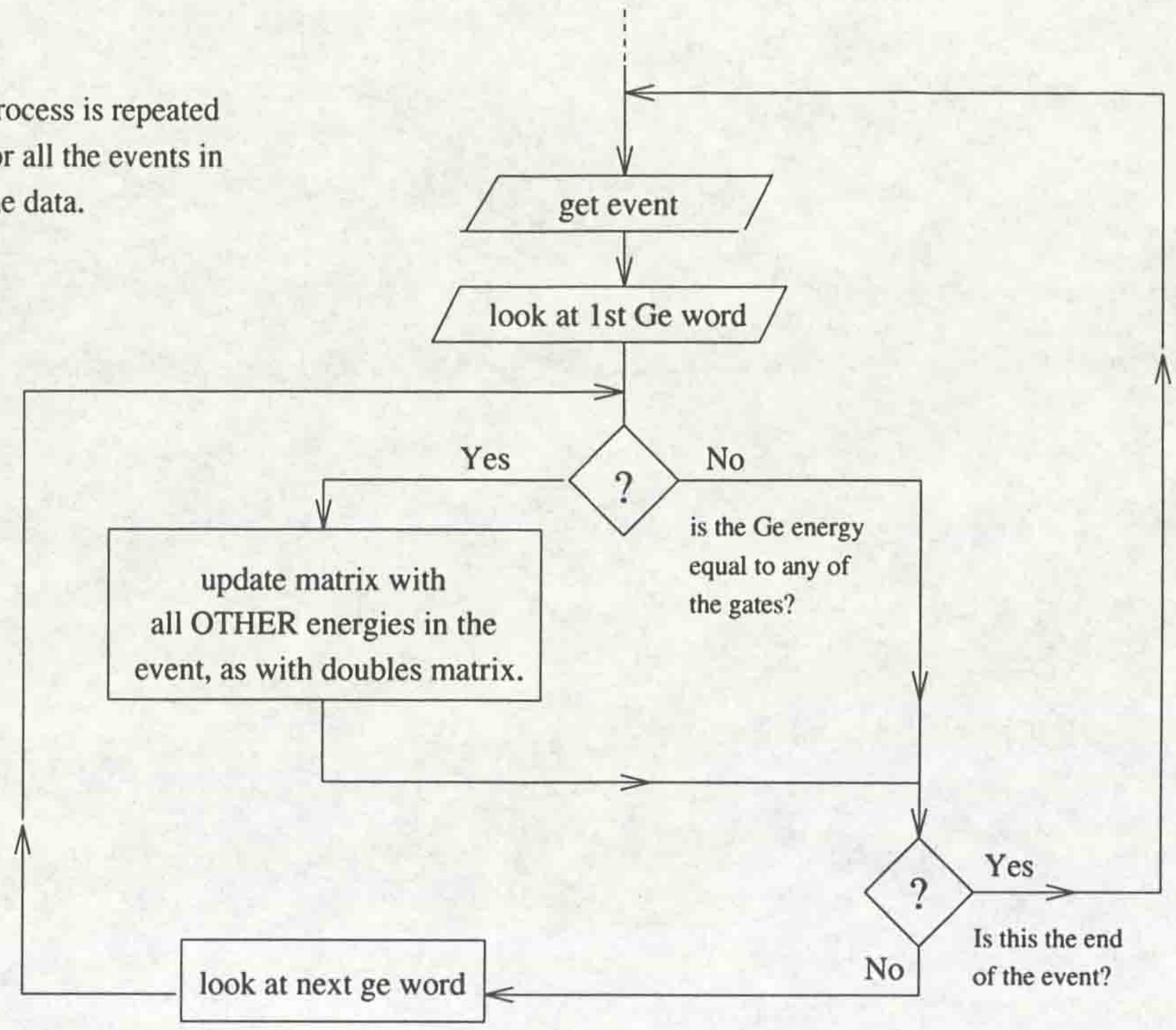

Figure A.4: *Flow diagram describing the sorting process used in a triples matrix.*

To build a triples matrix a constraint is added to the sorting process, if an event contains any of the energies stipulated in a gate file (a list of energies corresponding to the particular reaction channel, or band to be studied) then it will be sorted into the matrix, if such an energy cannot be found, the event is ignored. Therefore the event is only accepted if it is in coincidence with the energies in the gate file. A flow diagram is shown in figure A.4 describing the creation of a single gated $\gamma-\gamma$ (triples) matrix. It can be seen from figure 3.4 that each E_γ can be described as a 'channel selector', ie. if the gating condition is satisfied by the particular E_γ word being looked at, the matrix is updated with the other E_γ's in the event.

A.2.3 Quadruples (γ-γ-γ-γ) Matrices

Triples matrices select reaction channels or a structure of interest reasonably well, in order to reduce the background and enhance high spin transitions even further quadruples (double gated $\gamma-\gamma$) matrices are used. Again, this method exploits the coincidences between $\gamma-$rays, background is reduced further.

As with triples matrices, energy gates are used, but, in the case of quadruples, the event has to contain at least a pair of the energy gates.

Following is a description of the creation of a quadruples matrix. For example, let an event contain Ge energies

$E_{\gamma 1}$, $E_{\gamma 2}$, $E_{\gamma 3}$, $E_{\gamma 4}$, $E_{\gamma 5}$

the matrix is then incremented as follows:

i. take $E_{\gamma 1}$, $E_{\gamma 2}$

ii. if $E_{\gamma 1}$ AND $E_{\gamma 2}$ are gates, increment matrix with the OTHER three energies, as with the doubles matrix

iii. repeat using all combinations of pairs of energies in step i.

Two 'channel selectors' are used when creating a quadruples matrix.

A.2.4 Gating on Matrices

The gating method is also referred to "slicing" or creating a "window". Gating enables coincidence spectra to be produced and hence coincidence analysis to be carried out.

The matrix can be visualised as layers of spectra (each spectrum as wide as a single channel) running in both the y and x direction while a gate is a slice of specified channels of the matrix in either the x or the y direction. An example of a gate made on the x axis of a matrix is shown in figure A.2.4. The gate has width δx, the gate spectrum is a sum of all the spectra from channel x_1 to x_2 (δx channels) in the y plane. This method is used for building level schemes and for general coincidence work, see section 5.1.2.

A.2.5 ESCL8R

To aid in the analysis of data, many packages have been developed. Following is a description of ESCL8R, the package used in this analysis.

ESCL8R is an interactive graphical analysis of γ–γ matrices package, developed by D.C. Radford ([DR93] and [DR92]).

Coincidence data sets (doubles matrices) contain γ–ray energy peaks and background events. The peaks and background can be fitted, the energy and intensity of the peaks are measured. The resulting coincidence information, peak energies and intensities are stored in a database, referred to as a level scheme file. The intensities of the transitions are corrected for internal conversion using the Hager-Seltzer table [HS68].

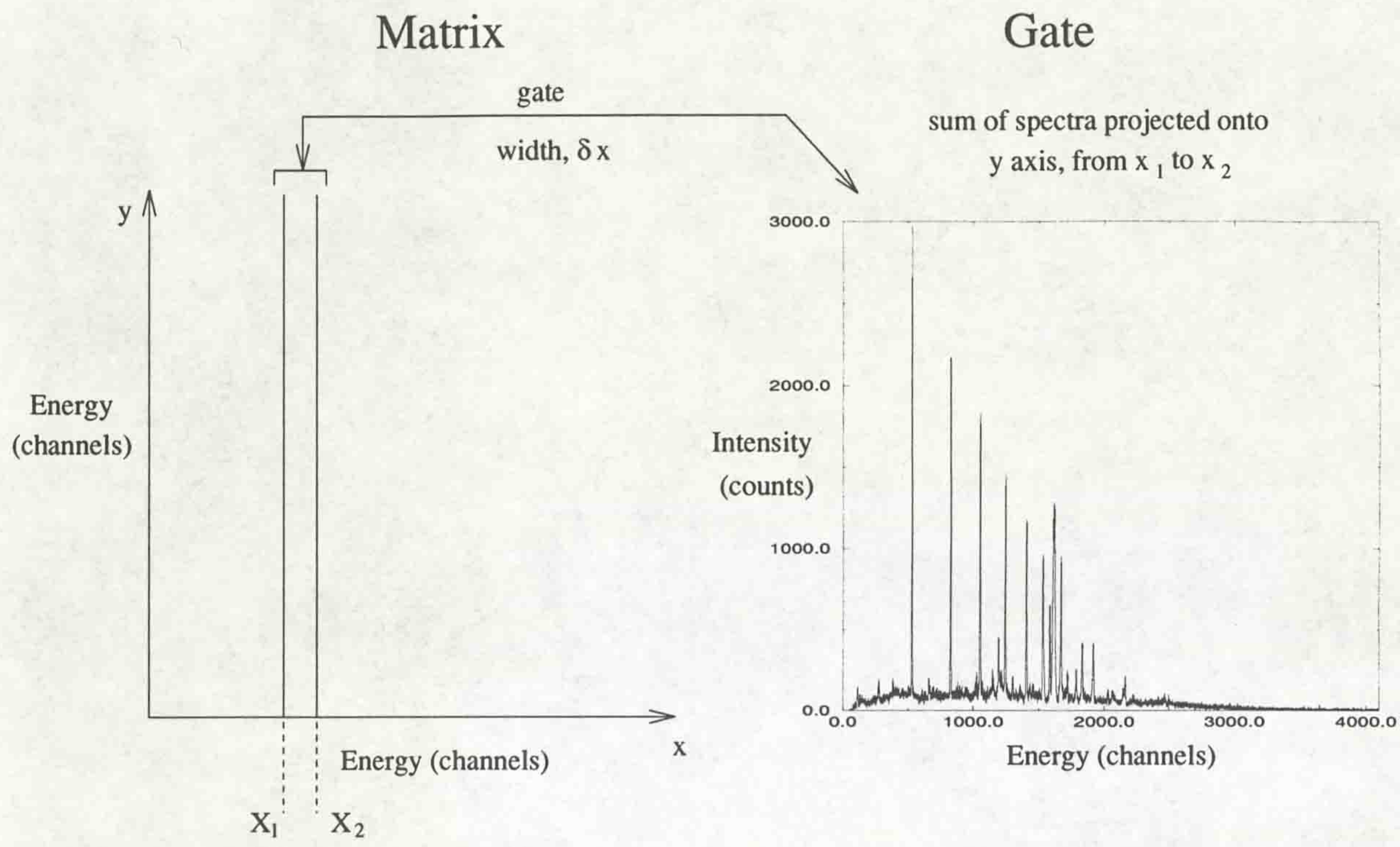

Figure A.5: *Gating on a 2D matrix.*

Background subtraction is carried out using an algorithm similar to the Palameta and Waddington method [PW85]. ESCL8R fits the matrix as a whole, ie. the fits are two dimensional and not dependent on gates set.

A.2.6 Angular Correlation Ratio Measurements

Angular correlation ratios to measure the difference between multipoles, see section 3.2.1. The angular correlation matrices created to measure the ratios are not symmetric.

Ten detectors in the Eurogam array are placed at $\sim 90°$ (5 detectors at 86° and 5 at 94°), and 10 detectors are at 134°. These sets of detectors are to be used in the collection of angular correlation data.

Two methods measuring angular correlation ratios (A.C.R.'s) were used. Following is a description of the A.C.R. measurement techniques.

For the low spin (higher intensity transitions) the traditional method of creating

asymmetric matrices was used. With these matrices each axis holds different information (one axis holds the [90°, 90°] coincidence information and the other the [90°, 134°] coincidence information). The intensity of a particular peak is measured by gating on each axis and then the ratios of these intensities are calculated. The accuracy of this method relies on the equivalence of the widths of the gates and background subtraction of both axes.

The second method was developed because the A.C.R. matrix described above holds data on every reaction channel, therefore the measurement of a high spin transition with very low intensity was incredibly difficult and inaccurate. Due to ESCL8R's excellent background selection and it's removal of known contaminants a method of measuring angular correlations using this package was developed. ESCL8R is designed for symmetric matrices. Two symmetric matrices were created from the A.C.R. data using the same conditions as general A.C.R. matrix creation. One matrix held the [90°, 90°] coincidence data and the other the [90°, 134°] coincidence data. The intensity of a peak is measured in both matrices and the ratios extracted. The ratios were calibrated by measuring transitions of known multipolarity. Where possible these results were then checked by comparison to the ratios measured using a non-symmetric matrix.

Appendix B

Table of Results

B.1 ^{157}Er Table of Results

The table includes, excitation energies E_x, γ-ray energies E_γ, relative intensities I_γ, angular correlation ratios A.C and spin - parity assignments for the transitions in ^{157}Er observed in this work. Transition energies are accurate to ± 0.2 keV for the strong transitions and ± 1.0 keV for the weakest transitions (intensity $\leq 1\%$). Excitation energies are relative to the $\frac{13}{2}^+$ transition in the yrast band. The absolute excitation energy of this state relative to the $\frac{3}{2}^-$ ground state is not known.

Notes For Table

[a] angular correlation ratio for the 803, 809, 806 triplet

[b] total intensity and angular correlation ratio for the 834, 835 doublet

[c] the intensity of the 192.9 keV transition in the strongly coupled band is $\sim 1.3\%$ of the 414.8 keV $\frac{21}{2}^+ \rightarrow \frac{17}{2}^+$ transition in the yrast band.

Band	$E_x(keV)$	E_γ (keV)	$I_\gamma(\%)$	A.C. ratio	$I_f^\pi \rightarrow I_i^\pi$
Yrast	Intensities relative to 414.8 keV transition				
$(+,+\frac{1}{2})$	0	–	–	–	$\frac{13}{2}+$
	266.2	266.2	> 100.0	–	$\frac{17}{2}+ \rightarrow \frac{13}{2}+$
	681.0	414.8	100.0 (0.7)	1.56 (0.02)	$\frac{21}{2}+ \rightarrow \frac{17}{2}+$
	1208.5	527.5	95.0 (0.7)	1.70 (0.02)	$\frac{25}{2}+ \rightarrow \frac{21}{2}+$
	1831.3	622.8	90.0 (0.7)	1.81 (0.02)	$\frac{29}{2}+ \rightarrow \frac{25}{2}+$
	2534.5	703.2	74.2 (0.6)	1.79 (0.03)	$\frac{33}{2}+ \rightarrow \frac{29}{2}+$
	3300.7	766.2	61.1 (0.7)	1.85 (0.04)	$\frac{37}{2}+ \rightarrow \frac{33}{2}+$
	4104.0	[a]803.3	53.2 (1.4)	1.75 (0.26)	$\frac{41}{2}+ \rightarrow \frac{37}{2}+$
	4913.0	[a]809.0	33.0 (5.3)	1.75 (0.26)	$\frac{45}{2}+ \rightarrow \frac{41}{2}+$
	5719.1	[a]806.1	33.3 (4.7)	1.75 (0.26)	$\frac{49}{2}+ \rightarrow \frac{45}{2}+$
	6511.0	791.9	37.17 (1.4)	1.4 (0.05)	$\frac{53}{2}+ \rightarrow \frac{49}{2}+$
	7345.9	[b]833.9	37.3 (1.0)	1.37 (0.06)	$\frac{57}{2}+ \rightarrow \frac{53}{2}+$
	8261.9	915.1	17.8 (0.5)	1.58 (0.07)	$\frac{61}{2}+ \rightarrow \frac{57}{2}+$
	9218.8	957.8	15.6 (0.6)	1.69 (0.09)	$\frac{65}{2}+ \rightarrow \frac{61}{2}+$
	10053.8	[b]834.8	37.3 (1.0)	1.37 (0.06)	$\frac{69}{2}+ \rightarrow \frac{65}{2}+$
	11133.7	1079.9	7.4 (0.6)	1.58 (0.33)	$\frac{73}{2}+ \rightarrow \frac{69}{2}+$
	11165.1	1111.3	1.8 (0.1)	–	$(\frac{73}{2})^+ \rightarrow \frac{69}{2}+$
	11991.8	858.1	6.2 (0.6)	–	$\frac{77}{2}+ \rightarrow \frac{73}{2}+$
	12884.4	892.6	4.5 (1.0)	1.33 (0.09)	$\frac{81}{2}+ \rightarrow \frac{77}{2}+$
	14118.2	1233.8	2.3 (0.2)	1.97 (0.23)	$\frac{85}{2}+ \rightarrow \frac{81}{2}+$
	13021.4	1029.6	1.3 (0.1)	–	$(\frac{81}{2})^+ \rightarrow \frac{77}{2}+$
$(+,-\frac{1}{2})$	10652.2	598.4	6.69 (0.31)	0.29 (0.02)	$\frac{71}{2}(+) \rightarrow \frac{69}{2}+$
	11543.4	891.2	2.8 (0.9)	0.48 (0.15)	$\frac{73}{2}(+) \rightarrow \frac{71}{2}(+)$
	11724.6	1072.4	1.9 (0.1)	1.56 (0.25)	$\frac{75}{2}(+) \rightarrow \frac{71}{2}(+)$
	12764.0	1039.4	1.3 (0.1)	–	$(\frac{79}{2})^+ \rightarrow \frac{75}{2}(+)$

Band	$E_x(keV)$	E_γ (keV)	$I_\gamma(\%)$	A.C. ratio	$I_f^\pi \rightarrow I_i^\pi$
Band 1	Intensities relative to 478.6 keV transition				
$(-,+\frac{1}{2})$	358.4	–	–	–	$\frac{9}{2}^-$
	515.2	156.8	> 2.1	–	$\frac{13}{2}^- \rightarrow \frac{9}{2}^-$
	893.9	378.7	2.1 (0.5)	1.15 (0.12)	$\frac{17}{2}^- \rightarrow \frac{13}{2}^-$
	1487.1	593.2	1.3 (0.3)	1.53 (0.10)	$\frac{21}{2}^- \rightarrow \frac{17}{2}^-$
	1924.4	437.3	1.0 (0.3)	1.16 (0.14)	$\frac{25}{2}^- \rightarrow \frac{21}{2}^-$
	1924.4	362.6	19.8 (0.1)	0.66 (0.02)	$\frac{25}{2}^- \rightarrow \frac{23}{2}^+$
	1924.4	714.4	33.3 (1.2)	1.22 (0.05)	$\frac{25}{2}^- \rightarrow \frac{25}{2}^+$
	1924.4	404.7	18.8 (0.3)	0.69 (0.06)	$\frac{25}{2}^- \rightarrow \frac{23}{2}^-$
	1519.7	837.9	–	–	$\frac{23}{2}^- \rightarrow \frac{21}{2}^-$
	1519.7	617.0	3.1 (0.7)	1.49 (0.18)	$\frac{23}{2}^- \rightarrow \frac{19}{2}^-$
	1519.7	490.0	5.2 (1.1)	1.49 (0.17)	$\frac{23}{2}^- \rightarrow \frac{19}{2}^-$
	1029.4	763.2	–	0.39 (0.16)	$\frac{19}{2}^- \rightarrow \frac{17}{2}^+$
	2403.0	478.6	100.0 (1.9)	1.80 (0.04)	$\frac{29}{2}^- \rightarrow \frac{25}{2}^-$
	2403.0	231.9	7.3 (0.3)	0.56 (0.02)	$\frac{29}{2}^- \rightarrow \frac{27}{2}^+$
	2403.0	570.9	36.5 (0.9)	1.20 (0.04)	$\frac{29}{2}^- \rightarrow \frac{29}{2}^+$
	2917.1	514.1	150.00 (2.54)	1.71 (0.03)	$\frac{33}{2}^- \rightarrow \frac{29}{2}^-$
	2917.1	252.9	11.5 (0.4)	0.69 (0.03)	$\frac{33}{2}^- \rightarrow \frac{31}{2}^-$
	2917.1	381.6	2.1 (0.4)	1.66 (0.13)	$\frac{33}{2}^- \rightarrow \frac{33}{2}^+$
	3491.9	574.8	145.8 (2.4)	1.70 (0.03)	$\frac{37}{2}^- \rightarrow \frac{33}{2}^-$
	3491.9	290.4	8.3 (0.4)	0.71 (0.03)	$\frac{37}{2}^- \rightarrow \frac{35}{2}^-$
	4143.5	651.6	169.8 (2.7)	1.74 (0.02)	$\frac{41}{2}^- \rightarrow \frac{37}{2}^-$
	4143.5	313.1	5.2 (0.4)	0.49 (0.03)	$\frac{41}{2}^- \rightarrow \frac{39}{2}^-$
	4871.3	727.8	142.7 (2.4)	1.40 (0.06)	$\frac{45}{2}^- \rightarrow \frac{41}{2}^-$
	4871.3	325.3	9.4 (0.4)	–	$\frac{45}{2}^- \rightarrow \frac{43}{2}^-$
	5672.7	801.4	133.3 (2.9)	1.77 (0.07)	$\frac{49}{2}^- \rightarrow \frac{45}{2}^-$
	6502.6	829.9	110.4 (2.5)	1.62 (0.05)	$\frac{53}{2}^- \rightarrow \frac{49}{2}^-$
	7305.8	803.2	87.5 (2.3)	1.64 (0.06)	$\frac{57}{2}^- \rightarrow \frac{53}{2}^-$
	8097.8	792.0	87.5 (1.9)	1.51 (0.04)	$\frac{61}{2}^- \rightarrow \frac{57}{2}^-$
	8974.2	876.4	69.8 (1.5)	1.46 (0.04)	$\frac{65}{2}^- \rightarrow \frac{61}{2}^-$
	9926.7	952.5	61.5 (1.3)	1.76 (0.05)	$\frac{69}{2}^- \rightarrow \frac{65}{2}^-$
	10867.3	940.6	36.36 (1.54)	1.54 (0.09)	$\frac{73}{2}^- \rightarrow \frac{69}{2}^-$
	11631.5	764.2	–	–	$\frac{77}{2}^- \rightarrow \frac{73}{2}^-$
	10909.1	982.4	29.5 (1.4)	1.66 (0.11)	$\frac{73}{2}^- \rightarrow \frac{69}{2}^-$

Band	$E_x(keV)$	E_γ (keV)	$I_\gamma(\%)$	A.C. ratio	$I_f^\pi \rightarrow I_i^\pi$
Band 1	Intensities relative to 478.6 keV transition				
$(-,+\frac{1}{2})$	10909.1	982.4	29.5 (1.4)	1.66 (0.11)	$\frac{73}{2}^- \rightarrow \frac{69}{2}^-$
	12036.6	1127	–	–	$(\frac{77}{2})^- \rightarrow \frac{73}{2}^-$
	11631.6	722.9	15.2 (1.0)	1.12 (0.06)	$\frac{77}{2}^- \rightarrow \frac{73}{2}^-$
	11631.6	316.8	2.4(0.4)	–	$\frac{77}{2}^- \rightarrow \frac{75}{2}^-$
	12947.1	1315.5	21.9 (1.2)	1.61 (0.20)	$\frac{81}{2}^- \rightarrow \frac{77}{2}^-$
	13868.1	921.0	25.7 (1.2)	1.60 (0.10)	$\frac{85}{2}^- \rightarrow \frac{81}{2}^-$
	14682.7	814.6	4.9 (0.5)	1.80 (0.15)	$\frac{89}{2}^- \rightarrow \frac{85}{2}^-$

Band	$E_x(keV)$	E_γ (keV)	$I_\gamma(\%)$	A.C. ratio	$I_f^\pi \rightarrow I_i^\pi$
Band 2	Intensities relative to 716.1 keV transition				
$(-,-\frac{1}{2})$	2663.8	833.4	29.51 (2.21)	0.68 (0.13)	$\frac{31}{2}^- \rightarrow \frac{29}{2}^+$
	3200.5	536.9	41.8 (1.3)	1.20 (0.05)	$\frac{35}{2}^- \rightarrow \frac{31}{2}^-$
	3200.5	665.3	51.0 (1.6)	0.56 (0.02)	$\frac{35}{2}^- \rightarrow \frac{33}{2}^+$
	3830.7	630.2	97.2 (1.3)	1.73 (0.05)	$\frac{39}{2}^- \rightarrow \frac{35}{2}^-$
	3830.7	530.3	37.8 (1.3)	0.24 (0.05)	$\frac{39}{2}^- \rightarrow \frac{37}{2}^+$
	4546.8	716.1	100.0 (2.6)	1.68 (0.04)	$\frac{43}{2}^- \rightarrow \frac{39}{2}^-$
	4546.8	441.8	–	–	$\frac{43}{2}^- \rightarrow \frac{41}{2}^+$
	5345.1	798.3	96.5 (2.6)	1.35 (0.05)	$\frac{47}{2}^- \rightarrow \frac{43}{2}^-$
	5345.1	474.4	16.7 (0.8)	–	$\frac{47}{2}^- \rightarrow \frac{45}{2}^-$
	6173.0	827.9	108.5 (2.9)	1.12 (0.05)	$\frac{51}{2}^- \rightarrow \frac{47}{2}^-$
	7011.8	838.8	88.4 (2.2)	1.09 (0.03)	$\frac{55}{2}^- \rightarrow \frac{51}{2}^-$
	7821.4	809.6	70.8 (2.4)	1.43 (0.09)	$\frac{59}{2}^- \rightarrow \frac{55}{2}^-$
	8611.6	790.2	68.7 (1.9)	1.91 (0.11))	$\frac{63}{2}^- \rightarrow \frac{59}{2}^-$
	9479.4	867.8	63.6 (1.2)	1.42 (0.04)	$\frac{67}{2}^- \rightarrow \frac{63}{2}^-$
	10374.3	894.9	58.4 (1.7)	1.36 (0.06)	$\frac{71}{2}^- \rightarrow \frac{67}{2}^-$
	11313.7	939.4	37.4 (1.5)	1.25 (0.08)	$\frac{75}{2}^- \rightarrow \frac{71}{2}^-$
	12300.1	671.2	21.0 (1.0)	0.69 (0.03)	$\frac{79}{2}^- \rightarrow \frac{77}{2}^-$
	12300.1	986.4	25.3 (1.4)	1.65 (0.15)	$\frac{79}{2}^- \rightarrow \frac{75}{2}^-$
	13226.0	278.7	3.9 (0.4)	–	$\frac{83}{2}^- \rightarrow \frac{81}{2}^-$
	13226.0	925.9	46.7 (1.6)	1.26 (0.07)	$\frac{83}{2}^- \rightarrow \frac{79}{2}^-$
	13875.9	649.9	32.6 (1.7)	1.74 (0.10)	$\frac{87}{2}^- \rightarrow \frac{83}{2}^-$

Band	$E_x(keV)$	E_γ (keV)	$I_\gamma(\%)$	A.C. ratio	$I_f^\pi \rightarrow I_i^\pi$
Band3	Intensities relative to 478.6 keV transition (band1)				
	1030.3	763.2	9.5 (5.8)	0.43 (0.14)	$\frac{19}{2}+ \rightarrow \frac{17}{2}+$
	1561.6	531.1	21.5 (5.8)	1.17 (0.08)	$\frac{23}{2}+ \rightarrow \frac{19}{2}+$
	1561.6	881.7	32.2 (1.5)	0.72 (0.04)	$\frac{23}{2}+ \rightarrow \frac{21}{2}+$
	2171.3	962.4	16.3 (1.3)	0.84 (0.09)	$\frac{27}{2}+ \rightarrow \frac{23}{2}+$
	2171.3	612.7	34.7 (1.4)	1.28 (0.05)	$\frac{27}{2}+ \rightarrow \frac{23}{2}+$

Band	$E_x(keV)$	E_γ (keV)	$I_\gamma(\%)$	A.C. ratio	$I_f^\pi \rightarrow I_i^\pi$
Band 4	Intensities relative to 678.4 keV transition				
	1306.0	1041.0	6.3 (1.3)	0.42 (0.42)	$(\frac{19}{2}) \rightarrow \frac{17}{2}+$
	1728.7	422.7	16.5 (1.7)	1.57 (0.15)	$(\frac{23}{2}) \rightarrow (\frac{19}{2})$
	1728.7	1048.3	29.6 (4.0)	0.64 (0.12)	$(\frac{23}{2}) \rightarrow \frac{21}{2}+$
	2244.2	515.5	60.7 (2.9)	1.35 (0.16)	$(\frac{27}{2}) \rightarrow (\frac{23}{2})$
	2244.2	1035.7	65.2 (4.7)	–	$(\frac{27}{2}) \rightarrow \frac{25}{2}+$
	2846.8	602.6	107.8 (3.0)	–	$(\frac{31}{2}) \rightarrow (\frac{27}{2})$
	2846.8	1015.5	–	–	$(\frac{31}{2}) \rightarrow \frac{29}{2}+$
	3525.2	678.4	100.0 (4.2)	1.72 (0.08)	$(\frac{35}{2}) \rightarrow (\frac{31}{2})$
	3525.2	990.6	–	–	$(\frac{35}{2}) \rightarrow \frac{33}{2}^+$
	4263.1	737.9	78.7 (4.2)	1.41 (0.09)	$(\frac{39}{2}) \rightarrow (\frac{35}{2})$
	5013.7	750.6	56.9 (3.6)	1.48 (0.36)	$(\frac{43}{2}) \rightarrow (\frac{39}{2})$
	5796.9	783.2	55.7 (5.7)	1.82 (0.13)	$(\frac{47}{2}) \rightarrow (\frac{43}{2})$
	6654.1	857.2	53.5 (4.5)	1.75 (0.19)	$(\frac{51}{2}) \rightarrow (\frac{47}{2})$
	7577.7	923.6	49.0 (3.5)	1.43 (0.21)	$(\frac{55}{2}) \rightarrow (\frac{51}{2})$
	8548.1	970.4	20.0 (2.6)	1.22 (0.25)	$(\frac{59}{2}) \rightarrow (\frac{55}{2})$

Band	E_x (keV)	E_γ (keV)	I_γ(%)	A.C. ratio	$I_f^\pi \rightarrow I_i^\pi$
SC Band	Intensities relative to 192.9 keV[c] transition				
	2395.7	1714.7	–	–	$(\frac{23}{2}^-) \rightarrow \frac{21}{2}^+$
	2500.5	104.8	–	–	$(\frac{25}{2}^-) \rightarrow (\frac{23}{2}^-)$
	2649.4	1440.9	–	–	$(\frac{27}{2}^-) \rightarrow \frac{25}{2}^+$
	2649.4	254.1	–	–	$(\frac{27}{2}^-) \rightarrow (\frac{23}{2}^-)$
	2842.3	342.2	12(2)	–	$(\frac{29}{2}^-) \rightarrow (\frac{25}{2}^-)$
	2842.3	192.9	100(2)	–	$(\frac{29}{2}^-) \rightarrow (\frac{27}{2}^-)$
	3067.7	1236.4	–	–	$(\frac{31}{2}^-) \rightarrow \frac{29}{2}^-$
	3067.7	418.3	–	–	$(\frac{31}{2}^-) \rightarrow (\frac{27}{2}^-)$
	3067.7	225.4	94(3)	–	$(\frac{31}{2}^-) \rightarrow (\frac{29}{2}^-)$
	3328.9	486.7	17(2)	–	$(\frac{33}{2}^-) \rightarrow (\frac{29}{2}^-)$
	3328.9	261.2	79(3)	–	$(\frac{33}{2}^-) \rightarrow (\frac{31}{2}^-)$
	3614.2	544.9	29(3)	–	$(\frac{35}{2}^-) \rightarrow (\frac{31}{2}^-)$
	3614.2	285.3	74(3)	–	$(\frac{35}{2}^-) \rightarrow (\frac{33}{2}^-)$
	3922.1	593.2	31(3)	–	$(\frac{37}{2}^-) \rightarrow (\frac{33}{2}^-)$
	3922.1	307.9	62(3)	–	$(\frac{37}{2}^-) \rightarrow (\frac{35}{2}^-)$
	4254.1	639.9	27(3)	–	$(\frac{39}{2}^-) \rightarrow (\frac{35}{2}^-)$
	4254.1	332.0	47(3)	–	$(\frac{39}{2}^-) \rightarrow (\frac{37}{2}^-)$
	4602.0	679.9	17(2)	–	$(\frac{41}{2}^-) \rightarrow (\frac{37}{2}^-)$
	4602.0	347.9	39(2)	–	$(\frac{41}{2}^-) \rightarrow (\frac{39}{2}^-)$
	4972.2	717.8	17(2)	–	$(\frac{43}{2}^-) \rightarrow (\frac{39}{2}^-)$
	4972.2	370.4	19(1)	–	$(\frac{43}{2}^-) \rightarrow (\frac{41}{2}^-)$
	5350.6	748.6	13(2)	–	$(\frac{45}{2}^-) \rightarrow (\frac{41}{2}^-)$
	5350.6	378.1	15(1)	–	$(\frac{45}{2}^-) \rightarrow (\frac{43}{2}^-)$
	5752.5	780.9	11(2)	–	$(\frac{47}{2}^-) \rightarrow (\frac{43}{2}^-)$
	5752.5	401.9	9(1)	–	$(\frac{47}{2}^-) \rightarrow (\frac{45}{2}^-)$
	6158.4	807.8	–	–	$(\frac{49}{2}^-) \rightarrow (\frac{45}{2}^-)$
	6158.4	405.9	–	–	$(\frac{49}{2}^-) \rightarrow (\frac{47}{2}^-)$
	6581.8	829.0	–	–	$(\frac{51}{2}^-) \rightarrow (\frac{47}{2}^-)$
	6581.8	423.2	–	–	$(\frac{51}{2}^-) \rightarrow (\frac{49}{2}^-)$
	7006.5	848.0	–	–	$(\frac{53}{2}^-) \rightarrow (\frac{49}{2}^-)$

B.2 ^{158}Er Table of Results

The table includes γ-ray energies E_γ, angular correlation ratios A.C and spin - parity assignments for the transitions in ^{158}Er.

Notes for Table

[d] angular correlation ratio for the 1010, 1011 doublet.

Band	E_x (keV)	E_γ (keV)	A.C. ratio	$I_f^\pi \rightarrow I_i^\pi$
(+,0)	9011	875	1.94 (0.02)	$30^+ \rightarrow 28^+$
	9917	906	1.90 (0.03)	$32^+ \rightarrow 30^+$
	10876	959	1.99 (0.03)	$34^+ \rightarrow 32^+$
	11893	1017	1.89 (0.04)	$36^+ \rightarrow 34^+$
	12951	1058	1.74 (0.03)	$38^+ \rightarrow 36^+$
	13778	827	2.19 (0.07)	$40^+ \rightarrow 38^+$
	15059	1281	1.86 (0.06)	$42^+ \rightarrow 40^+$
	16090	1031	2.36 (0.09)	$44^+ \rightarrow 42^+$
	17061	971	-	$46^+ \rightarrow 44^+$
	9474	1338	1.74 (0.06)	$30_2^+ \rightarrow 28_2^+$
	10281	807	-	$32_2^+ \rightarrow 30_2^+$
	10281	1270	1.79 (0.07)	$32_2^+ \rightarrow 30_2^+$
	11216	935	1.99 (0.15)	$32_2^+ \rightarrow 30^+$
	11216	1299	1.66 (0.07)	$34_2^+ \rightarrow 32^+$
	12232	1016	-	$36_2^+ \rightarrow 34_2^+$
	12232	1356	1.96 (0.07)	$36_2^+ \rightarrow 34^+$
	13169	937	-	$38_2^+ \rightarrow 36_2^+$
	13169	1276	1.28 (0.06)	$38_2^+ \rightarrow 36^+$
	13778	609	-	$40^+ \rightarrow 38_2^+$
	14153	1202	1.02 (0.07)	$40_2^+ \rightarrow 38^+$
	15363	1210	1.71 (0.10)	$42_2^+ \rightarrow 40_2^+$
	16507	1143	1.87 (0.10)	$44_2^+ \rightarrow 42_2^+$
	17659	1153	2.12 (0.18)	$46_2^+ \rightarrow 44_2^+$
	18869	1210	1.44 (0.47)	$48_2^+ \rightarrow 46_2^+$
	20143	1274	-	$50_2^+ \rightarrow 48_2^+$

Band	E_x (keV)	E_γ (keV)	A.C. ratio	$I_f^\pi \rightarrow I_i^\pi$
(−,0)	9456	854	-	$30^- \rightarrow 28^-$
	10336	880	1.53 (0.05)	$32^- \rightarrow 30^-$
	11234	898	1.52 (0.06)	$34^- \rightarrow 32^-$
	12172	939	-	$36^- \rightarrow 34^-$
	13157	985	2.00 (0.8)	$38^- \rightarrow 36^-$
	14186	1026	2.15 (0.10)	$40^- \rightarrow 38^-$
	15194	^{d}1011	1.36 (0.21)	$42^- \rightarrow 40^-$
	16357	1163	2.71 (0.21)	$44^- \rightarrow 42^-$
	17367	^{d}1010	1.36 (0.21)	$46^- \rightarrow 44^-$
	18131	764	2.35 (0.13)	$48^- \rightarrow 46^-$
(−,1)	9821	886	1.73 (0.08)	$31^- \rightarrow 29^-$
	10718	897	1.90 (0.5)	$33^- \rightarrow 31^-$
	11638	920	2.41 (0.08)	$35^- \rightarrow 33^-$
	12602	964	2.11 (0.08)	$37^- \rightarrow 35^-$
	13623	1021	2.01 (0.10)	$39^- \rightarrow 37^-$
	14697	1073	2.37 (0.12)	$41^- \rightarrow 39^-$
	15683	985	2.35 (0.23)	$43^- \rightarrow 41^-$
	17013	1330	2.05 (0.14)	$45^- \rightarrow 43^-$
	17013	1139	2.74 (0.41)	$45^- \rightarrow 43_2^-$
	18001	988	-	$47^- \rightarrow 45^-$
	18001	939	0.093 (0.07)	$47^- \rightarrow 46^+$
	18810	809	-	$49^- \rightarrow 47^-$
	15873	1176	2.74 (0.23)	$43_2^- \rightarrow 41^-$
	17121	1248	2.94 (0.29)	$45_2^- \rightarrow 43_2^-$
	17121	1439	2.12 (0.19)	$45_2^- \rightarrow 43^-$
	18345	1224	-	$47_2^- \rightarrow 45_2^-$

References

[AL84] A.J. Larabee, Phys. Rev. C29(1984).

[AG74] A.L. Goodman, Nucl. Phys. A230(1974)466.

[BF79a] R. Bengtsson and S. Frauendorf, Nucl. Phys. A314(1979)27.

[BF79b] R. Bengtsson and S. Frauendorf, Nucl. Phys. A327(1979)139.

[BF86] R. Bengtsson ans S. Frauendorf, Atomic and Nuclear Data Tables, 35(1986)15.

[BMV1] A. Bohr and B.R. Mottelson, "Nuclear Structure" Volume I(1969) W.A. Benjamin Inc.

[BMV2] A. Bohr and B.R. Mottelson, "Nuclear Structure" Volume II(1975) W.A. Benjamin Inc.

[BR85] T. Bengtsson and I. Ragnarsson, Nucl. Phys. A436(1985)14.

[BW91] J.M. Blatt and Weisskopf, "Theoretical Nuclear Physics" (1991) Dover Publications Inc. N.Y.

[CB88] C.R. Bingham etal., J. Phys. G14(1988)L77.

[CB92] C.W. Beausang et al, Meas. Nucl. Instrum. Meth. A313(1992)37.

[CT90] B. Castel and I.S. Towner"Modern Theories of Nuclear Magnetic Moments" (1990) Oxford University Press.

[DR92] D.C. Radford et al., Nucl. Phys. A545(1992)665.

[DR93] D.C. Radford 1993 *in Proceedings of the International Seminar on The Frontier of Nuclear Spectroscopy, October, 1992, Kyoto*, edited by Yoshizawa Y, Kusakari H and Otsuka T (World Scientific, 1993, Singapore) p.229

[EG73] E. Grosse etal., Phys. Rev. Lett. 31(1973)841.

[EG90] General Eurogam Proposal, edited by Eurogam P.S.C. (1990).

[EM74] E.Der Mateosian, At. Data and Nucl. Data Tab. 13(1974)391.

[EP91] E.S. Paul et al., J. Phys. G17(1991)605.

[EP93] E.S. Paul et al., J. Phys. G19(1993)913.

[EP94] E.S. Paul et al., J. Phys. G20(1994)751.

[FB87] F.A. Beck et al., Phys. Letts. B192(1987)49.

[FD82] F.Dönau and S.Frauendorf, Proc. Conf. on High Angular Momentum Properties of Nuclei, Oak Ridge (1982)143 N.Y. Harwood.

[FD87] F.Dönau Nucl. Phys. A471(1987)469.

[FH93] F. Hanna, Ph.D. Thesis, University of Liverpool (1993) unpublished.

[FS72] F.S. Stephens et al., Phys. Rev. Lett. 54(1985)2584.

[FS85] F.S. Stephens et al., Nucl. Phys. A183(1972)257.

[GFK2] G.F. Knoll, "Radiation Detection and Measurement", 2nd edition, Wiley.

[GM58] Galagher and Moskowski, Phys. Rev. 111(1958) 1282.

[GM92] G.M. McPherson et al., IEEE Trans. on Nucl. Sci. 39(1992)886.

[HH88] H. Hübel et al., Z. Phys A329(1988)289.

[HS68] R.S. Hager and E.C.Seltzer, Nucl. Data Tables, A4 (1968) 476.

[HT92] H. Timmers, Diplomarbeit in Physik, Liverpool University,1992.

[IL92] I. Lazarus et al., IEEE Trans. on Nucl. Sci. 39(1992)1352.

[IR86] I. Ragnarsson et al, Phys. Scr. 34(1986)651.

[IR94] I. Rgnarsson, private communication (1994).

[JA92] J. Alexander et al., IEEE Trans. on Nucl. Sci. 39(1992)886.

[JC82] J.M. Cassels, "Basic Quantum Mechanics", second edition, Macmillan Press (1982).

[JC91] J.R. Cresswell, Eurogam Document, EDOC073 (1991).

[JGSS] J. Garrett summer school, "Frontiers in Nuclear Dynamics" Dronten, The Netherlands (1985).

[JL82] J.S. Lilley, Phys.Scr.25(1982)435.

[JM89] J.D. Morrison et al., J. Phys G. 15(1989)1871.

[JS82] J. Simpson, Ph.D. Thesis, University of Liverpool (1982) unpublished.

[JS84] J. Simpson et al., Phys. Rev. Lett. 53(1984)648.

[JS87] J.Simpson et. al., J. Phys. G. 13(1987)847.

[JS89] J. Simpson et al., J. Phys. G. 15(1989)643.

[JS92] J. Simpson et al., J. Phys. G. 18(1992)1207.

[JS93] J.Simpson, private communication (1993).

[JS94] J. Simpson et al., Phys. Lett. B327(1994)187.

[JSS88] J.F. Sharpey-Schafer and J.Simpson, "Progress in Particle and Nuclear Physics" Vol.21(1988)293.

[KK73] K.S. Krane et al.,Nucl. Data Tab. 11(1973)351.

[KK87] K.S. Krane, "Introductory Nuclear Physics", (1987) Wiley.

[LF59] L.W. Fagg et al., Rev. Mod. Phys. 38(1967)306.

[LR80] L.L. Riedinger et al., Phys. Rev. Letts. 44(1980)568.

[LS78] C.M. Lederer & V.S.Shirley "Table of Isotopes" VII edition, John Wiley & sons(1978).

[MR84a] M.A. Riley, PhD Thesis University of Liverpool(1984).

[MR84b] M.A. Riley, Phys. Letts. 135B(1984)275.

[MR86a] M.A. Riley et al., Phys. Letts. 177B(1986)15.

[MR86b] M.A. Riley et al., Nucl. Phys. A486(1986)456.

[MR88] M.A. Riley et al., Nucl. Phys. A486(1988)456.

[MR94a] M.A. Riley private communication (1994).

[MR94b] M.A. Riley, "High K Structures in Light Erbium Isotopes", to be published.

[PG72] P.W. Green et al., Nucl. Instrum. Meth. 103(1972)109.

[PJ94] P.M. Jones, submitted to Nucl. Instrum. Meth (1994).

[PM84] P.V.E.McClintock et al., "Matter at Low Temperatures" (1984) Blackie and Son Ltd.

[PN82] P.J. Nolan et al. Nucl .Instrum. Meth. 201,433(1982).

[PN90] P.J. Nolan, Nucl. Phys. A520(1990)657c.

[PS79] P.J. Nolan and J.F. Sharpey-Schafer, Rep. Prog. Phys. 42(1979)1.

[PS92a] P.B. Semmes et al., Phys. Rev. lett. 68(1992)460.

[PS92b] P.B. Semmes et al., private communication.

[PT73] P.J. Twin, Nucl. Instr. Meth. 106(1973)481.

[PT85] P.O. Tjøm et al., Phys. Rev. Lett. 61(1988)46.

[PW85] G. Palameta and J.C.Waddington, Nucl. Instr. and Meth. A234 (1985)476.

[RB89] R. Bengtsson et al., Phys. Scr. 39(1989)196.

[RB90] R. Bengtsson et al., Nucl. Phys. A512(1990)124.

[RC92] R.M. Clark, private communication (1992).

[RE55] R.D. Evans, "The Atomic Nucleus" (1955) M^{c}Graw-Hill.

[RG75] R.D. Gill "Gamma-Ray Angular Correlations" Academic Press(1975).

[RS80] P. Ring and P. Schuck "The Nuclear Many-Body Problem" (1980) Springer-Verlag

[SJ87] P.J. Siemens and A.S. Jensen, "Elements of Nuclei" (1987) Addison and Wesley

[SF92] Sally Forbes, PhD thesis, University of Liverpool, 1992.

[SH65] S.M. Harris, Phys. Rev. 138(1965)B509.

[TB87] T. Byrski et al., Nucl. Phys. A474(1987)193.

[TB90] T. Bengtsson et al., Nucl. Phys. A512(1990)124.

[VP92] V.F.E.Pucknell, IEEE Trans. on Nucl. Sci. 39(1992)892.

[VS67] V.M. Strutinsky, Nucl. Phys. A95 (1967) 420.

[WB79] W.E. Burcham, "Elements of Nuclear Physics" (1979) Longman Scientific and Technical.

[WN84] W. Nazarewicz et al., Phys. Rev. Letts. 52(1984)1272.

[WN90] W. Nazarewicz et al., Nucl. Phys. A512(1990)61.

[WN93] W. Nazarewicz Proc. of Requiem for an Accelerator (1993) Daresbury Laboratory, SERC, U.K.